Advancements in Langmuir probe diagnostic for measurements in RF sheath and in modelling of the ICRF slow wave

Mariia Usoltceva

École doctorale "C2MP" ED 606
Sciences et Technologies

Thése

pour l'obtention du titre de

Docteur de l'Université de Lorraine

présentée par:

Mariia Usoltceva

Advancements in Langmuir probe diagnostic for measurements in RF sheath and in modelling of the ICRF slow wave

Thèse soutenue publiquement le 26 Avril 2019 à Nancy devant le jury composé de:

Prof. Gérard Henrion	Président du jury - ULorraine
Prof. Daniel De Zutter	Co-président du jury - UGent
Prof. Hartmut Zohm	Rapporteur - MPI
Prof. Stéphane Bechu	Rapporteur – CNRS Grenoble
Prof. Hendrik Rogier	Examinateur - UGent
Prof. Jean-Marie Noterdaeme	Examinateur - UGent/MPI
Prof. Kristel Crombé	Co-directeur de thése - UGent/ERM
Prof. Stéphane Heuraux	Co-directeur de thése - ULorraine
Dr. Eric Faudot	Co-directeur de thése - ULorraine

IJL - Université de Lorraine, Ghent University

Acknowledgments

"I've heard it said
That people come into our lives for a reason,
Bringing something we must learn."
"Wicked" the musical

This work would not be possible without the people who supervised, directed and advised me during the 3.5 years: Dr. Roman Ochoukov (IPP Garching), Dr. Eric Faudot (IJL, Université de Lorraine), Prof. Stéphane Heuraux (IJL, Université de Lorraine), Prof. Kristel Crombé (Ghent University) and Prof. Jean-Marie Noterdaeme (IPP Garching/Ghent University). I had a chance to learn from them many aspects of physics and of scientific skills in general. Thank you all for the amount of work you have done to ensure my progress and achievement of the final result – this doctoral dissertation. I would also like to acknowledge the high quality of the Fusion-DC program and its great variety of the learning opportunities for young scientists, I am glad to be a part of this international program.

Many other people also helped and supported me in my PhD work. I am grateful to the ICRF department of IPP and to the plasma physics group of ULorraine, as well as to external collaborators. I am pleased to acknowledge the help offered by Ana Kostic, Guillermo Suárez, Wouter Tierens, Jonathan Jacquot, Rodolphe D'Inca, Stéphane Devaux, Georgiy Zadvitskiy, Jordan Cavalier and others during the course of this work. We shared very interesting theoretical discussions, experimental time on the test stands, data analysis, exchange of ideas, etc. I hope to continue fruitful collaboration with many of them in the future.

I am happy that I had friends who surrounded me in always nice and friendly atmosphere during the years in Garching. Thanks to Anton for bringing me to the river surfing and for guaranteeing me a black eye on my very first week at work. Serhiy, you have been always a very welcoming and fun friend to me and we won so many battles together. Dmytro, thank you for introducing me to the tasty food of France and to many other nice things from the French life, as well as for the discussions of the plasma physics theory. My big gratitude to Wanja for wonderful photos, for your patience, kindness and for the inspiration. With Filip we have had a great time enjoying the nature, mountains, sheep, fish, swimming and skiing. Ana has been a very close person to me, not only because her table was next to mine in the office, but because we shared so many discussions and even some adventures. Thanks to all great people in Garching, so many awesome things happened, that I cannot recall them all.

Thanks to Georgiy for the best time in Nancy, for making my dreams come true and just for being a very good friend. Jordan, I appreciate that you controlled the quality of the tea. I am very grateful to Sophie and Eric with whom I had luck to live under the same roof. They showed incredible hospitality

and made me feel at home in a new country. Thanks to all amazing people who I met in France and had very nice time with.

As going through the years of the PhD research also means going through the years of constantly changing and challenging life, thanks to my family for supporting me through it and to Ramon, I am who I am today because I know you and because of all I learned from you, for good.

Summary of the thesis

Coupling power to the plasma with ion cyclotron range of frequencies (ICRF) waves is a promising method for heating tokamak plasmas to fusion relevant temperatures. To ensure good ICRF wave accessibility to the plasma center, the ICRF antenna must be placed close to the plasma. In experiments on multiple tokamaks, active ICRF antennas modify key plasma edge parameters (electron temperature, plasma density, and plasma potential), as well as enhance plasma-wall interactions, i.e. changes in the edge plasma density profiles, increased heat loads and hot spot formations on limiters and enhanced sputtering of plasma facing components. The plasma ions accelerated in the radio-frequency (RF) sheath have been found to be the main cause of the observed deleterious effects. RF sheath is an additional sheath that exceeds standard Bohm sheath in voltage and is present during active ICRF operation. ICRF parallel electric field accelerates electrons towards the wall along the magnetic field lines; it leads to a negative charge on the surfaces and a positive charge of the bulk edge plasma where slow ions remain. At the end a DC potential is formed between the wall and the plasma and such a process, called RF sheath rectification, leads to further strong acceleration of ions into the plasma facing components.

No unified guideline exists on optimal ICRF antenna design, as observed effects and found solutions differ from one machine to another. Conclusions are usually empirical and based on consequential parameters like impurities concentration, RF currents or temperature of antenna limiting structures, but not on the direct measurements of the RF-induced parallel electric field. Such measurements are hard to perform in a tokamak. One of possible approaches to study parallel electric field of an ICRF antenna directly is to move to a simple specially designed experiment.

This thesis presents work carried out on two dedicated devices, Aline (A LINear Experiment) and IShTAR (Ion cyclotron Sheath Test Arrangement), testbeds that are fully focused on ICRF studies and exhibit plasma conditions that are similar to the tokamak edge but quite simplified in order to provide easier accessibility for dedicated diagnostics and to decouple ICRF physics from many other phenomena existing in a complex plasma machine.

Aline is a linear low-temperature plasma device with a capacitive radio-frequency discharge created by a simple antenna of a disk shape and it focuses on plasma characterization with the Langmuir probe diagnostic. The diagnostic setup has numerous advantages over common Langmuir probes setups in tokamaks. The probe inside the plasma vessel can be exchanged or modified quickly and at any time, even during the experimental day. A Langmuir probe is fixed on a 3D movable manipulator. The movement accuracy is 10 μm which is required to achieve precise spatial resolution for measurements in a sheath, the later itself being of the order of μm-mm size. The probe can reach the whole space around the RF antenna which is centered in the vacuum chamber. Very long (hours) and stable plasma discharges guarantee reliable measurements and absence of transient events changing the density profile globally or locally.

To be able to do measurements for the RF sheath relevant studies, it is first necessary to develop a routine method of Langmuir probe data analysis in magnetized plasma that would be applicable in quite broad range of plasma conditions characteristic for Aline. The presence of magnetic field leads to the fact that conventional methods of data analysis are not applicable, because of completely different particle transport in magnetized plasma compared to the non-magnetized one, especially when using small cylindrical Langmuir probes parallel to the magnetic field or at a small angle to it. This case is realized in Aline and such probes are the most suitable for measurements in narrow sheaths.

In this thesis theories are presented which were developed for Langmuir probe data processing for magnetized plasma and which finally enabled measurements on Aline in the presence of the magnetic field. Techniques for density, temperature and plasma potential extraction from the data are described. First results of Langmuir probe density measurements in magnetized plasma on Aline are also presented, as well as measured line-averaged densities by interferometry and its comparison to the probe data. Presented data analysis techniques are not only important for application on Aline but can be used on any machine with magnetized plasma, including tokamaks.

IShTAR is even closer to tokamak conditions for ICRF waves and plasma interactions than Aline. The main difference is the antenna, which mimics tokamak ICRF antennas. A metallic strap couples power inductively to plasma, it is surrounded by limiters and the geometry is adjusted to the plasma shape to replicate poloidal symmetry.

In the framework of this thesis the objective is to study comprehensively the ICRF wave propagation in IShTAR configuration and to explore different scenarios. The first step of the study included development, installation and calibration of Langmuir probe and B-dot probe diagnostics to quantify the relevant plasma parameters (plasma density, electron temperature, plasma potential in the vicinity of the antenna) and the relevant ICRF wave fields (components of magnetic field). At the same time a 3D model of IShTAR was developed in COMSOL software and first straightforward comparisons were possible for vacuum fields. COMSOL simulations also allowed performing studies of the B-dot probe calibration and the field disturbance by a probe.

ICRF wave propagation is calculated theoretically for IShTAR conditions and it is concluded that only the slow wave mode of ICRF waves can propagate and be studied in IShTAR. Therefore it is possible to decouple the role of the different ICRF modes in contributing to the RF sheath effects. Numerical simulations of the ICRF slow wave were done in COMSOL software. Plasma was implemented as a material with manually assigned physical properties. Field structures obtained for the slow wave differ significantly from the other mode, the fast wave, and exhibit strong dependence on the density profile on the plasma edge. COMSOL software is a powerful tool, able to provide not only spatial distribution of all components of the fields, but also absorbed power, Poynting vector, current on the antenna strap and much more.

The last necessary task was to measure the power sent to plasma in IShTAR experiments in order to adjust the experimental matching system and to calibrate COMSOL simulations and obtain correct absolute values of the fields. Forward and reflected power was measured in the matched line with a directional coupler, and some conclusions have been drawn based on these results. Further necessary measurements are described.

Experimental, theoretical and numerical results of the work included in this thesis contribute to the goal of studying RF sheath physics on dedicated linear devices, as well as to the physics of ICRF waves on the plasma edge in general. In ICRF simulations for tokamak devices such as RAPLICASOL or TOPICA the edge plasma layer is replaced with a vacuum layer and the whole part of the slow wave propagation on the edge is avoided. Results of this thesis can be used to improve the complex tokamak ICRF simulations.

Résumé de la thèse

Injecter de la puissance dans un plasma magnétisé via des ondes à des fréquences proches des Fréquences Cyclotrons Ioniques (FCI) est une méthode prometteuse pour chauffer les plasmas de tokamak jusqu'aux températures requises pour réaliser la fusion thermonucléaire. Pour s'assurer que le maximum de puissance portée par l'onde FCI atteigne le centre du plasma, l'antenne FCI doit être placée au plus proche du plasma de bord. Dans des expériences réalisées sur de nombreux tokamaks, il a été observé que les antennes FCI activées modifient les paramètres clés de bord de tokamaks (température électronique, densité et potentiel plasma) et augmentent les interactions plasma/parois, comme le montre des changements dans les profils de densité, l'augmentation des flux de chaleur et de formation de points chauds sur la structure d'antenne, et l'accroissement de la pulvérisation de la paroi exposée au plasma. Il a été démontré que l'accélération des ions dans la gaine radio-fréquence (RF) est la cause principale des effets délétères mentionnés précédemment. La gaine RF est une séparation de charges oscillante dont la tension continue est généralement supérieure à celle de la gaine classique de Bohm. Ce type de gaine est présent durant l'utilisation du chauffage FCI. Le mécanisme générateur de cette tension continue élevée s'appuie sur le champ électrique parallèle qui accélère les électrons en direction de la paroi le long des lignes de champ magnétique; la paroi se charge alors négativement et le bord de plasma positivement du fait de l'inertie des ions, donc peu mobiles. A l'équilibre, un potentiel DC se forme entre la paroi et le plasma et un tel phénomène, appelé redressement RF induit par la gaine RF, "RF rectification" en anglais, conduit à une forte accélération supplémentaire des ions vers les éléments de la paroi faisant face au plasma pour maintenir la quasi-neutralité du plasma.

Il n'existe pas de solution optimale concernant la fabrication d'antenne FCI, puisque les effets observés et les solutions trouvées sont différents d'une machine à l'autre. Les règles de conception sont en général empiriques et basées sur des paramètres induits tels que la concentration d'impuretés, le courant RF ou la température de la structure protégeant l'antenne, plutôt que sur la mesure directe du champ électrique parallèle RF. La raison est que de telles mesures sont difficiles à réaliser sur un tokamak, et il est alors préférable d'étudier le champ électrique parallèle d'une antenne FCI sur une machine simple et spécialement conçue à cet effet.

Cette thèse synthétise le travail réalisé sur deux machines, Aline (A LINear Experiment) et IShTAR (Ion cyclotron Sheath Test Arrangement), bancs d'essai dédiés aux études reliées au chauffage FCI car possédant des conditions plasma similaires à celles des plasmas de bord de tokamaks, mais ces bancs sont simplifiés, pour permettre des mesures à l'aide de diagnostics dédiés et pour mieux découpler la physique du chauffage FCI des nombreux phénomènes complexes existant dans les tokamaks.

Aline est une machine linéaire dans laquelle une décharge capacitive RF est créée par une simple antenne en forme de disque et dont la caractérisation du plasma est principalement réalisée à l'aide de sonde de Langmuir. L'implémentation du diagnostic dans cette machine a de nombreux avantages par rapport à l'utilisation classique des sondes de Langmuir dans les tokamaks. Par exemple, la sonde à l'intérieur de la machine peut être changée ou modifiée rapidement et n'importe quand, même durant un jour où des expériences sont planifiées. Ce dispositif expérimental comporte une sonde de Langmuir fixée sur un manipulateur se déplaçant en 3D. Le positionnement de la sonde s'effectue en théorie à 10 micromètres, précision requise pour obtenir une résolution spatiale suffisamment fine dans la gaine, celle-ci ayant une taille de l'ordre d'une centaine de microns aux millimètres. La sonde peut atteindre tout l'espace autour de l'antenne RF. Des décharges stables sur les longs temps (plusieurs heures) garantissent des mesures fiables et l'absence d'événements transitoires qui pourraient modifier le profil de densité globalement ou localement.

Afin d'être capable de réaliser des mesures pertinentes dans le cadre de l'étude des gaines RF, il est d'abord nécessaire de développer une méthode d'analyse des données de sonde de Langmuir en plasma magnétisé pouvant être utilisée dans une large gamme de paramètres plasma accessibles sur Aline. La présence d'un champ magnétique a pour conséquence de rendre les méthodes conventionnelles d'analyse des données de sonde non applicables, en raison du transport complètement différent des particules par rapport au cas non magnétisé, en particulier lors de l'utilisation de petites sondes cylindriques de Langmuir parallèles au champ magnétique ou possédant un petit angle avec celui-ci. Ce cas de figure correspond à ce qui est réalisé sur Aline car ce type de sonde est le mieux adapté aux mesures dans des gaines généralement peu larges.

Dans cette thèse, les théories présentées ont été développées pour l'analyse des données de sondes de Langmuir dans les plasmas magnétisés et permettent des mesures pertinentes sur Aline en présence d'un champ magnétique. Des techniques pour l'obtention de la densité, de la température et du potentiel plasma à partir des données expérimentales sont décrites. Les premiers résultats de mesure de densité par sonde de Langmuir sur Aline en présence d'un champ magnétique sont présentés, ainsi que des mesures de densité intégrée le long de la ligne de visée d'un interféromètre et leur comparaison aux données de sonde. Les techniques d'analyse présentées ne sont pas seulement importantes pour les études réalisées sur Aline mais peuvent également être utilisées sur n'importe quelle machine à plasma magnétisé, incluant les tokamaks.

La machine IShTAR se rapproche encore plus des conditions que l'on trouve dans un tokamak pour les ondes FCI et les interactions plasma que celles présentes dans Aline. La différence principale réside dans l'antenne qui, dans le cas d'IShTAR, copie les antennes FCI des tokamaks. Un ruban métallique sert à coupler la puissance émise par l'antenne au plasma, celle-ci étant entourée par des limiteurs et ayant une géométrie adaptée à la forme du plasma pour préserver la symétrie poloidale.

Dans cette partie l'objectif est d'étudier en détails la propagation des ondes FCI dans les différentes configurations d'IShTAR et d'explorer différents scénarios possibles. La première étape de l'étude inclut le développement, l'installation et la calibration de diagnostic des sondes de Langmuir pour quantifier les paramètres plasma pertinents (densité plasma, température électronique, potentiel plasma proches de l'antenne) et les champs FCI (composantes du champ magnétique) avec des sondes dénommées B-dot. En parallèle, un modèle numérique 3D de IShTAR a été développé à l'aide

du logiciel COMSOL. Ce modèle a permis d'effectuer les premières comparaisons avec des mesures ses champs dans le vide. Les simulations COMSOL permettent également de réaliser des études pour la calibration de la sonde B-dot et de la perturbation du champ produite par la sonde.

La propagation des ondes FCI a été calculée théoriquement pour les conditions réalisées sur IShTAR et il est démontré que seul le mode lent émis par l'antenne FCI se propage et peut être étudié sur cette machine. Par conséquent, il est possible de découpler le rôle des différents modes FCI contribuant à l'effet RF sur la gaine. Dans ce cadre, des simulations numériques d'ondes FCI ont été réalisées à l'aide du logiciel COMSOL. Pour cela le plasma a été modélisé par un milieu à propriétés physiques fixées manuellement. Les structures du champ obtenues pour le mode lent sont significativement différentes de celles obtenues pour l'autre mode, dit "rapide", et manifestent une forte dépendance avec le profil de densité du plasma de bord. Le logiciel COMSOL semble être un outil puissant, capable non seulement d'obtenir la distribution spatiale de tous les composants des champs, mais aussi la puissance absorbée, le vecteur de Poynting, le courant sur le « strap » de l'antenne et bien plus.

Le dernier objectif fut de mesurer la puissance reçue par le plasma dans les expériences réalisées sur IShTAR afin d'ajuster le système d'accord d'impédance, de calibrer les simulations COMSOL et obtenir des valeurs absolues correctes des champs. Les puissances émise et réfléchie ont été mesurées avec un coupleur directionnel, et des conclusions ont été tirées basées sur ces résultats. Les mesures plus poussées à effectuer pour la poursuite de cette étude sont également décrites dans cette thèse.

Les résultats expérimentaux, théoriques et numériques du travail inclus dans cette thèse contribuent aux études de la physique des gaines RF sur des machines dédiées à ce sujet, ainsi qu'à la physique des ondes FCI en bord de plasma en général. Dans les simulations FCI pour les tokamaks, telles que les simulations RAPLICASOL ou TOPICA, la couche de plasma de bord est remplacée par une couche de vide afin de supprimer la propagation de l'onde lente sur le bord du plasma. Les résultats de cette thèse peuvent être utilisés pour étudier l'effet de ce mode, usuellement négligé, et pour améliorer les simulations complexes des tokamaks FCI.

x

Samenvatting van het proefschrift

Het koppelen van vermogen in een plasma via radiofrequente (RF) golven, waarvan de frequentie overeenstemt met de cyclotronfrequentie van de ionen rond het magneetveld, is een geschikte manier om plasma's in een tokamak te verhitten tot de hoge temperaturen die nodig zijn voor kernfusie. Deze methode wordt meestal afgekort als ICRF (ion cyclotron range of frequencies) verhitting. Om het centrum van het plasma te kunnen bereiken moet de ICRF antenne dichtbij de plasmarand worden geplaatst. In experimenten in vele tokamaks verandert echter een actieve ICRF antenne belangrijke parameters van het randplasma (zoals de temperatuur van de elektronen, de plasmadichtheid, en de plasmapotentiaal). Bovendien worden de plasma-rand-interacties versterkt, de dichtheidsprofielen aan de rand veranderen, en ongewenste verhitting van bepaalde antenne- en randcomponenten kan leiden tot zogenaamde 'hot-spots' en een verhoogde 'sputtering' van wand- en antennematerialen. Ionen die versneld worden in de RF 'sheath' zijn de belangrijkste oorzaak van deze ongewenste effecten. De RF sheath is een bijkomende sheath bovenop de standaard Bohm sheath, die opgewekt wordt tijdens ICRF operatie via het volgende mechanisme: de component van het oscillerende ICRF elektrisch veld die parallel is aan het magneetveld, versnelt elektronen naar de wand van de machine langs de magneetveldlijnen. Dit leidt tot een negatieve lading op het metaaloppervlak en een positieve lading in het randplasma, waar de zware ionen achterblijven. Uiteindelijk wordt een DC potentiaal gevormd tussen de wand en het plasma. Dit proces van gelijkrichting heet 'RF sheath rectification' en versnelt de ionen uit het plasma naar de randcomponenten. De ionen zijn zwaar en kunnen door hun impact wandmaterialen beschadigen.

Er bestaan geen standaard richtlijnen om een ICRF antenne optimaal te ontwerpen om deze effecten tegen te gaan. De gevonden oplossingen verschillen van machine tot machine en zijn tot hiertoe gebaseerd op empirische resultaten en ad-hoc aanpassingen afhankelijk van machine- en plasmaparameters, zoals de onzuiverheidsconcentratie, de RF stromen of de temperatuur van de randstructuren van de antenne. Een directe meting van de parallelle elektrische velden geïntroduceerd door de RF operatie is nergens routinematig beschikbaar, omdat ze zeer moeilijk te meten zijn in een tokamak plasma. Daarom werd geopteerd om experimenten uit te voeren op specifiek ontworpen opstellingen voor dit probleem, die eenvoudiger zijn dan de complexe fusiemachines.

Voor de thesis werd gewerkt op twee opstellingen die speciaal zijn ontworpen voor studies van ICRF sheaths en die plasma's hebben die gelijkaardig zijn aan plasma's aan de rand van een tokamak. Het zijn Aline (A LINear Experiment) en IShTAR (Ion cyclotron Sheath Test Arrangement). De opstellingen zijn gemakkelijk toegankelijk voor het installeren en testen van nieuwe diagnostieken en maken het mogelijk om de ICRF fysica te ontkoppelen van andere fenomenen. Dit alles is veel moeilijker in een complexe plasmamachine.

Aline is een lineaire opstelling waarbij lage-temperatuur plasma's worden gecreëerd met een capacitieve RF ontlading m.b.v. een schijfvormige antenne. Met een Langmuir sonde worden de

plasma parameters gekarakteriseerd. De sonde kan gemakkelijk en snel verwisseld worden, zelfs tijdens een dag met experimenten. Ze is gemonteerd op een manipuleerbare arm die in 3 richtingen kan bewegen, en tot 10 µm nauwkeurig kan worden gepositioneerd. Deze hoge ruimtelijke precisie is nodig om in de sheath te kunnen meten. De sheath heeft immers een radiale dimensie van enkele µm tot enkele mm, afhankelijk van de plasmadichtheid. De sonde kan de volledige ruimte rond de RF antenne bereiken. De RF antenne bevindt zich in het centrum van het vacuümvat van Aline. Het plasma is stabiel voor lange ontladingen (tot enkele uren) waardoor betrouwbare metingen uitgevoerd kunnen worden, zonder dat er met overgangsverschijnselen rekening moet worden gehouden, die de plasmaprofielen lokaal of globaal zouden kunnen veranderen.

Om metingen te kunnen doen die relevant zijn voor de studies rond RF sheaths, is het nodig om eerst de data van de Langmuir sondes in een gemagnetiseerd plasma routinematig te kunnen analyseren, tenminste voor de typische plasmacondities in Aline. Door het magneetveld zijn conventionele methodes echter niet bruikbaar, omdat het deeltjestransport te sterk verschilt van een niet-gemagnetiseerd plasma. Dit is zeker van belang wanneer een dunne cilindervormige Langmuir sonde wordt gebruikt, die bovendien parallel aan het magneetveld gericht is, of zelfs onder een kleine hoek. Deze oriëntatie is precies van toepassing voor Aline, omdat dergelijke sondes het meest geschikt zijn om in de dunne laag van de sheath te meten.

In de thesis worden theorieën voorgesteld die werden ontwikkeld voor het analyseren van data van Langmuir sondes in een gemagnetiseerd plasma. Daardoor was het mogelijk om betrouwbare metingen in de plasma's in Aline uit te voeren. Technieken worden beschreven voor het afleiden van de plasmadichtheid, de temperatuur en de plasmapotentiaal uit de ruwe data. De eerste resultaten van dichtheidsmetingen met de Langmuir sonde op Aline worden eveneens voorgesteld. Deze worden vergeleken met lijn-geïntegreerde dichtheden verkregen met een interferometer. De in deze thesis ontworpen data-analyse beperkt zich echter niet tot de Aline opstelling. Ze kan eveneens worden gebruik in andere plasmamachines met een magneetveld, zoals de meer complexe tokamaks.

De IShTAR (Ion cyclotron Sheath Test Arrangement) opstelling staat dichter bij een tokamak voor wat ICRF golven en plasma interactie betreft dan Aline. Het belangrijkste verschil is de antenne, die een vereenvoudigde tokamak ICRF antenne is. Een metalen strip koppelt vermogen op een inductieve manier in het plasma. Rond de strip zijn limiters (begrenzende componenten) aangebracht en de geometrie is aangepast aan de vorm van het plasma, zodat een poloïdaal symmetrisch probleem ontstaat, gelijkaardig aan de situatie in een tokamak.

In deze thesis werd de voortplanting van ICRF golven in IShTAR bestudeerd in verschillende operationele scenario's. De eerste stap van de studie was de ontwikkeling, de installatie en de kalibratie van Langmuir sondes om de relevante plasma parameters te meten (de plasma dichtheid, de elektronen temperatuur, de plasma potentiaal in de buurt van de antenne) en van B-dot sondes om de velden van de ICRF golven (in dit geval zijn dat de componenten van het magneetveld) te kennen. Tegelijkertijd werd een 3D model van IShTAR ontwikkeld met het COMSOL software pakket. In vacuüm waren de vergelijkingen tussen het model en de experimentele metingen vrij eenvoudig en succesvol. Dankzij de COMSOL simulaties was het mogelijk om de kalibratie van de B-dot te bestuderen alsook de perturbatie door de sonde op het totale magneetveld.

De voortplanting van de ICRF golven in IShTAR plasma's werd theoretisch berekenend en er werd gevonden dat enkel de trage golf component van de oplossing kan propageren in IShTAR. Daardoor is het inderdaad mogelijk om de rol van de verschillende ICRF modes bij de RF sheath effecten apart te bestuderen, wat precies de opzet was van IShTAR. Numerieke simulaties van de ICRF golven zijn

gebeurd in COMSOL. Het plasma werd geïmplementeerd als een materiaal waarvan de fysische eigenschappen manueel werden gedefinieerd. De veldstructuren die werden gevonden voor de trage golf component, verschillen fundamenteel van die van de snelle golf, en blijken sterk afhankelijk van het dichtheidsprofiel van het randplasma. De COMSOL software is een krachtig pakket dat niet alleen de ruimtelijk verdeling van alle veldcomponenten berekend, maar ook het geabsorbeerd vermogen, de Poynting vector, de stroom op de antenne strip en veel meer.
De laatste stap was om het vermogen dat in het plasma wordt gestuurd bij een IShTAR experiment te meten, om zo de experimentele matching goed te kunnen bepalen en de simulaties in COMSOL te kunnen kalibreren, zodat ook de absolute waarde van de veldcomponenten vastgelegd kan worden. De voorwaartse en gereflecteerde fracties van het vermogen werden gemeten met een directionele koppeling. De eerste conclusies gebaseerd op deze resultaten worden beschreven, maar verdere metingen zijn nog nodig.
De experimentele, theoretische en numerieke resultaten van het werk in deze thesis dragen in het bijzonder bij tot het bestuderen van de RF sheath op de twee lineaire machines, Aline en IShTAR. Bovendien helpen ze ook meer algemeen om de fysica van ICRF golven in randplasma's te begrijpen. Vaak wordt in ICRF simulaties van tokamaks de plasmarand immers vervangen door vacuüm laag. De gebruikte eindige elementen methodes slagen er immers meestal niet in om te convergeren rond de lower hybrid (LH) resonantie zone. Dit is bijvoorbeeld het geval in codes als RAPLICASOL of TOPICA. Doordat plasma's met lage dichtheden (beneden de LH resonantie) worden benaderd door vacuüm, zal daarmee ook de hele fysica van de trage golf van tafel worden geveegd, alsook het effect ervan op de RF sheaths. De resultaten van deze thesis kunnen een eerste stap zijn om deze zone op de vullen met een lage dichtheidsplasma en zo de complexe simulaties van ICRF golven in tokamaks te verbeteren, althans voor de condities waarvoor een convergent resultaat kon worden gevonden.

Content

Acknowledgments ..... *i*

Summary of the thesis ..... *iii*

Résumé de la thèse ..... *vii*

Samenvatting van het proefschrift ..... *xi*

Content ..... *xv*

1 Introduction 1

1.1 Plasma heating 1

1.2 Plasma in a tokamak 2

1.3 Ion Cyclotron Resonance Heating 3

1.3.1 ICRF wave issues on the plasma edge – RF sheath 3

1.4 Dedicated experimental devices for RF sheath studies 5

1.4.1 Aline 6

1.4.2 IShTAR 8

References 11

2 Theoretical and experimental background of this thesis 13

2.1 Theory of ICRF waves 13

2.1.1 Wave equation and dielectric tensor 13

2.1.2 Wave propagation: cut-off and resonance 16

2.1.3 Electric field polarization 17

2.1.4 Shapes of the wavefront 19

2.2 RF wave energy absorption 22

2.3 RF modelling in COMSOL software 23

2.3.1 COMSOL and its existing applications for fusion plasma 23

2.3.2 Framework of simulations for IShTAR 24

2.3.3 Perfectly Matched Layer (PML) in COMSOL 25

2.4 Basics of diagnostics employed in this thesis 27

2.4.1 Langmuir probe 27

2.4.2 B-dot probe 29

2.4.3 Interferometry 30

2.5 Conclusions 33

References 33

3 Langmuir probe diagnostic on Aline 37

3.1 State of the art of Langmuir probe data analysis in magnetized plasma 37

3.2 Criterion of plasma magnetization 39

3.3 Current collection at plasma potential 39

3.4 General theory for a probe at arbitrary angle 41

3.4.1 Effective collecting area 41

3.4.2 Application to experimental data 43

3.4.3 Comparison to Laframboise-Rubinstein theory 46

3.4.4 Peculiarities of the theory application 48

3.5 Precise theory for a probe parallel to B 49

3.5.1 Effective collecting area 50

3.5.2 Application to experimental data and comparison with interferometry measurements 53

3.6 Applicability analysis 56

3.7 Plasma potential evaluation 58

3.7.1 Plasma potential from 1^{st} derivative 58

3.7.2 Plasma potential at intersection 59

3.8 Electron temperature evaluation 61

3.9 Conclusions 64

References 65

4 ICRF waves in IShTAR 67

4.1 Waves in IShTAR in cold plasma approximation 67

4.2 Calibration of magnetic diagnostic components in experiments and simulations 69

4.2.1 Calibration of logarithmic detectors 71

4.2.2 B-dot probe radial calibration in the coaxial line 73

4.2.3 Disturbance of the fields by the presence of a B-dot probe 76

4.2.4 Field evanescence inside a B-dot probe 81

4.3 Experimental magnetic field of the IShTAR ICRF antenna waves 83

4.4 COMSOL model of IShTAR with vacuum 85

4.5 3D modelling of the slow wave 89

4.5.1 Plasma implementation and testing in COMSOL 89

4.5.2 Results with antenna in vacuum 91

4.5.3 Results with antenna in plasma 93

4.5.4 Results with collisional losses 95

4.5.5 Results with antenna limiters 98

4.6 Power coupled to plasma in IShTAR 100

4.6.1 Measurements in matched line 101

4.6.2 Matching system in COMSOL 103

4.6.3 Outlook for future measurements 106

4.7 Conclusions 106

References 108

Conclusions 109

1 Introduction

1.1 Plasma heating

Plasma is a quasineutral gas of charged and neutral particles, which exhibits collective properties. Plasma state of matter is achieved by transferring energy to gas. A simplest example is the Townsend discharge where free electrons in gas are accelerated by an electric field and strike at increased velocities into neutral atoms or molecules, releasing further electrons, producing ions and starting an electron avalanche. Thereby a plasma discharge is formed. In a discharge the ionization process in general can result from collisions with other atoms, molecules and ions, as well as with subatomic particles, or through interaction with electromagnetic fields. Simultaneous recombination processes lead to plasma destruction. The same negative outcome happens in any system with finite dimensions due to charged particles hitting the walls. Only with sufficient energy input can ionization processes be sustained on a level exceeding charged particle loss. The energy transfer, which is in many cases equal to plasma heating, is an essential process for the plasma production and maintenance.

With sufficient plasma heating it is possible to achieve conditions where interesting physics processes start to happen, such as thermonuclear fusion of fully ionized atoms. The order of magnitude of the temperature needed for such a process is a few hundred million degrees Celsius, or a few tens of keV. Corresponding conditions are naturally present in stars and are attempted to be achieved on Earth by means of creating and confining hot plasma. The confinement method relevant to the present study is the magnetic confinement. This approach to produce thermonuclear fusion power is one of the major topic of fusion energy (and in general sustainable energy) research. The reason for this is the fact that it has been actively developed since 1940s, has undergone major breakthroughs since then and is more promising for a reactor power production than other fusion research areas. A possibility to control the amount of power outcome is something that differs fusion greatly from renewable energy sources and places it high in sustainable energy research priorities.

Present day experiments of magnetic confinement fusion focus their studies on a whole range of physics challenges that need to be solved in order to achieve stable power generation: materials that face plasma, particle transport, plasma diagnostics, magnetic configurations, etc. Plasma heating is among them. Many heating techniques use electromagnetic radiation: Electron Cyclotron Resonance Heating (ECRH), Lower Hybrid Heating (LH), Ion Cyclotron Resonance Heating (ICRH); another method is based on kinetic energy transfer from fast moving neutral particles sent from outside plasma – Neutral Beam Injection (NBI); and ohmic heating is achieved by driving a current through plasma.

1.2 Plasma in a tokamak

Magnetic confinement fusion concept is based on the idea of limiting outgoing particle and energy flux from plasma by applying magnetic field and thus confining plasma in a limited volume and keeping plasma particles on certain looped tracks defined by the magnetic field configuration. The most common device for magnetic confinement fusion studies is a tokamak, a toroidal vacuum chamber with external magnetic coils (Fig. 1.1). Toroidal magnetic field is created by the coils and plasma particles spiral around the magnetic field lines instead of freely running away in all directions. However, a toroidal field alone is not enough because of its asymmetry on the outer and inner sides of the torus (stronger on the inner side) that leads to radial drifts of plasma particles and to quick loss of confinement. An additional poloidal magnetic field is created by a current driven through plasma in toroidal direction. The resulting twisted magnetic field provides much better confinement and is thus used as a basis model for fusion studies.

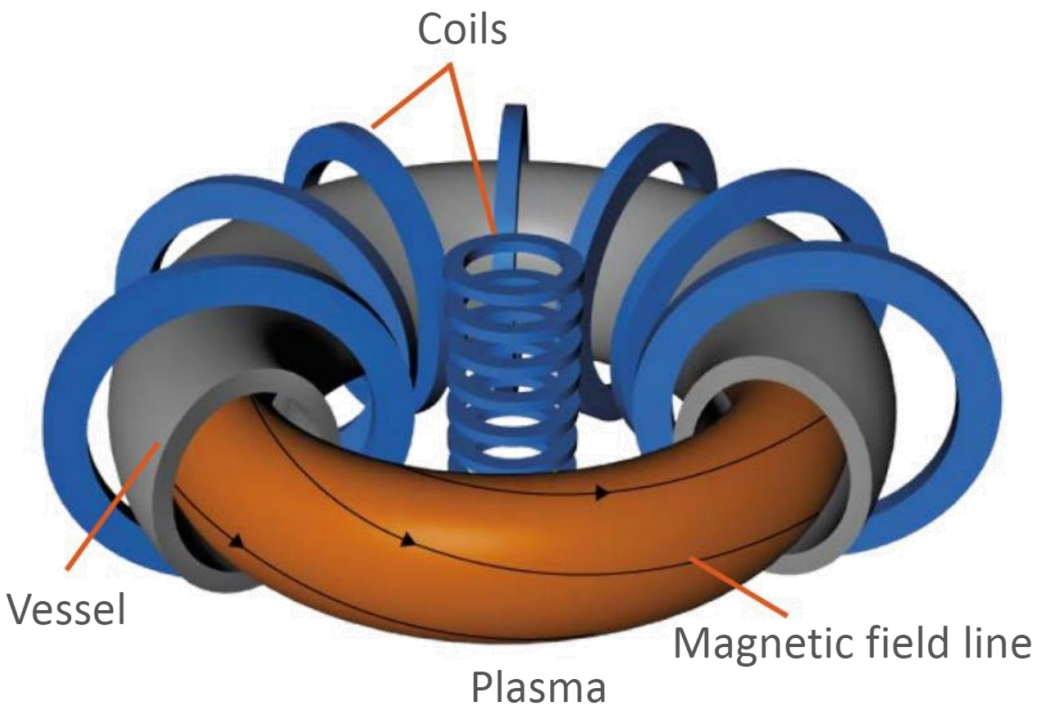

Fig. 1.1. Tokamak schematic representation.

In the same device plasma hot core and cold metallic vacuum vessel coexist and their interaction needs to be minimized. The few last centimeters of plasma, called plasma edge, is a very important boundary where physics different from the plasma core physics happens. Huge gradients of plasma parameters appear on very small spatial scale. Examples of plasma density and temperature profiles in a tokamak in so-called H-mode (high confinement mode) are shown in Fig. 1.2 as functions of dimensionless radius ($\rho = 1$ at the last closed magnetic surface – separatrix). H-mode is characterized by high and relatively constant density values in the center and very fast decay on the edge associated with the formation of edge transport barrier. The decay length and the core high values are correlated strongly with what is happening in the thin layer near the separatrix. At the

current stage of the fusion research, the physics of the plasma edge is at least as important as the physics of the core plasma or even more important considering the amount of diagnostics concentrated on measurements there and great variety of configurations that need to be studied.

Plasma parameters in present day tokamaks are constantly monitored during a plasma discharge and depending on their evolution all systems interacting with plasma must adjust their behaviour. It needs to be done firstly to prevent plasma disruptions that can be dangerous for the machine and secondly to increase the performance or to achieve specific parameters of a discharge. ICRH is one of the systems that are very sensitive to the shifts in the density profile; its efficiency can change dramatically if plasma conditions vary.

1.3 Ion Cyclotron Resonance Heating

Charged particles are sensitive to electromagnetic fields, under their influence particles can change the direction of movement, slow down or accelerate. The latter process is equivalent to gaining energy, or in other words to "heating" of plasma particles. Non-zero net energy transfer happens when resonant conditions are present. An example of such resonance is a wave with the same frequency ω as the frequency of ions rotation around magnetic field lines (Larmor frequency) Ω_{ci}.

The principle of an ICRH system is schematically explained in Fig. 1.3. At first, radio-frequency (RF) signal at 25-100 MHz is generated using the power from the electrical grid. It is amplified and sent to the tokamak via coaxial transmission lines. This kind of waveguides is suitable for transferring electromagnetic waves of the RF frequency range. A metallic strap, connected at one end to the inner conductor of the transmission line and grounded on the other end, serves as an antenna. The RF current flowing on its surface excites electromagnetic waves which can propagate in plasma. A resonant condition is present at some location inside plasma, in our case this condition is $\omega = \Omega_{ci}$, and the energy transfer happens in this resonance zone, from the wave to ions of plasma. In thermalisation process energy of heated ions is redistributed to other ion species and to electrons.

The ICRH method has been proven to be very effective for heating ions in plasma and it is used on nearly all large fusion devices around the world. Studies of ICRH are carried out for future largest devices (ITER, DEMO) where it should deliver dozens of MW of power to plasma. Various heating scenarios and operating regimes on different tokamaks are described in an overview paper [Becoulet1996]. In this thesis extensive details on the heating process itself and on the physics and engineering associated with it are omitted, since the subject of this thesis is the ICRH waves not in the core plasma, but on the edge where its behaviour is less understood. The need to investigate the ICRH physics at the edge plasma comes from the fact that the heating processes in the core plasma rely substantially on the edge conditions.

1.3.1 ICRF wave issues on the plasma edge – RF sheath

To ensure good ICRF (Ion Cyclotron Range of Frequencies) wave accessibility to the plasma core, the ICRF antennas must be placed close to the plasma. In experiments on multiple tokamaks, active ICRF antennas modify key plasma edge parameters (electron temperature, plasma density and plasma potential), as well as enhance plasma-wall interactions. Examples of such interactions include

changes in scrape-off layer plasma density profiles, increased heat loads and hot spot formations on limiters and enhanced sputtering of plasma facing components [Noterdaeme1992].

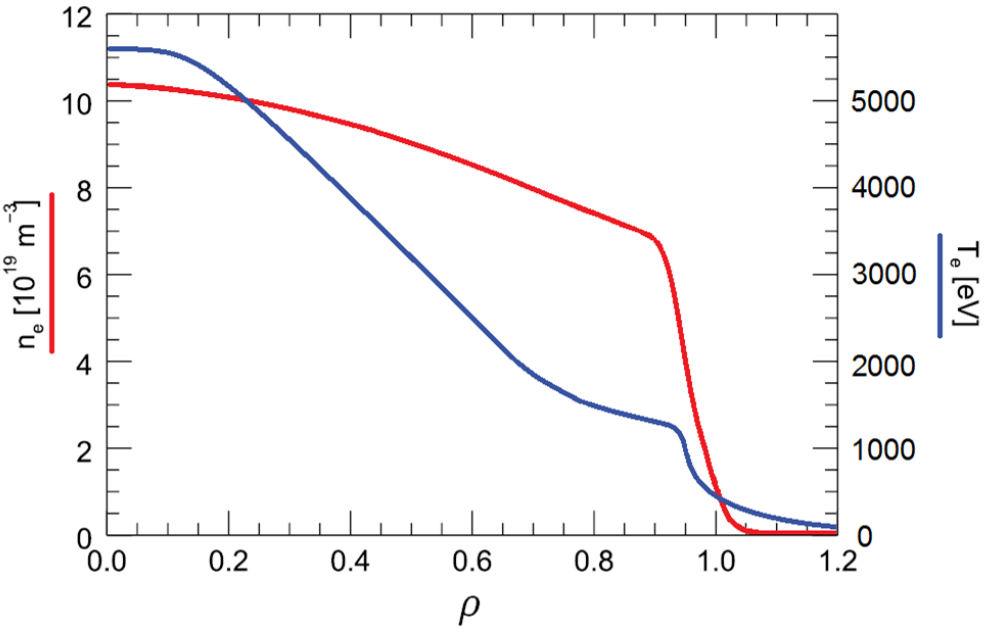

Fig. 1.2. Example of density and temperature profiles in a tokamak.

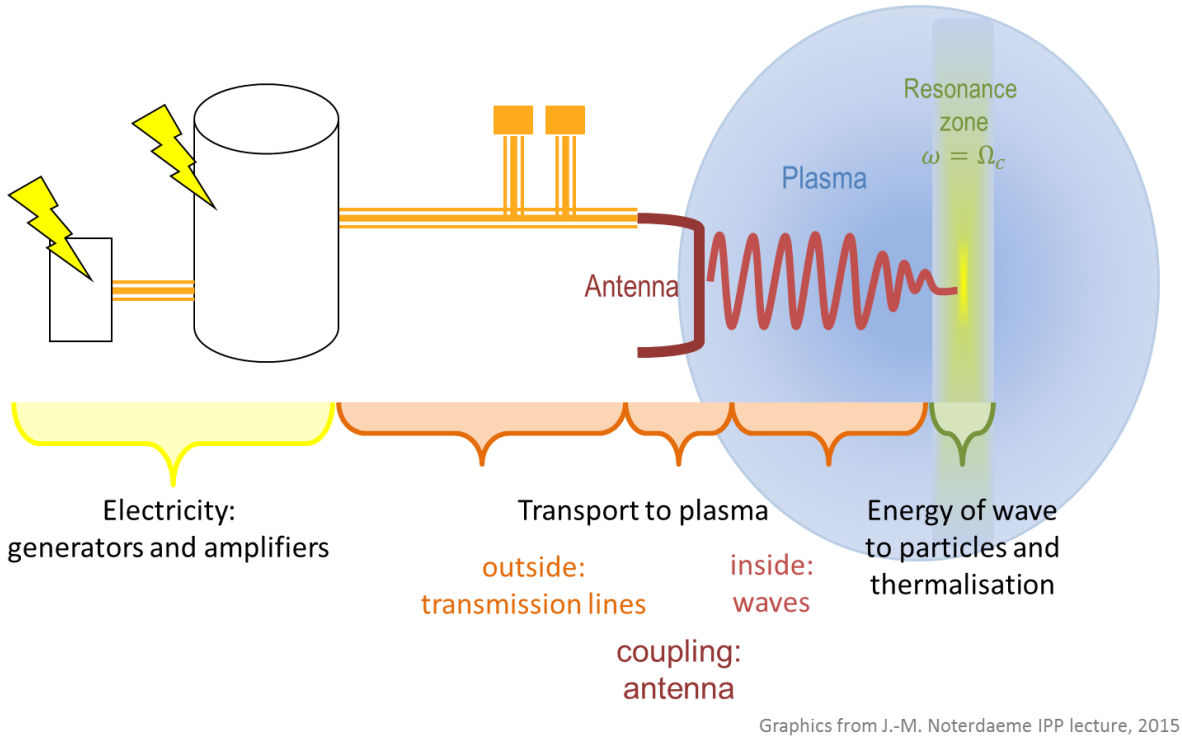

Fig. 1.3. ICRH system operating principle.

Metal impurity sputtering and its further influx to plasma increases the effective charge of plasma leading to a quadratic increase in Bremsstrahlung radiation as well as causes line radiation losses of plasma power in the regions of lower temperatures where heavy ions are not fully ionized [EquipeTFR1975]. Radiation losses in this case are directed to tokamak walls instead of preferable power exhaust in the divertor region. Density profiles are modified both locally by the impurities and

globally as a consequence of overall plasma conditions changes due to all ICRF induced parasitic effects. ICRF heating efficiency relies directly on the density profile in front of the antenna: if the region of wave propagation is farther from the ICRF antenna, the wave has to tunnel through a broader evanescent region and less power is delivered to plasma core [Clairet2004], [Y.Q.Yang2017], [Krivska2011]. Moreover, simultaneous use of other systems can be affected by the ICRF-induced density modifications, for example Lower Hybrid (LH) heating [Ekedahl2003].

Consequences of interaction between ICRF waves and plasma have been a subject of profound research since the beginning of ICRF applications. Progress in understanding these interactions is described in details in [Noterdaeme1992] from the early experiments until the steady conclusion of the RF sheath accelerated ions to be the main reason of impurities release and heat loads. RF sheath is an additional sheath that exceeds standard Bohm sheath in voltage and is present during active ICRF operation. Oscillations of parallel electric field at very high frequency of ICRF can be sensed only by the lightest and most mobile particles of the plasma – electrons. During an RF cycle they get accelerated towards the ends of magnetic field lines that end on antenna limiters and other plasma facing structures; negative charge builds up on the surfaces simultaneously with increasing positive charge of the bulk edge plasma where slow ions remain for much longer period of time. At the end a DC potential is formed between a wall and plasma and such a process, called RF sheath rectification, leads to further strong acceleration of ions into the plasma facing components.

Attempts have been made theoretically and experimentally on different machines to reduce negative effects by introducing Faraday screen [Yoshikawa1966], alignment of the Faraday screen bars with the magnetic field to reduce the parallel electric field component [Jacquot2013Thesis], varying phasing of the current for multi-strap antennas [Bures1991PPCF], [Bobkov2016], etc. Significant progress has been achieved as a result but edge plasma-antenna interactions have not been completely eliminated. No unified guideline exists on optimal ICRF antenna design, as observed effects and found solutions differ from one machine to another. Conclusions are usually empirical and based on consequential parameters like impurities concentration, RF currents or temperature of antenna limiting structures, but not on the direct measurements of RF-induced parallel electric field. Such measurements would provide quantitative characterization of the RF sheath but they are hard to perform in a tokamak. One of possible approaches to study parallel electric field of an ICRF antenna directly is to move from a complex tokamak environment to a simple specially designed experiment.

1.4 Dedicated experimental devices for RF sheath studies

ICRF antennas in big plasma devices such as tokamaks are insufficiently accessible for installation of dedicated diagnostics. On top of that, unstable plasma events can lead to conditions in which some diagnostics fail to provide results or results are hard to interpret. It is also beneficial to decouple ICRF physics from many other phenomena existing in a complex plasma machine; a simplification often leads to higher degree of physics understanding.

Based on such premises it was decided to set up experiments that would be fully focused on ICRF studies and would exhibit similar but simplified plasma conditions. For this thesis, work has been done on two dedicated devices, Aline and IShTAR, and their description is given in this section. These

two test stands have recently (2014) been taken into operation for the study of the plasma-antenna interactions. One of main advantages of dedicated facilities is that antennas with simple geometry can be used, with the flexibility to design and modify the antennas at will, allowing more straightforward comparison with numerical codes. Naturally, unrestricted access is available for appropriate diagnostics and experimental time is unconstrained by experimental campaigns as on larger machines.

1.4.1 Aline

Located at Université de Lorraine in Nancy, Aline (A LINear Experiment) is a linear plasma chamber (Fig. 1.4) of 1 m length and 15 cm in radius [Faudot2015], [Devaux2017NME]. A capacitive RF discharge is created by an RF antenna of a simple geometry (disk), as seen in Fig. 1.5. The power sent to plasma is kept relatively low and this allows avoiding large potentials and arcing when measuring with Langmuir probes in close proximity of the RF antenna. The limit of the forwarded power is set by the amplifier at 600 W and around half of the forwarded power is typically reflected.

The main diagnostic feature of Aline is a Langmuir probe manipulator (Fig. 1.4). It is able to move 50 cm along the main axis parallel to the magnetic field and 10 cm in both other directions. The RF antenna is centred in this range. The movement accuracy of the manipulator is 10 µm which is required to achieve precise spatial resolution for measurements in a sheath, the later itself being of the order of µm-mm size. Automated position scans are possible through the programmed software.

At the end of the manipulator, inside the vacuum chamber, is a Langmuir probe tip (Fig. 1.5) that can be easily exchanged to tips of different sizes, orientations or materials. RF compensation is designed and built-in for the frequency currently used during device operation – 25 MHz, in order to avoid shifting of the measured IV characteristics. The probe can be biased from −200 to +100 V and collect maximum current of 1 A. Each IV curve is routinely obtained as a result of averaging over multiple measurements, enabling high signal-to-noise ratio.

Six coils located along the vacuum chamber create a uniform magnetic field that can reach 0.104 T. The neutral gas pressure in Aline can be varied from 10^{-3} to 10^{-1} mbar (0.1 to 10 Pa) and different gases can be used, the most common ones being argon and helium in our experiments. Plasma density in helium is within the range 10^{15} to 10^{17} m^{-3} and electron temperatures are around few eV. In these conditions the plasma can be considered as strongly magnetized, which will be quantitatively shown in Chapter 3.1.

In 2015 the device was stably working and a full device description was published in [Faudot2015], as well as first results of Langmuir probe measurements without magnetic field (2D maps of floating and plasma potentials and density). Some results and data analysis techniques were described in [Devaux2017EPS] for non-magnetized plasma, namely an ion current fitting technique and ion density maps obtained using it. In another paper by S. Devaux et al [Devaux2017NME], large 3D maps of floating potential (V_{fl}) are presented for unmagnetized plasma and a 2D plot of V_{fl} for magnetized plasma.

An essential target of the experiments on Aline since the beginning of the device exploitation was to measure main plasma parameters, density and temperature, in the presence of the magnetic field. The presence of magnetic field led to the fact that conventional methods of data analysis would

bring too erroneous results, because of completely different particle transport in magnetized plasma compared to the non-magnetized one. Especially errors would increase when using small cylindrical Langmuir probes parallel to the magnetic field or at a small angle to it. These probes are the most (and probably the only) suitable option for measurements in narrow sheaths, where high spatial resolution is needed. For this reason they are employed in Aline.

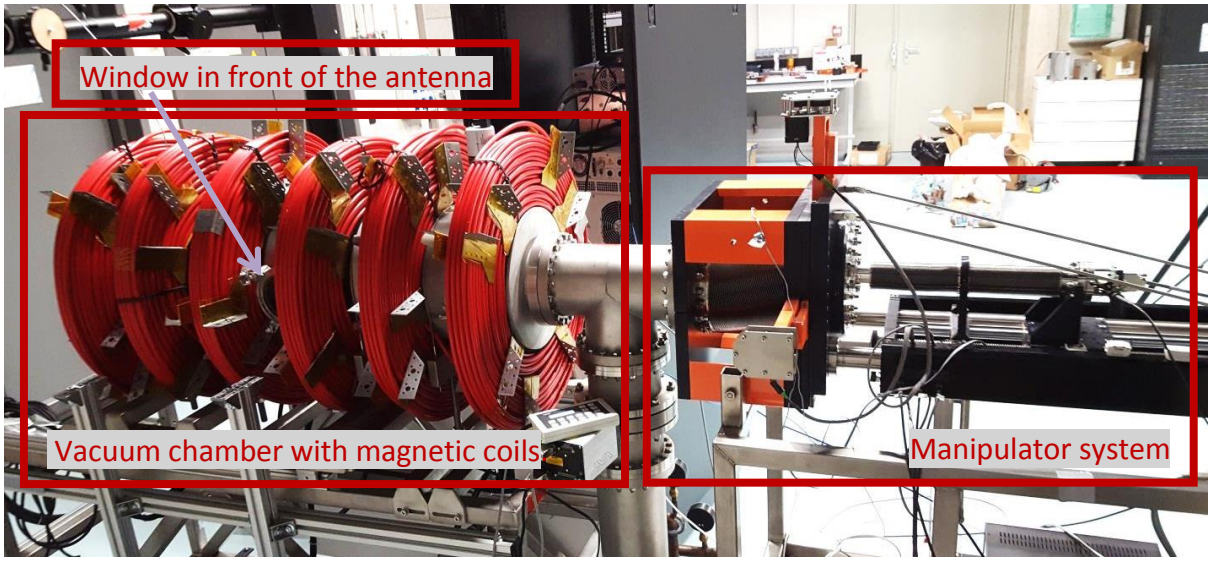

Fig. 1.4. Photo of Aline.

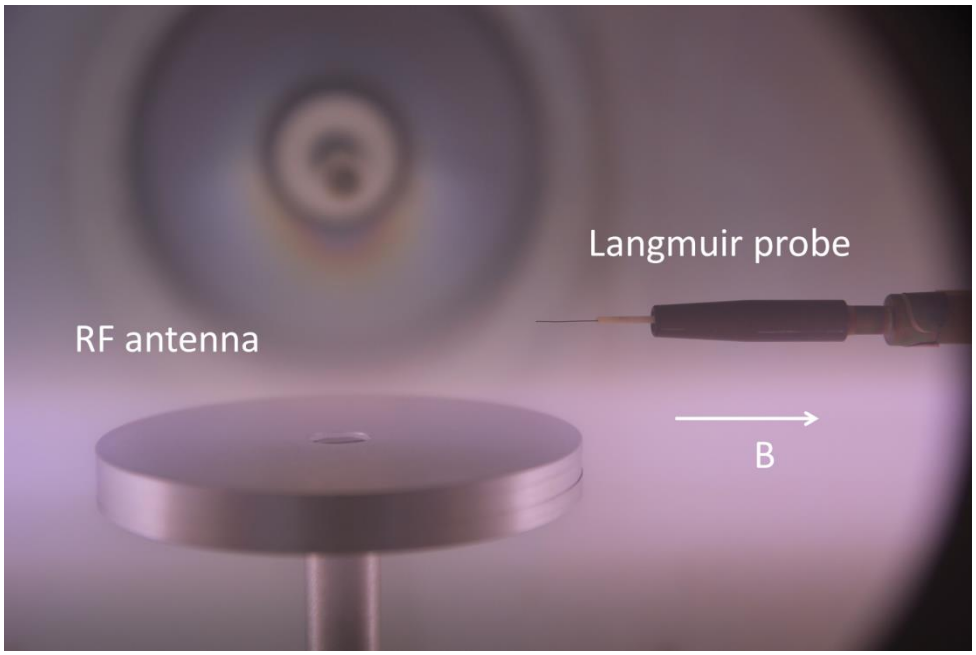

Fig. 1.5. RF antenna of a disk shape and Langmuir probe on a manipulator in Aline.

In this thesis theories are presented which were developed for Langmuir probe data processing for magnetized plasma and which finally enabled measurements on Aline in the presence of magnetic field. Techniques for density, temperature and plasma potential extraction from the data are described in Chapter 3 and can be also found in [Usoltceva2018PoP] and [Usoltceva2018RSI]. First results of Langmuir probe density measurements in magnetized plasma on Aline are also presented

in Chapter 3, as well as measured line-averaged densities by interferometry and its comparison to the probe data.

For fusion applications, Langmuir probes are used in devices where magnetic field is present. Hence, presented data analysis techniques are not only important for application on Aline but can be used on any machine with magnetized plasma. Small cylindrical Langmuir probes parallel to the magnetic field provides a benefit of good spatial (radial) resolution of measured plasma parameters, which would not be possible with big planar probes.

1.4.2 IShTAR

The objective of the experiment IShTAR (Ion cyclotron Sheath Test Arrangement) is to come even closer to tokamak conditions for ICRF waves and plasma interactions than on Aline. The main difference is the antenna available at the test stand, which was specially designed for IShTAR to mimic tokamak ICRF antennas (Fig. 1.6). Fed by a coaxial line, a metallic strap couples power inductively to plasma, as in a tokamak, the strap is surrounded by limiters and the geometry is adjusted to the plasma shape to replicate poloidal symmetry along the strap length.

In Fig. 1.7 a scheme of IShTAR is shown with all main features indicated. The vacuum chamber consists of two adjacent cylindrical parts, the big one made of steel and the small one from quartz glass. The glass is needed to enable creation and sustenance of plasma by a helicon antenna located around the glass tube. Confined by 2 sets of magnetic coils, plasma takes a form of a cylinder extended along the whole length of IShTAR, providing densities in the big chamber (where the ICRF antenna is located) of the same order of magnitude as in the helicon tube due to high parallel transport. By varying neutral pressure, gas species, magnetic fields configuration and helicon injected power it is possible to achieve very broad range of plasma conditions, e.g. density magnitudes and profile shapes, degree of plasma magnetization, collision rates and angles of incidence of magnetic field lines to the antenna walls. Operational parameters of IShTAR are summarized in Table 1.

IShTAR started to operate in 2014 in its first simplified configuration [D'Inca2015], [Crombe2015]. Non-axisymmetric plasma was hard to control and interpretation of measurements with a stellarator ICRF antenna, installed as a first test object, was not straightforward. Other issues were present, like poor neutral pressure control and lack of reliable diagnostics. However, those first operations defined the framework for dedicated antenna design and necessary diagnostics, as well as showed the capability of the helicon antenna to create plasma with quite high densities, up to $1.8*10^{18}$ m^{-3} in Ar according to [Morgal2015Thesis] (narrow density peak of around 7 cm). Based on the density measurements from the first IShTAR campaign, a theoretical study was done to define relevant frequency for the planned ICRF antenna [Crombe2016JPP].

Significant changes happened in the second half of 2016 when the dedicated antenna (Fig. 1.6) was manufactured and installed in IShTAR, and at the same time axissymmetry of the plasma was achieved by shifting the helicon chamber to the center of the big vessel. The new state of the device, diagnostics improvements and achieved plasma parameters with scans of injected power and magnetic field were reported in [Crombe2016IAEA]. Major diagnostic improvements happened mostly to Langmuir probes, as their reliability improved. Densities measured in the new centred

configuration appeared to be lower, $5*10^{17}$ m^{-3} in argon plasma. In the same paper spectroscopic methods of measuring electric field in the sheath near the antenna limiters was suggested, which were later studied for feasibility [Kostic2017] and developed for IShTAR [Kostic2018].

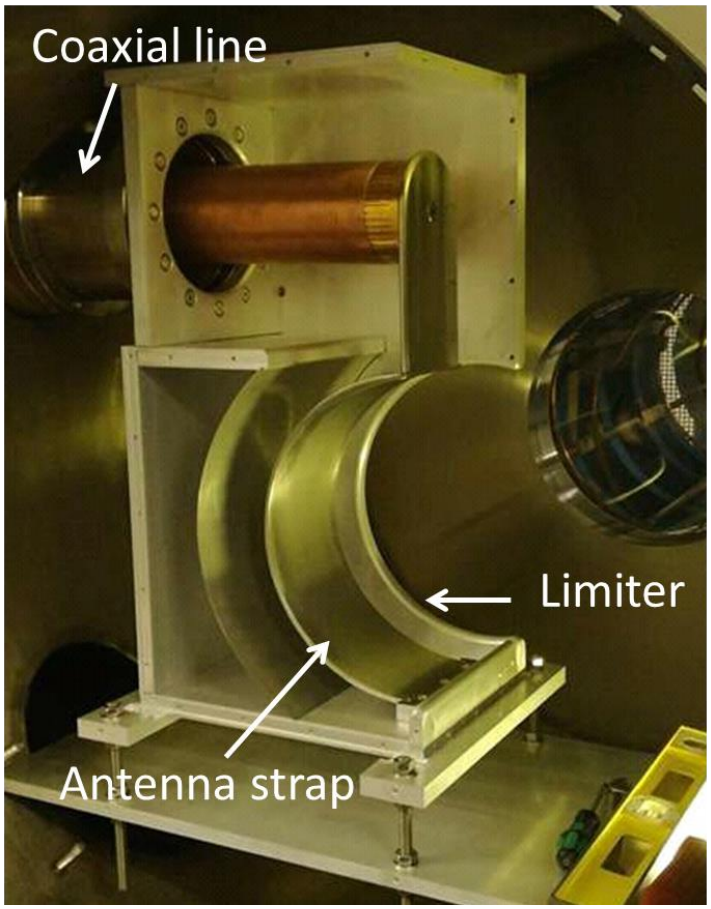

Fig. 1.6. IShTAR ICRF one-strap antenna without one side wall to exhibit the antenna structure.

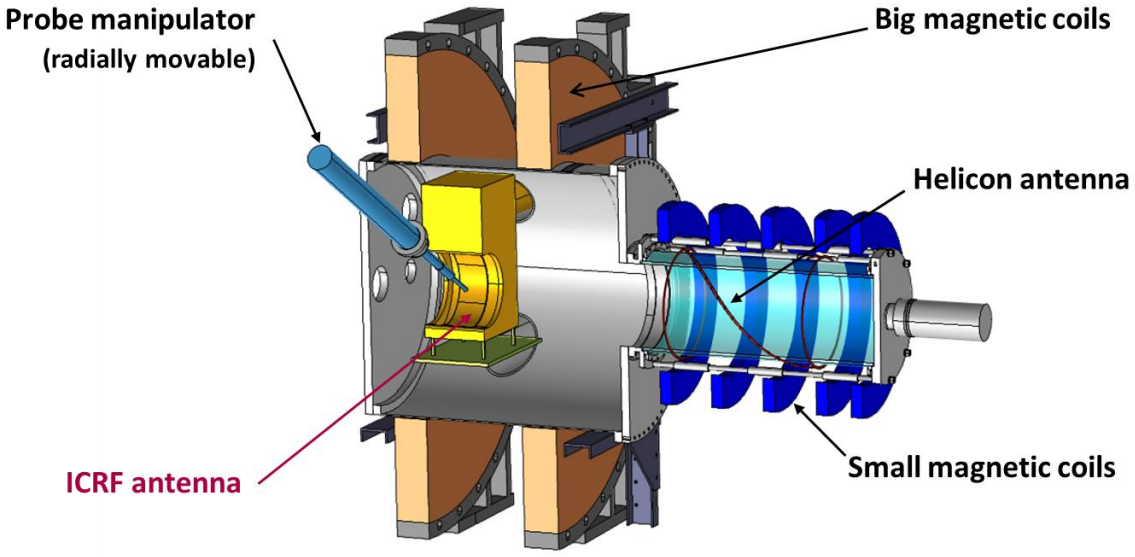

Fig. 1.7. IShTAR model with all main components.

Parameter	Value
Gas	He, Ar
Magnetic field	0.272 T - big coils, 0.0635 T - small coils
Chamber length	1.126 m - big chamber, 1.103 m - small chamber
Chamber radius	0.5 m - big chamber, 0.2 m - small chamber
Helicon injected power	Up to 3 kW
Helicon frequency	11.76 MHz
ICRF power	Up to 1 kW
ICRF frequency	5-6 MHz (adjusted for matching)
Density maximum	$5*10^{16}$ m^{-3} - He, $5*10^{17}$ m^{-3} - Ar
Temperature maximum	~5 eV

Table 1. IShTAR operational parameters.

This thesis includes a few aspects of work done on IShTAR. The objective was to study ICRF waves propagation in IShTAR configuration, explore different scenarios and as a final step provide input data regarding best possible scenarios in which spectroscopic electric field measurements should be done (topic of another PhD thesis).

The first step of the study included the development and installation of probe diagnostics to quantify the relevant plasma parameters (plasma density, electron temperature, plasma potential in the vicinity of the antenna) and the relevant ICRF wave fields (components of magnetic field). Langmuir and B-dot probes were installed on a radially movable manipulator (Fig. 1.7) and obtained results are shown in Chapter 4. At the same time a 3D model of IShTAR was developed in COMSOL software, and first straightforward comparisons were possible for vacuum fields in the model and in the experiments [Usoltceva2017].

ICRF waves propagation was calculated theoretically for IShTAR conditions and it was concluded that only one of two ICRF modes, the so-called slow wave, can propagate and be studied in IShTAR. Therefore it is possible to decouple the role of the different ICRF modes in contributing to RF sheath effects. Calculations are given in Chapter 2. After that, numerical simulations of ICRF waves were done in COMSOL using RF module of the software. Plasma was implemented as a material with manually assigned physics properties, similarly to the one described in [Jacquot2013Thesis]. Theoretical basis is explained in Chapter 2 and results are given in Chapter 4. Field structures obtained for the slow wave differ significantly from the other mode, the fast wave, and exhibit strong dependence on the density profile on the plasma edge. COMSOL software appeared to be a powerful tool, able to provide not only special distribution of all components of the fields, but also absorbed power, Poynting vector, current on the antenna strap and much more.

The last necessary task was to measure the power coupled to plasma in IShTAR experiments in order to calibrate COMSOL simulations and obtain correct absolute values of the fields. Forward and reflected power was measured in the matched line with a directional coupler. Detailed description of the experimental setup and measured values for different plasma conditions can be found in Chapter 4, as well as an outlook for next necessary measurements.

Experimental, theoretical and numerical results of the work on IShTAR included in this thesis contribute to the goal of studying RF sheath physics on a dedicated device, as well as to the physics

of ICRF waves on the plasma edge in general. In ICRF simulations for tokamak devices such as RAPLICASOL [Jacquot2013Thesis], [Tierens2018] or TOPICA [Lancellotti2006], [Milanesio2009] the edge plasma layer is replaced with a vacuum layer and the whole part of wave propagation on the edge is avoided. Results of this thesis can be used to fill in this gap and improve the complex tokamak ICRF simulations.

References

[Becoulet1996] – A. Becoulet, "Heating and current drive regimes in the ion cyclotron range of frequency", Plasma Phys. Control. Fusion **38** (1996) A1

[Bobkov2016] – V. Bobkov et al., "Progress in reducing ICRF-specific impurity release in ASDEX upgrade and JET", Nuclear Materials and Energy **12** (2016) 1194

[Bures1991PPCF] – M. Bures et al., "Impurity release from the ICRF antenna screens in JET", Plasma Phys. Control. Fusion **33** (1991) 937

[Clairet2004] – F. Clairet et al., "ICRF coupling and edge density profile on Tore Supra", Plasma Phys. Control. Fusion **46** (2004) 1567

[Crombe2015] – K. Crombé et al., "Studies of RF sheaths and diagnostics on IShTAR", AIP Conference Proceedings **1689** (2015) 030006

[Crombe2016IAEA] – K. Crombé et al., "IShTAR: a helicon plasma source to characterise the interactions between ICRF and plasma", presented at the 26th IAEA Fusion Energy Conference (2016)

[Crombe2016JPP] – K. Crombé and D. Van Eester, "Parameter study of ICRH wave propagation in IShTAR", J. Plasma Phys. **82** (2016) 905820203

[D'Inca2015] – R. D'Inca et al., "First experimental results on the IShTAR testbed", AIP Conference Proceedings **1689** (2015) 050010

[Devaux2017NME] – S. Devaux, E. Faudot, J. Moritz, S. Heuraux, "ALINE: A device dedicated to understanding radio-frequency sheaths ", Nuclear Materials and Energy **12** (2017) 908

[Devaux2017EPS] – S. Devaux, E. Faudot, J. Moritz, S. Heuraux, "3D investigations of a radio-frequency plasma with a Langmuir Probe", presented at the 44th EPS Conference on Plasma Physics (2017)

[Ekedahl2003] – A. Ekedahl et al., "Density convection near radiating ICRF antennas and its effect on the coupling of Lower Hybrid waves", AIP Conference Proceedings **694** (2003) 259

[EquipeTFR1975] – Equipe TFR, "Line radiation in the visible and in the ultraviolet in TFR tokamak plasmas", Nucl. Fusion **15** (1975) 1053

[Faudot2015] – E. Faudot et al., "A linear radio frequency plasma reactor for potential and current mapping in a magnetized plasma", Rev. Sci. Instrum. **86** (2015) 063502

[Jacquot2013Thesis] – J. Jacquot, "Description non-linéaire auto-cohérente de la propagation d'ondes radiofréquences et de la périphérie d'un plasma magnétisé", PhD Thesis (2013)

[Kostic2017] – A. Kostic et al., "Feasibility study of Passive Optical Emission Spectroscopy for the electric field measurements in IShTAR", EPJ Web of Conferences **157** (2017) 03025

[Kostic2018] – A. Kostic et al., "Development of a spectroscopic diagnostic tool for electric field measurements in IShTAR (Ion cyclotron Sheath Test ARrangement)", Rev. Sci. Instrum. **89** (2018) 10D115

[Krivska2011] – A. Krivska et al., "Density profile sensitivity study of ASDEX Upgrade ICRF Antennas with the TOPICA code", AIP Conference Proceedings **1406** (2011) 93

[Lancellotti2006] – V. Lancellotti et al., "TOPICA: an accurate and efficient numerical tool for analysis and design of ICRF antennas", Nucl. Fusion **46** (2006) S476

[Milanesio2009] – D. Milanesio et al., "A multi-cavity approach for enhanced efficiency in TOPICA RF antenna code", Nucl. Fusion **49** (2009) 115019

[Morgal2015Thesis] – I. Morgal, "Characterization and optimization of the helicon plasma source in the IShTAR test facility", Master Thesis (2015)

[Noterdaeme1992] – J-M. Noterdaeme, "Interaction Between ICRH and the Plasma Edge: An Overview", AIP Conference Proceedings **244** (1992) 71

[Tierens2018] – W. Tierens et al., "Validation of the ICRF antenna coupling code RAPLICASOL against TOPICA and experiments", Nucl. Fusion (2019) **59** 046001

[Usoltceva2017] – M. Usoltceva et al., "IShTAR ICRF antenna field characterization in vacuum and plasma by using probe diagnostic", EPJ Web of Conferences **157** (2017) 03058

[Usoltceva2018PoP] – M. Usoltceva et al., "Effective collecting area of a cylindrical Langmuir probe in magnetized plasma", Phys. Plasmas **25** (2018) 063518

[Usoltceva2018RSI] – M. Usoltceva et al., "Theory of a cylindrical Langmuir probe parallel to the magnetic field and its calibration with interferometry", Rev. Sci. Instrum. **89** (2018) 10J124

[Yang2017] – Y.Q. Yang et al., "Investigation of energy confinement during ICRF heating on EAST", Plasma Phys. Control. Fusion **59** (2017) 095001

[Yoshikawa1966] – S. Yoshikawa, R.M. Sinclair and M.A. Rothman , "Ion Heating in the C Stellarator", Plasma Physics and Controlled Nuclear Fusion Research, IAEA **2** (1966) 925

2 Theoretical and experimental background of this thesis

In this chapter the theoretical description of electromagnetic waves propagation in plasma is introduced. Based on the cold plasma approximation two solutions for ICRF waves are obtained and their properties are discussed in details. An example of plasma conditions and ICRF parameters typical for ASDEX Upgrade tokamak is chosen and is used to illustrate the relevant behaviour of and differences between the two ICRF modes - the slow and the fast wave. The results are given in Section 2.1.

Energy transfer from the RF waves to plasma particles depends both on the plasma state and on parameters of the launched wave. Different mechanisms of energy exchange come into play during a plasma discharge. What those mechanisms are and how big their influence on the total energy absorption is, will be discussed in Section 2.2.

In Section 2.3 of this chapter COMSOL Multiphysics® Modeling Software is described and numerical modelling approach in COMSOL is shown in terms of the theoretical basis of the ICRF waves given in the first section of the chapter. Existing simulation tools for the waves of the RF range are mentioned. The framework of the IShTAR simulations is defined.

For experimental characterization of plasma, various diagnostics were applied during the work on this thesis. Electrical probes (i.e. Langmuir probes), magnetic B-dot probes and interferometry were employed on the experimental devices to measure plasma density, temperature, RF fields and other important parameters. The diagnostics principles are explained in the Section 2.4 of the current chapter.

2.1 Theory of ICRF waves

2.1.1 Wave equation and dielectric tensor

Ideal magnetohydrodynamic (MHD) description couples Maxwell's equations and hydrodynamics and provides theoretical description of waves' behavior in plasma [Stix1992], [Jacquot2013PPCF]. Stationary ideal homogeneous conditions are the initial state of the single-fluid plasma, with static and spatially uniform magnetic field $\boldsymbol{B} = \boldsymbol{B_0} + \delta\boldsymbol{B}$ and density $n = n_0 + \delta n$ in zero order with small first order perturbations and other quantities only as first order fluctuations: electric field $\boldsymbol{E} = \delta\boldsymbol{E}$, velocity of charged species s of plasma $\boldsymbol{v_s} = \delta\boldsymbol{v_s}$ and plasma current $\boldsymbol{j} = \delta\boldsymbol{j}$.

Using the differential form of Maxwell's equations,

$$\begin{cases} \nabla \times \boldsymbol{E} = -\partial \boldsymbol{B}/\partial t \\ \nabla \times \boldsymbol{B} = \mu_0 \boldsymbol{j} + \partial \boldsymbol{D}/\partial t \end{cases} \tag{2.1}$$

(where $\boldsymbol{D}$ – the electric displacement field, $\boldsymbol{H}$ – the magnetic induction and ρ – the space charge, μ_0 – the permeability of free space) and replacing the time derivatives for RF fields, oscillating in time as $e^{-i\omega t}$ with angular frequency ω, by $-i\omega$, we get:

$$\begin{cases} \nabla \times \boldsymbol{E} = i\omega \boldsymbol{B} \\ \nabla \times \boldsymbol{B} = \boldsymbol{j} - i\omega \boldsymbol{D} \end{cases} \tag{2.2}$$

The constitutive relations for anisotropic materials are: $\boldsymbol{D} = \bar{\bar{\varepsilon}}\boldsymbol{E}$ and $\boldsymbol{B} = \bar{\bar{\mu}}\boldsymbol{H}$ with the dielectric tensor $\bar{\bar{\varepsilon}}$ and the magnetic permeability tensor $\bar{\bar{\mu}}$. Combining equations (2.2) and the constitutive relations we obtain a wave equation in Helmholtz form:

$$\nabla \times \bar{\bar{\mu}}^{-1}(\nabla \times \boldsymbol{E}) + \frac{\omega^2}{c^2}\bar{\bar{\varepsilon}}\boldsymbol{E} = i\omega\mu_0 \boldsymbol{j} \tag{2.3}$$

where μ_0 is the vacuum permeability.

We consider $\bar{\bar{\mu}} = \bar{\bar{1}}$ and assume a plane wave oscillating as $\exp(-i\omega t + i\boldsymbol{k}\cdot\boldsymbol{r})$, where $\boldsymbol{k}$ is the wave vector and $\boldsymbol{r}$ is the space vector, to be a solution of (2.3), so we can replace ∇ by $i\boldsymbol{k}$ in (2.3). Then for $\boldsymbol{j} = 0$ the wave equation looks like:

$$\mathbf{k} \times (\mathbf{k} \times \boldsymbol{E}) + \frac{\omega^2}{c^2}\bar{\bar{\varepsilon}}\boldsymbol{E} = 0 \tag{2.4}$$

Or with the index of refraction $\boldsymbol{n} = \boldsymbol{k}c/\omega$ (c is the speed of light in vacuum):

$$\boldsymbol{n} \times (\mathbf{n} \times \boldsymbol{E}) + \bar{\bar{\varepsilon}}\boldsymbol{E} = 0 \tag{2.5}$$

The dielectric tensor is derived by Stix [Stix1992] using the equation of motion of the cold plasma fluid:

$$\bar{\bar{\varepsilon}} = \begin{pmatrix} \varepsilon_\perp & -i\varepsilon_X & 0 \\ i\varepsilon_X & \varepsilon_\perp & 0 \\ 0 & 0 & \varepsilon_\parallel \end{pmatrix} \tag{2.6}$$

where the Stix parameters are defined as:

$$\varepsilon_\parallel = 1 - \sum_s \frac{\omega_{ps}^2}{\omega^2} \tag{2.7}$$

$$\varepsilon_R = 1 - \sum_s \frac{\omega_{ps}^2}{\omega(\omega+\Omega_{cs})} \tag{2.8}$$

$$\varepsilon_L = 1 - \sum_s \frac{\omega_{ps}^2}{\omega(\omega-\Omega_{cs})} \tag{2.9}$$

$$\varepsilon_\perp = \frac{(\varepsilon_R+\varepsilon_L)}{2} = 1 - \sum_s \frac{\omega_{ps}^2}{(\omega^2-\Omega_{cs}^2)} \tag{2.10}$$

$$\varepsilon_X = \frac{(\varepsilon_R-\varepsilon_L)}{2} = 1 - \sum_s \frac{\Omega_{cs}\omega_{ps}^2}{\omega(\omega^2-\Omega_{cs}^2)} \tag{2.11}$$

where the Larmor frequency for species s of plasma particles that have mass m_s, charge q_s, density n_s and (ε_0 is the permittivity of free space) is given by:

$$\Omega_{cs} = \frac{q_s B}{m_s} \tag{2.12}$$

and the plasma frequency for particles of the kind s is defined as:

$$\omega_{ps}^2 = \frac{q_s^2 n_s}{m_s \varepsilon_0} \tag{2.13}$$

The coordinate system in [Stix1992] is chosen such that $\boldsymbol{B}$ is parallel to z and the two other directions are equivalent for homogenous plasma. It is useful to assume the y-component of the wave vector to be zero, so the perpendicular component is only in x direction and $n = n_\perp \boldsymbol{x} + n_\parallel \boldsymbol{z}$. This way we simplify the calculations and this assumption is usually valid for experimental ICRF antennas. The wave equation becomes:

$$\begin{pmatrix} \varepsilon_\perp - n_\parallel^2 & -i\varepsilon_X & n_\parallel n_\perp \\ i\varepsilon_X & \varepsilon_\perp - n_\perp^2 - n_\parallel^2 & 0 \\ n_\parallel n_\perp & 0 & \varepsilon_\parallel - n_\perp^2 \end{pmatrix} \begin{pmatrix} E_x \\ E_y \\ E_z \end{pmatrix} = 0 \tag{2.14}$$

The determinant of the left matrix has to be zero for the wave equation to have nontrivial solutions. This requirement gives us the dispersion relation:

$$\left(\varepsilon_\perp - n_\parallel^2\right)\left(\varepsilon_\perp - n_\perp^2 + n_\parallel^2\right)(\varepsilon_\parallel - n_\perp^2) - \varepsilon_X^2(\varepsilon_\parallel - n_\perp^2) - n_\parallel^2 n_\perp^2\left(\varepsilon_\perp - n_\perp^2 - n_\parallel^2\right) = 0 \tag{2.15}$$

This is a 4[th] order equation for $n_\perp$ which can be rewritten as:

$$An_\perp^4 + Bn_\perp^2 + C = 0 \tag{2.16}$$

where $A = \varepsilon_\perp$, $B = (n_\parallel^2 - \varepsilon_\perp)(\varepsilon_\parallel + \varepsilon_\perp) + \varepsilon_X^2$, $C = \varepsilon_\parallel\left(\left(n_\parallel^2 - \varepsilon_\perp\right)^2 - \varepsilon_X^2\right)$. So the full solutions are:

$$n_\perp^2 = \frac{-B \pm \sqrt{B^2 - 4AC}}{2A} \tag{2.17}$$

Simplified version of the solutions can be obtained if approximations are used:

$$n_{\perp FW}^2 = \frac{(\varepsilon_R - n_\parallel^2)(\varepsilon_L - n_\parallel^2)}{(\varepsilon_\perp - n_\parallel^2)}, \text{ when } \left|\varepsilon_\parallel\right| \gg \left|n_{\perp FW}^2\right| \tag{2.18}$$

$$n_{\perp SW}^2 = \varepsilon_\parallel\left(1 - \frac{n_\parallel^2}{\varepsilon_\perp}\right), \quad \text{when } \left|\varepsilon_\parallel\right| \approx \left|n_{\perp SW}^2\right| \tag{2.19}$$

as well as $\left|\varepsilon_\parallel\right| \gg \left|n_\parallel^2\right|, |\varepsilon_\perp|, |\varepsilon_X|$ and $\varepsilon_\perp \neq n_\parallel^2$ for both of them. These simplified solutions of the cold plasma dispersion relation are referred to as the fast wave (FW) and the slow wave (SW).

Within the ideal MHD description there are two types of Alfvén waves: isotropic compressional Alfvén wave and anisotropic shear Alfvén wave. In the wave classification the fast wave belongs to the compressional Alfvén wave type. It means that in the low frequency limit ($\omega \ll \Omega_{ci}$) the FW is equivalent to compressional oscillations of the magnetic field lines. The slow wave is a shear (or torsional) Alfvén wave. The discussed waves are also called fast and slow magnetosonic waves.

The terminology of the wave classification is somehow inconsistent in different literature. The names "fast wave" and "slow wave" might be used in a different way from the one defined here. It was, for example, the case in [Stix1992] as explained in [Bingren1999].

2.1.2 Wave propagation: cut-off and resonance

When $n_\perp^2$ (or $k_\perp^2$) < 0, the value of $n_\perp$ is imaginary, so the wave of the form $\exp(i\boldsymbol{k}\cdot\boldsymbol{r})$ is evanescent. $n_\perp^2$ has to be positive for the wave to propagate. Transitions between these two states are called resonance and cut-off. A cut-off occurs when $n_\perp^2 = 0$, for the fast wave it corresponds to:

$$n_\parallel^2 = \varepsilon_R \tag{2.20}$$

$$n_\parallel^2 = \varepsilon_L \tag{2.21}$$

And for the slow wave:

$$n_\parallel^2 = \varepsilon_\perp \tag{2.22}$$

$$\varepsilon_\parallel = 0 \tag{2.23}$$

In experimental devices $n_\parallel$ is defined by the ICRF antenna geometry and typically $n_\parallel > 1$. Both The right cut-off (2.20) and the left cut-off (2.21) of the FW can be present in plasma. They are usually located in different plasma layers, the right cut-off being closer to the plasma edge.

$\varepsilon_\perp > 1$ is needed for the condition (2.22) to be achievable, which is only possible when $\Omega_{ci} > \omega$. Such a case might be present in some devices, for example in a tokamak that has the magnetic field growing towards the geometrical center of the tokamak, so the cyclotron frequency increases as well and overcomes the ICRF wave frequency at some point. In ASDEX Upgrade tokamak under typical operating conditions the cut-off (2.22) can be present in the core plasma. Since it happens at quite a large distance from the plasma edge, where the antennas are located, the SW cannot reach this cut-off. The cut-off (2.23) for the SW lies in the region of small densities; such conditions might be present inside the antenna box in a tokamak as well as in other devices where densities are lower than on the tokamak plasma edge.

Resonances happen when $n_\perp^2 \to \infty$. For the FW it means $n_\parallel^2 = \varepsilon_\perp$ which is equal to (2.22) and can exist in the tokamak core plasma, as explained above. For the SW a resonance is at

$$\varepsilon_\perp = 0 \tag{2.24}$$

and it corresponds to the Lower Hybrid resonance. This resonance happens at higher densities than the cut-off (2.23).

A common behaviour of the SW in plasma with density gradient and constant magnetic field (Fig. 2.1) is that it is evanescent for densities below the cut-off (2.23), then propagates until the resonance (2.24) and then it is evanescent again in higher density plasma. The FW often meets the cut-off (2.21) at densities higher than the SW propagation and transforms at this point from evanescence to propagation. When such a distinction happens, it allows the physics of the SW and the FW to be studied independently in two separate locations. Otherwise both wave modes can

propagate simultaneously and then their effects are mixed. Parameters used to plot the Fig. 2.1 are typical parameters for ICRF antennas in ASDEX Upgrade tokamak: gas mixture: 98.5% D + 1.5% H, frequency: 36.5 MHz, magnetic field: 2T, $k_{\parallel}$ = 8.98 rad/m. The magnetic field is considered constant for the simplicity, which leads to the absence of the SW cut-off and the FW resonance defined by (2.22) as well as the FW left cut-off (2.21). This simplification is allowed because it does not affect the physics studied in this thesis.

In Fig. 2.1 full solutions of the dispersion relation as given by (2.17) are also plotted. As we can see in this case, the approximate solutions (2.18) and (2.19) match exactly the full roots. This is not always true, but can happen for wide variety of cases with different parameters.

The y-axis in Fig. 2.1 might be not obvious for a reader. The values correspond to the decimal logarithm of $\left|k_{\perp}^2\right|$ multiplied by the sign of $k_{\perp}^2$ for each point:

$$\lg\left(\left|k_{\perp}^2\right|\right) * sign(k_{\perp}^2) \tag{2.25}$$

This way the part of the plot corresponding to positive $k_{\perp}^2$ (propagation) lies fully above 0 and the evanescent regions (negative $k_{\perp}^2$) lie below 0. However, $\lg\left(\left|k_{\perp}^2\right|\right)$ can have negative sign for positive $k_{\perp}^2$ and then $\lg\left(\left|k_{\perp}^2\right|\right) * sign(k_{\perp}^2) < 0$. This happens only when $k_{\perp}^2 < 1$, so for very small $k_{\perp}^2$. We neglect those points and assigne them a value equal to zero (otherwise for $k_{\perp}^2$ = 0.01, for example, the value on y axis would be -2, so a sudden spike would appear). Similarly, all points which have negative $k_{\perp}^2$ (evanescence) lie only below 0 on this plot. Very few points (sometimes none) are affected by this correction and it does not introduce any inaccuracies. Such an artificial y-axis leads to easily readable visual representation of the data and the mentioned correction is needed to avoid confusing spikes that could be visually mistaken with a resonance, as was the case for example in [Crombe2016JPP].

2.1.3 Electric field polarization

From the eigenvectors of the matrix in (2.14) it is possible to calculate the relative strength of each electric field component. From the second row of the matrix in the SW approximation:

$$\left|\frac{E_y}{E_x}\right| = \left|\frac{\varepsilon_{\perp}}{n_{\perp}^2}\right| \ll 1 \tag{2.26}$$

And from the third row of the matrix in the FW approximation:

$$\left|\frac{E_z}{E_x}\right| = \left|\frac{n_{\parallel} n_{\perp}}{\varepsilon_{\parallel} - n_{\perp}^2}\right| \ll 1 \tag{2.27}$$

Therefore, the E_y component of SW and E_z component of FW are negligibly small. In Fig. 2.2 an example of eigenvectors values (in linear scale) is plotted for the same conditions as in Fig. 2.1.

In the range of SW propagation the wave can be considered electrostatic; it satisfies the electrostatic dispersion relation:

$$\varepsilon_{\perp} k_{\perp}^2 + \varepsilon_{\parallel} k_{\parallel}^2 = 0 \tag{2.28}$$

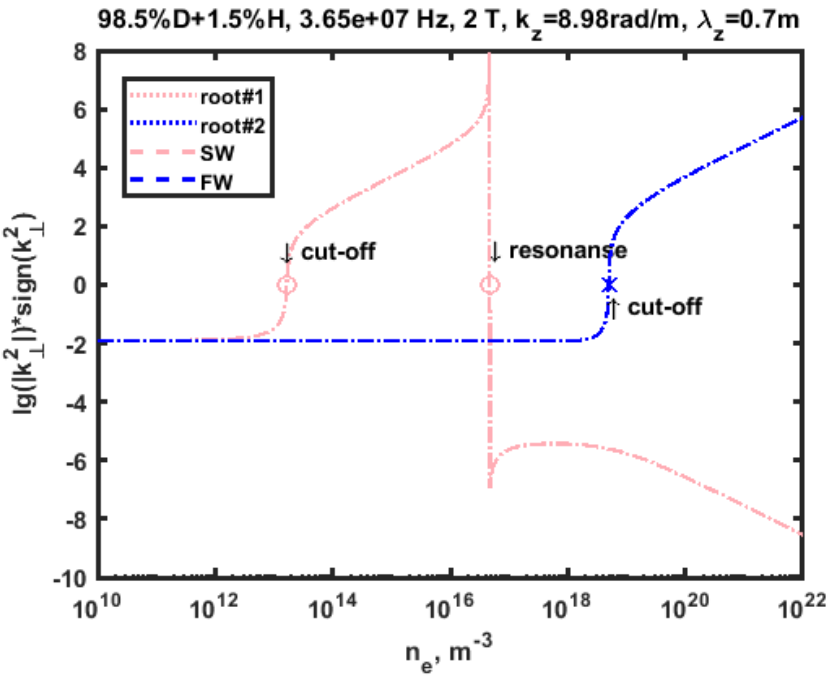

Fig. 2.1. Slow and fast waves behaviour depending on density.

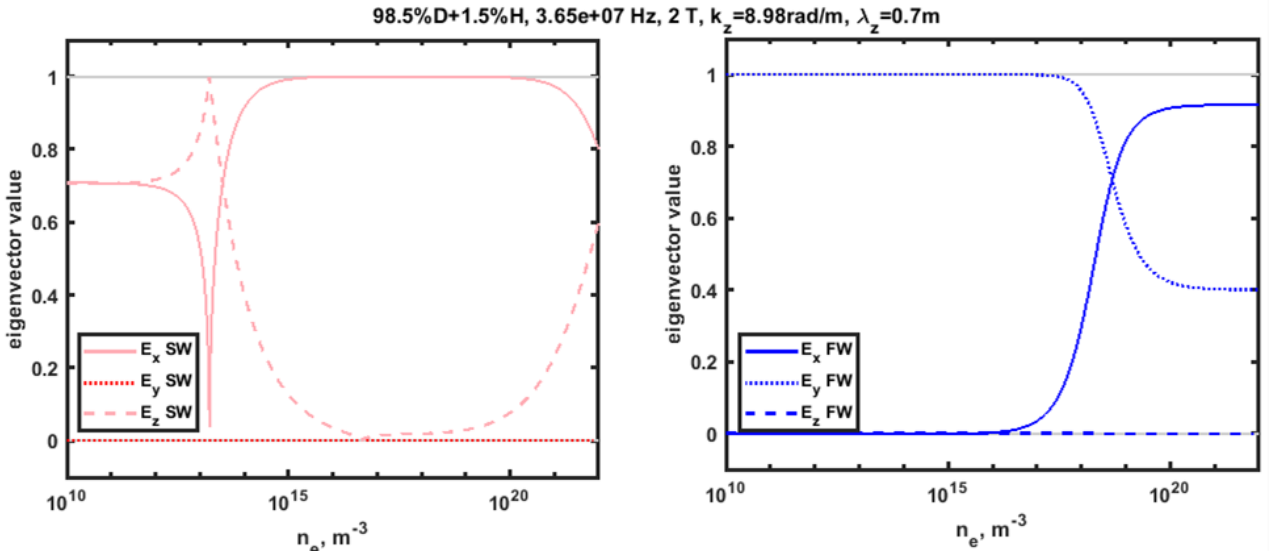

Fig. 2.2. Eigenvector components of the wave electric field for the SW and FW.

And since $\boldsymbol{E} = -i\boldsymbol{k}\varphi$ for electrostatic waves, where φ is the scalar potential, we get:

$$\left|\frac{E_x}{E_z}\right| = \left|\frac{k_\perp}{k_\parallel}\right| = \sqrt{\left|\frac{\varepsilon_\parallel}{\varepsilon_\perp}\right|} \tag{2.29}$$

Equation (2.29) defines the direction of the resulting vector of the electric field (and wave vector) by the ratio of its components. As can be seen from Fig. 2.2 and will also be shown below in the plots of the Stix parameters, the electric field of the ICRF FW is purely perpendicular to the background magnetic field with both perpendicular components having similar order of magnitude for the range of densities where the wave propagates. Parallel component E_z^2 amounts to less than 0.03 % of the total field which makes FW to be a less probable candidate for generation of significant RF sheath

along magnetic field lines. It is true at least in the frame of this simplified calculation, when any realistic non-zero y-component of the wave vector produced by antennas in practice is neglected as well as other factors like finite thickness and electrical conductivity of the antenna strap and the presence of various metallic parts inside the antenna box. The simplified analytical approach still gives the correct electric field polarization of the FW in the region outside of the antenna box on a distance where all local effects become insignificant.

On the contrary, the parallel component of the SW electric field has a non-negligible value in the region of its propagation. At very small densities the parallel direction is even dominant and such field could generate high voltage gradients in the sheath. Then its percentage drops fast with the density growth. In fact, such small densities as 10^{13} m^{-3} are not present in modern tokamaks. The density at the radial position of the antenna limiters is often even higher than the resonance of the SW. In the outer radial direction densities decrease exponentially from the theoretical point of view and in the real machines the decrease is characterized by a more complicated function.

Reliable experimental values have not been measured neither for the densities outside of the ICRF antennas in the limiters shadow, nor for the densities in the antenna box. In a tokamak, transient plasma events as ELMs (Edge Localized Modes - short-time periodic distortion of the plasma boundary), filaments (smaller distortions of the plasma edge), magnetic perturbations, core and edge instabilities constantly change density profiles radially and poloidally during a discharge and happen on different time scales. This is one of the factors that complicate significantly any practical study of RF sheath effects. Densities appropriate for SW propagation can exist at the plasma edge during the discharge; however the exact distribution is unknown.

2.1.4 Shapes of the wavefront

Plasma is one of the materials that have indefinite permittivity tensor. It means that the principal elements of the dielectric tensors can have different signs. Such phenomenon is observed in photonic band gap materials and in electromagnetic metamaterials, artificial media created by subwavelength structuring [Smith2003], [Poddubny2013]. Many unusual properties of these materials are rarely or never observed in nature.

The elements of the dielectric tensor in the cold plasma approximation can change sign depending on the density. The following analysis is performed for the tokamak example conditions that were used in Fig. 2.1 and 2.2. There are two regions where all tensor diagonal elements ($\varepsilon_\perp$ and $\varepsilon_\parallel$) have the same sign (Fig. 2.3). First, it happens before the SW cut-off. Both the SW and the FW are evanescent here. Second, the same signs appear after the SW resonance; the SW is evanescent in this whole region and the FW propagates after the FW cut-off. The signs of $\varepsilon_\perp$ and $\varepsilon_\parallel$ are opposite in the middle region in between these two and this is the region of SW propagation. The real part of the non-diagonal elements, ε_X, is also plotted in Fig. 2.3 to provide an idea of simultaneous behaviour of this dielectric tensor component, though it doesn't affect the wave shape.

The Stix parameters ε_R and ε_L affect the dielectric tensor elements ε_X and $\varepsilon_\perp$ (and thus the wave propagation and the wavefront). Besides that, they indicate the cut-offs of the FW. In Fig. 2.4 ε_R and ε_L are plotted and it can be seen that there is a point where ε_R becomes equal to $n_\parallel^2$, so the condition (2.20) is met. In the considered simple case of a constant magnetic field the left cut-off

(2.21) is not present. In tokamaks, the behaviour of the parameters ε_R and ε_L is different at higher densities, because it is affected by the magnetic field inhomogeneity, which leads to the appearance of both cut-offs.

A second-order partial differential equation can have parabolic, hyperbolic or elliptic form. It is formally defined by the discriminant of the equation:

- $Disc < 0$: elliptic
- $Disc = 0$: parabolic
- $Disc > 0$: hyperbolic

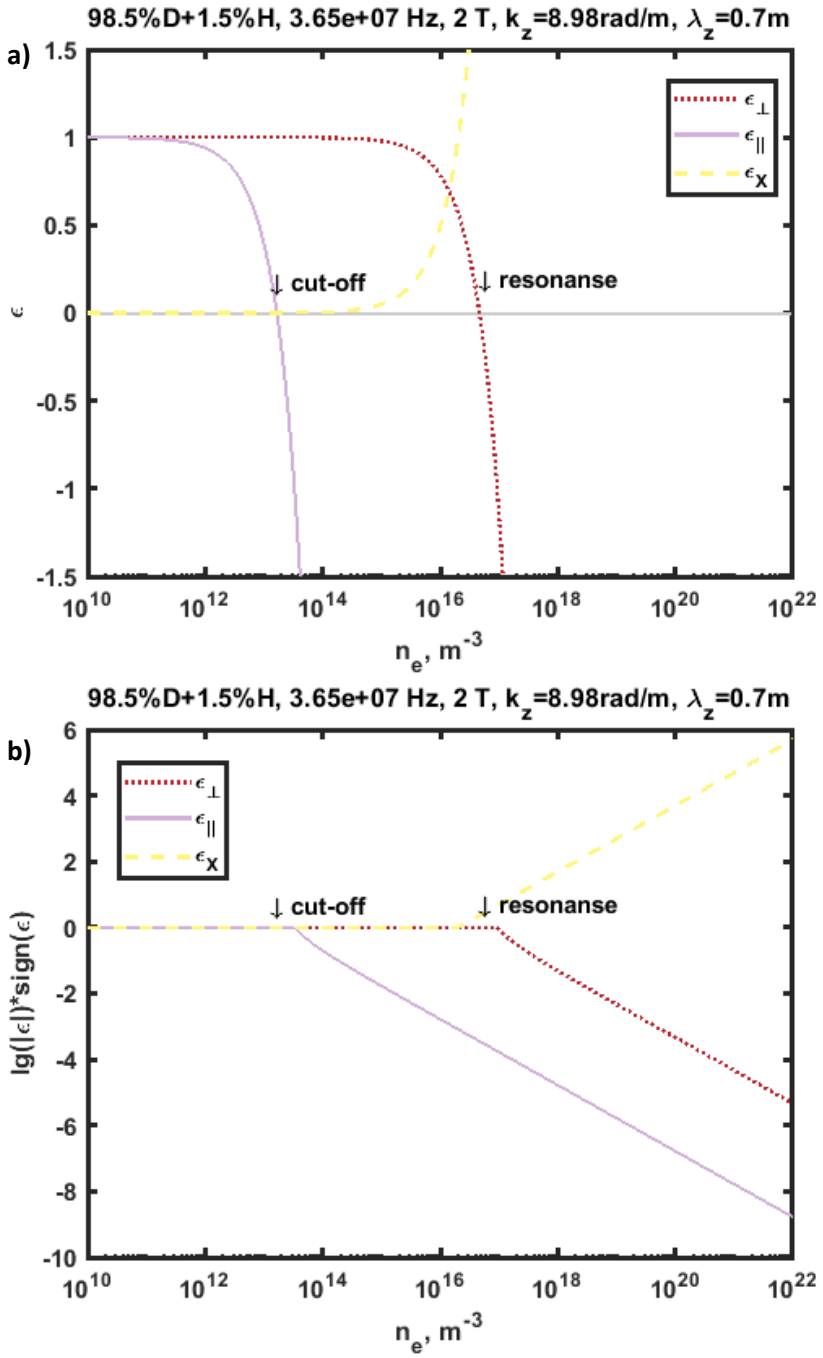

Fig. 2.3. Elements of dielectric tensor $\varepsilon_\perp$, $\varepsilon_\parallel$, ε_X as a function of density: a) part of the range in linear scale to show the small values, b) same in logarithmic scale to show the big values.

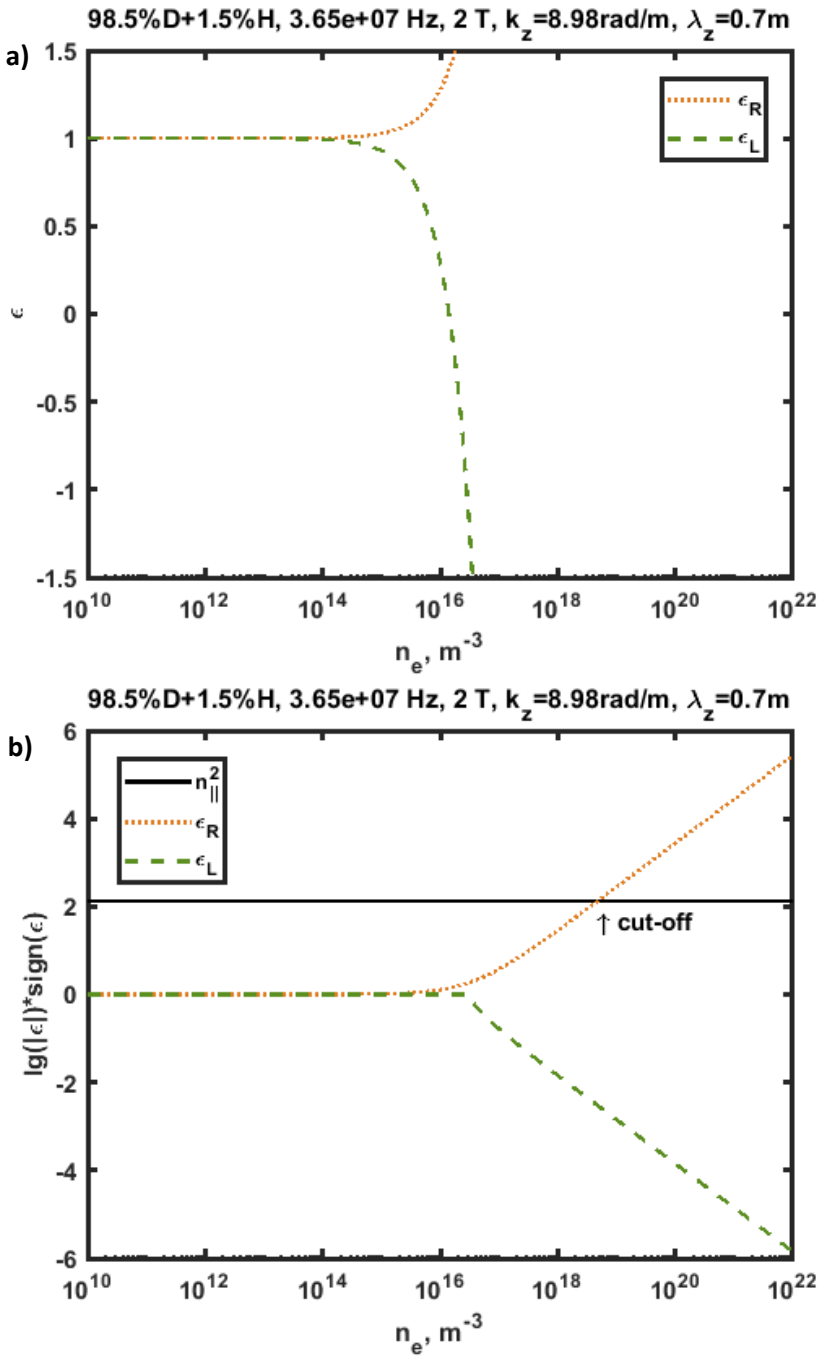

Fig. 2.4. Elements of dielectric tensor ε_R, ε_L as a function of density: a) part of the range in linear scale to show the small values, b) same in logarithmic scale to show the big values. $n_{\|}^2$ is also plotted to indicate the cut-off.

For our case of equation (2.3) (or equivalent (2.5)), the equation is not full, so the determinant cannot be equal to zero and only elliptic and hyperbolic forms are possible. The spatial shape of a wavefront corresponds to the form of the wave equation. In the two regions with the same sign of the diagonal elements the wavefronts will look like ellipses. In the region where the signs of $\varepsilon_\perp$ and $\varepsilon_{\|}$ are opposite, the wavefront will be a hyperbola or as it is often called a resonance cone (RC). RCs were first measured in plasma half a century ago [Fisher1969] and have been studied for many years after (see references in [Myra2008]), also in metamaterials. A specific quality of the RCs is that these waves do not exhibit a periodic structure propagating spatially in the direction of $\boldsymbol{k}$, on contrary to the more common elliptic waves. The wave energy is concentrated in a thin cone and not

transferred further than one single wavefront. The field amplitude oscillates inside the cone in space and time, but is negligibly small outside of the cone. The cone thickness is defined by the size of the oscillation source; the size of a cross-section parallel to the magnetic field corresponds to the width of the ICRF antenna strap that excites the wave (will be demonstrated in Chapter 4).

In plasma, conditions suitable for RCs occur not only for the SW in the ICRF range, but also for the Lower-Hybrid (LH) range of frequencies. Important modelling of RC interaction with a self-consistent radio-frequency sheath near conducting walls perpendicular to the magnetic field was done by J.R. Myra and D.A. D'Ippolito [Myra2008]. The authors showed that RCs are able to transport strong localized RF voltages to RF sheaths at the wall. When a threshold is exceeded, an order unity fraction of the launched RC voltage couples to the sheath. The threshold is defined analytically in the article and is a function of the antenna parallel wavenumber, launched RF voltage amplitude, parallel component of the dielectric tensor and plasma parameters. By adjusting all characteristics to stay below the threshold, sheath voltages are expected to be minimized.

2.2 RF wave energy absorption

The principle of plasma heating with waves is similar for all frequency ranges. Electromagnetic waves carry energy from the generators through transmission lines to the plasma machine, where the vacuum waves get converted into plasma waves and travel in plasma to the region of absorption. Absorption mechanisms can be classified as resonant processes (non-collisional) and collisional processes without a resonance condition [Sagdeyev1958]. Resonant absorption of the wave energy is the most effective way to heat plasma and can absorb the maximum of carried power. Smaller fractions of the wave energy can be also lost in the course of propagation due to non-resonant mechanisms of absorption. In both types of the processes the energy is received by usually a small portion of plasma particles and it is then redistributed to the bulk plasma during thermalisation, so that the Maxwellian distribution is eventually restored.

A resonance condition means either a large accumulation of the wave field in case of the wave resonance or a strong sensitivity of the particle's motion to the wave in the wave-particle resonance. Theoretical definition of the wave resonances was given in Section 2.1: $k_\perp^2 \to \infty$. As a wave approaches the resonance from the region of lower densities, the wave vector grows, so the wave slows down (i.e. the group velocity goes to zero) and it stops at the point of the resonance. Continuous incoming waves build-up the wave amplitude at the resonant position and on top of that the damping mechanisms are strengthened by the fact that the wavelength becomes very small at the vicinity of the resonance, so a large amount of oscillations happen is a small spatial area.

The wave-particle resonances include Landau damping, ion and electron cyclotron damping, etc. [Louche-Koch-lecture]. Landau damping occurs when a particle sees the wave electric field as constant and is accelerated in this field. For this the resonance condition is that the particle speed is equal to the wave phase velocity $v_{ph} = \omega/k$. The zero-order velocity v_0 have to comply with this requirement, while the first-order correction will appear as a result of acceleration (Z is the particle charge equal to the atomic number for fully stripped ions, x_0 is the zero-order coordinate of unperturbed particle motion):

$$v_1 = \frac{ZeE}{m} cos(kx_0)t \tag{2.30}$$

The energy can be transferred from the wave to the particle (acceleration) or vice versa (deceleration). Positive net energy transfer happens when there are more particles in the velocity distribution that have a velocity slightly smaller than the wave phase velocity than those which are faster. This is the case for Maxwellian distribution. Similarly to the Landau damping, another mechanism exists due to a propagating wave modulation, magnetic rather than electric.

The cyclotron damping is the main mechanism for the ICRF heating. Ions rotate around magnetic field lines at the ion cyclotron frequency Ω_{ci}. Rotating electric field of the wave at the frequency equal to Ω_{ci} enhances the perpendicular energy of the ions. Lots of various scenarios exist for the ICRF heating with the fast wave in tokamaks [Becoulet1996], the main ones being minority heating, harmonic heating and few-species heating scenarios. The ion cyclotron mechanism of the energy absorption is also widely applied to enable current drive in the plasma, using the asymmetric phasing on the antenna straps. Theoretical estimation of the power radiated by the fast wave in plasma obtained from the Poynting theorem is given in [Louche-Koch-lecture]. The simple theory neglects the detailed geometry of the antenna, poloidal antenna inhomogeneity, presence of feeders or limiters and realistic plasma density profile, but is still able to reproduce the main picture of the power coupling of ICRF antennas.

Any wave-particle resonance means energy transfer only to a small fraction of the particle distribution. If the acceleration happens much faster than collisional relaxation of the velocity distribution, particles of resonant velocities will quickly escape the resonance condition and heating will terminate. For a continuous energy transfer the velocity distribution flattening in the interaction range should be compensated by collisions and other processes, so that the distribution remains Maxwellian. Besides collisions another reason of thermalisation is inhomogeneities of the magnetic field along the field line.

Non-resonant direct dissipation of the electromagnetic wave due to collisions is characterized by the ratio of the collisional frequency to the frequency of the wave ν/ω. When the ratio is small, the wave dissipation is negligible, unless large perturbations in the particle motion occur.

2.3 RF modelling in COMSOL software

2.3.1 COMSOL and its existing applications for fusion plasma

The COMSOL software [https://www.comsol.com/] is a very powerful tool for simulations of various designs and processes, in fields of fluid dynamics, chemistry, mechanics, electromagnetics, etc., as well as in a combination of all possible equations into one multiphysics model. By its very nature, plasma is a multiphysics system which requires a combination of sets of equation from different physics branches in order to be described (only approximately in most cases). Existing simulations of electromagnetic waves interaction with fusion (high-density) plasma include models done in COMSOL: RAPLICASOL and SSWICH.

RAPLICASOL (Radiofrequency wAve couPLing for Ion Cyclotron Antenna in Scrape-Off-Layer) is a 3D Finite Element linear solver for Maxwell's equations in the cold plasma approximation

[Jacquot2013PPCF], [Jacquot2013Thesis] designed to simulate a realistic 3D geometry of ICRF antennas, 3D density profiles [Tierens2017] and a part of fast wave propagation region of plasma, without the hot core where a different plasma description is needed and without any non-linear sheath phenomena. Substantial work was done to develop an absorbing material in COMSOL - Perfectly Matched Layer (PML) - suitable for plasma [Jacquot2013PPCF], which is needed to replace the part of the hot core plasma where in a tokamak power absorption takes place and which allows to reduce significantly the size of a numerical model. RAPLICASOL was validated against TOPICA [Tierens2018], a 3D code developed earlier [Lancellotti2006], [Milanesio2009] to simulate fast wave propagation, and also against experiments. It showed results comparable to TOPICA (2% deviation on the reflection coefficients) at much lower numerical cost (18-fold decrease in CPU requirements).

SSWICH (Self-consistent Sheaths and Waves for Ion Cyclotron Heating) is a 2D code that aims at modelling of RF sheaths in a self-consistent manner to determine the non-linear interaction of RF waves with the edge plasma in a tokamak [Jacquot2012], [Colas2012]. It is used in combination with RAPLICASOL, taking parallel electric field profiles from it as an input for RF sheath voltages calculation [Jacquot2015], [Jacquot2017]. It was previously also coupled with TOPICA instead of RAPLICASOL in simulations for the Tore Supra tokamak [Jacquot2014]. Improvements of SSWICH in order to account for the full RF field polarization, curved walls and the tilt of to the background magnetic field are published in [Lu2016PPCF], [Lu2018], [Lu2016Thesis].

2.3.2 Framework of simulations for IShTAR

In the scope of this thesis COMSOL models are developed for wave-plasma interaction by relying on the same main principles as in RAPLICASOL:

- plasma is simulated as a dielectric medium with dielectric tensor derived in the cold plasma approximation (described in the section 2.1);
- PML is used to absorb the wave energy and replace infinite (or simply big) regions of wave propagation and absorption (described in the next section);
- simulations are done in 3D using COMSOL RF module [https://www.comsol.com/rf-module].

Presented simulation work is intended to support the experimental studies of RF sheaths on IShTAR. Different tasks are addressed, including diagnostics calibration, impedance matching tests, achievement of coupling conditions equal to the experiment, power losses through the use of PMLs on the outer edges and through the collisional mechanism in the plasma bulk, vacuum simulations of realistic IShTAR geometry and comparison of vacuum ICRF fields to the experimental measurements of B-dot probes. All of the results are demonstrated in Chapter 4.

Even though the physics basis is inherited from RAPLICASOL, the IShTAR density range, suitable only for SW propagation and little wave absorption in plasma, determine special conditions for simulations, different from the ones in RAPLICASOL. The PML had to be adjusted and collisional absorption needed to be implemented. The slow wave propagation, which is fully avoided in RAPLICASOL, was for the first time simulated in 3D. In order to study the physics of SW, a simple geometry was created and further complexity was introduced step-by-step, so that numerical effects on the obtained solutions can be always decoupled from the physics effects. The realistic

IShTAR geometry with numerous small details was simplified for plasma simulations to avoid very high numerical costs and large computational times.

The 3D modelling of the slow wave developed in this thesis can be used together with SSWICH to obtain the sheath potentials around limiters of IShTAR ICRF antenna. Spectroscopic experimental measurements foreseen on IShTAR [Kostic2018] should provide a validation of the numerical codes for the conditions different from those that they were used in before. The slow wave propagation, always avoided in RAPLICASOL, is now characterized and could be potentially implemented there as well.

2.3.3 Perfectly Matched Layer (PML) in COMSOL

Perfectly Matched Layer was first suggested in 1994 [Berenger1994] and since then is commonly used as a radiating boundary conditions at infinity. It is built-in in the COMSOL software, however the functionality is rather limited and makes it suitable for usage only with usual dielectrics. In RAPLICASOL the PML was for the first time implemented for high-density plasma as a manually defined material.

The PML in reality is not a boundary but a layer that surrounds the interior simulation region on all the boundaries which the wave is expected to penetrate. The goal of the PML is to imitate the outgoing propagating wave without any reflection on the interface and this is the crucial feature that differs the PML from other absorbing materials or boundaries.

The wave equation is solved continuously from the main simulation domain to the PML region, but the coordinate x in the direction of the wave damping is transformed from real to the complex stretched coordinate by the stretching function $S_x(x) = 1 + \frac{i\sigma(x)}{\omega_0}$:

$$x \to \int_0^x S_x(x')dx' = x + \frac{i}{\omega_0}\int^x \sigma(x')dx' \tag{2.31}$$

where ω_0 is the wave frequency and $\sigma(x)$ is a damping function satisfying

$$\begin{cases} \sigma(x) = 0, x < 0, \\ \sigma(x) > 0, x > 0 \end{cases} \tag{2.32}$$

This transformation leads to propagating oscillating waves being replaced by exponentially decaying ones, as will be shown below.

When $\sigma(x) > 0$ the limit of the integral in (2.31) is infinity:

$$\int^x \sigma(x')dx' > 0 \Rightarrow \lim_{x\to+\infty} \int^x \sigma(x')dx' \to +\infty \tag{2.33}$$

For a forward ($k > 0$) plane (e^{ikx}) wave travelling in $+x$ direction it means:

$$ikx \to ik\left(x + \frac{i}{\omega_0}\int^x \sigma(x')dx'\right) = ikx - \frac{k}{\omega_0}\int^x \sigma(x')dx' \tag{2.34}$$

And because $\lim_{x\to+\infty} e^{-\frac{k}{\omega_0}\int^x \sigma(x')dx'} = 0$, it follows that

$$\lim_{x\to+\infty} e^{ikx} e^{-\frac{k}{\omega_0}\int^x \sigma(x')dx'} = 0 \tag{2.35}$$

It means that the wave is completely decayed at infinity.

For the x derivative the stretching is also applied:

$$\partial_x \to \frac{1}{1+\frac{i\sigma(x)}{\omega_0}}\partial_x \tag{2.36}$$

The spatial gradient length is therefore $\sim\sigma/\omega_0$. The higher the coefficient, the faster the wave attenuates.

In a general 3D case where the direction of damping is undefined, the stretching functions are applied as in (2.31) to all 3 coordinates:

$$\bar{\bar{S}} = \begin{pmatrix} S_x(x) & 0 & 0 \\ 0 & S_y(y) & 0 \\ 0 & 0 & S_z(z) \end{pmatrix} \tag{2.37}$$

When the differential operator ∇ in Maxwell equations (2.2) is replaced by a corresponding modified operator $\nabla_S = \bar{\bar{S}}^{-1}\nabla$ in stretched coordinates, the dielectric tensor in PML becomes:

$$\bar{\bar{\varepsilon}}_{PML} = \begin{pmatrix} \varepsilon_{xx}\frac{S_y(y)S_z(z)}{S_x(x)} & \varepsilon_{xy}S_z(z) & \varepsilon_{xz}S_y(y) \\ \varepsilon_{yx}S_z(z) & \varepsilon_{yy}\frac{S_z(z)S_x(x)}{S_y(y)} & \varepsilon_{yz}S_x(x) \\ \varepsilon_{zx}S_y(y) & \varepsilon_{zy}S_x(x) & \varepsilon_{zz}\frac{S_x(x)S_y(y)}{S_z(z)} \end{pmatrix} \tag{2.38}$$

And the same transformation happens to the permeability tensor $\bar{\bar{\mu}}_{PML}$. Of course, these tensors are not always full and apart from that for many applications some of the stretching functions can be for simplicity taken as 1.

The mathematical form of coordinates stretching is different for time domain and frequency domain calculations. The theory derived here is applicable to the frequency domain only and all COMSOL simulations in the present work are done as frequency domain studies. The PMLs in all following models are implemeted as a dielectric with tensors $\bar{\bar{\varepsilon}}_{PML}$ and $\bar{\bar{\mu}}_{PML}$ defined in this section and tensor elements ε_{xx}, ε_{xy}, etc. defined in Section 2.1. The same wave equation is solved in all simulation domains (vacuum, plasma, PML) and only material properties vary from one domain to another.

The form of stretching functions in RAPLICASOL is chosen to be polynomial:

$$S_x(x) = \begin{cases} 1, & x < 0 \\ 1 + (S_x' + iS_x'')\left(\frac{x}{L_{PMLx}}\right)^{p_x}, & x > 0 \end{cases} \tag{2.39}$$

with coefficients L_{PMLx} the PML depth, p_x the order of the stretching function, S_x' the real stretch and S_x'' the imaginary stretch. A thorough study of the coefficients of the polynomial stretching function and of their influence on the wave reflection from the PML was done in [Jacquot2013Thesis]. It allowed to apply the same polynomial function form and to have a starting point for choosing the coefficients in the models presented in Chapter 4.

It should be remembered that the PML in the present formalism is not able to handle both forward and backward waves simultaneously. In general, a wave is considered a forward (backward) wave if the scalar product of the phase and group velocities is positive (negative). The fast wave is by definition a forward wave and the slow wave is a backward wave. This did not cause any troubles in the simulations for IShTAR, because SW and FW propagation were separated in the modeled conditions. It will be also seen from the results of the simulations that for the SW only the PMLs on the sides are crucial, while it is known from the FW simulations that FW propagates mostly forwards, so the front PML is the one that has to absorb it. It means that both waves can be propagating and coexist in one simulation domain if a combination of different PMLs is used (FW PML in front and SW PML on the sides) and each of the wave modes is strongly evanescent in the direction of propagation of the other one, so no significant power fraction of FW reaches the SW PML even in the evanescent wave form and vice versa.

COMSOL software provides an opportunity to plot the direction of the Poynting vector and the distribution of the power absorption, so this way the correctness of the chosen stretching function coefficients is double-checked in the performed simulations.

2.4 Basics of diagnostics employed in this thesis

2.4.1 Langmuir probe

A Langmuir (or electric) probe is a metal electrode of small size, which is introduced into the plasma. Through the voltage source, the probe is connected to a reference electrode, which may be the anode or the cathode of the discharge tube, metal wall of the discharge chamber or a specially designed electrode. Measurements of the probe current depending on the value of the applied voltage allow determining the probe IV characteristic. From the IV curve local – at the location of the probe – parameters of undisturbed plasma can be defined. Such capability is based on the fundamental property of plasma screening of external static or quasi-static electric field. The characteristic size of the screening is the Debye radius, which size is generally much smaller than the size of the plasma (and the size of the probe), so the perturbation region is localized near the probe surface. A small value of the current collected by the probe provides a small perturbation introduced by it into the distribution of discharge currents and concentrations of charged particles in plasma.

It is the locality of the measured characteristics that is the main and undeniable advantage of the probe diagnostic. Another advantage is the simplicity of the equipment used, which allows to obtain the result quickly and without high costs. Finally, the number of measured parameters and their measurement ranges are so large that they have no analogues among other diagnostic methods. The field of application covers the range of the gas pressure from 10^{-5} to 10^{3} Torr and the concentrations of charged particles from 10^{13} to 10^{21} m^{-3}. This set of qualities ensures the relevance of the Langmuir probes from the first studies of gas discharges [Langmuir1923], [Langmuir1924], [Mott-Smith1926] to the present time.

However, the undoubted advantages of the probe method are burdened by the complexity of the theoretical description due to a number of factors affecting the IV characteristic of the probe. A sufficiently strict analytical description is only possible in few limiting cases. Changing the

parameters of plasma or the dimensions of the probe means a change in the physics of the interaction of the plasma with the probe, and consequently the theory needs to be adjusted for data interpretation. Proportions of three characteristic sizes of the probe, λ_D – Debye shielding length, r_{pr} – probe dimension, λ_i, λ_e – mean free path for ions, electrons, define the transport of charged particles near the probe and their collection:

- $\lambda_{i,e} \gg \lambda_D \gg r_{pr}$ – Collision-free movement of ions and electrons in thick sheath (orbital-motion-limited (OML) theory of Langmuir and associates [Mott-Smith1926]).
- $\lambda_{i,e} \gg r_{pr} \gg \lambda_D$ – Collision-free movement of charge particles in thin sheath (space charge limit).
- $\lambda_D \gg \lambda_{i,e} \gg r_{pr}$ – Probe current is determined by collisions of charged and neutral particles in space-charge sheath around the probe. Ion temperature is of the order of temperature of neutrals.

During the century that passed since the invention of the Langmuir probe, the electrical probes found broad applications. A lot of variations of the probes have been developed: Langmuir probes of planar, cylindrical and spherical shape, heated probes, emissive probes, plasma oscillation probes, Mach probes, Ball-pen probes, etc. Complex systems of double or multiple probes are constructed in an attempt to improve the diagnostic. When the range of application is chosen correctly, advanced methods of electrical probes can provide results inaccessible for a classical Langmuir probe and, most importantly, can simplify the interpretation of the results.

The general idea of the applied voltage sweep results in an IV characteristic with three distinct regions of current collection (Fig. 2.5):

I. Ion saturation: when the probe potential is less than the potential of the plasma V_{pl}, electrons are repelled and positive ions are accelerated towards the probe; the ion current saturates when a positive sheath is formed around the probe that prevents further ion collection.
II. Electron retardation: at small negative (relative to V_{pl}) potentials electrons are retarded in the field of the probe sheath but some of them can still reach the probe, so the current is a sum of both ion and electron contribution; when the two contributions are equal, the net current is zero and this point on the IV curve is called floating potential V_{fl}.
III. Electron saturation: at V_{pl} the potentials of the probe and the plasma are equal, so both species of charged particles can move freely and be collected by the probe; much higher electron mobility in reality results that already at V_{pl} the ion current is negligibly small and at higher potentials only electrons are collected, with the same saturation mechanism as in the ion saturation branch.

From the different regions various plasma parameters can be obtained: plasma density (n), plasma temperature (T), ion flux, floating and plasma potentials (V_{fl}, V_{pl}) and electron energy distribution function (EEDF).

Depending on the plasma environment, i.e. presence of magnetic field or radio-frequency oscillations in plasma, the design and data interpretation of the probes need to be adjusted. This is the case for tokamaks and many other plasma devices. RF compensation circuits are introduced to

avoid shifts of the potential in the IV characteristics [Chatterton1991], [Sudit1994]. In magnetized plasmas, additional characteristic size comes into play: Larmor radii of cyclotron rotation around magnetic field lines r_{ce} and r_{ci} of electrons and ions. When they are smaller than the probe size, theories for non-magnetized plasma may be applicable [Kudrna1997], otherwise the local transport is affected strongly by the magnetic field. In this thesis, Langmuir probes application in magnetized plasmas is of interest. Chapter 3 is dedicated to the detailed discussion of the probe data interpretation in such plasmas and two theories for probe effective collecting area are elaborated. Langmuir probes are also applied in the experimental studies of Chapter 4.

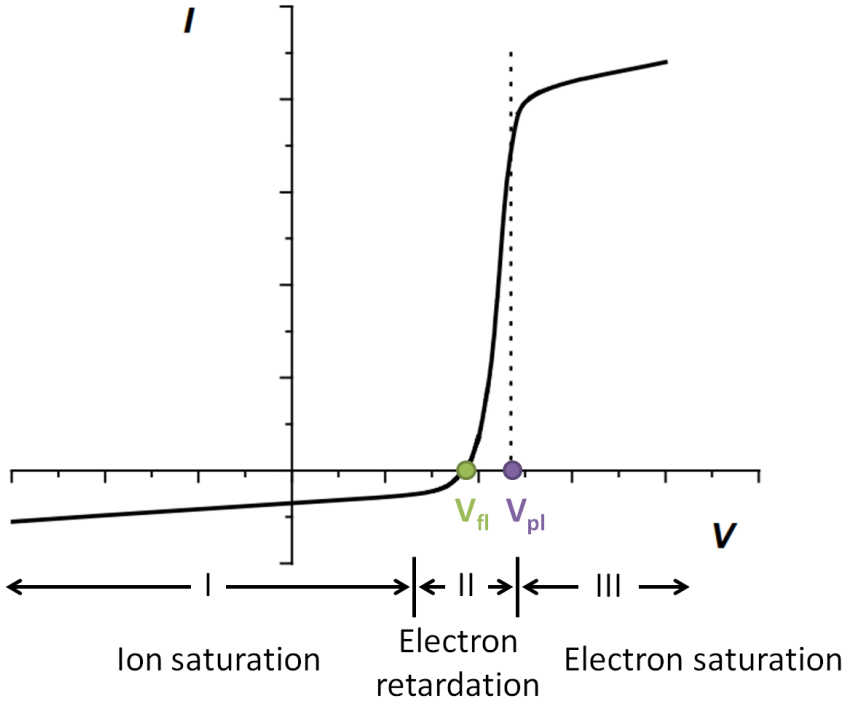

Fig. 2.5. Regular IV characteristic measured by a Langmuir probe in plasma.

2.4.2 B-dot probe

Magnetic measurements provide some of the most fundamental and essential information about plasma: plasma current, internal inductance, boundary shape, thermal energy, currents in the magnet coils, strength of the magnetic fields confining the plasma, information about the internal characteristics of the plasma and Halo currents in machine structures. Magnetic diagnostics on tokamaks are essential for equilibrium reconstructions, real-time plasma shape and position control, they are external, passive and robust.

Global inductive magnetic sensors include Rogowski coil, Flux loops and Mirnov coils and they target measurements of total electric current flowing through the enclosed surface (plasma, plasma + vessel, external coils, passive conductors). Local inductive magnetic probes, or B-dot probes, measure components of the local magnetic field strength and they usually consist of solenoidal wire, with dimensions small compared to the gradient scale length of the magnetic field. The general principal of the measurement is the same for both global and local sensors and is based on Faraday's

Law [Hutchinson2005]. The solenoidal wire of several loops is placed in a plane perpendicular to the direction of the magnetic field component that is intended to be measured (Fig. 2.6).

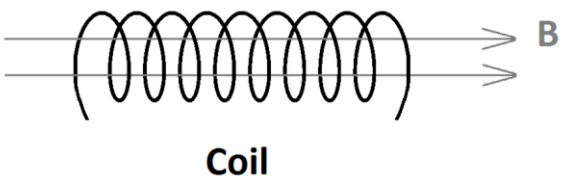

Fig. 2.6. Schematic magnetic probe.

Measured voltage between two ends of the wire is induced by varying magnetic field intersecting the loop:

$$V = \oint \boldsymbol{E}\, d\boldsymbol{l} = -\dot{\Phi} = NA\dot{B} \tag{2.40}$$

where $d\boldsymbol{l}$ is a vector element of the circular contour, Φ is the magnetic flux, N is the number of turns in the coil of area A and the dot denotes time derivative. The time derivative of B can be directly calculated from this formula and the magnetic field itself can be obtained by integration of the induced signal either digitally or through an integrating circuit.

B-dot probes are one of the diagnostics used on IShTAR to characterize the magnetic field distribution of the ICRF antenna waves. Details on the probe design and data acquisition system as well as experimental results are presented in Chapter 4.

2.4.3 Interferometry

The phenomenon of interference occurs when two (or more) coherent waves propagate through different paths between the source and the detector (Fig. 2.7). The resulting pattern gives information on the phase shift and the amplitude change of the two waves. When one of the wave path goes through the plasma, its optical length varies because of the change in refractive index connected with the increase and the decrease of the electron density. Measurement of the phase shift relative to a wave that went on an undisturbed reference path outside the plasma provides directly the line-averaged plasma density. Microwave interferometry is based on the described method and is one of the standard tokamak plasma diagnostics [Wesson2004]. Theoretical basics of interferometry are well described in many literature, for example, [Hugenholtz1990] and is shortly summarized below.

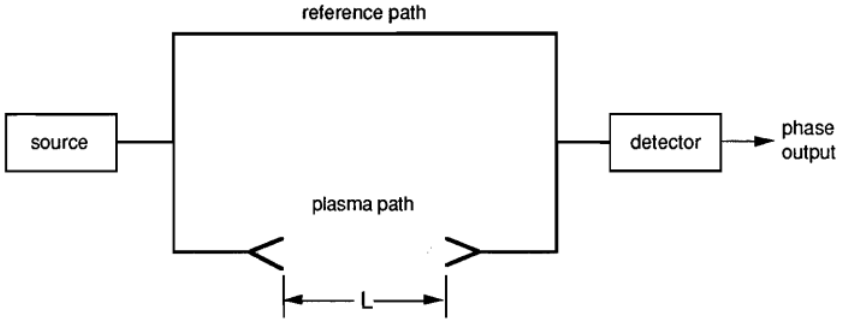

Fig. 2.7. Basic interferometer with signal split into two parts: one going on the reference path and one passing through plasma; both are collected and interfered in the receiving detector.

The reference path length L contains a number a of vacuum wavelengths λ_0: $L = a\lambda_0$, with $a = \frac{\varphi_0}{2\pi}$, and the path in the plasma accounts b times of λ_0: $L = b\lambda_0$, with $b = \frac{\varphi_p}{2\pi}$, where φ_0 and φ_p are the phases of the waves after travelling through vacuum and through plasma, respectively. Therefore, $\varphi_0 = \frac{L}{\lambda_0}2\pi$ and $\varphi_p = \frac{L}{\lambda_p}2\pi$. The refractive index is

$$\mu = \frac{c}{v_{ph}} = \frac{\lambda_0}{\lambda_p} \tag{2.41}$$

where c is the velocity of light and v_{ph} the phase velocity in the medium.

The measured phase shift between two paths is calculated as

$$\Delta\varphi = \varphi_0 - \varphi_p = 2\pi L\left(\frac{1}{\lambda_0} - \frac{1}{\lambda_p}\right) = \frac{2\pi L}{\lambda_0}(1-\mu) \tag{2.42}$$

In collisionless cold magnetized plasma for ordinary wave propagation ($\boldsymbol{E}$ of the wave parallel to the background magnetic field) the refractive index can be written as

$$\mu = \sqrt{1 - \frac{f_p^2}{f^2}} \tag{2.43}$$

where f is the frequency of the probing beam and f_p is the plasma frequency:

$$f_p = \sqrt{\frac{e^2 n_e(r)}{4\pi^2 \varepsilon_0 m_e}} = 8.98\sqrt{n_e} \tag{2.44}$$

e is the electronic charge, m_e is the electron mass, $n_e(\mathrm{r})$ is the local electron density, which may vary in space and ε_0 is the permittivity of the free space.

For a particular probing frequency there is a critical density n_c above which the probing beam will not propagate through the plasma. It can be found from (2.43): $1 > \frac{f_p^2}{f^2}$ should hold true. Plasma densities in tokamak experiments range from 10^{18} to 10^{21} m^{-3}; this corresponds to probing frequencies of 10 GHz to 300 GHz (microwave range).

Equation (2.43) can be rewritten as

$$\mu = \sqrt{1 - \frac{n_e(r)}{n_c}} \tag{2.45}$$

So the phase difference from (2.42) is equal to

$$\Delta\varphi = \frac{2\pi}{\lambda_0}\int_0^L [1 - \mu(n_e(r))]dL \tag{2.46}$$

The frequency of interferometer is chosen in practice such that it is much higher than the plasma frequency, so (2.45) can be approximated by

$$\mu \approx 1 - \frac{1}{2}\frac{n_e(r)}{n_c} \tag{2.47}$$

which leads to

$$\Delta\varphi \approx \frac{\pi}{\lambda_0 n_c}\int_0^L n_e(r)dL = \frac{8.98^2\pi}{cf}\int_0^L n_e(r)dL = \frac{8.4*10^{-7}}{f}\langle n_e\rangle L \qquad (2.48)$$

where <ne> is line-averaged density of plasma which is then defined as

$$\langle n_e\rangle = 1.18 * 10^{15}\, f\Delta\varphi\frac{1}{L}, \qquad (f \text{ in GHz}) \qquad (2.49)$$

Plasma collisionality can be accounted for in (2.43). Considering collision frequency ν to have non-zero but small value compared to both plasma angular frequency ω_p and the frequency of the wave ω, we can rewrite the refractive index expression [Robinson1963]:

$$\mu = \sqrt{1-\frac{\omega_p^2}{\omega^2+\nu^2}} = \sqrt{1-\frac{\omega_p^2}{\omega^2\left(1+\frac{\nu^2}{\omega^2}\right)}} \approx 1-\frac{1}{2}\frac{n_e(r)}{n_c\left(1+\frac{\nu^2}{\omega^2}\right)} \qquad (2.50)$$

Line-averaged density for collisional plasma is then found as

$$\langle n_e\rangle = 1.18 * 10^{15}\, f\Delta\varphi\frac{1}{L}\left(1+\frac{\nu^2}{\omega^2}\right), \qquad (f \text{ in GHz}) \qquad (2.51)$$

An electromagnetic wave undergoes refraction when passing through the plasma. The refraction angle must be kept small, otherwise the wave would miss the receiving antenna. In order to monitor how big the refraction is, not only the phase of the wave needs to be measured, but the amplitude as well. At critically big angles of refraction only small portion of the wave is collected by the receiver and the low resulting amplitude would indicate a refraction. Wave attenuation measurements can be also used to obtain plasma density.

On Aline device (Chapter 3) 26.5 GHz microwave interferometer MWI 2650 produced by Miwitron company is used for density measurements. The system consists of an emitting and a receiving horn antennas and a control unit with digital output that can be connected either to an oscilloscope or to a computer (Fig. 2.8). The densities are calculated according to the equation (2.51). The minimum phase shift level that the MWI 2650 can detect is 0.1°. Critical density for the chosen frequency is $8.7*10^{18}$ m^{-3} which is above expected densities in Aline. The interferometer is quite straightforward to use, the only measures which are needed before measurements are calibration and zero adjustments without plasma.

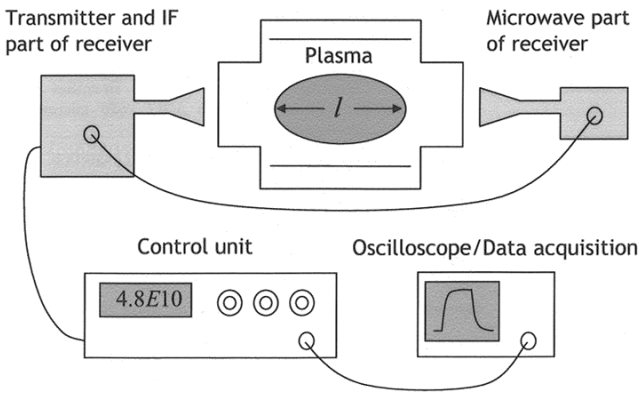

Fig. 2.8. Principle setup of MWI 2650

2.5 Conclusions

It is shown that the full solutions of the wave equation in the cold plasma approximation can be replaced with simplified solutions called fast wave and slow wave, when several conditions are fulfilled. This is the case for the considered tokamak example parameters. The fast wave, which is used for the plasma heating in tokamaks, is seen to propagate at high densities. The slow wave mode is evanescent at high densities but propagates in the region of the lower densities which can be present inside ICRF antennas or at the very edge of the tokamak plasma, in the shadow of the antenna limiters. The calculations show that the parallel component of the SW electric field has a non-negligible value in the region of its propagation, which can be the reason of the deleterious effects of the ICRF antennas operation. The SW will be studied in this thesis in details for the conditions of the dedicated experimental device IShTAR.

Mechanisms of RF wave energy absorption in plasma are described, the role of resonances is explained and the non-resonant mechanisms are mentioned. The SW can meet resonant conditions at the highest density of its propagation region, and it can also transfer energy to the plasma particles through other mechanisms of absorption. The processes of the energy transfer will be further explored and applied in simulations.

The main features of modelling software COMSOL used in this work are introduced in this chapter and previous simulations in COMSOL are described. This allowed defining the framework of the simulations of the SW in the IShTAR conditions.

Various experimental diagnostics are used in this thesis. Basic principles of a Langmuir probe, a B-dot probe and an interferometer is described in order to provide the theoretical background for the results given in the following chapters.

References

[Becoulet1996] – A. Becoulet, "Heating and current drive regimes in the ion cyclotron range of frequency", Plasma Phys. Control. Fusion **38** (1996) A1

[Berenger1994] – J-P. Berenger, "A perfectly matched layer for the absorption of electromagnetic waves", J. Computional Physics **114** (1994) 185

[Bingren1999] – S. Bingren, "A note on classification of ICRF Fast and Slow Waves", China Nuclear Information Center (1999) 72

[Chatterton1991] – P.A. Chatterton, J.A. Rees, W.L. Wu, K. Al-Assadi, Vacuum **42(7)** (1991) 489

[Colas2012] – L. Colas et al., "Self consistent radio-frequency wave propagation and peripheral direct current plasma biasing: Simplified three dimensional non-linear treatment in the “wide sheath” asymptotic regime", Phys. Plasmas **19** (2012) 092505

[Crombe2016JPP] – K. Crombé and D. Van Eester, "Parameter study of ICRH wave propagation in IShTAR", J. Plasma Phys. **82** (2016) 905820203

[Fisher1969] – R.K. Fisher and R.W. Gould, "Resonance Cones in the field pattern of a short antenna in an anisotropic plasma", Phys. Rev. Lett. **22** (1969) 1093

[Hugenholtz1990] – C.A.J. Hugenholtz, "Microwave interferometer and reflectometer techniques for thermonuclear plasmas", Technische Universiteit Eindhoven (1990)

[Hutchinson2005] – I.H. Hutchinson, "Principles of Plasma Diagnostics", second edition. Cambridge University Press, 2005

[Jacquot2012] – J. Jacquot et al., "Recent advances in self-consistent RF sheath modeling and related physical properties: Application to Tore Supra IC antennae", Proceedings of the 39th EPS Conference & 16th ICPP **36F** (2012) 2

[Jacquot2013PPCF] – J. Jacquot et al., "2D and 3D modeling of wave propagation in cold magnetized plasma near the Tore Supra ICRH antenna relying on the perfecly matched layer technique", Plasma Phys. Control. Fusion **55** (2013) 115004

[Jacquot2013Thesis] – J. Jacquot, "Description non-linéaire auto-cohérente de la propagation d'ondes radiofréquences et de la périphérie d'un plasma magnétisé", PhD Thesis (2013)

[Jacquot2014] – J. Jacquot et al., "Radio-frequency sheaths physics: Experimental characterization on Tore Supra and related self-consistent modeling", Phys. Plasmas **21** (2014) 061509

[Jacquot2015] – J. Jacquot et al., "Full wave propagation modelling in view to integrated ICRH wave coupling/RF sheaths modelling", AIP Conference Proceedings **1689** (2015) 050008

[Jacquot2017] – J. Jacquot et al., "Sequential modelling of ICRF wave near RF fields and asymptotic RF sheaths description for AUG ICRF antennas", EPJ Web of Conferences **157** (2017) 03020

[Kostic2018] – A. Kostic et al., "Development of a spectroscopic diagnostic tool for electric field measurements in IShTAR (Ion cyclotron Sheath Test ARrangement)", Rev. Sci. Instrum. **89** (2018) 10D115

[Kudrna1997] – P. Kudrna, E. Passoth, "Langmuir Probe Diagnostics of a Low Temperature Non-Isothermal Plasma in a Weak Magnetic Field", Contrib. Plasma Phys. **37** (1997) 417

[Lancellotti2006] – V. Lancellotti et al., "TOPICA: an accurate and efficient numerical tool for analysis and design of ICRF antennas", Nucl. Fusion **46** (2006) S476

[Langmuir1923] – I. Langmuir and H.M. Mott-Smith, Gen. Electr. Rev. **26** (1923) 731

[Langmuir1924] – I. Langmuir and H.M. Mott-Smith, Gen.Electr. Rev. **27** (1924) 449, 538,616,762,810

[Louche-Koch-lecture] – F. Louche and R. Koch, "The coupling of electromagnetic power to plasmas", FZ-Juelich

[Lu2016PPCF] – L. Lu et al., "Ion cyclotron wave coupling in the magnetized plasma edge of tokamaks: impact of a finite, inhomogeneous density inside the antenna box", Plasma Phys. Control. Fusion **58** (2016) 055001

[Lu2016Thesis] – L. Lu, "Modelling of plasma-antenna coupling and non-linear radio frequency wave-plasma-wall interactions in the magnetized plasma device under ion cyclotron range of frequencies", PhD Thesis (2016)

[Lu2018] – L. Lu et al., " Modelling of radio frequency sheath and fast wave coupling on the realistic ion cyclotron resonant antenna surroundings and the outer wall", Plasma Phys. Control. Fusion **60** (2018) 035003

[Milanesio2009] – D. Milanesio et al., "A multi-cavity approach for enhanced efficiency in TOPICA RF antenna code", Nucl. Fusion **49** (2009) 115019

[Mott-Smith1926] – H.M. Mott-Smith and I. Langmuir, "The Theory of Collectors in Gaseous Discharges", Phys. Rev. **28** (1926) 727

[Myra2008] – J.R. Myra and D.A. D'Ippolito, "Resonance Cone interaction with a self-consistent radio-frequency sheath", Phys. Rev. Lett. **101** (2008) 195004

[Poddubny2013] – A. Poddubny, I. Iorsh, P. Belov and Yu. Kivshar, "Hyperbolic metamaterials", Nature Photonics **7** (2013) 948

[Robinson1963] – L. C. Robinson and L. E. Sharp, "Microwave Interferometry for Plasma Studies", Australian Journal of Physics **16** (1963) 439

[Sagdeyev1958] – R.S. Sagdeyev and V.D. Shafranov, "Absorption of high-frequency electromagnetic energy in a high-temperature plasma", Proceedings of the second United Nations international conference on the peaceful uses of atomic energy **31** (1958) 118

[Smith2003] – D. R. Smith and D. Schurig, "Electromagnetic Wave Propagation in Media with Indefinite Permittivity and Permeability Tensors", Phys. Rev. Lett. **90** (2003) 077405

[Stix1992] – T.H. Stix, "Waves in plasma", second edition. AIP, 1992

[Sudit1994] – I.D. Sudit, F.F. Chen, "RFcompensated probes for hidh-density discharges", Plasma Sources Sci. Technol. **3** (1994) 162

[Tierens2017] – W. Tierens et al., "3-Dimensional density profiles in edge plasma simulations for ICRF heating", EPJ Web of Conferences **157** (2017) 03053

[Tierens2018] – W. Tierens et al., "Validation of the ICRF antenna coupling code RAPLICASOL against TOPICA and experiments", Nucl. Fusion (2019) **59** 046001

[Wesson2004] – J. Wesson, "Tokamaks", third edition. Oxford University Press, 2004

3 Langmuir probe diagnostic on Aline

The Aline device, described in details in Chapter 1, aims at studies of RF plasmas in a linear configuration with plasma densities similar to the tokamak edge plasma. Measurements of magnetized plasma characteristics are carried out mainly by using an RF-compensated cylindrical Langmuir probe on a 3D-movable highly-precise manipulator. This chapter is devoted to the work on improvements of the data analysis for the Langmuir probe diagnostic on Aline. Developed theoretical approaches are tested in an attempt to handle experimental data. Several steps precede the obtainment of a final fit of an IV curve, including work on estimation of plasma potential and current collecting area. Then electron temperature and density can be calculated.

Comparison of results from cylindrical and planar Langmuir probes makes it possible to calibrate the measurements of the cylindrical probe, since the simpler analysis of planar probe signals grants good confidence in its results. Small size of the cylindrical probes provides a benefit of good spatial resolution of measured plasma parameters, which would not be possible with a big planar probe. In addition to the probes, interferometry is applied on Aline to measure line-averaged densities at different discharge parameters. Spatial scans are performed with the cylindrical Langmuir probe on the line-of-sight of the interferometer and the densities are averaged from the points of the scan. The obtained results are compared for the two diagnostics and an analysis of all measurement errors is done.

The current state of Langmuir probe data analysis in magnetized plasma is reviewed in Section 3.1. In Section 3.2 the plasma magnetization criterion is derived and considered for the Aline conditions. Section 3.3 introduces the dependency of the plasma density on the collected current for non-magnetized plasma and its validity is discussed in the presence of magnetic field. The first, more general, theory is derived in Section 3.4, discussed in details, applied to experimental data and compared to another theoretical study. Formulation of the second, precise, theory and experimental application of it is provided in Section 3.5. Both theories are compared and the applicability limits are discussed in Section 3.6. Sections 3.7 and 3.8 are devoted to the advanced techniques of plasma potential and electron temperature evaluation from the IV characteristic. Conclusions are drawn in the last Section 3.9.

3.1 State of the art of Langmuir probe data analysis in magnetized plasma

Langmuir probes, in principle, provide a simple and relatively inexpensive way of measuring plasma parameters and the analysis of a Langmuir probe IV characteristic is relatively straightforward for cases of non-magnetized plasmas. However, a complete theory of Langmuir probes used in the presence of the magnetic field has never been developed. Plasma collisionality and magnetization level, as well as the probe type and orientation, each affects significantly the approach of data

interpretation. An extensive list of references for various probes in various conditions can be found in [Tichy1997].

Of those works very few try to examine cylindrical probes [Laframboise1976], [Rubinstein1978], [Kudrna1997], [Mihaila2013], [Mihaila2014], [Popov2012], [Popov2016]. Two articles published by co-authors Laframboise and Rubinstein [Laframboise1976], [Rubinstein1978] can be considered as foundational theoretical papers on the subject of a cylindrical Langmuir probe in magnetized plasmas. Here an attempt will be made to compare the newly developed model to theirs.

This work is focused only on the characterization of the electron current collected by a probe at the plasma potential (V_{pl}) (Fig. 2.5) where no sheath is present, as it is the simplest technique for deriving the electron density. It allows avoiding additional errors in particles motion calculation caused by the presence of a sheath around the probe. For simplicity the ion collection at V_{pl} is considered to be negligible.

In magnetized plasma less current is collected by a cylindrical Langmuir probe. It has been first shown in the theoretical papers [Laframboise1976], [Rubinstein1978] and then observed in experiments [Kudrna1997]. A widely used procedure in the presence of a magnetic field is to regard charged particles trajectories as helices around magnetic field lines that intersect only the area of the probe perpendicular to the magnetic field (or its projection on the perpendicular plane). This theory works well when the characteristic size of the probe in the perpendicular plane $d_\perp$ is much bigger than the Larmor radius r_c and than the probe size in the parallel direction $d_\parallel$:

$$d_\perp \gg r_c,\ d_\perp \gg d_\parallel \tag{3.1}$$

Since the ion Larmor radius is typically at least one order of magnitude larger than the electron one, these conditions in weak and medium magnetic fields are fulfilled only for electrons, while the ions rotate on orbits significantly bigger than a probe size. Then the common approach is to treat ions as non-magnetized [Kudrna1997].

This work attempts to fill in the gap in the theory for the conditions when (3.1) is not true, i.e. the probe parallel size is larger or comparable to the perpendicular one and the Larmor radius is not limited, i.e. for any magnetic field. This is the case when a cylindrical Langmuir probe is inserted in plasma parallel to the magnetic field lines, or at a small angle. The perpendicular projection of the probe surface is very small compared to the whole probe surface in this case and is obviously not applicable as a correct collecting surface. A substantial fraction of the current is collected by the probe side surface and it must be taken into account. Otherwise an underestimated collecting area would lead to an overestimated density value.

Two theories have been developed as an outcome of the presented work. Both of them are theories of the “effective” collecting area of a probe biased to V_{pl}. The theories account for particle velocities distributed according to the Maxwell equation and different mechanisms of particles collection depending on their speed. The absence of any additional perpendicular drifts, diffusion or anomalous transport in plasma is assumed. The first developed theory [Usoltceva2018PoP] is more general. Initially constructed for the conditions when (3.1) is not true, it is not limited to those, suggesting a solution for any ratio of the Larmor radii to probe sizes by the means of converging to the conventional non-magnetized theory when particle orbits are significantly bigger than a probe

characteristic size. The theory is presented for electrons but might be useful for ions as well, when their contribution is significant.

The second theory [Usoltceva2018RSI] is more precise, but derived only for a probe oriented parallel to the magnetic field. This model is an advancement of the previous one and it gives an exact formula connecting plasma density and collected current at V_{pl}. Only the case of a parallel probe is considered, since for a probe at an arbitrary angle to B an exact analytical solution would be excessively complex. The precise theory allows revising the applicability limits of the approximate theory.

3.2 Criterion of plasma magnetization

In weakly ionized plasma collisions with neutrals dominate over other sorts of collisions (electron-electron, ion-ion and ion-electron). The cross-section of inelastic electron-neutral collision is negligible for electron temperatures $T_e < 20\ eV$ [Franz2009]. For elastic collisions, measurements results of cross-sections $\sigma_{\mathrm{e-n}}$ are provided in [Franz2009] at different electron energies in Ar and He. For considered Aline conditions (5 eV of T_e, gas He) $\sigma_{\mathrm{e-n}} = 6 * 10^{-20}\,\mathrm{m}^{-2}$. Neutral density, calculated from $n = p/k_B T$ for pressure p = 1 Pa and temperature T = 300 K (k_B is Boltzmann constant equal to 1.38*10^{-23} J/K) , is equal to $n_n = 2.4 * 10^{20}\ m^{-3}$.

The mean free path of electrons is

$$\lambda_e = \frac{1}{n_n \sigma_{e-n}} = 7*10^{-2}\ m \tag{3.2}$$

Particles of species s in plasma can be considered as magnetized when their cyclotron frequencies exceed the collision frequency or, equivalently, their Larmor radii must be smaller than the mean free paths $r_{cs} < \lambda_s$.

$$r_{cs} = \frac{\sqrt{m_s k T_s}}{q_s B} \tag{3.3}$$

The magnetic field in Aline is varied up to 0.104 T. It is beneficial to find a limit of the magnetic field below which electrons are not magnetized. Minimum used field is 0.0024 T. For this value the condition of electron magnetization is fulfilled: $r_{ce} = 0.2 * 10^{-2}\ m < 7 * 10^{-2}\ m = \lambda_e$. Therefore, the data processing for the whole working range of magnetic field values [0.0024; 0.104] T can be addressed with approximation of collisionless magnetized plasma. Pressure diminution below the one considered here would make the mean free path bigger, so the conditions of magnetization would remain valid.

3.3 Current collection at plasma potential

The equation for the electron current at V_{pl} in non-magnetized plasma is well known and it reads:

$$I_e = e\Gamma_e S_{pr} = e\frac{n\bar{v}}{4} S_{pr} = en\left(\frac{kT_e}{2\pi m_e}\right)^{1/2} S_{pr} \tag{3.4}$$

Electron flux to a surface in one direction $\Gamma_e = n\left(\frac{kT_e}{2\pi m_e}\right)^{1/2}$ is given through the mean velocity $\bar{v}$ of a Maxwellian distribution with no limitations neither on the value, nor on the direction of the electrons velocity. The electrons are collected by the whole probe surface S_{pr} .

Is it possible to employ this formula for magnetized plasmas? As was shown by some experiments [Kudrna1997], it is indeed applicable for certain conditions. A convenient parameter for numerical characterization is the dimensionless magnetic field strength β:

$$\beta = \frac{r_{pr}}{r_{ce}} = \frac{r_{pr}eB}{\sqrt{m_e k T_e}} \tag{3.5}$$

So not the magnetic field itself should be considered as important parameter, rather the ratio of the probe radius r_{pr} and the electron Larmor radius. In [Kudrna1997] β was in the range 0.25-2 and the resulting error of the electron density evaluation with (3.4) was estimated as +/-20% for a cylindrical probe perpendicular to the magnetic field.

However, not the β parameter but the perpendicularity of the probe played the crucial role in that work, as the developed theory will demonstrate below. The collecting area of the probe in (3.4) was replaced in [Kudrna1997] by 2 times the cross-section of the probe in the plane perpendicular to the magnetic field. It is easy to see that the difference between this area and the whole surface of the probe is negligible for such probe orientation. That is why the conventional theory was able to provide such good results.

The question that arises next is whether and how the theory should be corrected for a probe at an arbitrary angle to the magnetic field. The idea of how to answer this question was obtained from experimental data.

Experiments were performed with cylindrical probes parallel to the magnetic field. A reference planar probe ($r_{pr} = 0.5\ cm$) was used for comparison. The planar probe dimensions satisfy (3.1) for all values of the magnetic field used in the experiments. The theory for such a probe in a magnetic field is much simpler and conventional methods are applicable for density extraction at V_{pl}. All probes were placed at the same position inside the plasma chamber and IV curves captured at the same values of pressure and magnetic field. With the density from the planar probe it is possible, using the same equation (3.4), to get an idea of how the collecting area of a cylindrical probe looks like: $S_{cyl} = \frac{I_{cyl}}{I_{planar}} S_{planar}$. The result for the smaller cylindrical probe ($r_{pr} = 75\ \mu m$) is shown in Fig. 3.1.

It is obvious that the same idea as in [Kudrna1997] would not work: the perpendicular area (a transverse cross-section of the cylinder) is $S_\perp = \pi r_{pr}^2 = 1.8 * 10^{-8}\ m^2$ in the considered here case, which is few orders of magnitude smaller than the experimental result. It is clearly observed from the experiment that the collecting area of a cylindrical probe at a small angle to the magnetic field is not a constant but a function of the magnetic field strength.

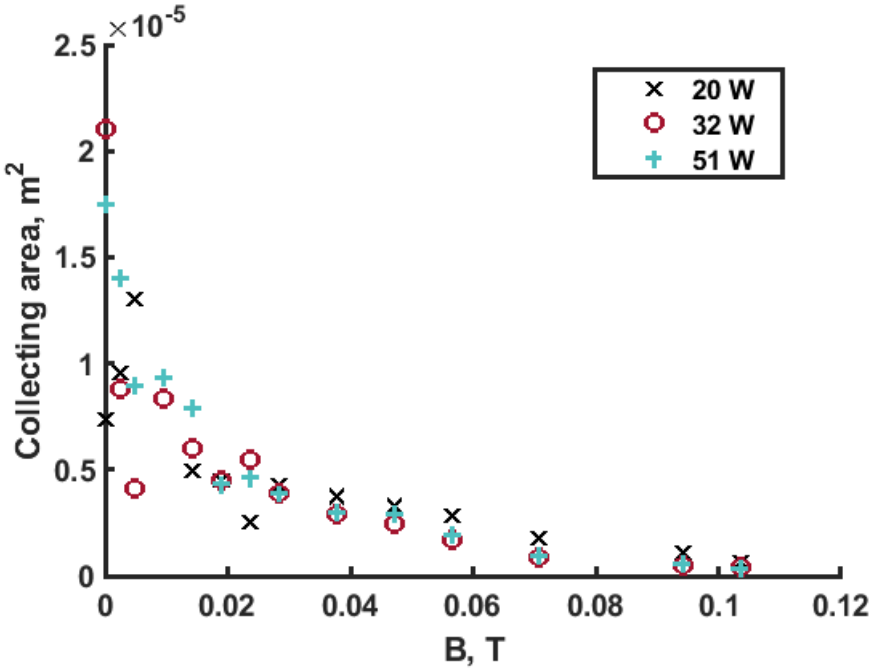

Fig. 3.1. Collecting area of the smaller cylindrical probe estimated using planar probe density measurements for 3 different forwarded RF power levels.

3.4 General theory for a probe at arbitrary angle

3.4.1 Effective collecting area

The proposed theory suggests an alternative "effective" collecting area of a cylindrical probe at an arbitrary angle θ to the magnetic field. In (3.4) the electron current is calculated with the assumption of all particles having the same mean velocity. In reality, electron velocities follow the Maxwellian distribution (which is also a subject of discussion, but outside of the scope of this work). The following step is to recalculate the collected current $I_e = e\Gamma_e S$, accounting for different mechanisms of electrons collection depending on their radial speed. Dependency on longitudinal velocities is neglected.

It is necessary to emphasize again that only the probe potential equal to V_{pl} is considered. A simple formula is sought for density evaluation from this exact point of an IV curve, without diving into complex particle transport theories for the current collection by a biased probe.

Generally speaking, at any given magnetic field the electrons have Larmor radii in some range of values. Assuming that those with $r_{ce} \leq r_{pr}$ are collected by the probe perpendicular cross-section, it follows that:

$$S_{\perp} = 2r_{pr}L_{pr}\, sin(\theta) + \pi r_{pr}^2 cos(\theta) \tag{3.6}$$

The mechanism of collection for the electrons with $r_{ce} > r_{pr}$ is in principle the same as the collection of particles in non-magnetized plasma. They are collected by the whole probe surface:

$$S_{pr} = 2\pi r_{pr}L_{pr} + \pi r_{pr}^2 \tag{3.7}$$

The electron current is then given by a nearly identical to (3.4) formula:

$$I = e\Gamma_e S_{eff}, = en\left(\frac{kT_e}{2\pi m}\right)^{1/2} S_{eff}, \tag{3.8}$$

except that the collecting surface here is the effective S_{eff}. The current is calculated as a sum of two contributions:

$$I = e(\Gamma_{magn} S_{\perp} + \Gamma_{n-magn} S_{pr}) \tag{3.9}$$

Here Γ_{magn} is the flux to a surface, calculated for "magnetized" electrons which have $r_{ce} \leq r_{pr}$ or, equivalently, the velocity in the perpendicular to B direction

$$v_r \leq v_{lim} = \frac{eBr_{pr}}{m} \tag{3.10}$$

The non-magnetized flux Γ_{n-magn}, on the contrary, is calculated with the opposite condition on the electron velocity.

Since in fact only the net current is measured in experiment, not the two contributions of electrons separately. It is better to not speak about different currents, but rather introduce the “effective collecting area” into terminology, defining it as:

$$S_{eff} = I/e\Gamma_e = (S_{\perp}\Gamma_{magn} + S_{pr}\Gamma_{n-magn})/\Gamma_e \tag{3.11}$$

A random particle flux to a surface is generally calculated as

$$\Gamma = n \int \overrightarrow{v_s} f(v) d^3 v \tag{3.12}$$

$\overrightarrow{v_s}$ being a speed normal to the surface.

Without loss of generality, one can calculate a flux of magnetized electrons to a plane perpendicular to B in cylindrical coordinates (z-direction is parallel to B) and with Maxwellian velocity distribution:

$$\Gamma = n\left(\frac{m_e}{2\pi k T_e}\right)^{\frac{3}{2}} \int_0^{+\infty} \int_0^{2\pi} \int_0^{+\infty} v_z v_r exp\left(-\frac{mv^2}{2kT_e}\right) dv_r d\varphi dv_z \tag{3.13}$$

After integration for v_z and φ:

$$\Gamma = n\left(\frac{m_e}{2\pi k T_e}\right)^{\frac{1}{2}} \int_0^{+\infty} v_r exp\left(-\frac{m{v_r}^2}{2kT_e}\right) dv_r \tag{3.14}$$

With limitation (3.10) instead of (0, +∞) in (3.14), the flux of the “magnetized” electrons yields:

$$\Gamma_{magn} = \Gamma_e\left(1 - e^{-\frac{\beta^2}{2}}\right) \tag{3.15}$$

Similarly, with v_r limited from v_{lim} to +∞:

$$\Gamma_{n-magn} = \Gamma_e\, e^{-\frac{\beta^2}{2}} \tag{3.16}$$

Hence, the expression for the effective area is obtained:

$$S_{eff} = S_{\perp}\left(1 - e^{-\frac{\beta^2}{2}}\right) + S_{pr}\, e^{-\frac{\beta^2}{2}} \tag{3.17}$$

For non-magnetized plasma ($\beta=0$) this expression turns into $S_{eff} = S_{pr}$, thus transforming (8) into conventional equation (3.4).

To give an idea of a typical profile of the effective collecting area given by (3.17), two illustrations are provided. In Fig. 3.2 is a plot of an example of the effective area for cylindrical probes of 1 cm length and 4 different radii, all parallel to the magnetic field. The electron temperature is kept constant at $T_e = 3\ eV$. For the smallest radius the value of β is small for the whole range of B, so the effective area declines very slowly. As the probe radius gets bigger, the curve correspondingly bends more. The dependence on the angle is shown on the Fig. 3.3, for the probe radius of $7.5*10^{-5}$ m. It is clear that the perpendicular projection of a cylindrical probe is biggest when the probe is inclined at 90° to the magnetic field. This contribution mostly plays role at larger magnetic fields.

3.4.2 Application to experimental data

An RF-compensated Langmuir probe [Sudit1994], [Chatterton1991] with two exchangeable tungsten cylindrical tips of $r_{pr} = 75\ \mu m$, $L_{pr} = 1\ cm$ and $r_{pr} = 500\ \mu m$, $L_{pr} = 1\ cm$ is installed on a 3D-movable manipulator parallel to the magnetic field direction. Each measurement is averaged over 20 sweeps of voltage from -70 to 70 V, much longer than one RF period. Perfect probe alignment is hardly possible in the experimental setup. To take this into account, it is assumed that the probe tip can deviate up to 5° from the direction parallel to the magnetic field. Measurements presented here were done at one spatial probe position above the RF cathode, x = 0 mm, y = 46 mm and z = -60 mm from the cathode centre (which is 40 mm in radius), far enough to avoid the effects of strong RF potential distortion, but at the same time close enough to the high density plasma region. The probe tip and the antenna are depicted in Fig. 1.5. As a reference for density and temperature measurements a planar probe perpendicular to the magnetic field ($r_{pr} = 0.5\ cm$) was used.

The probe design for the magnetic environment must be addressed with a special care. A gap between the probe tip and the compensation electrode was present for one of the cylinrical probes, bigger in size than the tip radius. The compensation electrod is a metallic cylinder of a bigger radius than the probe tip, and the probe tip is partially inserted in the electrode (Fig. 1.5). Since the mean electron Larmor radius is then comparable to the probe tip size, a large fraction of electrons could penetrate inside the gap and be collected by metallic parts there, thus the collecting area increased and saturated to a constant value, presumably the gap area. In the experiments with non-magnetized plasma this effect was never observed, but in the presence of a magnetic field it is important to not allow such gaps. The problem was solved by adding a ceramic piece to cover the hole (Fig. 3.4, compare to Fig. 1.5), then the difference in the current collection became noticeable and the collecting area was not anymore saturating at constant level (Fig. 3.5).

Now the developed theory can be checked in practice. The effective collecting area for two cylindrical probes at 5° angle to the direction of B is calculated using experimentally obtained data (realistic temperatures, varying for different points) and compared to the collecting area estimated from planar probe density measurements as was described above and displayed in Fig. 3.1.

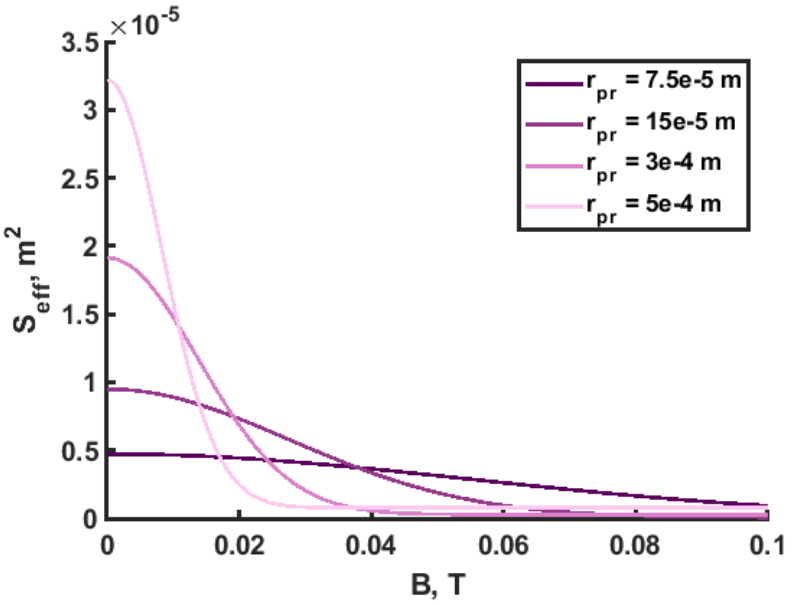

Fig. 3.2. Example of the effective collecting area for different probe radii at θ = 0.

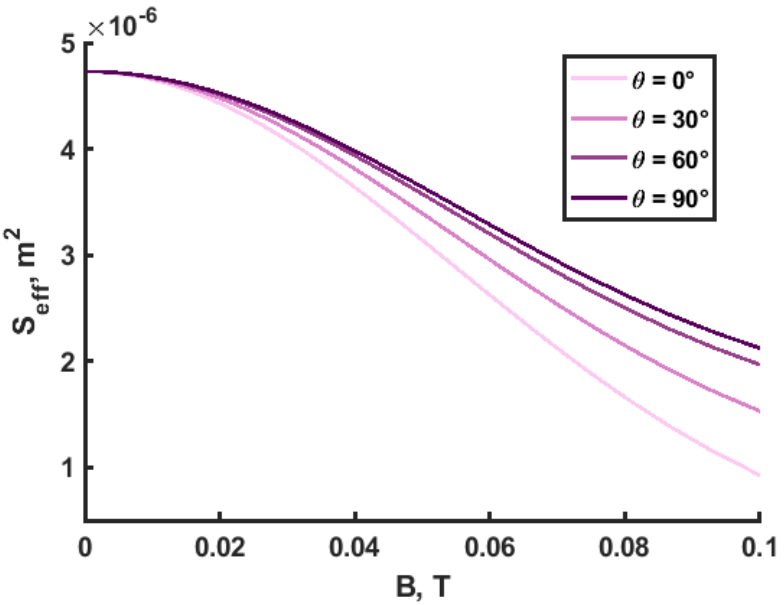

Fig. 3.3. Example of the effective collecting area for different probe inclination angle with r_{pr} = 75 μm.

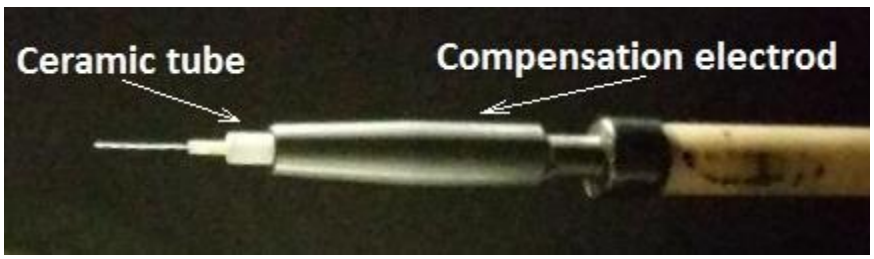

Fig. 3.4. The Langmuir probe in Aline with additional ceramic piece to cover a hole.

The agreement of the curves is remarkably good for bigger magnetic fields (Fig. 3.6 and 3.7). For the small fields the correct values are those of the effective area, not the planar probe reference values, simply because the upper possible limit for the collecting area is the whole probe area ($4.7*10^{-6}$ m^2

for the smaller probe and $3.2*10^{-5}$ m^2 for the bigger probe). The reason for the discrepancies with the collecting area from the planar probe at smaller B is the inaccurate estimation of the density for the planar probe in this region. Big uncertainty exists in the plasma potential evaluation from the IV curves at small magnetic fields, due to the absence of a clear transition from the exponential to the electron saturation part, which leads to erroneous values of the current at V_{pl} and calculated density (since density is linearly proportional to the current).

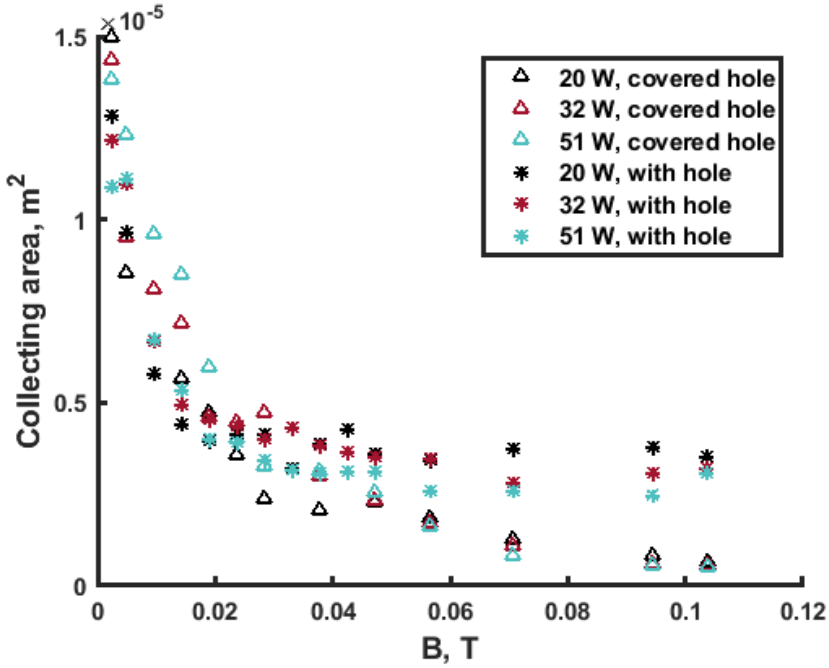

Fig. 3.5. Example of the collecting area for r_{pr} = 75 μm when a hole is present and when it is covered.

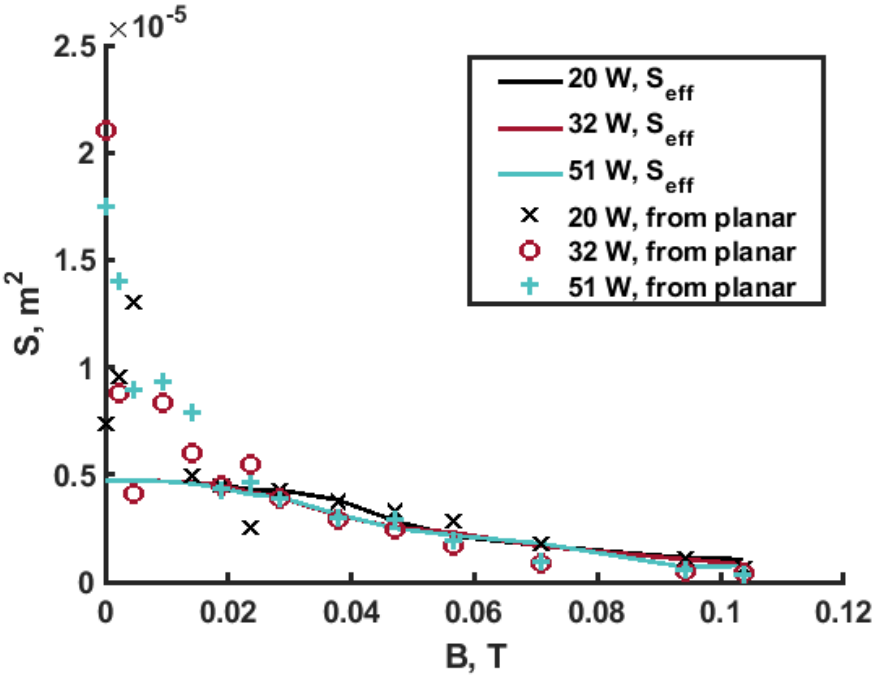

Fig. 3.6. Comparison of S_{eff} to the collecting area estimated using the planar probe for the smaller cylindrical probe.

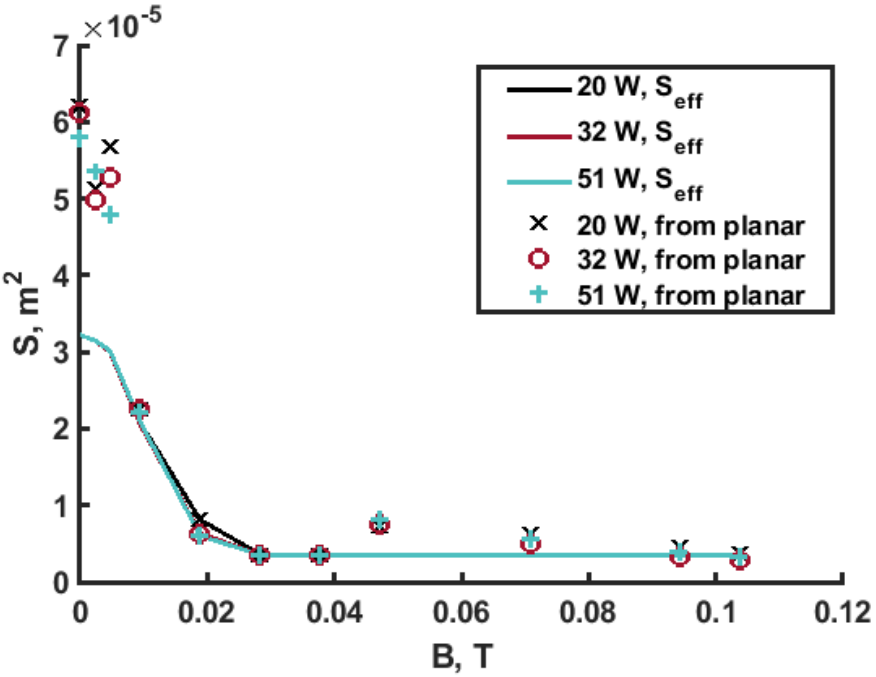

Fig. 3.7. Comparison of S_{eff} to the collecting area estimated using the planar probe for the bigger cylindrical probe.

Densities calculated using data from the planar probe and the cylindrical probes are compared in Fig. 3.8. The agreement of the results for all probes is satisfactory, considering typical probe measurements errors. The maximum difference in the obtained results reaches ± 100% for several points, in respect to the planar probe signal. Probe measurements usually aim on giving a correct order of magnitude, with further precision being a rare and great advantage.

It has to be stressed here that the density profiles provided in this paper should not be regarded as an attempt to give a dependency on the magnetic field. The coupled power was not constant at different B because of the difference in the matching quality. The RF antenna was directly connected to an RF amplifier (direct coupling) and measurements of the forwarded and reflected power were done. The difference between those, i.e. the coupled power, was varying nonlinearly between 5 and 35 W. Solely for the simplicity of representation the data in all plots is grouped into 3 curves for 3 values of the forwarded power (20, 32, and 51 W). The presence of a probe did not affect the matching significantly, so it is assumed that the measurements were done in identical conditions with all the probes, cylindrical and planar ones.

3.4.3 Comparison to Laframboise-Rubinstein theory

Theoretical papers of Laframboise and Rubinstein [Laframboise1976], [Rubinstein1978] focus on cylindrical probes in magnetized plasma. Their work covers all crucial parameters: the magnetic field strength and the probe size and orientation, providing an upper bound and an adiabatic limit (the mean gyroradius is much smaller than the characteristic scale of changes in the probe sheath electric field) for the current collected by the probe at different biasing potentials. The authors claim that at V_{pl} the upper bound and the adiabatic limit formulas coincide and give exact values of the current.

In [Laframboise1976] the current at V_{pl} can be numerically calculated from the general integral for each possible θ and β. A plot is presented in Fig. 3 in [Laframboise1976] for the normalized current at V_{pl}.

A similar plot can be constructed using S_{eff} as defined by (3.17) (Fig. 3.9). The current at V_{pl} (3.8) is normalized to the current for $\beta = 0$: $I_0 = en\left(\frac{kT}{2\pi m}\right)^{1/2} S_{pr}$, so that $i = \frac{I}{I_0} = \frac{S_{eff}}{S_{pr}}$. In [Laframboise1976] the probe length is assumed infinite. The probe dimensions used for Fig. 3.9 are $L_{pr} = 1\ cm$ and $r_{pr} = 75\ \mu m$, so that $\frac{L_{pr}}{r_{pr}} \gg 1$ and it can be also assumed infinite.

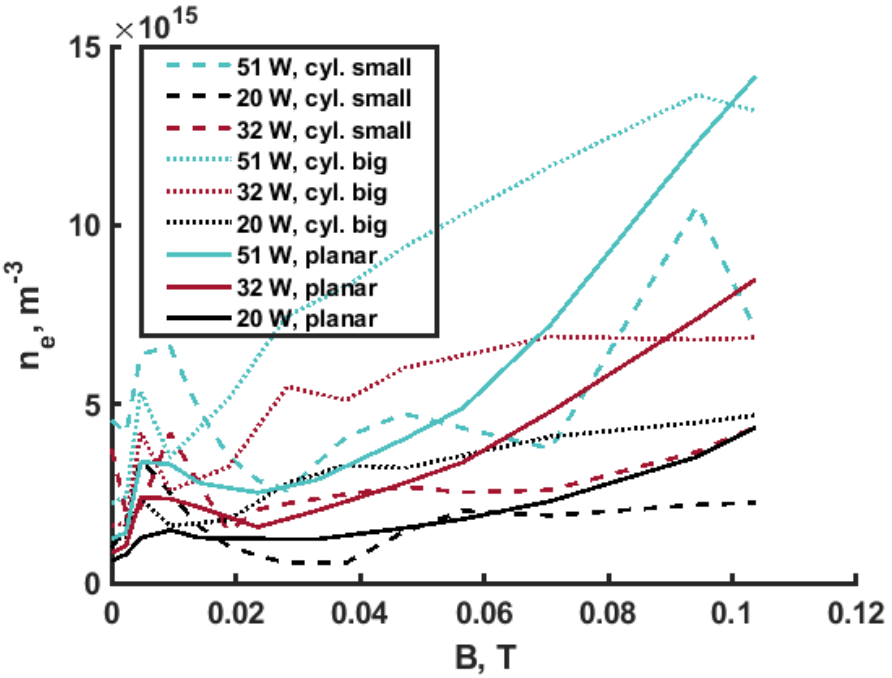

Fig. 3.8. Comparison of densities calculated for two cylindrical probes at 5° and the planar probe.

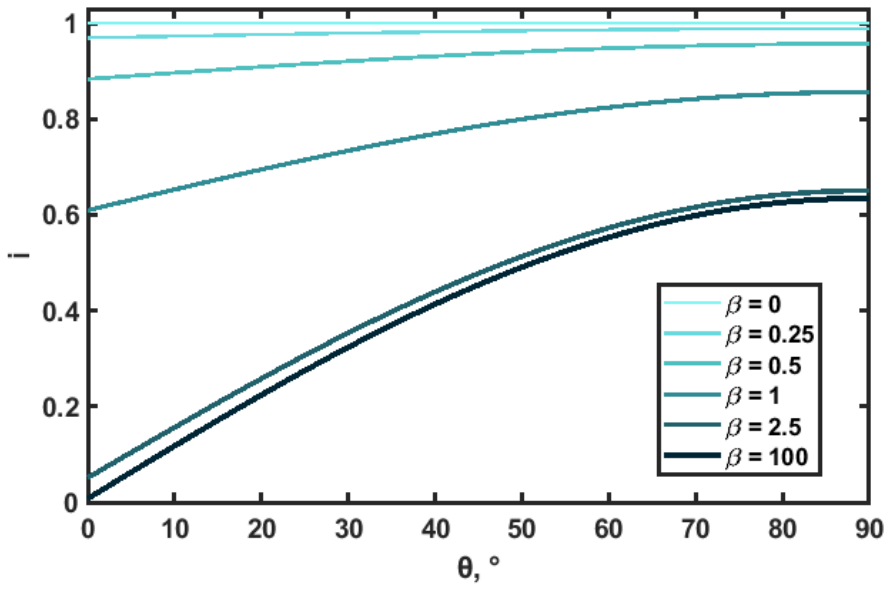

Fig. 3.9. Normalized current i as a function of the probe inclination angle for various dimensionless magnetic fields.

The currents agree well for big inclination angles and big dimensionless magnetic field. The cause of the discrepancies at small θ is that the current in [Laframboise1976] is calculated only for the electron collection on the longitudinal side of the probe. The end-effect current (collected on the transverse probe end) is given separately in [Laframboise1976] by following expression (here $\sigma = \beta * \pi^{1/2}/2$) :

$$\frac{I}{I_0^*} = \frac{1}{2}\left(1 + \frac{1-\exp(-\sigma^2)}{\sigma^2} + \frac{\pi^{1/2}\left(1+erfc(\sigma)\right)}{\sigma}\right) \tag{3.18}$$

It is not trivial to combine this expression for the end-effect current to the previous part. For the end-effect current, I_0^* is the current received by the perpendicular area of the probe (much smaller than the parallel area), and for a semi-infinite probe in the Laframboise-Rubinstein model it leads to a current rise in (3.18) up to infinity for $\beta \to 0$.

The present theory, on contrary, does not have any discontinuities in solutions and smoothly converges in the extrema to two possible solutions: non-magnetized case $i(\theta) = 1$ for $\beta \to 0$ (for any angle) and to $i = \frac{S_\perp}{S_{pr}}$ for $\beta \to \infty$ and relatively small θ. For $\beta \to \infty$ and not very small θ the parts proportional to r_{pr}^2 in (3.6) and (3.7) are insignificant, so $i \to \frac{2\,sin\theta}{\pi}$. The interesting fact is that the same dependence formula $i = \frac{2\,sin\theta}{\pi}$ is mentioned in [Rubinstein1978], which they derived using a different approach.

3.4.4 Peculiarities of the theory application

Two important aspects must be mentioned here. One concerns the fact that the probe perpendicular surface can be taken either once or twice in calculations. The other remark is about the assumption of an infinite probe and about probes with various finite dimensions.

In the processing of the experimental data the probe perpendicular area $S_\perp$ was taken as in (3.6). Behind the probe there is a holder with ceramic insulator, so the electrons can only be collected from one side. It is also taken into account in (3.7) for the whole probe area.

On the contrary, Fig. 3.9 was made for a probe that can collect particles from both directions along the magnetic field lines (but with the same area S_{pr}). It is closer to the conditions in which the theory in [Laframboise1976] was constructed. That's why a surface double as (3.6) was taken. To give an idea of how the current collection would change, the same currents are plotted as in Fig. 3.9, but a single perpendicular area is taken instead of a double (Fig. 3.10). The difference is especially significant for big β and θ, so the correct perpendicular area must be accurately chosen for each specific case.

The second valuable aspect is the case of a finite probe. An example of how the current collection would change for varying probe dimensions is in Fig. 3.11.

As would be empirically expected, the line for a probe with the length equal to the diameter $L_{pr} = 2r_{pr}$ is nearly symmetric. Such a probe would be close to a cube, so the perpendicular and planar orientaions are nearly equal in terms of the collected current. As the ratio $\frac{L_{pr}}{2r_{pr}}$ grows, the collected current approaches the extremum of the infinite probe. The last value is given for the

dimensions of the smaller cylindrical probe, the same as it was used for Fig. 3.9. All lines are for the same $\beta = 2$.

An important conclusion that can be drown here is that the theory presented here is not limited to the cylindrical shape of the probes. It can be applied to any shape, as long as the whole surface and its perpendicular projection are known.

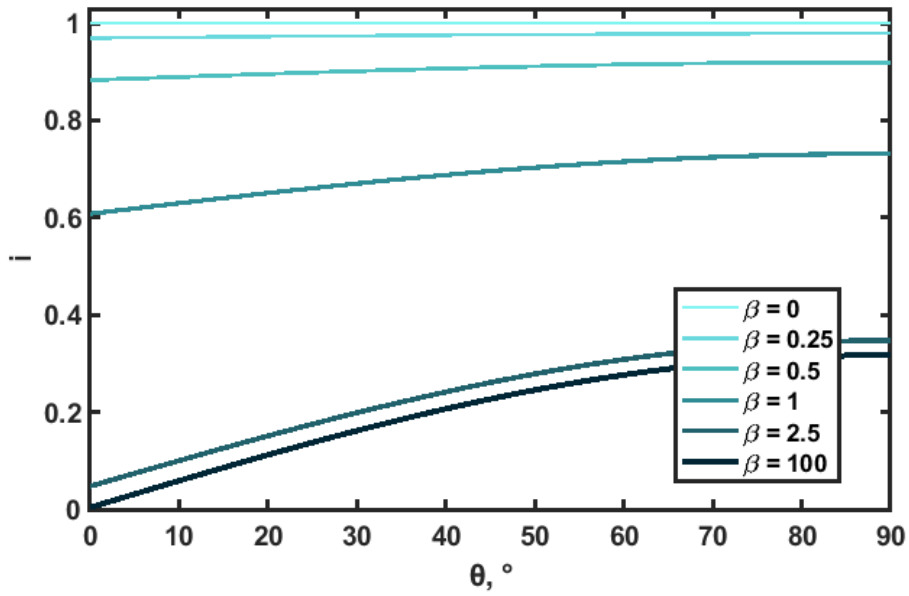

Fig. 3.10. i(θ) for various β. The perpendicular current collection is only from one direction.

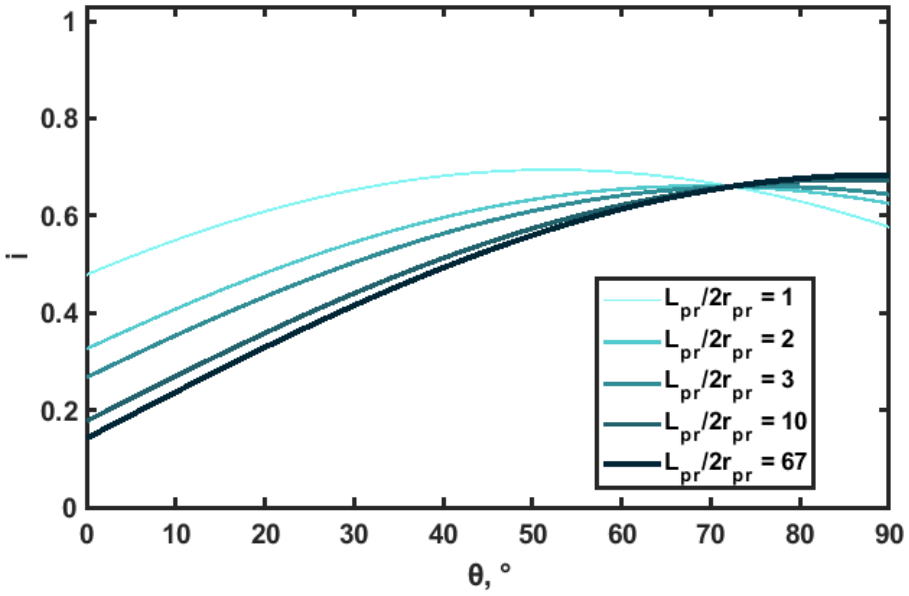

Fig. 3.11. i(θ) for various $\frac{L_{pr}}{2r_{pr}}$ (at $\beta = 2$).

3.5 Precise theory for a probe parallel to B

3.5.1 Effective collecting area

The basic idea behind the model presented here is the same as in the previous theory: separation of different contributions to the collected current by dividing the electrons into groups according to their velocity. The current for each contribution is calculated as a product of charge e, flux Γ and collecting area S:

$$I_e = e\Gamma S \tag{3.19}$$

In contrast to the previous theory, not only the flux is considered to be dependent on the particle speed but the collecting area as well. It leads to the fact that this theory doesn't use the same simplifying assumptions, so it can be considered precise, opposite to the general theory presented in the Section 3.4. Some assumptions, like Maxwellian velocity distribution, are still present and they cause differences between the theoretical descriptions and experimental reality.

The cylindrical coordinate system is adopted and the particle flux through a plane perpendicular to the probe axis (z axis) is examined. The collecting area S in (3.19) is an area in this plane which a guiding center of a rotating particle should cross for a particle to be collected. Due to the rotational symmetry no dependency on the azimuth φ is present. All electrons can be divided into 4 fractions:

1) $v_r \leq v_{\lim r}, v_z \leq v_{\lim z}$
2) $v_r \geq v_{\lim r}, v_z \leq v_{\lim z}$
3) $v_r \leq v_{\lim r}, v_z \geq v_{\lim z}$
4) $v_r \geq v_{\lim r}, v_z \geq v_{\lim z}$

where $v_{\lim r} = \frac{eBr_{pr}}{m}$ is the speed of an electron with a Larmor radius equal to the probe radius $r_c = r_{pr}$ and $v_{\lim z} = \frac{eBL_{pr}}{2\pi m}$ is the speed of an electron that completes one full rotation $\Delta\varphi = 2\pi$ during the same time as it travels the probe length L_{pr} in z direction ($\frac{2\pi}{\omega_c} = \frac{L_{pr}}{v_{\lim z}}$, where $\omega_c = eB/m$ is the electron cyclotron frequency). For experimental applications it would be correct to impose an upper limit for the radial speed as the value when the Larmor radius is equal to the vacuum chamber radius. This is a minor correction and it is omitted for the current theoretical formulation.

For each fraction of particles the current is calculated using the same formula, but with its own limits and its own collecting area (with Maxwellian velocity distribution):

$$I = en\left(\frac{m_e}{2\pi kT_e}\right)^{\frac{3}{2}} \int_{v_{z_1}}^{v_{z_2}} \int_0^{2\pi} \int_{v_{r_1}}^{v_{r_2}} S(v_r, v_z) v_z v_r exp\left(-\frac{mv^2}{2kT_e}\right) dv_r d\varphi dv_z \tag{3.20}$$

The assumptions and results for each of them are the following.

1) These particles are "slow" in z direction; they complete a full 2π rotation before reaching the end of the probe. If the perpendicular projection of a particle trajectory intersects the probe projection in at least one point (Fig. 3.12a,b), a particle is for sure collected.

With h being the distance between the probe center and the guiding center of a particle trajectory, the collecting area is found as:

$$S_1 = 2\pi \int_0^{r_{pr}+r_c} hdh = \pi(r_{pr} + r_c)^2 \tag{3.21}$$

Then the integration of (3.20) gives:

$$I_1 = e\Gamma_e \left(1 - e^{-\frac{v_{\lim z}^2}{a}}\right)\left[1 - 4e^{-\frac{\beta^2}{2}} + \frac{2}{\beta^2}\left(1 - e^{-\frac{\beta^2}{2}}\right) + \frac{\sqrt{2\pi}}{\beta}\,\mathrm{erf}\left(\frac{\beta}{\sqrt{2}}\right)\right]\pi r_{pr}^2 \tag{3.22}$$

where $\beta = \frac{r_{pr}}{r_{ce}} = \frac{r_{pr}eB}{\sqrt{m_e kT_e}}$ is non-dimensional magnetic field strength [Laframboise1976] and $\Gamma_e = n\left(\frac{kT_e}{2\pi m_e}\right)^{1/2}$ is the random thermal flux.

2) The same assumption is valid for the second fraction of electrons, except that the integration for h is done in different limits (see Fig. 3.12c,d):

$$S_2 = 2\pi \int_{r_c - r_{pr}}^{r_c + r_{pr}} hdh = 4\pi r_{pr} r_c \tag{3.23}$$

$$I_2 = e\Gamma_e \left(1 - e^{-\frac{v_{\lim z}^2}{a}}\right)\left[4e^{-\frac{\beta^2}{2}} + 2\frac{\sqrt{2\pi}}{\beta}\,\mathrm{erfc}\left(\frac{\beta}{\sqrt{2}}\right)\right]\pi r_{pr}^2 \tag{3.24}$$

3) A particle that is “fast” in z direction might never touch the probe, because it does not complete a full turn on $\mathrm{L_{pr}}$. This case should be approached probabilistically.

There are two sectors of the trajectory projection that correspond to the electron successful collection (Fig. 3.13). If a particle is in the sector 2α that belongs to the intersection part, it hits the probe perpendicular surface. From the law of cosines, $\alpha = \arccos\left(\frac{r_c^2 + h^2 - r_{pr}^2}{2r_c h}\right)$. The corresponding probability is $P_\perp = \frac{2\alpha}{2\pi}$. If a particle is in the sector $\gamma = \omega_c \frac{L_{pr}}{v_z}$, on the length L_{pr} in z direction it completes a part of a full turn that is enough to reach the probe. So, a particle hits the parallel probe surface with $P_\parallel = \frac{\gamma}{2\pi}$. Instead of S the product of S and the full probability $P = P_\perp + P_\parallel$ should be used:

$$SP = 2\pi \int_{h_1}^{h_2} \frac{2\alpha + \gamma}{2\pi} hdh = SP_\perp + 2\pi\gamma \int_{h_1}^{h_2} hdh \tag{3.25}$$

$$SP_\perp = h^2\, arccos\left(\frac{r_c^2 + h^2 - r_{pr}^2}{2r_c h}\right)\Bigg]_{h_1}^{h_2} - \frac{1}{2}\sqrt{2h^2\left(r_c^2 + r_{pr}^2\right) - h^4 - \left(r_c^2 - r_{pr}^2\right)^2}\Bigg]_{h_1}^{h_2} -$$

$$- r_{pr}^2\, arctan\left(\frac{r_c^2 - h^2 + r_{pr}^2}{\sqrt{2h^2\left(r_c^2 + r_{pr}^2\right) - h^4 - \left(r_c^2 - r_{pr}^2\right)^2}}\right)\Bigg]_{h_1}^{h_2} \tag{3.26}$$

With the limits $h_1 = 0$ and $h_2 = r_{pr} + r_c$ the result is:

$$SP_3 = \pi r_{pr}^2 + \frac{\omega_c L_{pr}}{2\pi v_z}\,\pi(r_{pr} + r_c)^2 \tag{3.27}$$

$$I_3 = e\Gamma_e e^{-\frac{v_{\lim z}^2}{a}}\left(1 - e^{-\frac{\beta^2}{2}}\right)\pi r_{pr}^2 +$$

$$+ e\Gamma_e\left[1 - 4e^{-\frac{\beta^2}{2}} + \frac{2}{\beta^2}\left(1 - e^{-\frac{\beta^2}{2}}\right) + \frac{\sqrt{2\pi}}{\beta}\operatorname{erf}\left(\frac{\beta}{\sqrt{2}}\right)\right]\sqrt{\frac{\pi}{2}}\frac{\beta}{2}\operatorname{erfc}\left(\frac{v_{\lim z}}{\sqrt{a}}\right) r_{pr}L_{pr} \quad (3.28)$$

4) Likewise the previous calculation, but with other limits for h, for the 4th fraction it yields:

$$SP_4 = 2\pi\int_{r_c - r_{pr}}^{r_c + r_{pr}} \frac{2\alpha+\gamma}{2\pi} h dh = \pi r_{pr}^2 + \frac{\omega_c L_{pr}}{2\pi v_z} 4\pi r_{pr} r_c \quad (3.29)$$

$$I_4 = e\Gamma_e\left(e^{-\frac{v_{\lim z}^2}{a}} e^{-\frac{\beta^2}{2}}\pi r_{pr}^2 + 2\left[\sqrt{\frac{\pi}{2}}2\beta e^{-\frac{\beta^2}{2}} + \pi\operatorname{erfc}\left(\frac{\beta}{\sqrt{2}}\right)\right]\operatorname{erfc}\left(\frac{v_{\lim z}}{\sqrt{a}}\right) r_{pr}L_{pr}\right) \quad (3.30)$$

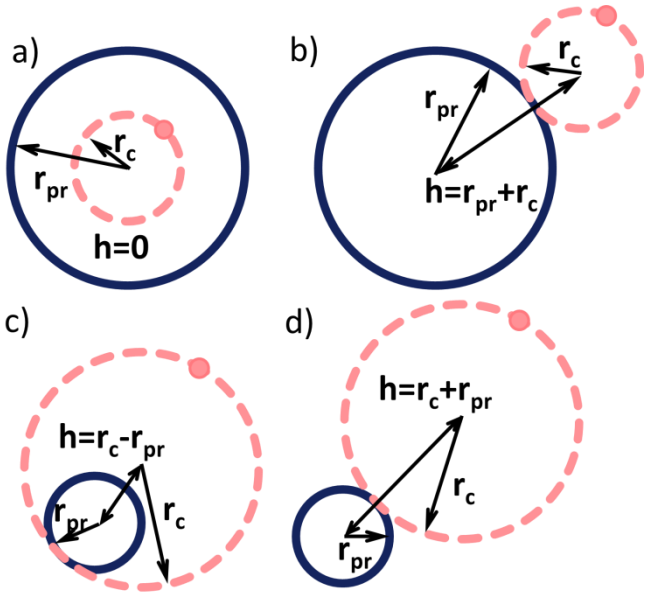

Fig. 3.12. Limiting cases for a particle to be collected, a)&b) for $r_c < r_{pr}$, c)&d) for $r_c > r_{pr}$. A dark circle represents the probe projection, a bright dashed circle – electron trajectory projection.

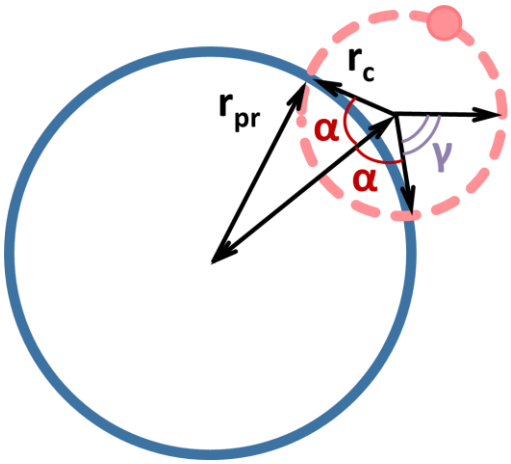

Fig. 3.13. Example of an intersection illustrating sectors 2α and γ.

The second term in I_4 has an additional factor of 2, to account for the particle collection from the opposite direction of z. It is not done for the first term, as well as for all other current contributions,

because the flow of the electrons is limited at the back of the probe tip by the probe body and the manipulator. Only particles with big r_c and big v_z are able to come from the back side.

The effective collecting area is the full collected current divided by $e\Gamma_e$:

$$S_{eff} = \frac{I_1+I_2+I_3+I_4}{e\Gamma_e} = \left(e^{-\frac{v_{\lim z}^2}{a}} + \left[1 - e^{-\frac{v_{\lim z}^2}{a}}\right] * \left[1 + \frac{2}{\beta^2}\left(1 - e^{-\frac{\beta^2}{2}}\right) + \frac{\sqrt{2\pi}}{\beta}\left(1 + \operatorname{erfc}\left(\frac{\beta}{\sqrt{2}}\right)\right)\right]\right)\pi r_{pr}^2 + \left[1 + \operatorname{erfc}\left(\frac{\beta}{\sqrt{2}}\right) + \frac{1}{\sqrt{2\pi}\beta}\left(\frac{\beta^2}{2} + 2\beta^2 e^{-\frac{\beta^2}{2}} + 1 - e^{-\frac{\beta^2}{2}}\right)\right] * \operatorname{erfc}\left(\frac{v_{\lim z}}{\sqrt{a}}\right)\pi r_{pr} L_{pr} \quad (3.31)$$

The expression is rather complicated but it is important to see here that for $\beta \to \infty$ it converges to $S_\perp = \pi r_{pr}^2$ and for $\beta \to 0$ to $S_{pr} = 2\,\pi\, r_{pr} L_{pr} + \pi\, r_{pr}^2$.

3.5.2 Application to experimental data and comparison with interferometry measurements

Theory validation has been performed using data from Aline. The experimental conditions were the same as in Section 3.4.2: 25 MHz capacitive RF discharge, magnetic fields of 0.0024–0.1 T, helium, 1 Pa. A scan of a probe position was performed in the direction perpendicular to B (x from -33 mm to +33 mm) at a constant height y = 36 mm above the antenna and at z = 0 mm along B, i.e. directly above the antenna center. In this region densities are expected to be higher than at the position of measurements in Section 3.4.2. Only one cylindrical probe tip of $r_{pr} = 75\ \mu m$, $L_{pr} = 1\ cm$ was used and it was accurately aligned with B. The smallest probe was chosen, since it provides the best spatial precision. Additionally, it is expected to have the largest variation of the effective collecting area over the range of the parameters scan (magnetic field and power), so it is the most suitable for the theory validation.

IV curves analysis, namely plasma potential and electron temperature calculation, has been done using accurate techniques described further in this Chapter. Densities obtained from the Langmuir probe are averaged along x and compared to line-integrated density measured by a 26.5 GHz microwave interferometer MWI 2650 from Miwitron (see Section 2.4.3 for the description), which was chosen because it suits the expected density range (Fig. 3.14). Interferometer, used only as a supportive diagnostic for probe calibration, was installed specifically for these tests on a temporary mounting and mechanical shaking caused not high accuracy. The lowest possible interferometry signal to measure was ~1e16 m^{-3} in the experiments. Above this level errors reached ± 1e16 m^{-3}.

Possible sources of errors in the Langmuir probe results are:

I. RF oscillation of the potential, leading to a shift in IV characteristics. They are eliminated by the compensation circuit of the probe.

II. Inaccurate V_{pl} evaluation, leading to wrong current values. Using intersection method of V_{pl} calculation (see section 3.7.2) it is made sure that this issue is only present for very low B, less than 0.005 T in the present experiments.

III. Uncertainties in temperature estimation affecting n directly as $1/\sqrt{T}$, as well as through the effective area. This should not give significant deviations when T is determined self-consistently with n (see Section 3.8).

An additional uncertainty in the interferometer density values comes from the fact that the line-integrated signal is divided by a plasma length which is not exactly defined. For all points it was divided by 20 cm, which is fairly realistic for low plasma magnetization and overestimated (no more than by a factor of 2) for the higher B. The profile shape variation can be seen even on a small profile part that is accessible for the probe, nearly flat for 0 T and with a defined peak for greater field values (Fig. 3.15).

The coupled power dependence on B was measured for different forwarded power (Fig. 3.16). The coupling is generally not affected by the probe presence.

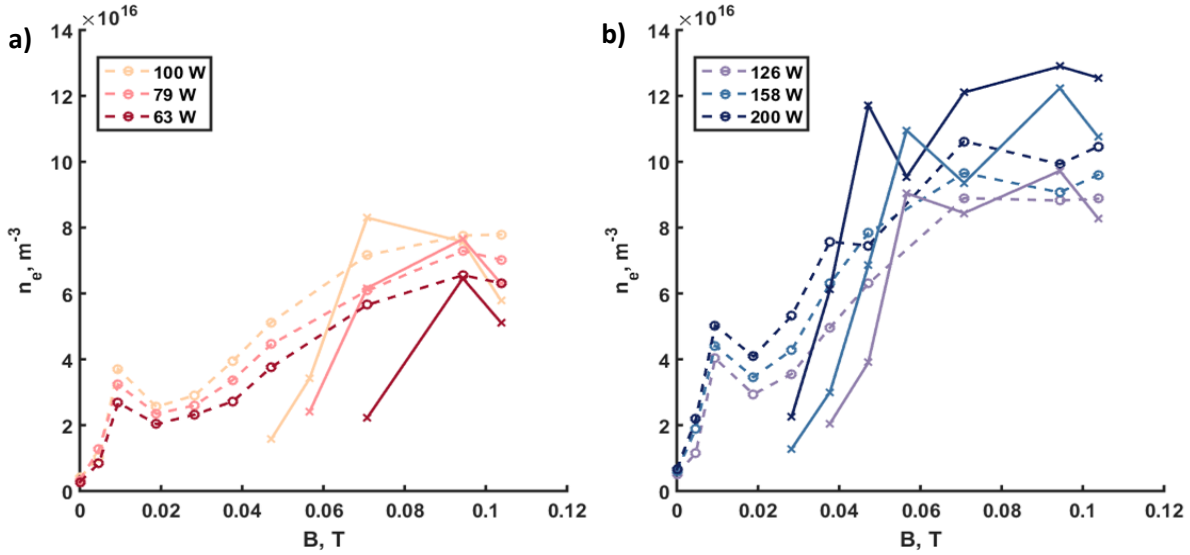

Fig. 3.14. Densities measured with Langmuir probe (dashed lines with circle markers) compared to interferometry (solid lines with cross markers) for different power levels: a) lower power, b) higher power.

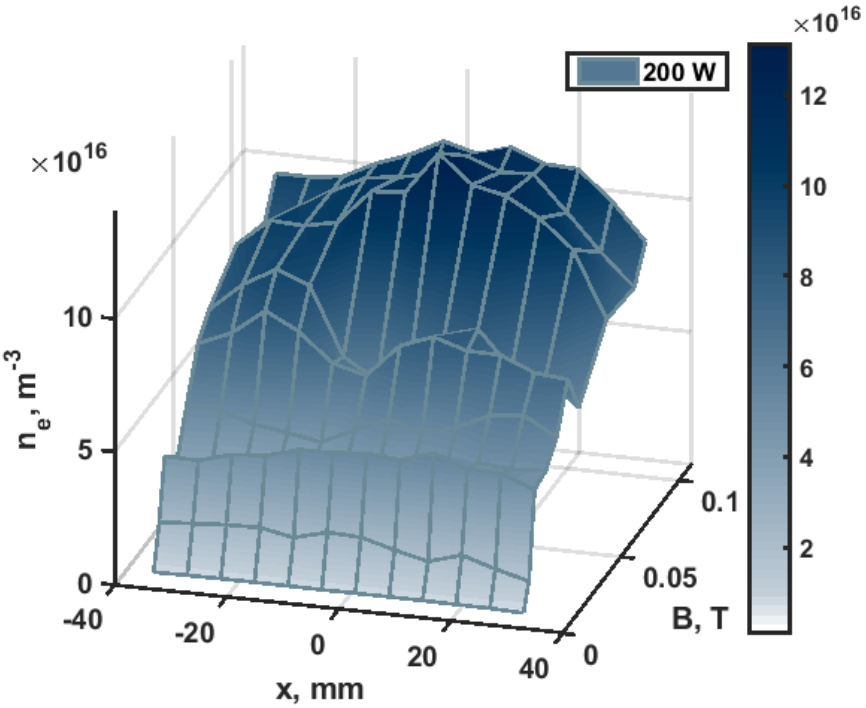

Fig. 3.15. Spatial density profiles for various B.

Now a 2D density profile can be constructed as a function of the coupled power and the magnetic field with both probe and interferometry measurements (Fig. 3.17). The discrepancies of the results are mostly within 20%, reaching 50% for few points of low interferometry signal. Considering all the sources of errors explained above, it means that a good validation is obtained for the density calculation method employing the effective collecting area (3.31).

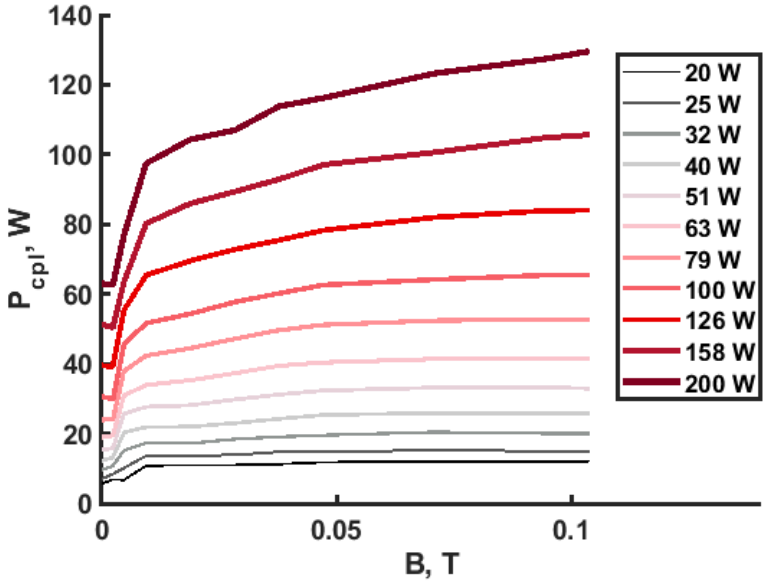

Fig. 3.16. Variation of the coupled power for various forwarded power.

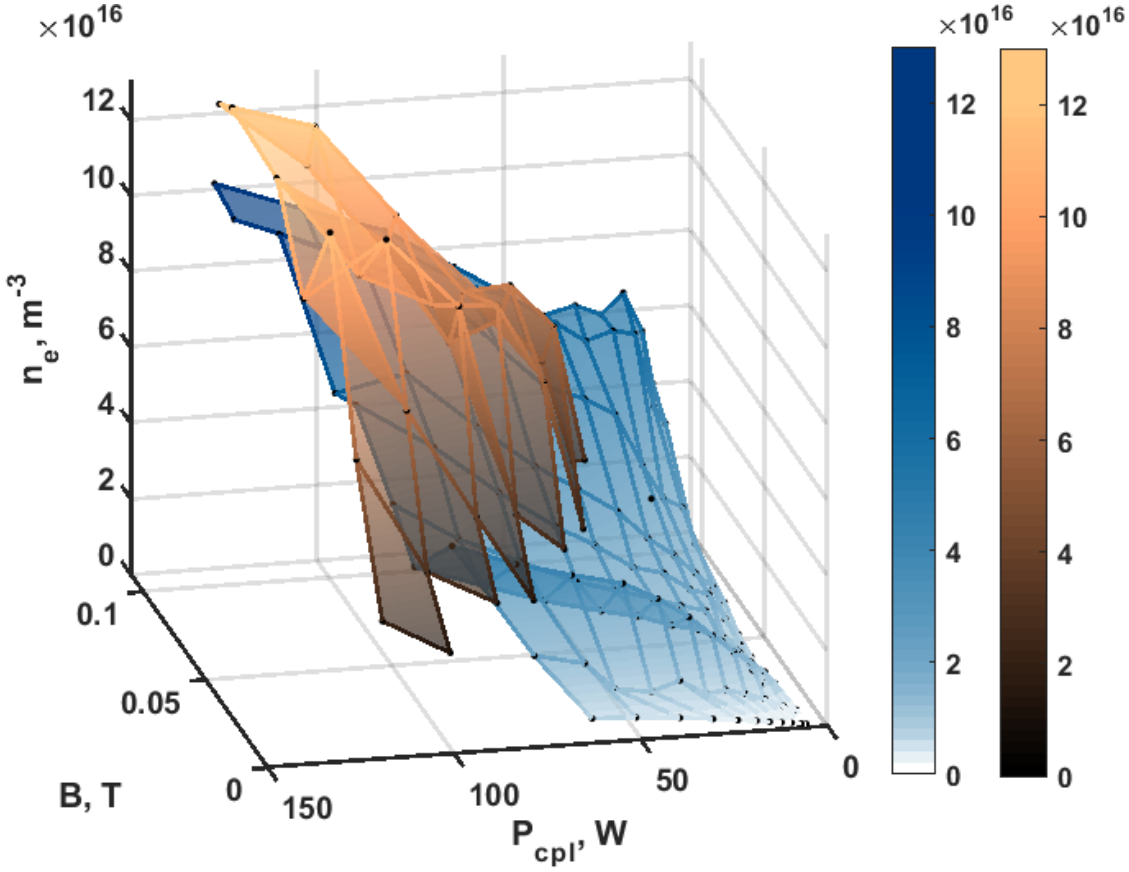

Fig. 3.17. Density profiles obtained from the interferometry (black to orange color scale) and the Langmuir probe data (white to blue).

3.6 Applicability analysis

An exact formula is undoubtedly preferable to an approximate theory. The equation (3.31), while being very complex, should be used instead of the inexact effective area formula (3.17) when a probe parallel to B is considered. However, exact analytical calculations for an arbitrary angle of inclination θ are not possible. Instead an analysis of the applicability of the approximate theory is conducted.

The simplicity of the resulting formula (3.17) is achieved by neglecting the fact that the collecting areas depend on a particle speed. Moreover, no distinction for different speeds in z direction is drawn. Consequently, the effective area is not an exact expression but an approximation. Limits to its application can be set by revising separately the two terms of equation (3.11).

1) The "non-magnetized" flux $\Gamma_{\mathrm{n-magn}}$ defined by the condition of the radial speed to be bigger than $\mathrm{v_{lim\,r}}$ is said to be collected by the whole probe area $\mathrm{S_{pr}}$, which is an overestimation. In reality, an electron with $\mathrm{v_z} \le \mathrm{v_{lim\,z}}\cos(\theta)$ strikes a probe no later than one revolution of the cyclotron orbit: $\mathrm{L_z} = \mathrm{v_z} * 2\pi/\omega_c$, so all such particles are collected by a smaller area $2\pi \mathrm{r_{pr}} \mathrm{L_z} + \pi\, \mathrm{r_{pr}^2}$. Only particles with $\mathrm{v_z}$ bigger than $\mathrm{v_{lim\,z}}$ are collected randomly along the whole probe length. For the equation (3.17) to be applicable they should constitute the majority of the velocity distribution. It is roughly true when the mean thermal velocity $\bar{\mathrm{v}}$ is bigger than $\mathrm{v_{lim\,z}}\cos(\theta)$.

The described overestimation seems to be significant for bigger magnetic fields and smaller θ, when most of the electrons have v_z smaller than the limit. However, for bigger magnetic fields the limitation $v_r \ge v_{\mathrm{lim}\,r}$ leads to a small number of particles in Γ_{n-magn}, since $v_{\mathrm{lim}\,r}$ is also quite big (depending on the temperature). Quantitatively the conditions for the first remark to be insignificant can be expressed as:

$$\begin{cases} \bar{v} > v_{\mathrm{lim}\,z} cos(\theta) \text{ for any } r_{pr} \\ \bar{v} < v_{\mathrm{lim}\,z} cos(\theta) \text{ and } \bar{v} < v_{\mathrm{lim}\,r} \end{cases} \tag{3.32}$$

2) The second limitation concerns the "magnetized" flux. If a center of the cyclotron rotation of an electron with $\mathrm{v_r} \le \mathrm{v_{lim\,r}}$ lies outside the perpendicular probe projection but at a distance no longer than r_{ce} from it, the electron trajectory intersects the probe and such a particle is collected. However, it may be collected not only by the perpendicular surface as was assumed previously, but also by a part of the parallel surface proportional to its speed $\mathrm{v_z}$. The "magnetized" flux is large only in strong magnetic fields. At the same time most of the electrons have speeds $\mathrm{v_z} < \mathrm{v_{lim\,z}}\cos(\theta)$, so the additional area $2\pi \mathrm{r_{pr}} \mathrm{L_z}$ is quite small. The second correction is always very small and negligible compared to the effect of the first correction.

Finally, the criteria of the applicability of the approximate theory are those described by (3.32). When they are not satisfied, the effective area is overestimated up to the factor of $S_{pr}/S_{\perp}$. A more precise overestimation value can hardly be provided.

The application to the experimental data carried out in Section 3.4.2 for two cylindrical probe tips can be reviewed. For the smaller tip of $r_{pr} = 75\ \mu m$, $L_{pr} = 1\ cm$, the equation (3.32) gives that S_{eff} is acceptable only for $B < 0.0076$ T and $B > 0.114$ T at $\theta = 5°$, which means that for nearly the whole range of B the resulting densities are underestimated. The bigger probe (r_{pr} = 500 μm, L_{pr}

= 1 cm) data gave larger span of reliable results: $B < 0.0076$ T and $B > 0.017$ T, so only a small part in between these two values resulted in overestimated S_{eff} and underestimated n.

The equations (3.31) and (3.17) for $\theta = 0°$ (Fig. 3.18 and 3.19) are plotted to check the results from the paragraph above and thus the validity of the assumptions (3.32). All curves are for a constant temperature of 5 eV. The boundaries of B are prolonged beyond the ones used in the experiment to see the upper threshold value where the two theories start to match.

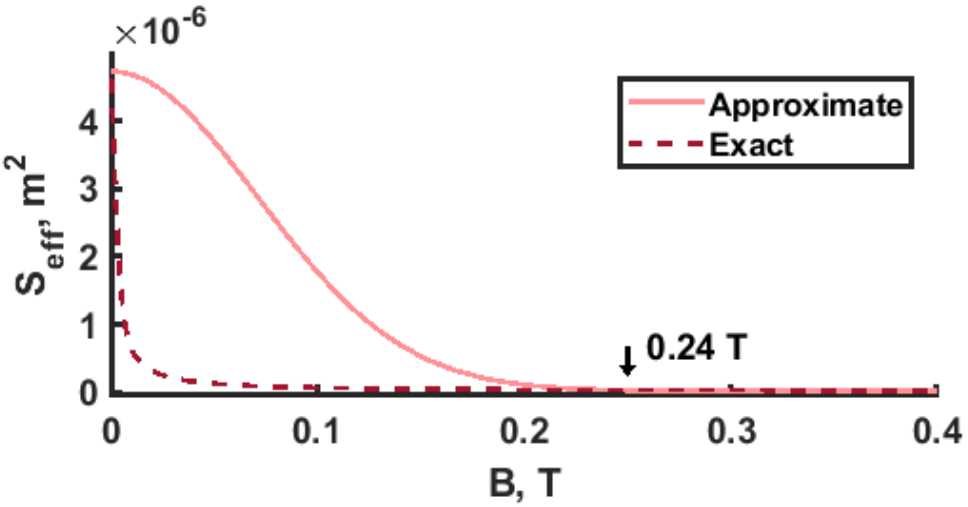

Fig. 3.18. Comparison of the two theories for r_{pr} = 75 μm. The arrow indicates the intersection.

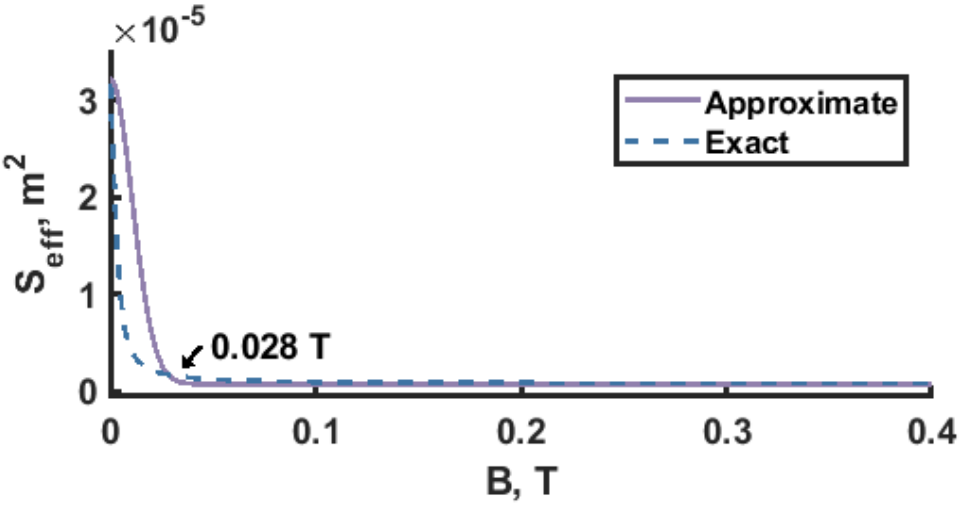

Fig. 3.19. Comparison of the two theories for r_{pr} = 500 μm. The arrow indicates the intersection.

No lower threshold value is observed. The values of the upper threshold in both cases are twice bigger than those obtained from (3.32). This can serve as a guidance to take the criteria for the approximate theory applicability as those in (3.32) but with a factor of 2 for $\bar{v} < v_{\lim r}$. After some transformations they look like:

$$\begin{cases} B < \frac{2\pi m_e \bar{v}}{eL_{pr}cos(\theta)}, \text{for any } r_{pr} \\ B > \frac{2\pi m_e \bar{v}}{eL_{pr}cos(\theta)} \text{ and } B > 2\frac{m_e \bar{v}}{er_{pr}} \end{cases} \quad (3.33)$$

The second criterion should be quite correct for a broad range of parameters at $\theta = 0°$ and even more so for non-zero angle, since the overestimation of the area reduces with the angle. The first criterion might be applicable for some non-zero angles, but this question requires further investigations.

The comparison above is done for $\theta = 0°$ but θ was around $5°$ in the experiments shown in Section 3.4.2, so the real overestimation of S_{eff} is somewhat lower than what is predicted for a parallel probe. The experimental data (Fig. 3.8) shows that the underestimation of n for the small probe is maximum of the factor of 2 compared to the big probe. One of the reasons for that is the non-zero angle, but there might be other factors which affected the current collection.

3.7 Plasma potential evaluation

The methods of density evaluation at the plasma potential with effective collecting areas are useless without a sufficiently precise and robust technique for evaluation of the plasma potential itself. In this section the conventional method of V_{pl} calculation from the maximum of the first derivative of the current [Lieberman2005] is examined and another method, which showed better robustness in applications, is introduced.

3.7.1 Plasma potential from 1st derivative

The most common method of V_{pl} calculation from the first derivative of the current in a magnetized plasma often gives too low unrealistic values. Taking the first minimum of the second derivative after the point where the first derivative has maximum is another possible method. It gives slightly bigger values for V_{pl}, but is only applicable to data with a very low noise level.

The underestimation of V_{pl} values is not the only weakness of the first derivative approach. More importantly, a reason for the search of alternative methods is given by the revealed low robustness of the first derivative technique. It is illustrated in the following example.

The IV characteristics (smaller cylindrical probe) for similar values of 0.0236 and 0.0283 T are nearly the same for each RF power (Fig. 3.20), except the disturbance introduced around the plasma potential. Consequently, V_{pl} and the current at V_{pl} should be nearly the same for the two cases. It is not true for the 32 W power level. A bump which is present at the bigger 0.0283 T field, does not appear at 0.0236 T. The nature of this bump is not fully understood. An attempt to study this phenomenon has been done in [Mihaila2013], [Mihaila2014], showing that there is a dependence of the bump height on the magnetic field strength and on the ratio of the probe radius and length. This bump changes the shape of the first derivative, thus influencing the obtained V_{pl}. This causes a difference of two times in the current at V_{pl} and hence the same difference in the density evaluated using this current.

One more type of a problem has been observed when using the 1st derivative technique. The sought peak of dI/dV is not always clear. If it is blurred, an uncertainty in V_{pl} identification of the order of few volts can follow. It has been noted from the experimental data that a shift of 1 V in V_{pl} can cause a difference of more than 100% in the current at V_{pl} and consequently it affects the electron density.

This effect is especially strong for the IV curves obtained in the presence of a high magnetic field. The transition region is very narrow in this case, only few volts.

3.7.2 Plasma potential at intersection

In this method V_{pl} is found as the x-coordinate of the intersection of 2 lines:

- linear interpolation of the region between V_{fl} and V_{pl};
- linear interpolation of the electron saturation current.

Not the full regions are taken, but only those parts which have linear shape. For the used data it was the last 30 V of the electron saturation current and 1/3 of the region between V_{fl} and the first approximation of V_{pl} found with the classical 1st derivative approach.

A similar technique has been published (for example in [Merlino2007]). The difference is that usually the current is taken in the log scale. In the used Aline data there is no clear linear region for the transition part of the IV curve in the log scale. That is why the "log intersection" method is not applicable, but the intersection at the linear scale works, as will be shown below.

The same data as in the section 2.1 is used to compare the techniques. In Fig. 3.21 the prolonged lines of the fits and the obtained points of intersection can be seen. It can be seen that this method is not affected by the bump phenomenon. With this technique V_{pl} for 32 W and corresponding values of the current are similar for the two magnetic field values. The tendency of the increase of the current at V_{pl} with the increase of the injected RF power is also a good sign.

The intersection method is not always applicable. For very small magnetic fields (< 0.005 T) the knee of an IV curve is hard to define, since the slopes of the two adjoining regions are very similar. In such cases it is impossible to apply the intersection methode. V_{pl} from 1st derivative is taken instead.

The evaluation of the plasma potential with the intersection technique results in a point right at the edge of the knee. This plasma potential estimation is reliable in low-pressure, unmagnetized, dc discharges. In collisional or magnetized plasmas the magnitude of I_{es} is supposed to be lowered and the knee blurred, so the real V_{pl} becomes hard to determine. In addition, RF fluctuations of $V_{pl} - V_{pr}$ can be significant when the RF amplitude is much bigger than kT_e/e.

If V_{pl} as well as the current at V_{pl} are overestimated, it can lead to:

1) Larger density values due to linear dependency $n \sim I$;
2) Imprecise collecting area definition. At values higher than the real plasma potential an expansion of a sheath begins, so a bigger area must be used in calculations. Since $n \sim 1/S$, it adds up to the rise of the resulting density estimation.

Error bars for the density can be obtained for each case by comparing the current at V_{pl} for the two techniques. In the presented experiments this ratio was typically in the range of 1-2. Possible sheath expansion was neglected.

The important fact is that the robustness of the intersection approach is much higher than the 1st derivative one. More consistency of the behaviour of the current at V_{pl} can be seen in Fig. 3.22. This fact outweighs possible consequences of slight overestimation of V_{pl} and current at V_{pl} values.

In the end, it can beconcluded that processing Langmuir probe data in the presence of a magnetic field using only the 1st derivative method is not acceptable. The intersection technique is adopted as more reliable, with an exception for low B values leading to the final combined method.

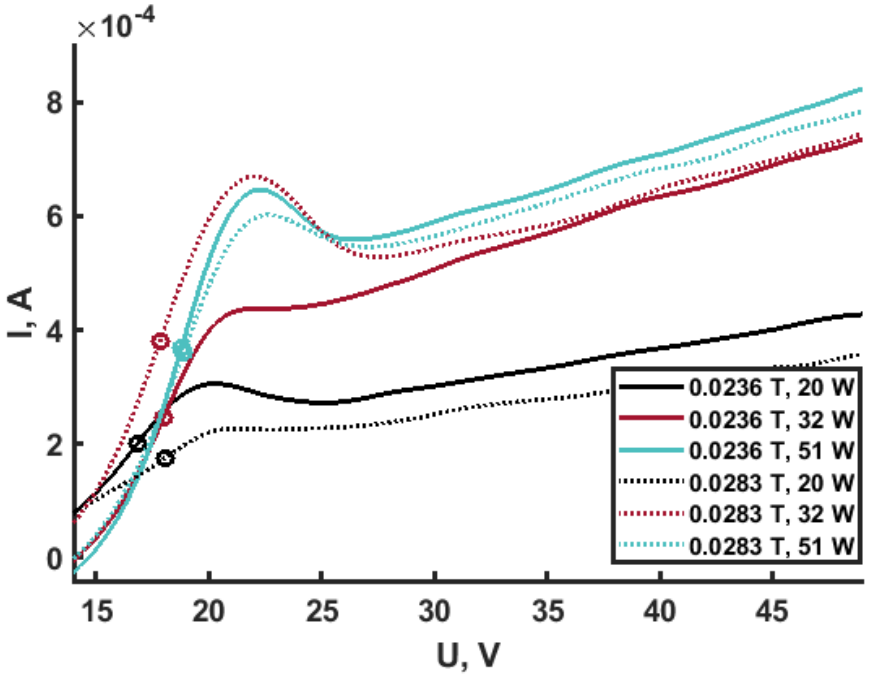

Fig. 3.20. Example of V_{pl} from the 1st derivative method (circle markers).

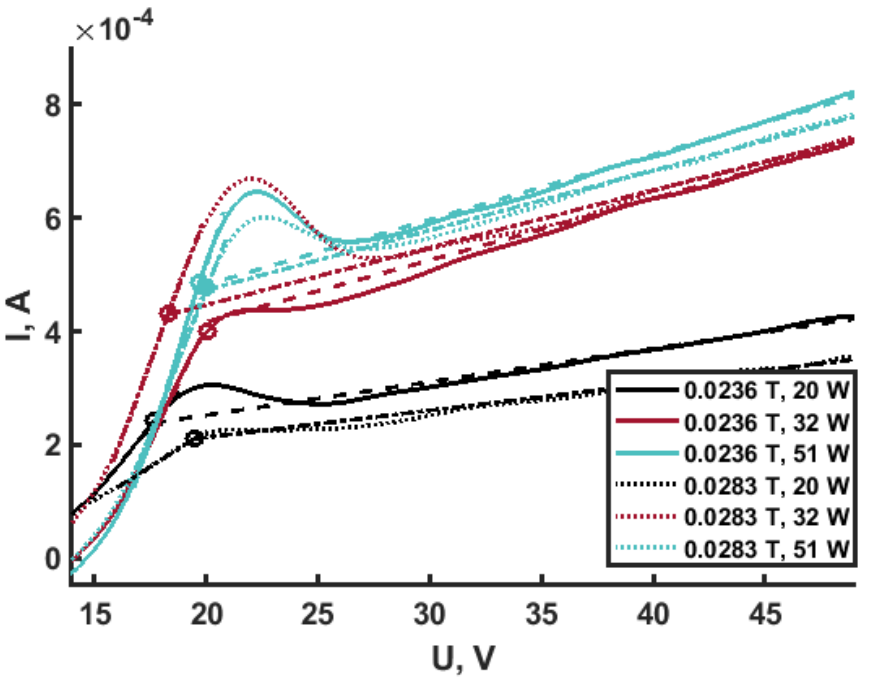

Fig. 3.21. Example of V_{pl} at intersection (circle markers).

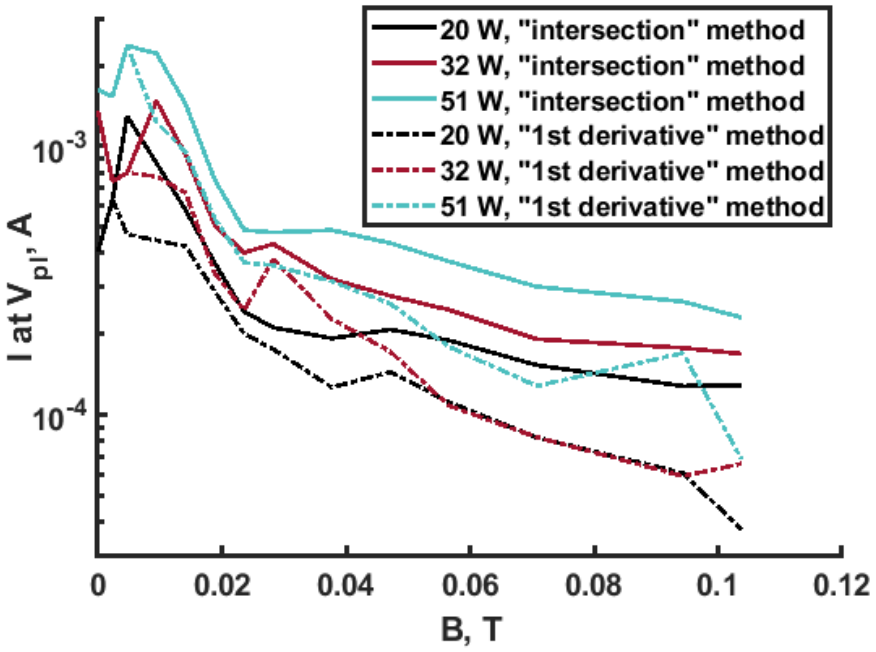

Fig. 3.22. Comparison of the current at V_{pl} for two methods.

3.8 Electron temperature evaluation

In Langmuir probe data processing the precision of the estimation of all relevant parameters is important, since they are all self-consistent and an error in one parameter enhances errors in others. Here an improved approach of the calculation of the electron temperature is described.

Electron temperature can be obtained from the slope of an IV curve between floating and plasma potentials. Electron current as a function of voltage for $V \leq V_{pl}$ is expressed as [Chen2003]

$$I_e(V) = I_{es}\, exp\left(-\frac{e(V_{pl}-V)}{kT_e}\right) \tag{3.34}$$

A slope of a linear fit to the logarithm of electron current is used to determine T_e:

$$T_e = \frac{V_2 - V_1}{ln\, I_2 - ln\, I_1} \tag{3.35}$$

where indexes 1 and 2 refer to any two points on the line.

An inverse mean value of the gradient $\frac{d\, ln\, I_2}{dV}$ for a part of the region between V_{fl} and V_{pl} is taken in the data processing. This part is the central third part of the whole span. The reason why not take the whole region is taken is that the measured current is a sum of the electron and the ion current, which means that the pure exponential shape is disturbed. The measured current is shifted down from the values of the electron current by some $I_i(V)$. The ion current in this region is not constant, it decays towards V_{pl}, but since it happens relatively slowly and the determination of the correct law for this decay is very sophisticated in the presence of the magnetic field, it is assumed to be constant in these calculations.

A shift of an exponential function by a constant does not result in a parallel linear shift of the same function in the log scale (Fig. 3.23). It means that if the whole region from V_{fl} to V_{pl} is considered, the current would have a shape as that of the brightest line in Fig. 3.23: ($y = exp(x) - 1$).

That's why the whole region should not be used for the temperature evaluation. The resulting average curve slope will be overestimated, and consequently the temperature will be underestimated. When the used region is cut on the left at around 1/3, the explained error can be strongly reduced. The reason to cut 1/3 on the right has a different nature: V_{pl} can be overestimated as was previously discussed, so the part close to V_{pl} is ignored.

The temperature obtained from the central part of the current linear fit in log scale is regarded as the lower limit. Then it is used as the starting point for an iterative algorithm that self-consistently calculates densities and temperatures. First, the temperature is used to determine the density and then the ion current is calculated theoretically for a point of the voltage that is approximately the value of T_e (in eV) below V_{pl}:

$$I_i = 0.6en\left(\frac{kT_e}{2\pi m_i}\right)^{1/2} S_i \tag{3.36}$$

The equation for the collecting area S_i is the same as for the whole probe surface (3.7) except that instead of the probe radius the sum of the radius and the sheath length s is taken. At that point the negative sheath is not yet too large and can be determined as given in [Chabert2011]:

$$s(V) = \frac{2}{3}\left(\frac{\varepsilon_0}{I_i/S_i}\right)^{1/2}\left(\frac{2e}{m_i}\right)^{1/4}\left(V_{pl} - V\right)^{3/4} \tag{3.37}$$

Taking the ratio I_i/S_i from (3.36) and the Debye length definition $\lambda_D = \left(\frac{\varepsilon_0 kT}{ne^2}\right)^{1/2}$, equation (3.37) transforms into:

$$s(V) = 1.02\,\lambda_D\left(\frac{e(V_{pl}-V)}{kT_e}\right)^{3/4} \tag{3.38}$$

The calculated ion current is then subtracted from the net current and the result is used to determine the next iteration of the T_e the same way as was described above, from the central part of the current between V_{fl} and V_{pl} in log scale. The iterations continue until a stable value of the temperature is reached.

The described procedure was applied to the data processing of the cylindrical probe. For the planar probe the ion saturation current is negligibly low comparing to the electron saturation current, so the iterative algorithm does not change much the values of the lower limit of the temperature. Resulting temperatures acquired with the planar probe are similar to the ones from the cylindrical probes (the error is less than 50%, except for the part between 0.02 T and 0.06 T where the deviation reaches around 100% which is still a good agreement for this type of data) and have the same tendency to descend with increasing B and n_e (Fig. 3.24).

The transition region used for the density evaluation is very narrow for big magnetic fields, so increased error level may be expected there.

While the temperature obtained after the iterations is bigger than the lower limit and closer to the real one, it is still underestimated. The proper procedure would be to subtract the ion current as a function of the voltage. Since it is a descending function (in absolute values), the right part of the net current should be shifted less after the subtraction, which means that the slope will be lower and the temperature bigger. This effect is ignored in the data processing, but it might be important to take it into account for some other conditions.

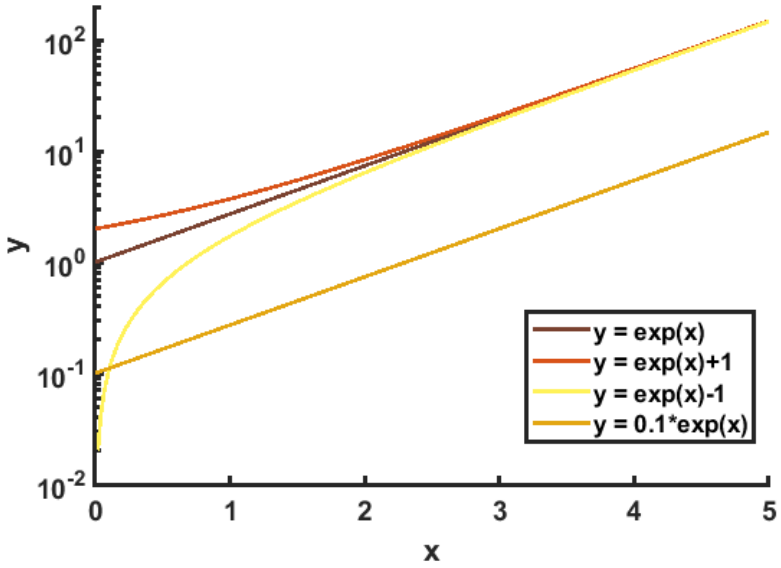

Fig. 3.23. Shifted exponential functions in logarithmic scale.

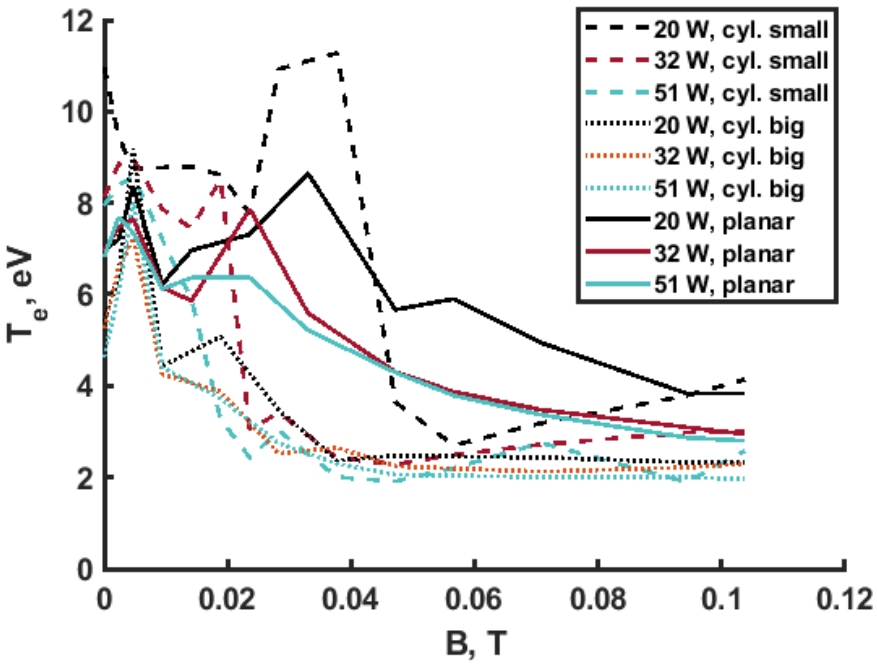

Fig. 3.24. Temperature comparison for three probes.

3.9 Conclusions

The developed general theory of the effective collecting area calculation provides a rather simple method of density evaluation with a cylindrical Langmuir probe in magnetized plasma. The experimental validation of the applicability has shown positive results, which allows further use of cylindrical probes in magnetized conditions at various angles. The advantage of such diagnostic is the accuracy of local measurements, allowing precise mapping of a small plasma region. In the proximity of the extreme limit (3.1) the theory approaches the existing technique of using a perpendicular projection of a probe as the collecting area. On the other hand, the constructed formula demonstrates the typical function of the current collection by a cylindrical probe. With increasing dimensionless magnetic field (with all other plasma parameters unchanged) the collecting area is reduced to some limit (bigger than the perpendicular area) and then decays very slowly. This matches the experimental observations on Aline.

The presented general theory for the effective collecting area can be applied to a broad range of experimental conditions. No limitation on the probe size or orientation is imposed. The shape of the probe is as well not limited to the cylinder only. As long as the probe whole surface and the perpendicular to B projection area are known, the theory remains valid.

In the second theory, an exact analytical solution is given for the electron current collected at V_{pl} by a cylindrical Langmuir probe oriented parallel to the magnetic field. Only this case is calculated, since for a probe at arbitrary angle the analytical calculations would not be feasible. The general approximate theory is compared to the exact model for the parallel probe orientation and applicability criteria are formulated. The overestimation of the collecting area by the approximate theory seems big, but the experimental underestimation of density is only of the order of 2.

The constructed theories for interpretation of a cylindrical Langmuir probe data allowed for the first time to obtain reliable density profiles in magnetized plasma on Aline. Results are obtained for a broad range of the magnetic fields as well as the coupled power levels. Interferometry measurements of line-integrated densities have been carried out for the same range of parameters. Values that are well above the noise level of 1e16 m^{-3} match the densities obtained with the probe with up to 20% error. Possible causes of errors are listed.

Correct plasma potential evaluation is crucial for calculations of the density from the current at the plasma potential. The conventional technique employing the 1st derivative of the current is ineligible for magnetized plasma due to the explained low robustness. The intersection method is a better alternative, shown to be consistent for various magnetic fields. The only exception appears when the field is very small, because the transition and the electron saturation regions are indistinguishable. In those occasions the 1st derivative technique is employed as the only possible one.

A detailed explanation is given for the procedure of the electron temperature evaluation from a part of the transition region. The resulting values seem to be quite accurate and this accuracy is extremely valuable for the correct density estimation.

References

[Chen2003] – F.F. Chen, "Lecture Notes on Langmuir Probe Diagnostics" (2003)

[Chabert2011] – P. Chabert and N. Braithwaite, "Physics of Radio-Frequency Plasmas".Cambridge University Press, 2011

[Chatterton1991] – P.A. Chatterton, J.A. Rees, W.L. Wu and K. Al-Assadi, "A self-compensating Langmuir probe for use in rf (13.56 MHz) plasma systems", Vacuum **42(7)** (1991) 489

[Devaux2017NME] – S. Devaux, E. Faudot, J. Moritz, S. Heuraux, "ALINE: A device dedicated to understanding radio-frequency sheaths ", Nuclear Materials and Energy **12** (2017) 908

[Faudot2015] – E. Faudot et al., "A linear radio frequency plasma reactor for potential and current mapping in a magnetized plasma", Rev. Sci. Instrum. **86** (2015) 063502

[Franz2009] – G. Franz, "Low Pressure Plasmas and Microstructuring Technology", ISBN 978–3–540–85849–2, 2009

[Kudrna1997] – P. Kudrna, E. Passoth, "Langmuir Probe Diagnostics of a Low Temperature Non-Isothermal Plasma in a Weak Magnetic Field", Contrib. Plasma Phys. **37** (1997) 417

[Laframboise1976] – J.G. Laframboise and J. Rubinstein, "Theory of a cylindrical probe in a collisionless magnetoplasma", Phys. Fluids **19**, 1900 (1976)

[Lieberman2005] – M.A. Lieberman, "Principles of Plasma Discharges and Materials Processing", second edition, ISBN 0-471-72001-1, 2005

[Merlino2007] – R.L. Merlino, "Understanding Langmuir probe current-voltage characteristics", Am. J. Phys. **75**, 1078 (2007)

[Mihaila2013] – I. Mihaila, L. Solomon, C. Costin, G. Popa, "On Electrical Probes Used in Magnetized Plasma Diagnostics", Contrib. Plasma Phys. **53**, No. 1, 96–101 (2013)

[Mihaila2014] – I. Mihaila, S. Costea, C. Costin, G. Popa, "On Negative Slope of Probe Characteristics in MagnetizedvPlasmas", Contrib. Plasma Phys. **54**, No. 3, 291–297 (2014)

[Popov2012] – Tsv.K. Popov, "Langmuir probe measurements of the electron energy distribution function in magnetized gas discharge plasmas", Plasma Sources Sci. Technol. **21**, 025004 (2012)

[Popov2016] – Tsv.K. Popov, "Advances in Langmuir probe diagnostics of the plasma potential and electron-energy distribution function in magnetized plasma", Plasma Sources Sci. Technol. **25**, 033001 (2016)

[Rubinstein1978] – J. Rubinstein and J.G. Laframboise, "Upper-bound current to a cylindrical probe in a collisionless magnetoplasma", Phys. Fluids **21**, 1655 (1978)

[Sudit1994] – I.D. Sudit and F.F. Chen, "RF compensated probes for high-density discharges", Plasma Sources Sci. Technol. **3** (1994) 162

[Tichy1997] – M. Tichy et al., "Langmuir Probe Diagnostics for Medium Pressure and Magnetised Low-Temperature Plasma", J. Phys. IV France **07** (1997) C4-397-C4-411

[Usoltceva2018PoP] – M. Usoltceva et al., "Effective collecting area of a cylindrical Langmuir probe in magnetized plasma", Phys. Plasmas **25** (2018) 063518

[Usoltceva2018RSI] – M. Usoltceva et al., "Theory of a cylindrical Langmuir probe parallel to the magnetic field and its calibration with interferometry", Rev. Sci. Instrum. **89** (2018) 10J124

4 ICRF waves in IShTAR

In this chapter the ICRF antenna of IShTAR is studied comprehensively, in the context of the whole device. These studies form the basis of the knowledge about the ICRF fields in IShTAR and its interaction with the plasma, which is necessary for future exploration of the local non-linear sheath physics of the antenna.

In Section 4.1 the analytical solutions from Section 2.1.1 are applied to obtain information about the propagating and evanescent ICRF wave modes in IShTAR conditions. As a first step of the ICRF antenna characterization in IShTAR, the magnetic field of the waves emitted by the antenna was characterized in vacuum. Experimentally it was achieved by the use of the B-dot probes diagnostic which components required calibration measurements described in Section 4.2. How much a B-dot probe disturbs the fields outside and inside of the probe is also examined in Section 4.2. The measurements results are given in Section 4.3. A realistic model of the IShTAR geometry done in COMSOL is presented in Section 4.4, as well as a comparison of the experimentally measured magnetic fields to the simulation in COMSOL.

Section 4.5 is devoted to the modelling study of the slow wave propagation in a simplified 3D geometry. Plasma and PML are implemented and tested and then results are obtained in various plasma conditions. Analysis and comparison lead to the conclusions on the most interesting cases to be studied in IShTAR experimentally in the future. Measurements of the power sent to the plasma in the experiment in different scenarios are the last topic of this chapter and will be discussed in Section 4.6.

4.1 Waves in IShTAR in cold plasma approximation

The theoretical description given in the first section of Chapter 2 can be applied to IShTAR in order to investigate the wave behaviour that can be expected in the experiment. A preliminary theoretical study was conducted in [Crombe2016JPP] before the final design of the ICRF antenna and the achievable range of the plasma conditions were known. Here the calculations are done for the actual present-day IShTAR conditions.

As was mentioned in Chapter 2, $k_{\parallel}$ is defined by the ICRF antenna geometry and typically $n_{\parallel} > 1$. For a single strap antenna of a width w it is $k_{\parallel} \sim \pi/\mathrm{w}$ [Louche-Koch-lecture], which for w = 0.12 m leads to $k_{\parallel_{theor}}$ = 26.17 rad/m as the first and the strongest peak in the $k_{\parallel}$ spectrum for the IShTAR antenna. However, the spectrum of a real antenna with finite width is more complex than this one peak, and it is also affected by the presence of the limiters. The spectrum of $k_{\parallel}$ is found from the COMSOL model of IShTAR ICRF antenna (the model will be presented in Section 4.3). A 1D profile of the parallel magnetic field component H_z is taken in front of the antenna (Fig. 4.1) and a Fourier

transform is performed (Fig. 4.2). The resulting antenna spectrum has multiple peaks of finite width, as can be seen in Fig. 4.2. The biggest peak is at $k_{\parallel}$ = 20.93 rad/m, it can be seen that because of the finite width the $k_{\parallel_{theor}}$ is quite close to this peak. $k_{\parallel}$ = 20.93 rad/m is taken for further calculations of $n_{\perp}^2$ and other components of the $k_{\parallel}$ spectrum are ignored.

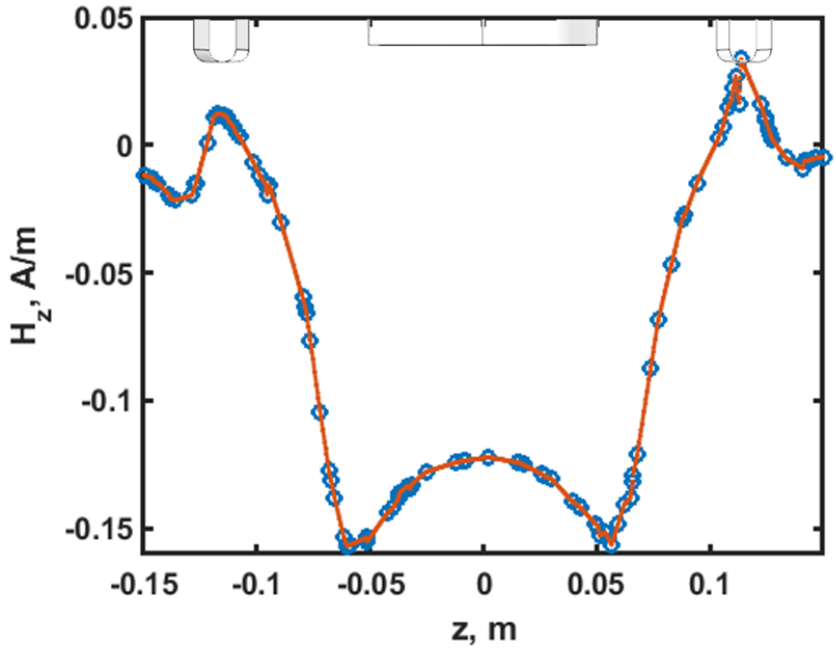

Fig. 4.1. IShTAR antenna magnetic field component parallel to B. Antenna strap and limiters are schematically indicated at the top of the picture.

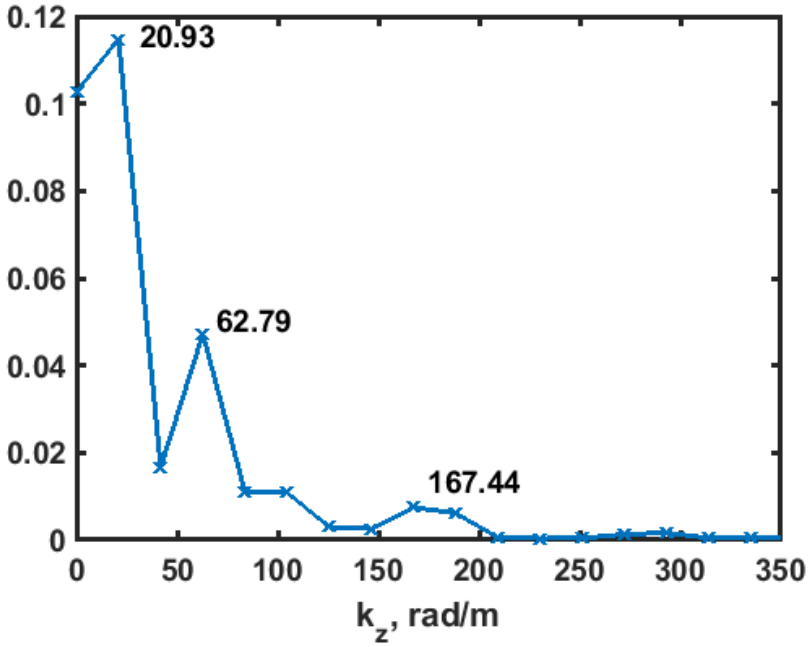

Fig. 4.2. Fourier spectrum of the parallel component of the wave vector of the IShTAR antenna.

The following conditions are considered for IShTAR: gas – pure Ar or He, frequency – 6 MHz, magnetic field – 0.1 T, $k_{\parallel}$ = 20.93 rad/m. The two solutions of the wave dispersion relation (2.15),

the fast wave (2.18) and the slow wave (2.19) are plotted in Fig. 4.3 for argon and Fig. 4.4 for helium. The overall behaviour of the two modes is very similar to the tokamak example in Section 2.1.1, with same cut-offs and resonances present, but at different densities. A yellow box indicates the region of densities accessible on IShTAR. It can be seen that in IShTAR only the SW propagation is possible, so the RF sheath effects caused only by the SW can be studied, which is a big advantage for the understanding of the physics. The highest possible densities are achieved only in the very center of the plasma. On the edge, near the ICRF antenna, the densities in both Ar and He are below the LH resonance. Further increase of the densities can be possible with the machine upgrade but is not available at the moment.

Influence of the change of $k_{\parallel}$ (10.465, 20.93 and 62.79 rad/m) is shown in Fig. 4.5 for argon; the tendency is similar for helium. The main difference is the shift of the FW cut-off density value, it is higher for bigger $k_{\parallel}$. The SW cut-off and resonance remain at the same position. Values of the $k_{\perp}$ are also affected by the change of $k_{\parallel}$ in the region of SW propagation, important in the present work. The observed tendency gives a valuable conclusion: for FW studies in case of limited range of achievable densities it is beneficial to construct an antenna with lower $k_{\parallel}$, then it is easier to obtain a region of FW propagation.

If the $k_{\parallel}$ is kept constant, but the magnetic field is varied (0.06, 0.1 and 0.272 T), changes happen not only to the FW cut-off values, but to the SW resonance as well (Fig. 4.6). As the magnetic field is lowered, the FW cut-off and the SW resonance move towards each other, until a threshold is reached (B = 0.057 T in this case), after which the full roots coincide and the approximate SW and FW solutions become inapplicable (Fig. 4.7). For quite an extensive range of the magnetic field (0.1–0.272 T) the differences are very small for the SW in the IShTAR case. For the smaller fields the SW propagation region of densities is extended, but the maximum density achievable in the experiments anyway lies far below the part affected by the magnetic field change.

Electric field polarization, dielectric tensor elements and shapes of the wavefront are qualitatively the same in IShTAR as the results given in the Chapter 2 for the ASDEX Upgrade tokamak example case: the parallel electric field has significant values only for the slow wave and only at very low densities; the SW has the shape of a resonance cone.

4.2 Calibration of magnetic diagnostic components in experiments and simulations

The magnetic field of the RF waves in IShTAR is characterized by using the B-dot probe diagnostic which principle was described in Section 2.4.2. The experimental diagnostic setup consists of multiple probes that are installed inside the vacuum chamber, 50 Ohm wires going outside of the vessel and to the control room of IShTAR and logarithmic detectors which at the end are connected to the acquisition system of IShTAR. The description and calibration of the probes and detectors are given below. Some of the tests are done experimentally and some are simulated in COMSOL.

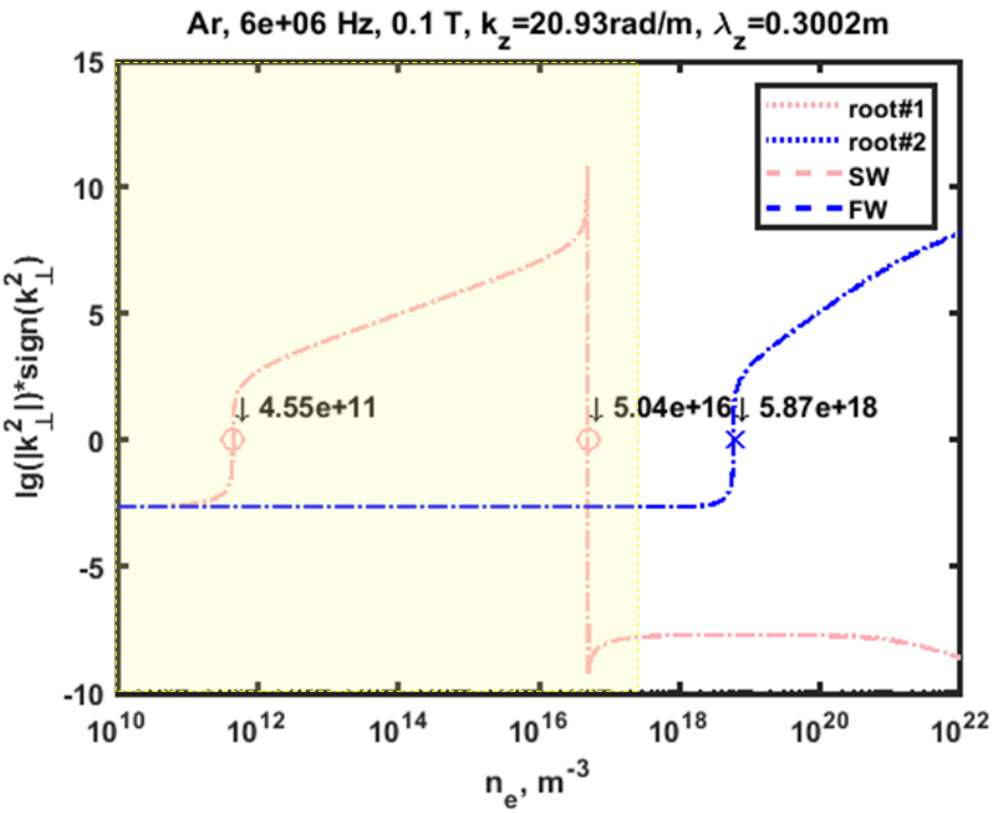

Fig. 4.3. Slow and fast waves behaviour in IShTAR depending on density, in argon.

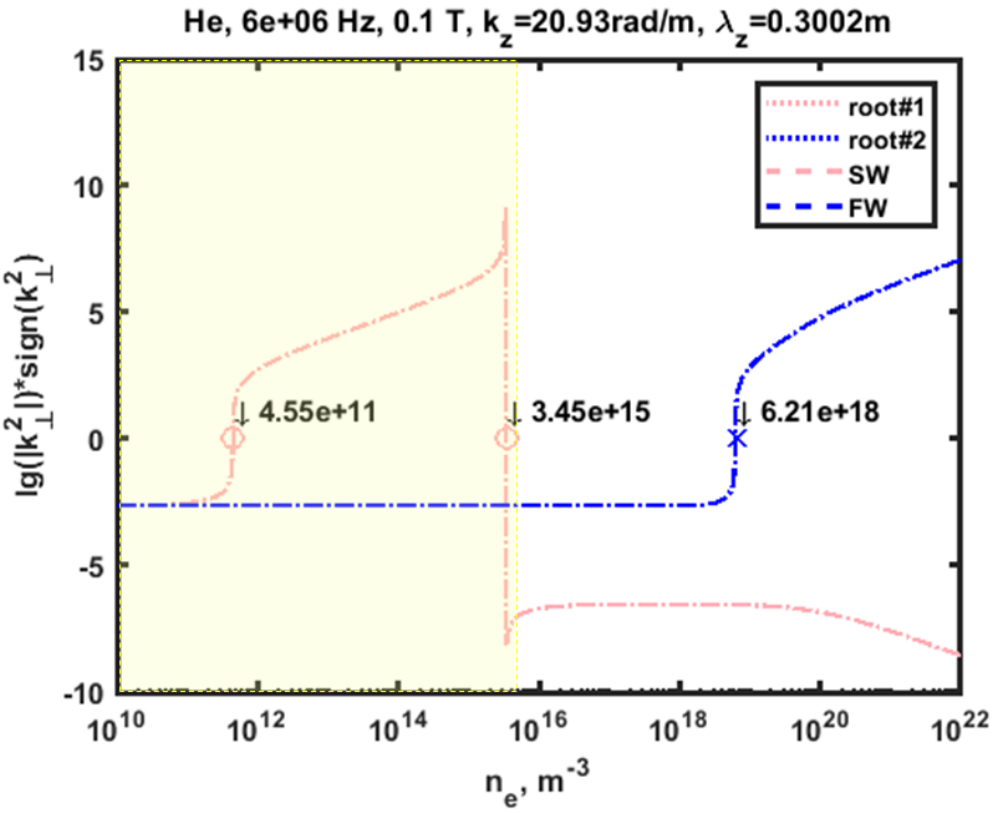

Fig. 4.4. Slow and fast waves behaviour in IShTAR depending on density, in helium.

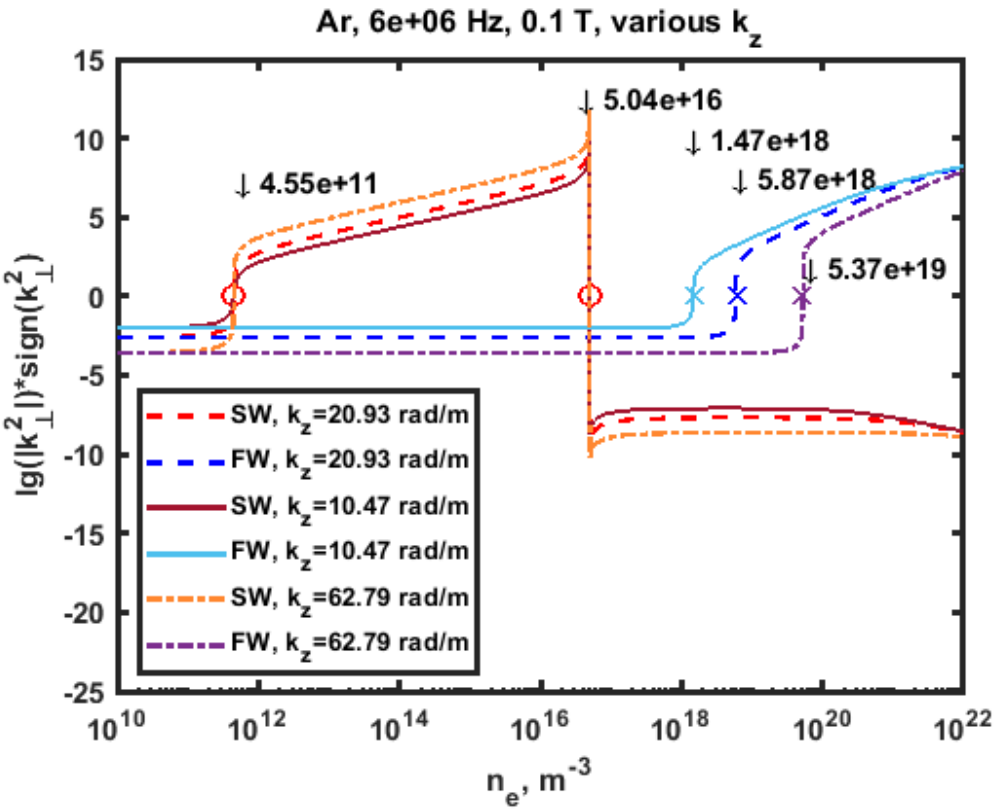

Fig. 4.5. SW and FW behaviour in IShTAR for various $k_{\parallel}$, in argon.

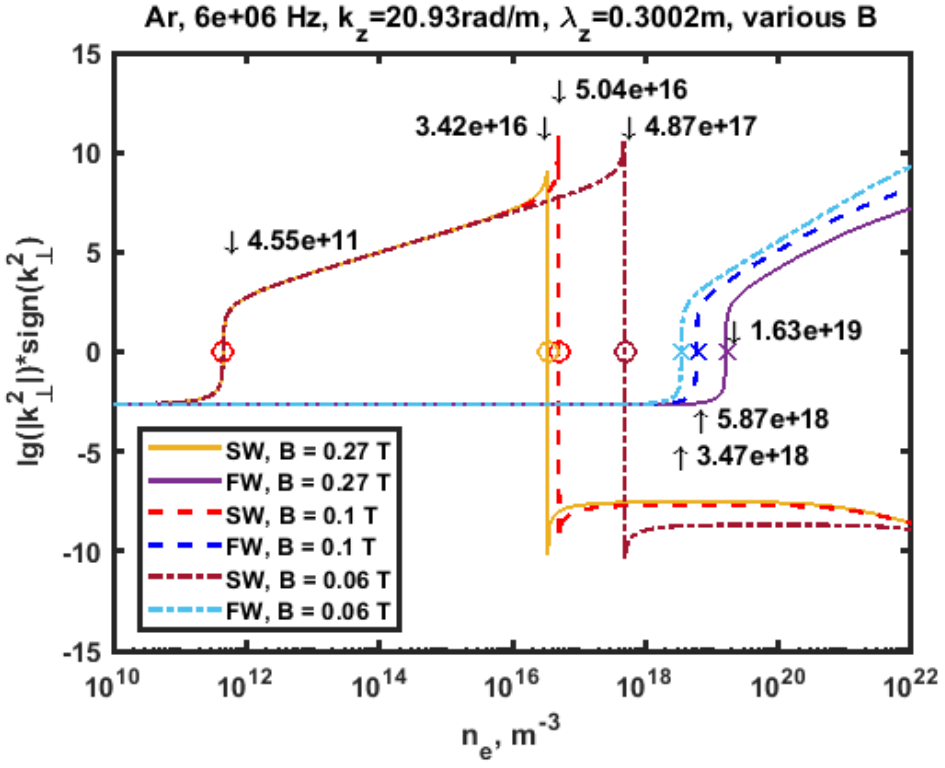

Fig. 4.6. SW and FW behaviour in IShTAR for various B, in argon.

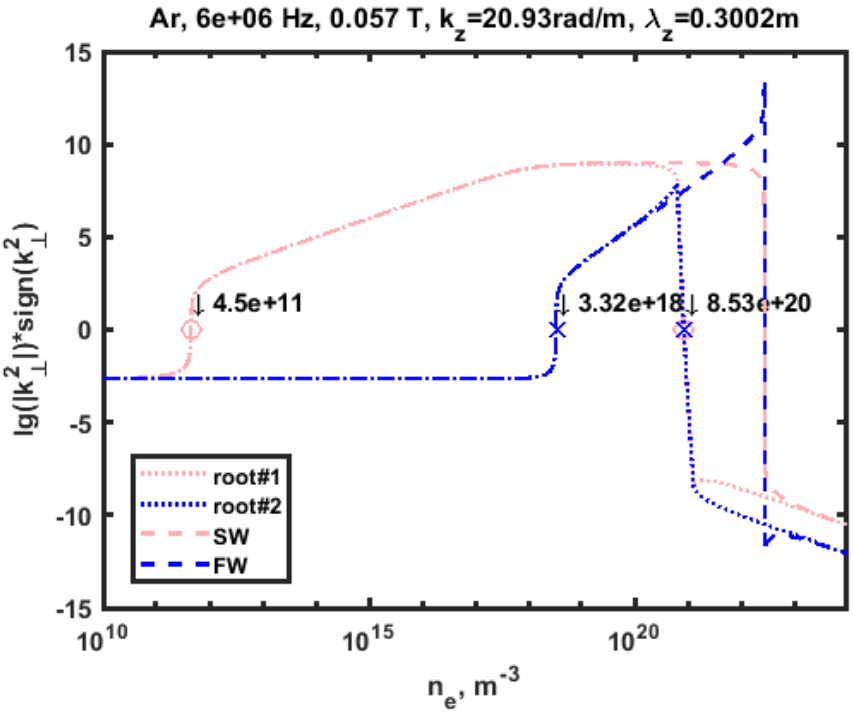

Fig. 4.7. SW and FW behaviour in IShTAR at the threshold B=0.057 T, in argon.

4.2.1 Calibration of logarithmic detectors

The logarithmic detectors (Fig 4.8) are called so because they have a logarithmic power scale in order to cover a very big range of measured power. Each detector has 2 channels for inputs (U1, U2) and on the output the converted signals are given (U1, U2), as well as the phase shift between the two channels (PH1) and the phase shift +90° (PH2); on the rear side a power supply with 6 V is connected.

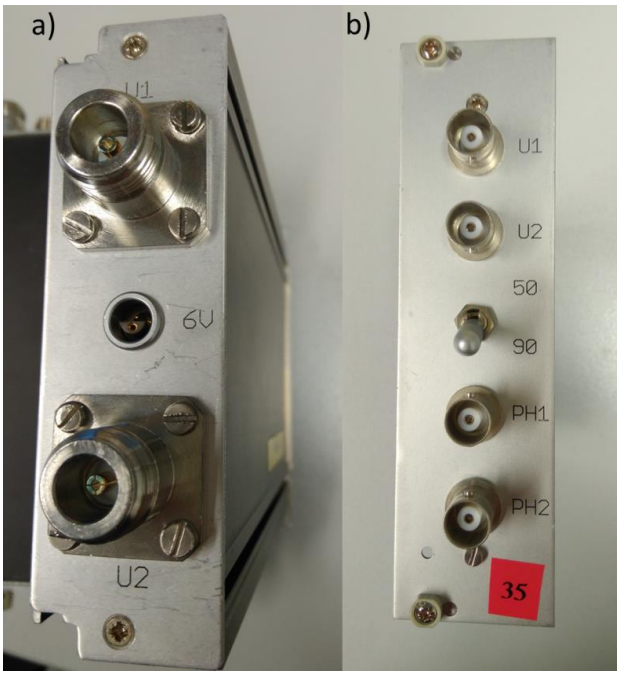

Fig. 4.8. Standard logarithmic detector: (a) rear view on inputs, (b) front view on outputs.

The detectors are produced locally at the Max Planck Institute of Plasma Physics (IPP) for the measurements on the ASDEX Upgrade tokamak. Since they are routinely used at frequencies around 36.5 MHz, they have a constant attenuation factor for frequencies greater than 10 MHz and much higher attenuation below 10 MHz (Fig. 4.9), thus aiming to cut the low-frequency noise. It is still possible to measure the 5-6 MHz signal of ICRF antenna with these detectors, but the signal is significantly weaker for this frequency.

It was possible to expand the frequency range and to achieve equal attenuation factor for both frequencies. Additional detectors of this new type were produced especially for IShTAR. The calibration of a detector with extended frequency range is also plotted in Fig. 4.9 to demonstrate the difference.

The third type of logarithmic detectors (produced also on demand for IShTAR) is a narrow-band detector which is able to attenuate strongly all signals on the frequencies outside a very small range. The central frequency of the selected range can vary, for this an additional input channel is provided (marked LO). The LO input must always be on the frequency of f+50 MHz at 10 dBm power level. An example of the detector frequency response can be seen in Fig. 4.10 for the frequency f = 5.923 MHz, outside of the plotted frequency range the output signal is 0.

The output of any two-channel detector in V is linearly proportional to the input power in dBm, i.e. logarithmically proportional to the input power in W. However, the same voltage corresponds to different power for different detectors and different frequencies. All the detectors employed are calibrated for each important frequency and an example of such calibration is given in Fig. 4.11.

All the measurements presented in Section 4.2.2 are done using the first (standard) type of the detectors. The two new types of the logarithmic detectors provide much higher precision and flexibility of the measurements and they are planned to be used in all future experiments on IShTAR.

4.2.2 B-dot probe radial calibration in the coaxial line

The B-dot probes used in IShTAR are also produced at IPP. A probe is a metallic box with a slit on the front side and a cable going out from the opposite side (Fig. 4.12). Inside the probe the cable is connected to the coil which performs the field detection and which is located just behind the slit. The dimensions are shown in the figure.

On the calibration test stand, the experimental output was the power P_{out} which can be recalculated to the field using the following procedure:

1. W to A. $P_{out} = R \times I^2$ – power of the RF signal from the inductance coil. $I = \left(\frac{P_{out}}{R}\right)^{1/2}$
2. A to A/m. $H_{out} = \frac{I \times N}{L}$ – connection between current flowing in an inductor and averaged magnetic field in the inductor volume. L – inductor length, N – number of turns.

For the IShTAR B-dot probes: L = 10 mm, N = 8. The final formula reads:

$$H_{out} = \frac{N}{L}\left(\frac{P_{out}}{R}\right)^{1/2} = \frac{800}{\sqrt{R}}\left(P_{out}\right)^{1/2} \quad (4.1)$$

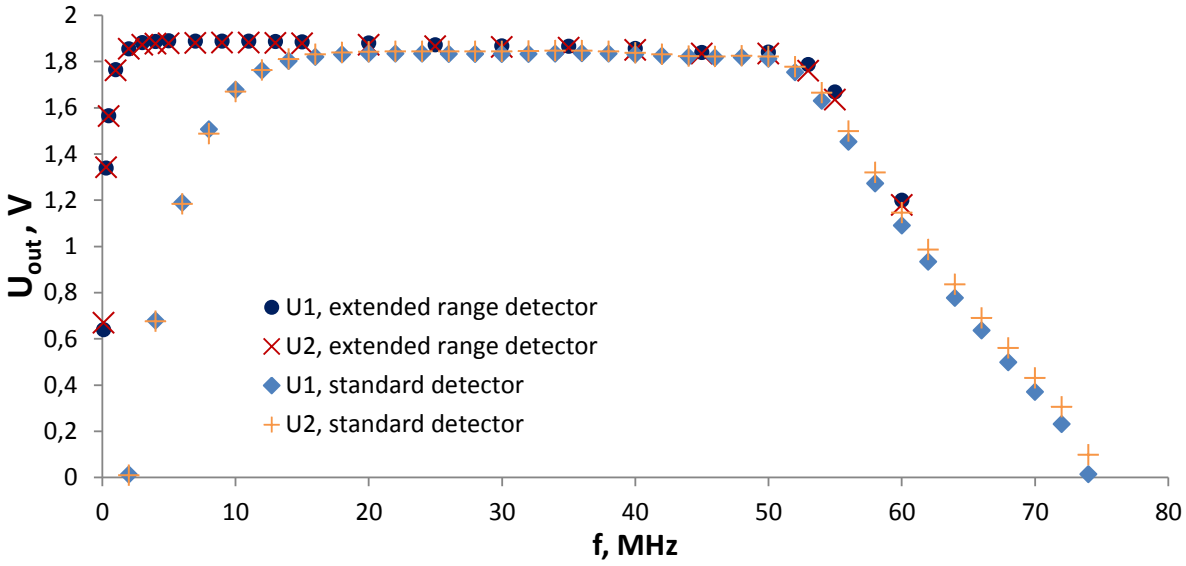

Fig. 4.9. Dependency of the signal attenuation on the frequency for two types of detectors.

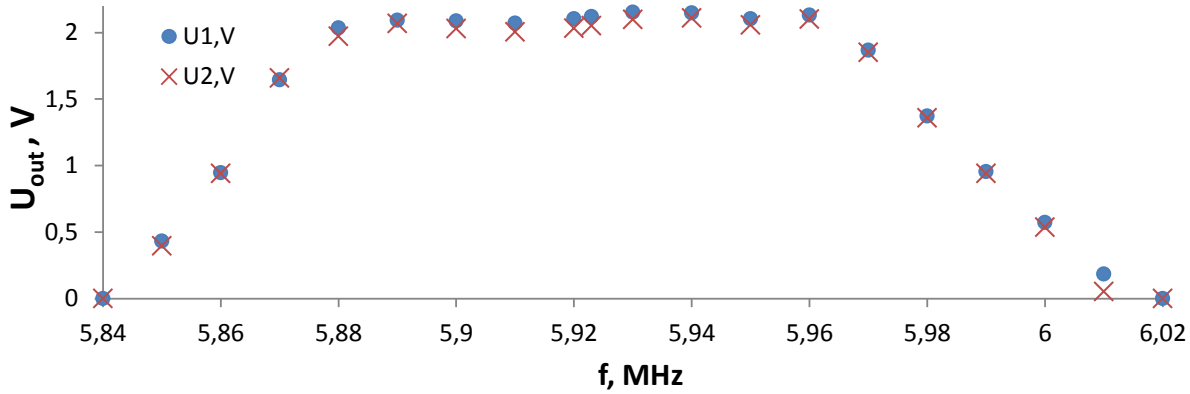

Fig. 4.10. Dependency of the signal attenuation on the frequency for the narrow-band detector.

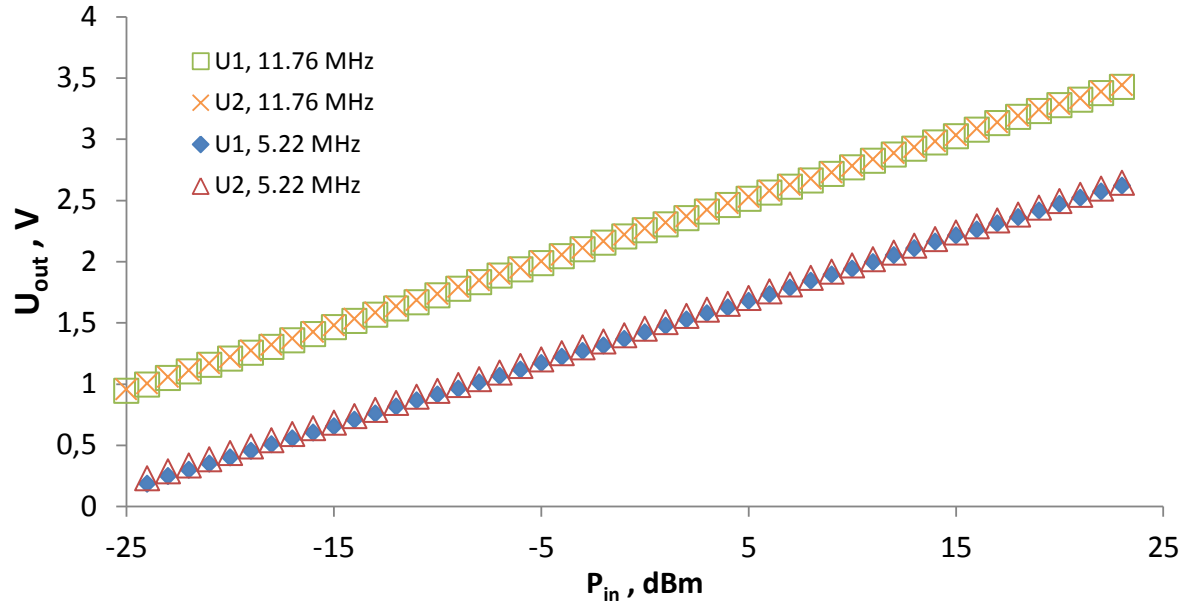

Fig. 4.11. Calibration of the output voltage of a logarithmic detector (example for the detector #69).

There is one unknown value here – the impedance R of the circuit where the signal is transferred. It prevents the calculation of absolute values of the measured fields. They can be obtained from the probe radial calibration in the coaxial line where the magnetic field distribution can be calculated theoretically.

Moreover, even if the impedance was known, the measured magnetic field would not correspond identically to the real unperturbed field in the region of the measurements. The metallic body of the probe introduces significant disturbance in the field, so the measurements correspond to the perturbed field in front of the probe slit. Furthermore, the field inside the probe at the position of the coil is not the same as outside, but attenuated. Comparison to the theoretical values in a coaxial line gives an opportunity to evaluate a dependency of the probe signal on the unperturbed "ideal" field.

A B-dot probe was installed in a 50 Ohm coaxial line and calibrated at 4 power levels. The probe was directed vertically with the slit facing the inner conductor and moved radially to measure the dependence of the output signal on the radial position. Theoretically, the magnetic field scales inversely with the radius:

$$H_{theor} = \frac{I}{2\pi r} = \frac{U}{2\pi r R_{cxl}} = \frac{1}{2\pi r}\sqrt{\frac{P_{in}}{R_{cxl}}} \tag{4.2}$$

where r – radial distance, R_{cxl} – impedance of the coaxial line, U and I – voltage and current in the coaxial line, P_{in} – input power.

In Fig. 4.13 the measured power $(P_{out})^{1/2}$ is plotted as a function of the theoretical field H_{theor} calculated for each value of P_{in} (6, 12, 18, 24 dBm) and for each radial position of the probe slit.

$(P_{out})^{1/2}$ (or equivalently H_{out}) is expected to scale linearly with H_{theor} and this is confirmed in the experiment. However, the linear trends are not the same for all radial positions. From $r = 100$ mm and higher r, the lines appear to deviate from the trend of the majority. The linear coefficient is approximately $6*10^{-4}$ for the big range of radial positions and significantly smaller when the probe is placed closer to the outside cylinder of the coaxial. It seems that the proximity of the outer cylinder together with the probe itself deforms the measured field more strongly and in a non-linear way.

The completed study provides quantitative coefficients for the calculation of the absolute values of the magnetic field measured by the B-dot probes and shows that those coefficients are different for different probe environment. When the probe slit is far from a conducting wall, the distortion of the measured field is constant and well-defined. In the proximity of a metallic structure on the sides of the probe, the coefficient for probe calibration changes non-linearly and may depend strongly on the shape of the wall and distance to it. For a probe used routinely far from conducting walls the correct calibration coefficient is the one measured with a probe inserted deep into the coaxial line, not in a position close to the outer cylinder.

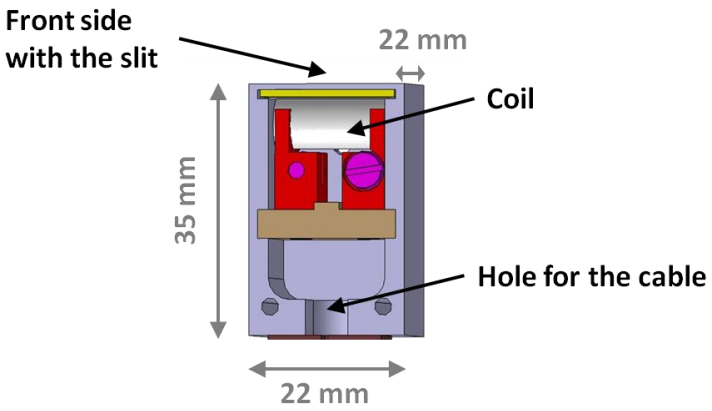

Fig. 4.12. Schematic picture of a B-dot probe used in IShTAR (top view).

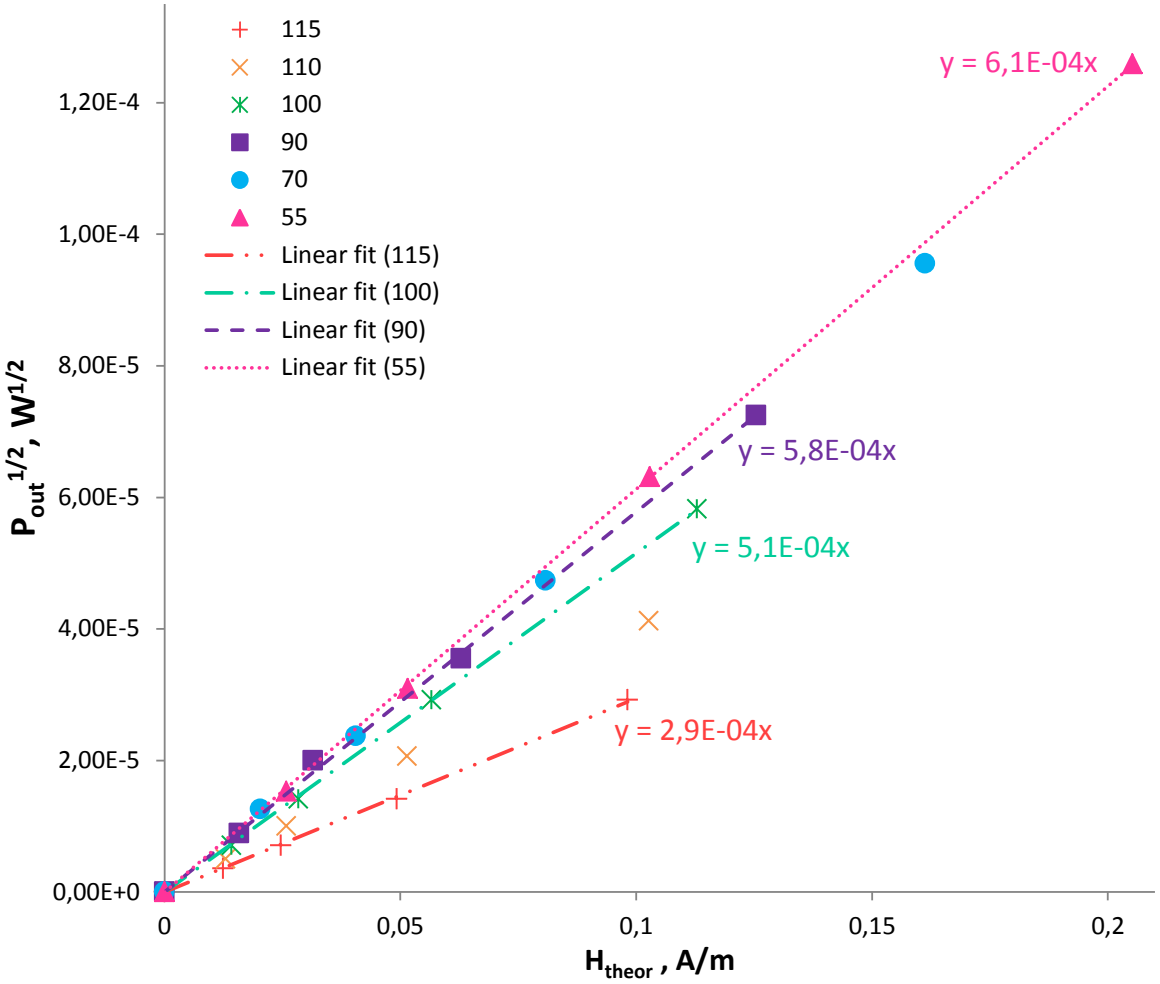

Fig. 4.13. Results of the probe radial calibration (radial positions in mm).

4.2.3 Disturbance of the fields by the presence of a B-dot probe

Disturbance of magnetic and electric fields at 11.76 MHz frequency was simulated in COMSOL inside a 50 Ω transmission line with the real dimensions of the B-dot probe and the line. The transmission line is 2 m long with coaxial cylinders radiuses r = 5 cm and R = 11.5 cm (Fig. 4.14). The dominant mode is TEM, with the electric field in radial and the magnetic field in poloidal directions. The probe

is a 22 mm × 22 mm × 35 mm box with a slit of 1 mm × 10 mm in the middle of the smallest face. The probe walls are 0.7 mm thick and made of steel. The long side of the probe is aligned with the direction of the main axis (x-axis) of the coaxial line and then rotated by 45 degrees in the x-y plane (Fig. 4.15). The probe is grounded with a strap to the outer coaxial cylinder of the transmission line. In a real B-dot probe, right after the slit (2 mm from outside) a vacuum-compatible inductor is placed.

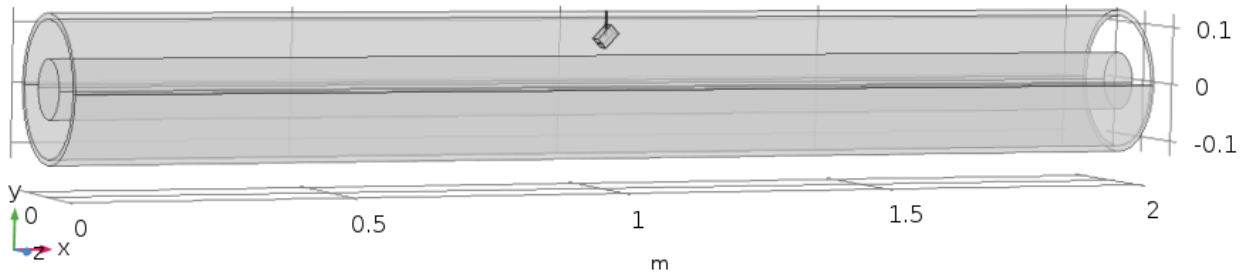

Fig. 4.14. Probe inside a coaxial line.

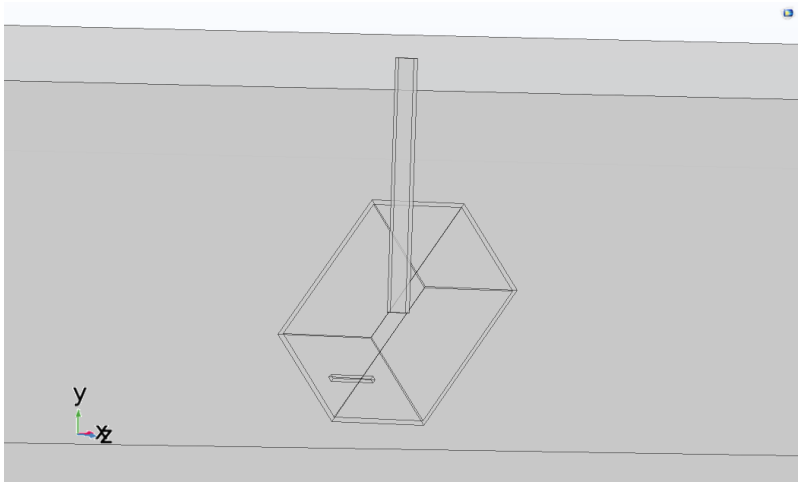

Fig. 4.15. B-dot probe geometry in COMSOL.

The components of the fields have been analyzed for the fact of a disturbance on two planes: x-y and y-z planes going through the middle of the coaxial cylinders. Results are presented in Fig. 4.16-4.18. In a coaxial transmission line the configuration of the fields is very well known theoretically: the electric field is radial and the magnetic field is oriented along the φ-coordinate. This can be seen on the plots.

To estimate the disturbance, the fields in the vicinity of the probe were compared to those in an undisturbed region far from the probe. Two lines are analyzed: along the x (Fig. 4.19) and φ (Fig. 4.20) coordinates.

The plots in Fig. 4.21-4.24 show all three components of the fields. Sharp jumps refer to the metallic boundaries of the probe, with almost zero fields inside and decaying disturbance outside of the probe. A criterion used to characterize the field disturbance is the distance from the probe, where the field value is at least 95 % of the value of the undisturbed field. This distance is estimated to be 5 cm for the electric field and 3 cm for the magnetic field. These results are important when an array

of B-dot probes is used and cross-disturbance between them should be avoided. The distance between two probes should be bigger than the disturbance length calculated here.

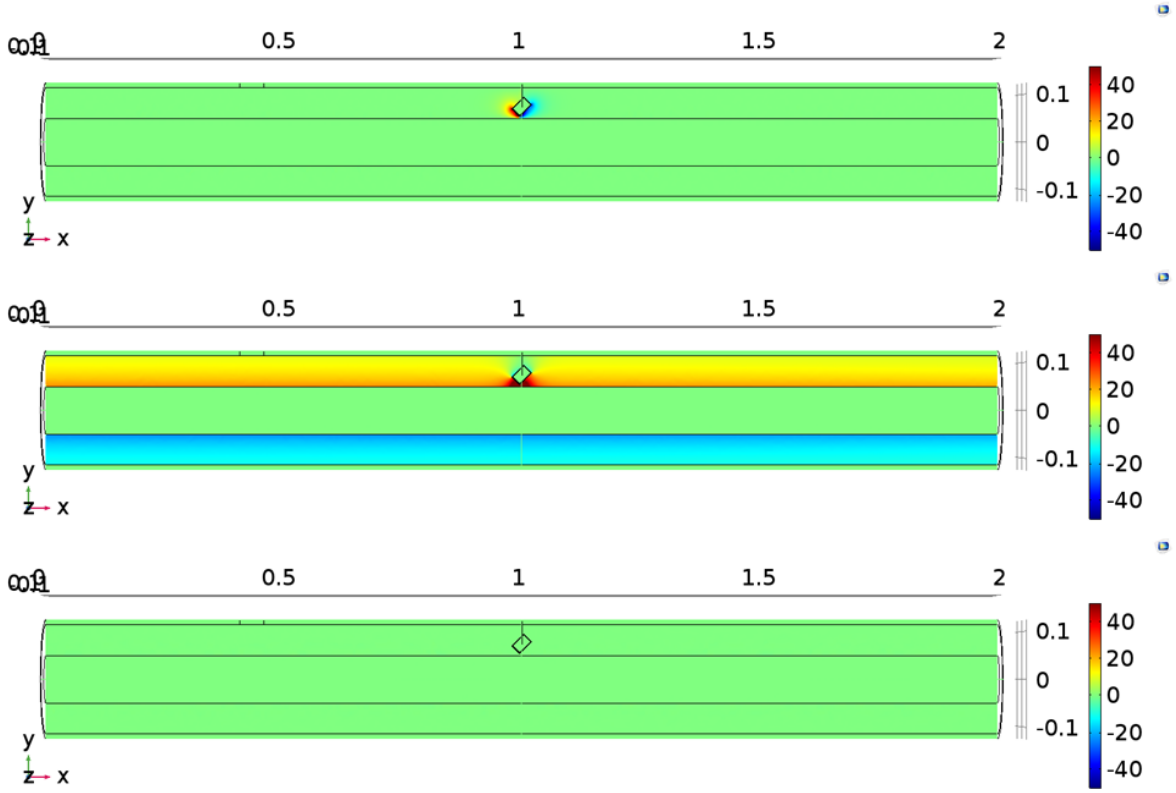

Fig. 4.16. Top to bottom: E_x, E_y, E_z [V/m].

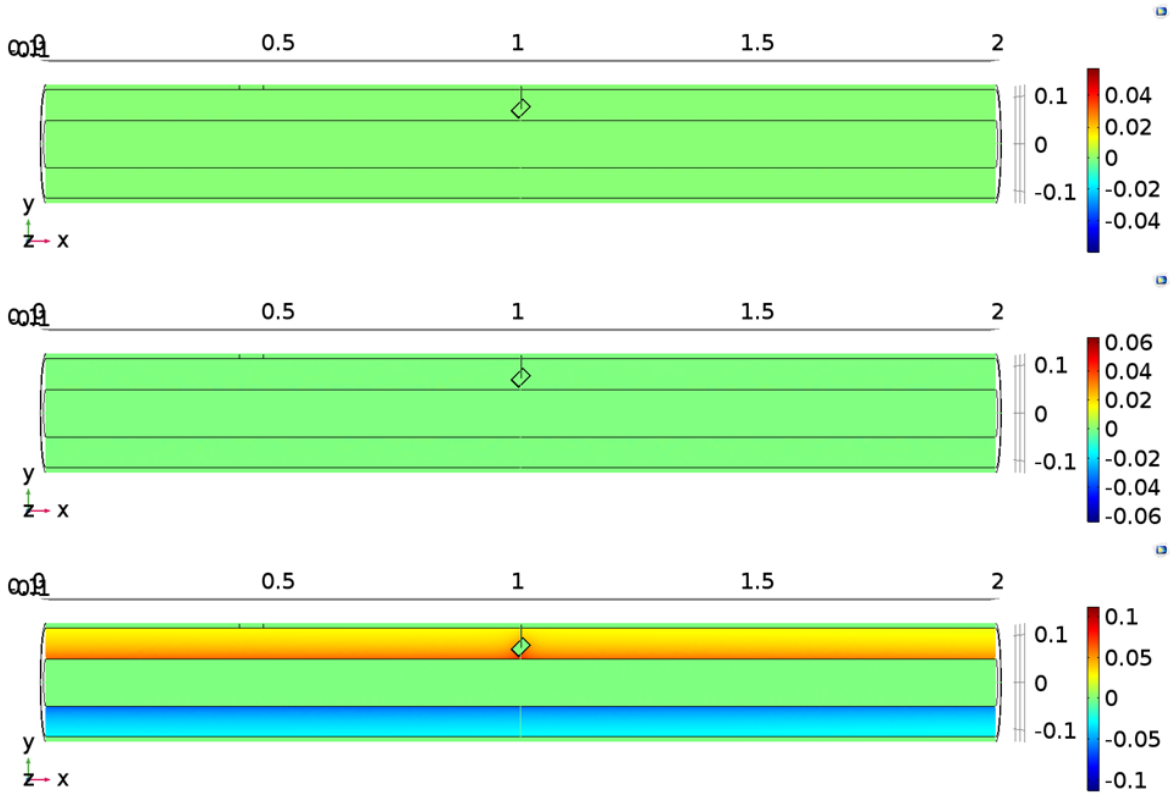

Fig. 4.17. Top to bottom: H_x, H_y, H_z [A/m].

To examine the dependence of the field disturbance on the frequency, a comparison for 5, 11.76 and 20 MHz was performed. Differences in the fields values observed are minor. A change in probe rotation in the x-y plane could cause some difference in the field distributions in the vicinity of the probe. However, for angles 25 and 65 degrees, taken for a test, no major difference compared to 45 degrees was observed.

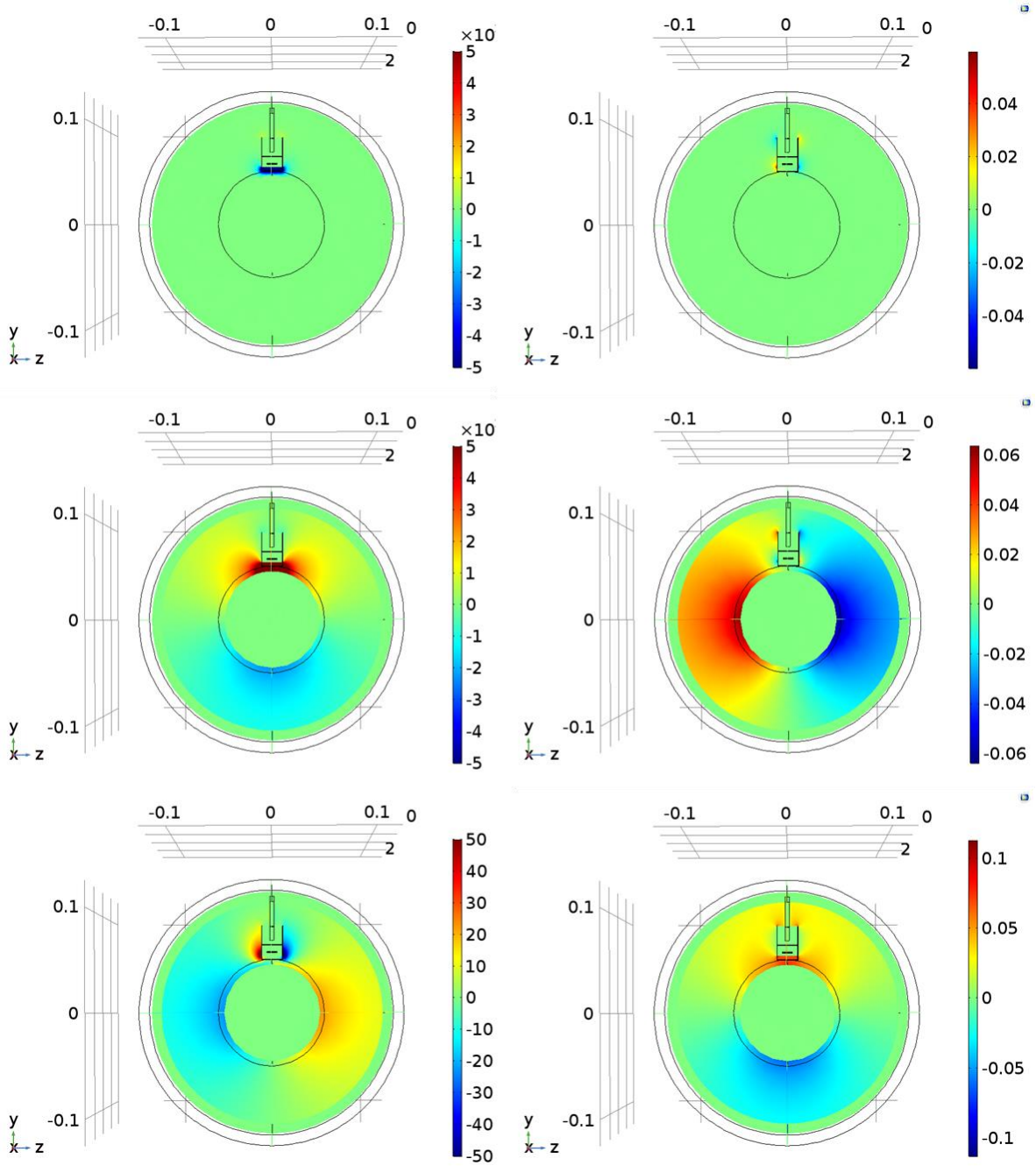

Fig. 4.18. Left, top to bottom: E_x, E_y, E_z [V/m]. Right, top to bottom: H_x, H_y, H_z [A/m].

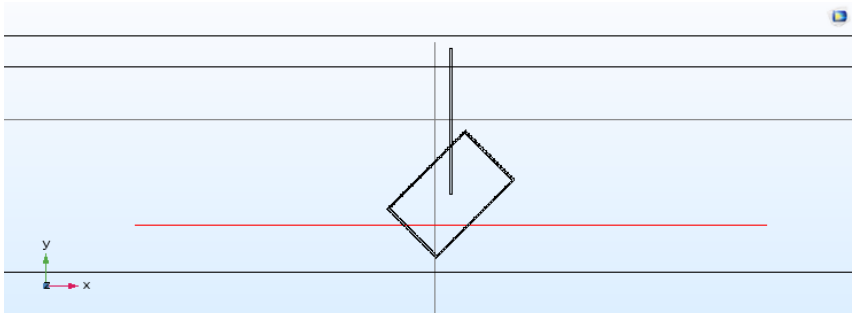

Fig. 4.19. Line in the x direction along which the field disturbance is characterized.

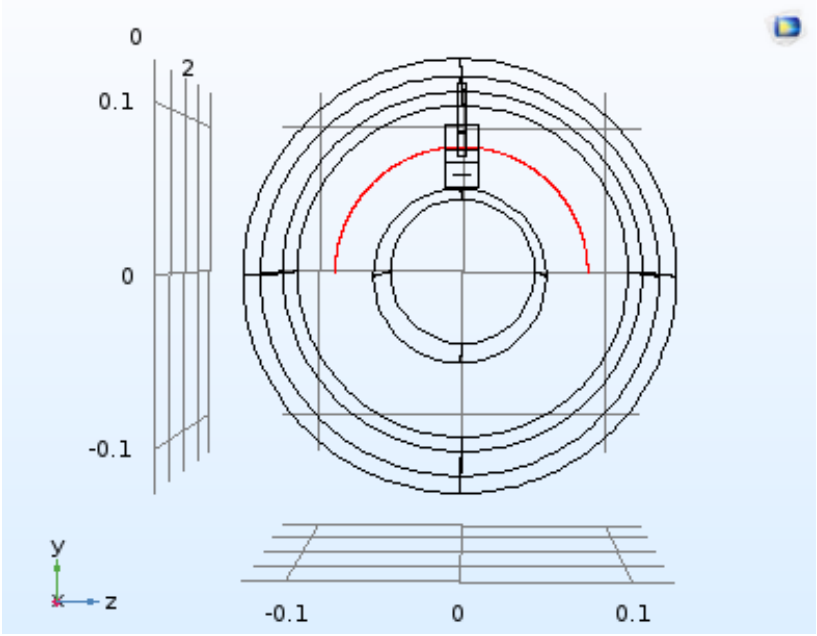

Fig. 4.20. Line in the φ direction along which the field disturbance is characterized.

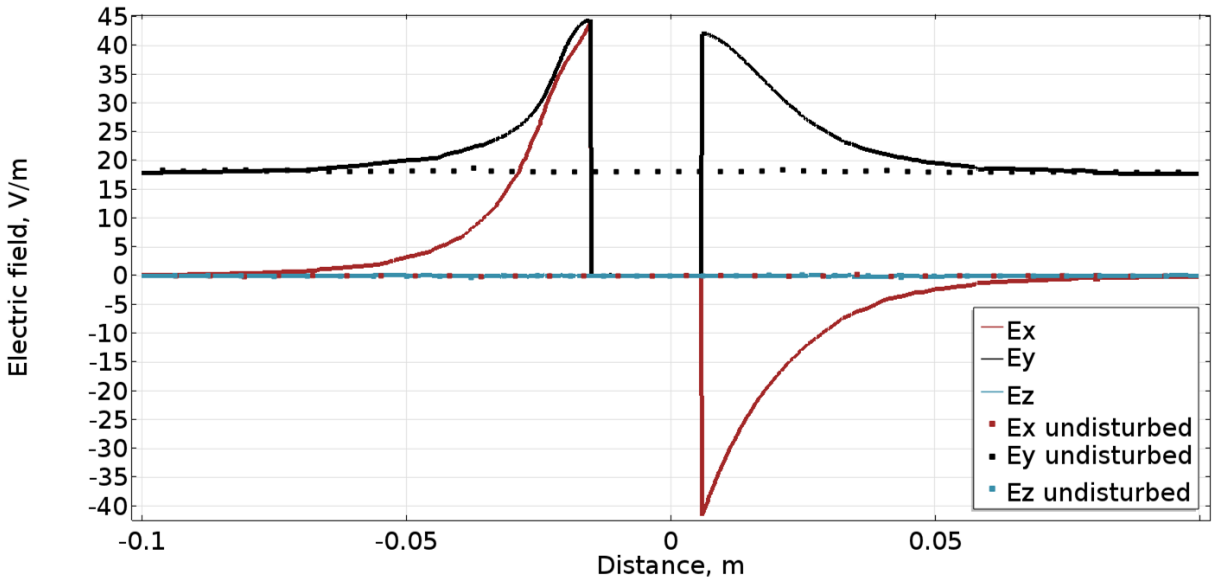

Fig. 4.21. Electric field disturbance along x.

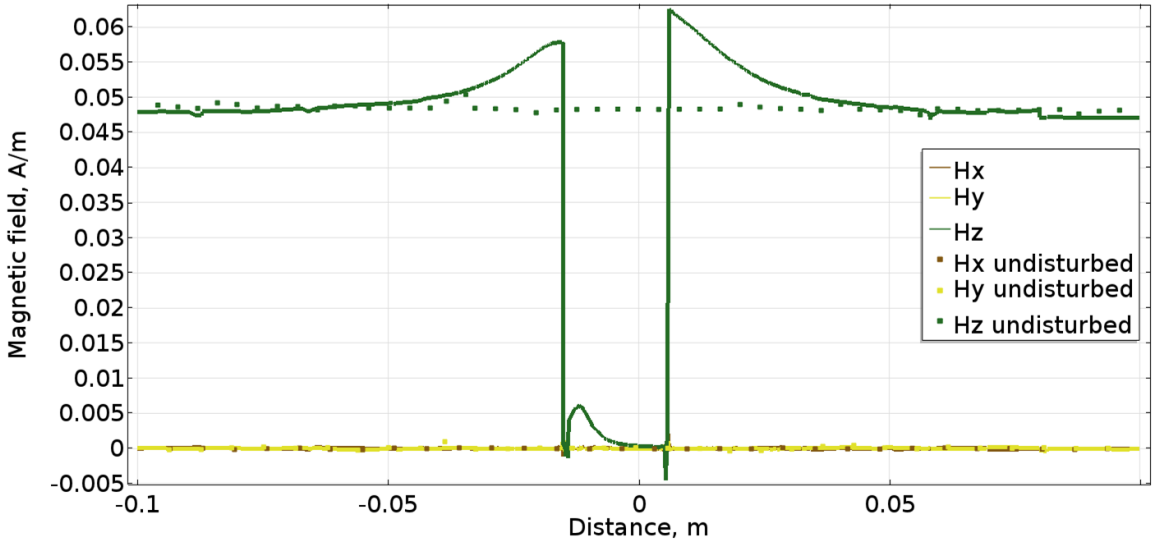

Fig. 4.22. Magnetic field disturbance along x.

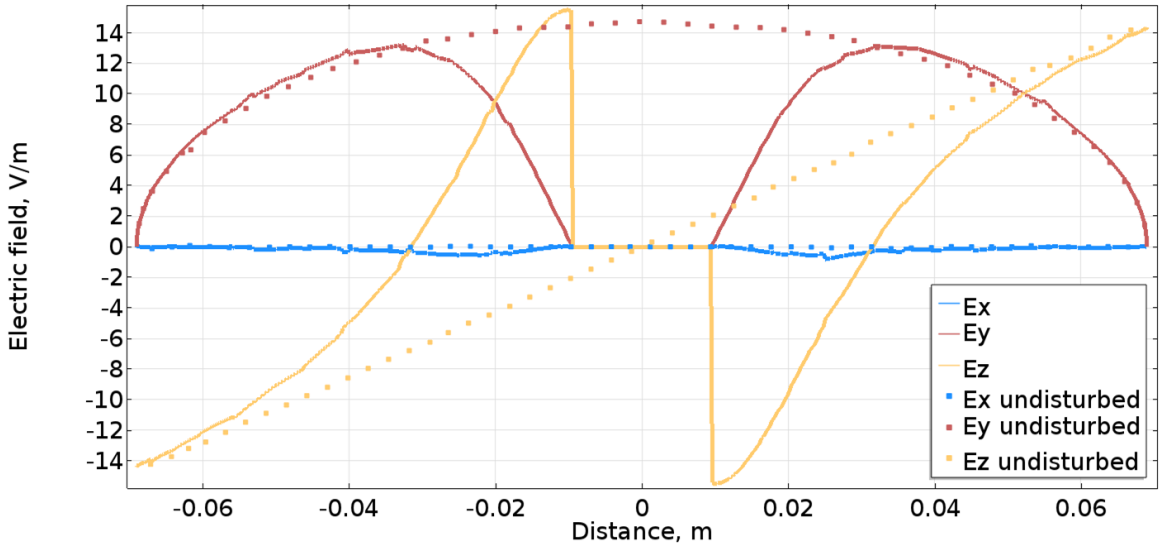

Fig. 4.23. Electric field disturbance along φ.

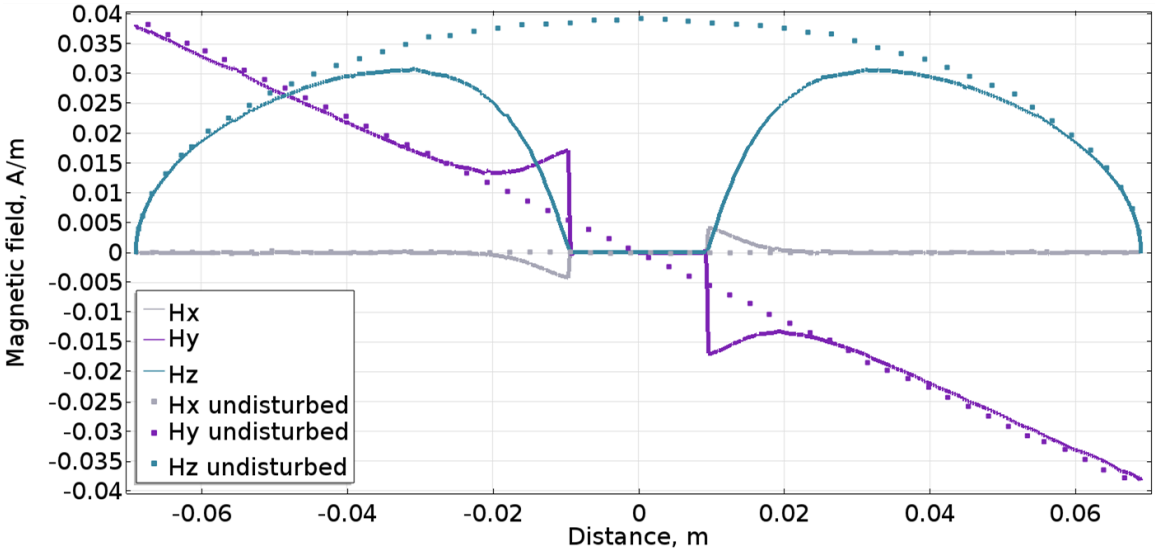

Fig. 4.24. Magnetic field disturbance along φ.

4.2.4 Field evanescence inside a B-dot probe

In a real B-dot probe, immediately after the slit (2 mm from outside) a vacuum-compatible inductor is placed (7 mm outer diameter). By measuring a signal from the inductor, one can evaluate the magnetic field inside the inductor volume. Since the field in that area is non-uniform, the calculated result shows only a value of the magnetic field averaged over the inductor volume. In the COMSOL simulations, the measurements of the magnetic field are represented by the average value of the field inside a cylinder that is placed at the same location where the inductor is situated in an experimental B-dot probe.

Here the same configuration as in the previous section is studied: a B-dot probe at an angle of 45 degrees to the main axis of the coaxial transmission line (Fig 4.14). In Fig. 4.25 radial profiles of H_z are compared. Two profiles calculated as a cylinder volume average are displayed, one corresponds to the inductor position inside the probe, and the other one is a cylinder of the same size placed far from the probe along the coaxial line (0.5 m). The second one shows undisturbed field averaged in a volume. At the same x location the undisturbed field value is plotted as a function of the radius. It is seen that the volume average of such a small cylinder does not show any noticeable deviation from the field along the radial line. The theoretical radial dependency is calculated according to (4.2) and it is in a good agreement with the simulated undisturbed field. The points taken from the volume average inside the probe lie on a curve which has a shape similar to the curve of the undisturbed field. The difference in the absolute values corresponds to the field attenuation (and disturbance) and is equal to 50.9.

These modelling results provide an idea of how big the evanescence of the measured field inside the B-dot probe is. The large coefficient of the attenuation obtained from the simulation (almost 2 orders of magnitude) highlights the fact that measurements with such a probe can be done only when the field outside of the probe is strong enough.

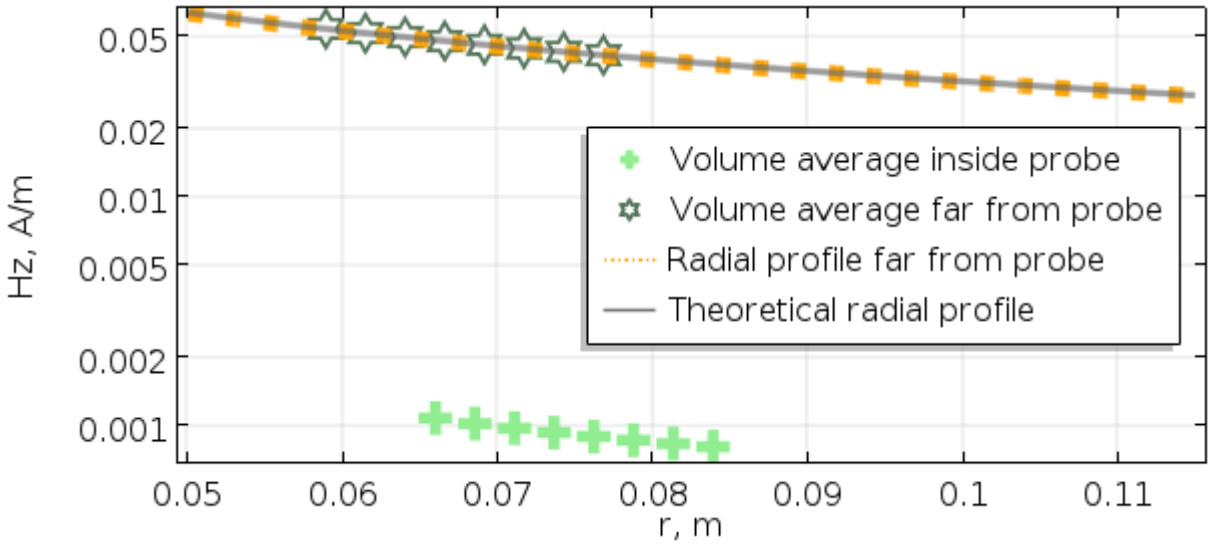

Fig. 4.25. Radial profiles of H_z on logarithmic scale.

4.3 Experimental magnetic field of the IShTAR ICRF antenna waves

In vacuum (or air) the waves of ICRF frequency in tokamaks (25-100 MHz) have wavelengths of several meters (3-12 m). The IShTAR ICRF antenna is routinely used at a frequency around 5-6 MHz (with variations for fine adjustments of coupling), which means λ = 50-60 m. Both for the tokamaks and for IShTAR it means that no propagation occurs in vacuum, since the vacuum chamber sizes are smaller than the wavelength. The plasma has dielectric properties different from the vacuum which leads to much smaller wavelengths and allows the radio-frequency waves to propagate. In some conditions the waves are electromagnetic, as in the fast wave mode of the ICRF waves that propagates to the hot core plasma and heats the plasma particles. In other conditions the wave can be purely electrostatic, as was shown for the slow wave in the example in Section 2.1.3. In the electrostatic wave the magnetic component of the wave is present as well, but in the evanescent form.

In IShTAR the only propagating component - the slow wave - is electrostatic for the whole range of IShTAR operation. Both in vacuum and in plasma the magnetic component of the wave is evanescent. The magnetic field emitted by the ICRF antenna in IShTAR was measured with an array of B-dot probes [Usoltceva2017]. 4 probes were positioned on the manipulator in front of the antenna at the same radial position at 10 cm distance (enough to avoid cross-disturbance), and a scan of the radial position was performed with the manipulator. The experimental setup is shown in Fig. 4.26.

The first thing that should be noted before proceeding to the experimental results is that there is more than one radio-frequency antenna in the experimental setup. The helicon antenna situated in the small chamber and dedicated to start a discharge also emits RF waves. Its presence complicates the task of ICRF antenna magnetic field measurements and its contribution must be taken into account. In order to distinguish the magnetic fields of the two antennas, following scenarios have been studied:

a) Plasma with the helicon antenna only.
b) Plasma with the ICRF antenna only (since this antenna is not designed to ignite plasma, only a weak plasma is produced).
c) Plasma with both antennas simultaneously.

Experimental results (Fig. 4.27) reveal the evident superposition of the two antenna fields. In the range of positive values of radius (farther away from the ICRF antenna) profiles of H_z for all 4 probes have a similar shape on two plots: Fig. 4.27c, which is for the case with two antennas, and Fig. 4.27a, which shows the case with helicon antenna only. In the vicinity of the ICRF antenna (negative r) measurements demonstrate the impact of the ICRF antenna field on the resulting signal. A significant rise of signal towards the ICRF antenna, similar in shape to that observed in Fig. 4.27b, is especially well seen for the two central probes. The H_z here are not absolute values, the calibration from the previous section could not be applied here because the calibration doesn't exist for the case when the signal is a mixture of 2 frequencies, so it was decided to plot all three graphs in similar arbitrary units to be able to compare them, but without the absolute calibration.

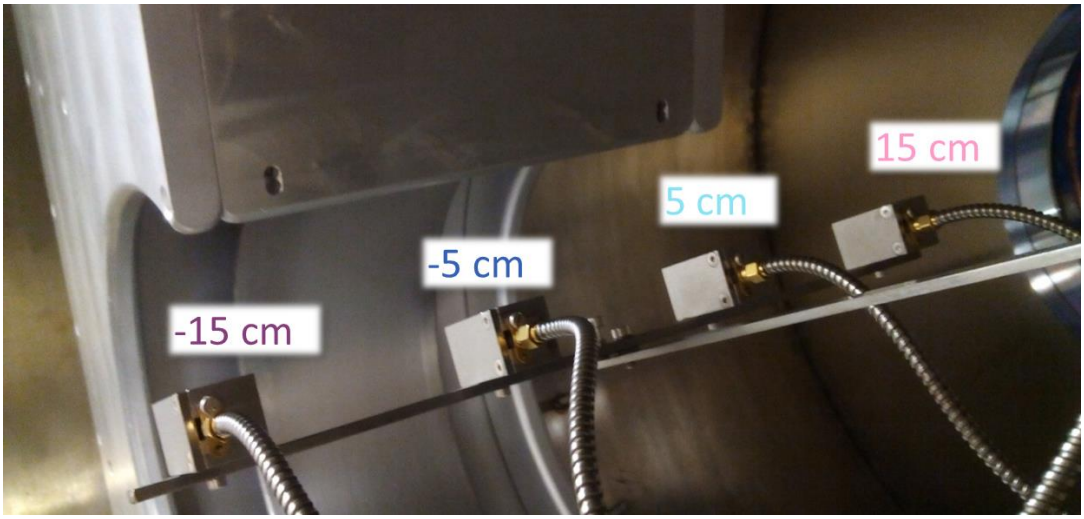

Fig. 4.26. Probe array on a manipulator in front of the ICRF antenna inside IShTAR.

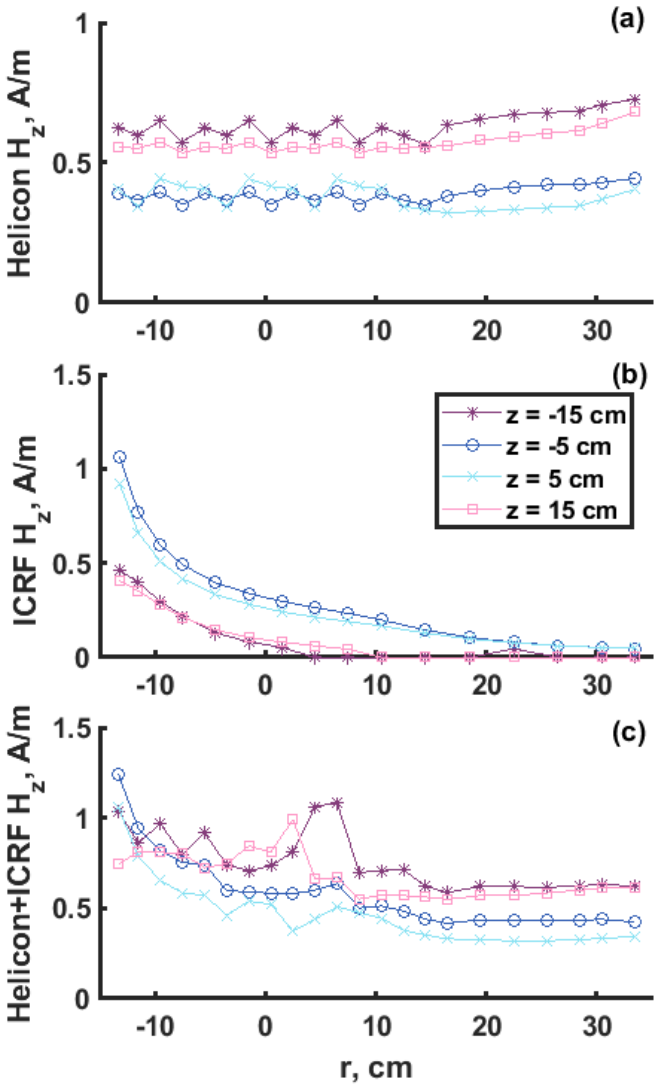

Fig. 4.27. Experimental $H_z(r)$ of: (a) helicon antenna, (b) ICRF antenna in plasma, (c) helicon and ICRF antennas together.

4.4 COMSOL model of IShTAR with vacuum

A realistic geometry of all in-vessel parts (including ICRF antenna, manipulator and probes) has been built in COMSOL Multiphysics®. Fig. 4.28a is a view on the ICRF antenna without a side wall: the antenna strap, the whole antenna structure and the feeding coaxial transmission line can be seen. In the background the small chamber is visible. It can be compared to the picture taken inside the experimental chamber, where some of the antenna walls are also removed to provide a view inside (Fig. 4.28c). The probe array on the manipulator is shown closer and from the front direction in Fig. 4.28b.

The IShTAR COMSOL model also includes the small vacuum chamber made from quartz glass which is transparent for the RF waves, the helicon antenna around it (modelled as a metallic tube which is not excited to emit waves) and some ports with glass windows (Fig. 4.29). Since some power can go outside IShTAR and be lost in the surrounding space, in the model it is represented by vacuum around IShTAR which is then surrounded by a closed rectangular box of the PML material (a part of it is removed in Fig. 4.29 to not obstruct the view). No big radiation is expected outside of IShTAR in the experiments, only a small amount in the form of evanescent waves.

The RF Module makes it possible to model the vacuum electromagnetic field of the IShTAR ICRF antenna. In vacuum, an RF wave of 5.22 MHz propagates in the coaxial transmission line and then becomes evanescent, causing very small fields inside the IShTAR chamber and only tiny fields going outside and reaching PML. As an example the magnetic field distribution on a logarithmic scale (log of A/m) is plotted in Fig. 4.30 (electric field looks similarly). It can be noticed that the strongest fields are located around the end of the coaxial line, as well as around the strap, especially between the strap and the back wall behind it. Similar field distribution have been observed in experiments when the ICRF antenna was powered without the helicon antenna plasma and it created a very-low-density plasma in which the evanescent wave structure resembles the vacuum case.

The magnetic field measured by a B-dot probe is represented in the simulation as an average field inside a cylindrical volume at the position and of the size of a real inductor used in a probe. Radial profiles of H_z at 5.22 MHz (arbitrary units) for the 4 probes (Fig. 4.31) have the same shape in the experiment and in the modeling. Due to a perfect symmetry of the ICRF antenna and the probes in the model, the results for the two outer and two central probes are identical, which is similarly reproduced in the experiment. Absolute values do not play any role here, since they are fully dependent on the amount of injected power and the matching system parameters. This can be always varied in the simulation, if needed.

Since a simulation of electromagnetic field in COMSOL gives all components of the field at any geometrical point, both the magnetic and the electric fields are thus known at any required position. H_z and E_z in front of the antenna are calculated on the plane in which the manipulator moves (shaded in Fig. 4.32) and plotted as examples in Fig. 4.33 and 4.34. The white spots on the plots correspond to the cross-section of the antenna strap, the limiters and the back wall behand the strap.

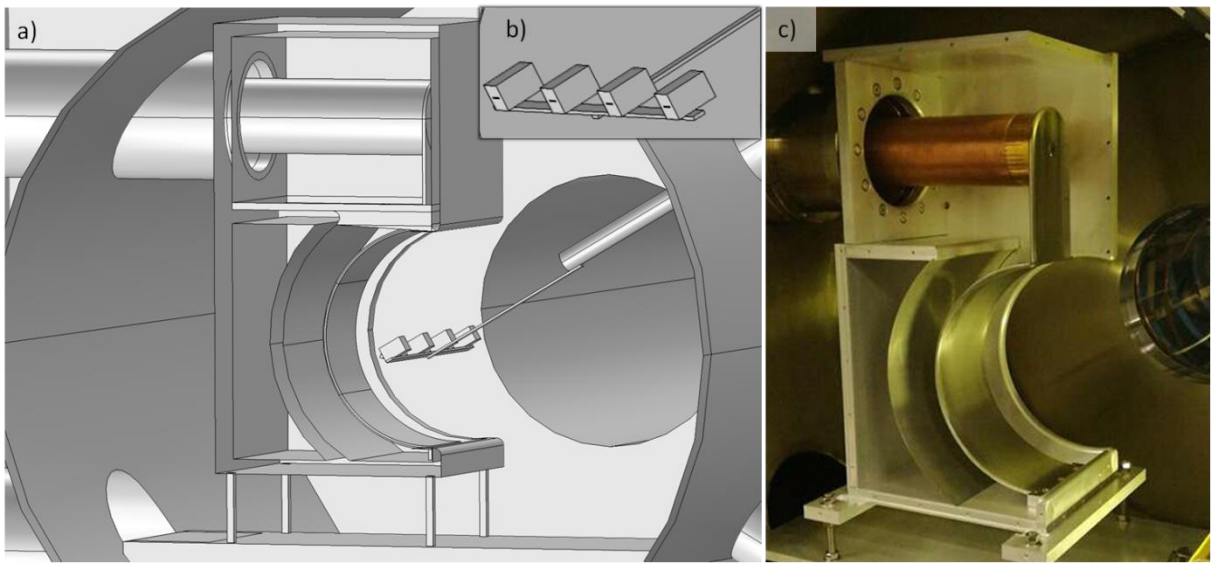

Fig. 4.28. (a) IShTAR model main components: ICRF antenna (side wall removed), manipulator and probes, (b) B-dot probe array on the manipulator (zoomed-in), (c) picture taken inside IShTAR.

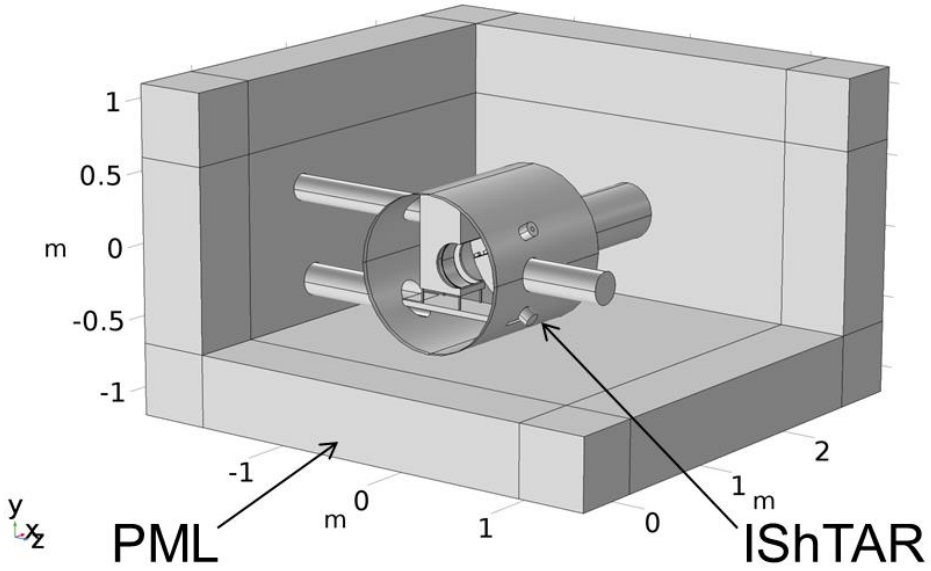

Fig. 4.29. View of the full IShTAR model, with surrounding PML.

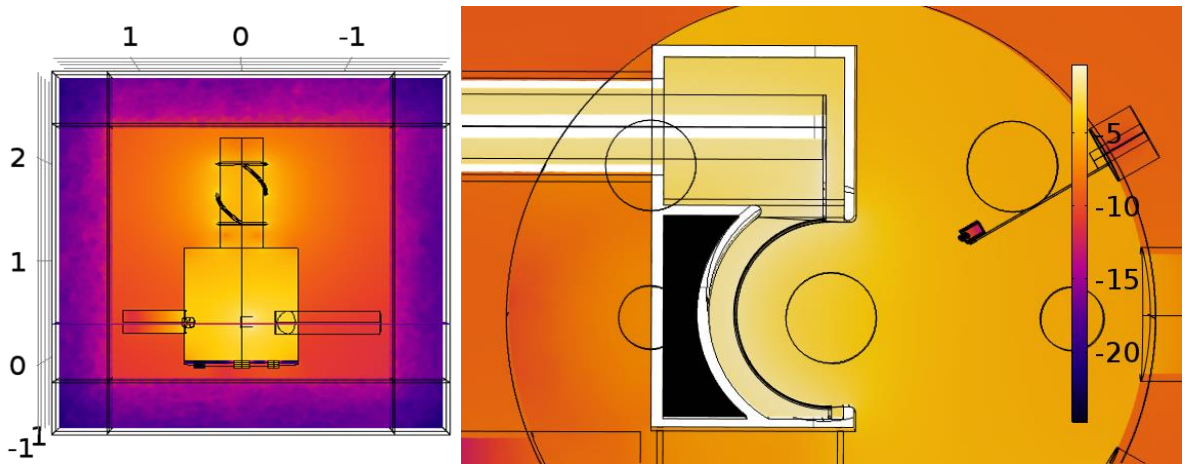

Fig. 4.30. Magnetic field of IShTAR ICRF antenna in vacuum in log scale:(a) top view, (b) side view, zoomed.

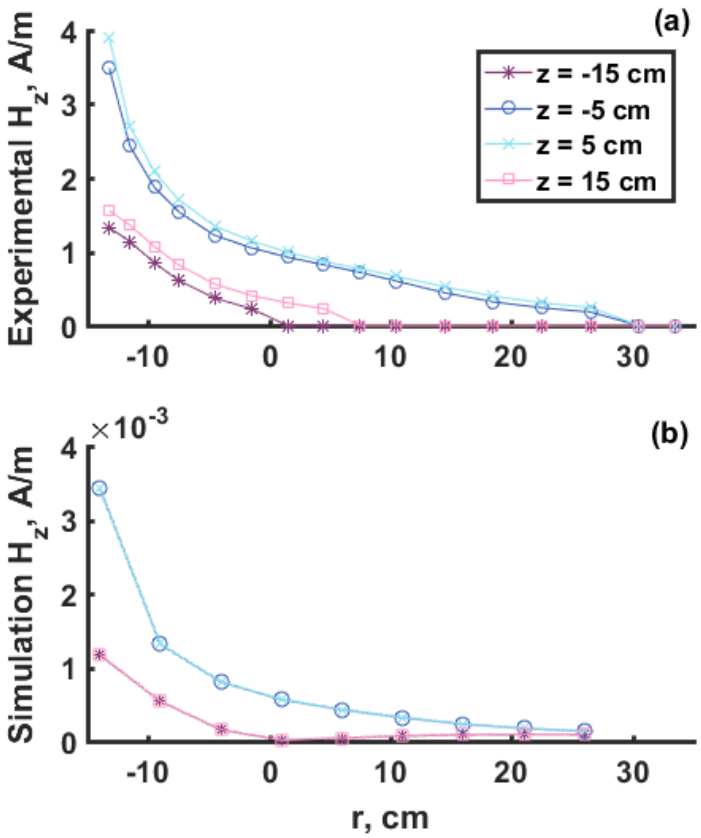

Fig. 4.31. $H_z(r)$ in vacuum: (a) measured in experiment, (b) calculated in simulation.

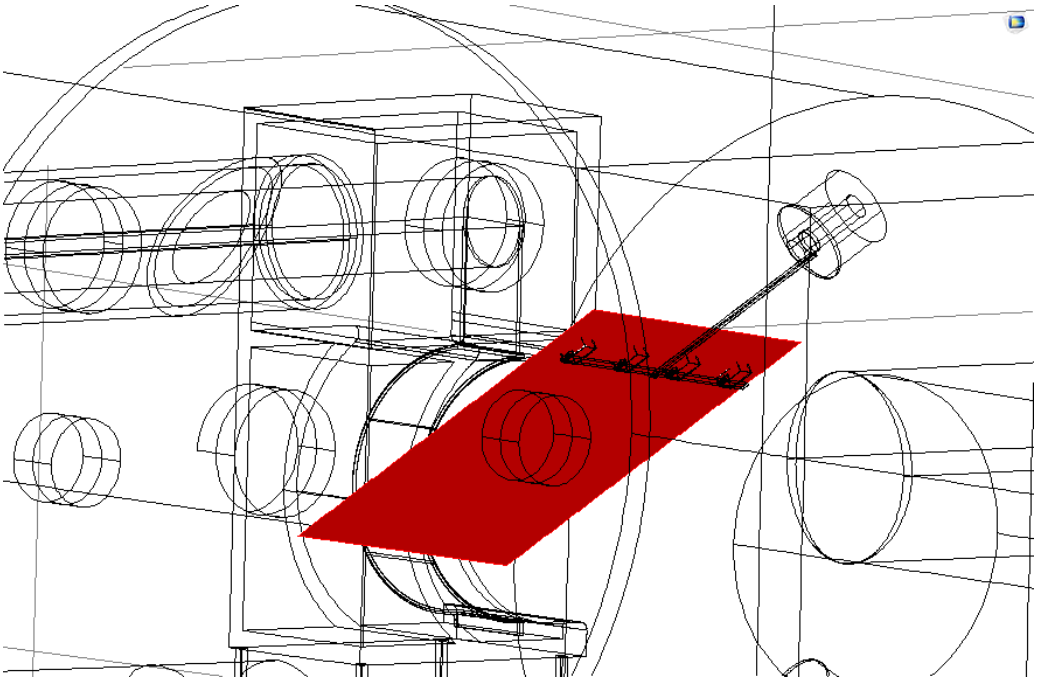

Fig. 4.32. The plane of the radial movement of the manipulator.

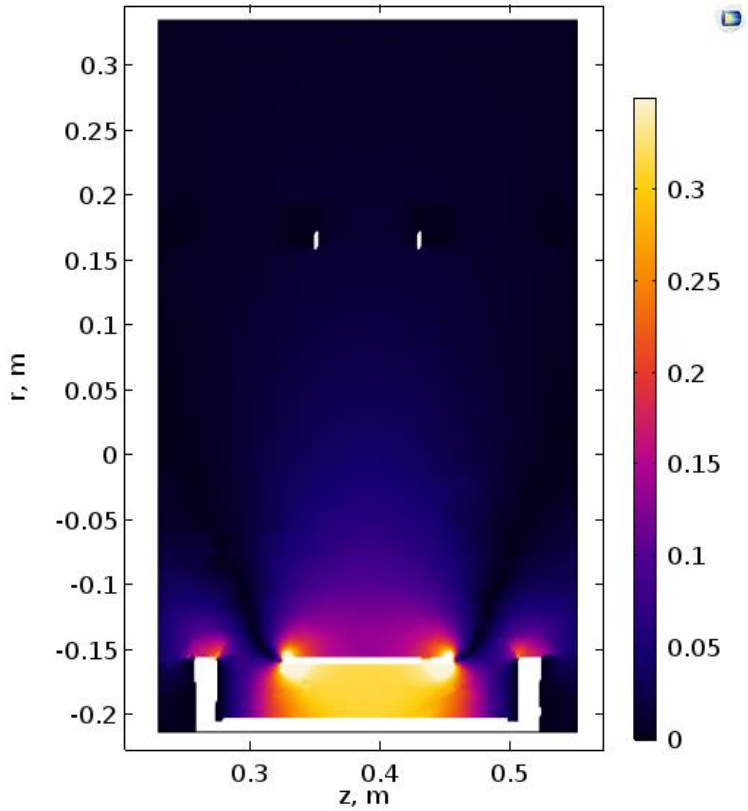

Fig. 4.33. Calculated 2D distribution of Hz (in A/m) in front of the ICRF antenna in vacuum.

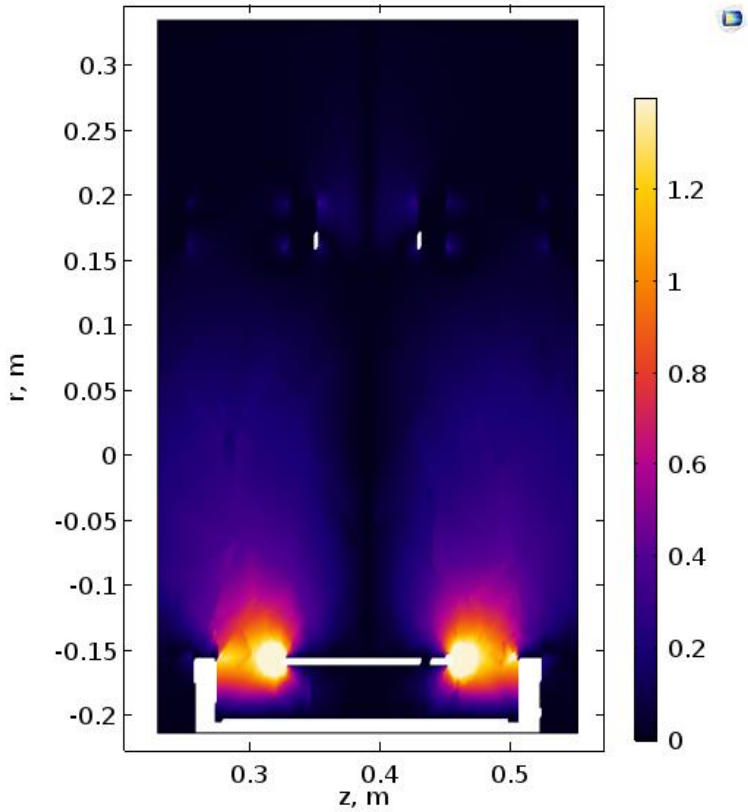

Fig. 4.34. Calculated 2D distribution of Ez (in V/m) in front of the ICRF antenna in vacuum.

4.5 3D modelling of the slow wave

A common problem attributed to the numerical simulation of the ICRF slow wave is the task of finding a solution in the vicinity of the Lower-Hybrid resonance. Very high perpendicular wavenumber (Fig. 2.1, Fig. 4.3) leads to extremely short wavelength that is reported to be a challenge to resolve in a numerical model [Crombe2014], [Lu2016Thesis]. At least 10 mesh elements per wavelength are needed normally to achieve sufficient convergence of the computations. Calculations on such a fine mesh are impossible with the present-day computers. With a coarser mesh the calculation either doesn't converge or results in a solution with artifacts that depend on the mesh size, as was shown for example in [Lu2016Thesis].

The true solution of a wave equation in plasma with radially varying density needs to be integrable in order to be able to justify the correctness of a numerical solution, which is not the case when a wave propagates through the region of the LH resonance. In this section it will be shown that the specific shape of the slow wave needs to be considered when discussing a solution near the LH resonance. It can be possible to obtain a solution in a domain where the SW propagates and the density layer corresponding to the LH resonant is present and such an example will be shown below. It can be done if the propagation region (usually very close to the antenna) is resolved correctly and the LH density layer is not directly at the radial location of the antenna, but further away in the plasma. For the simulations shown in [Lu2016Thesis] it is not clear what plasma conditions were present in the vicinity of the antenna strap and whether the correct propagating structure was obtained.

It is crucial in the numerical simulations to distinguish clearly the influence of the numerical noise introduced into the obtained solution. Since the problem with non-resolved wave features and associated numerical noise has been observed in the SW simulations before, in this work a step-by-step approach is adopted for increasing the complexity of the model. It will be discussed at each step what numerical noise is observed and whether a solution can be trusted or not.

4.5.1 Plasma implementation and testing in COMSOL

The simplest possible geometry for the model is a box with one-strap ICRF antenna (Fig. 4.35). The static magnetic field is directed along the z axis and the antenna configuration is typical for tokamaks and for IShTAR: a metallic strap along the poloidal axis (here it is y axis) grounded on the bottom to the box itself and fed with a coaxial 50 Ω line with a port where the wave is excited. The x axis corresponds to the radial direction in toroidal (or cylindrical) plasmas. In this configuration the plasma has a rectangular shape. On the example in Fig. 4.35 there are 3 types of domains with different materials: vacuum, plasma and PML (material in which the waves are damped). The coaxial feed line and the antenna are in vacuum. A plasma layer is in front of the antenna strap. Around the vacuum and plasma domains the PML layers are located. The domains varied in the simulations according to each task, sometimes only vacuum was used to fill the whole box, sometimes the antenna strap was inserted in plasma, sometimes PMLs were used only on the back and not on the sides, etc. In the first examples the configuration of Fig. 4.35 is assumed, and in the later examples all introduced changes are specified. The dimensions of the domains were changed according to the expected solution (to get realistic picture and to speed up the computation at the same time). On the top and on the bottom no PML was used since the homogeneity along y is expected to be sufficient and $k_y = 0$ can be considered according to the theory in Section 2.1.1.

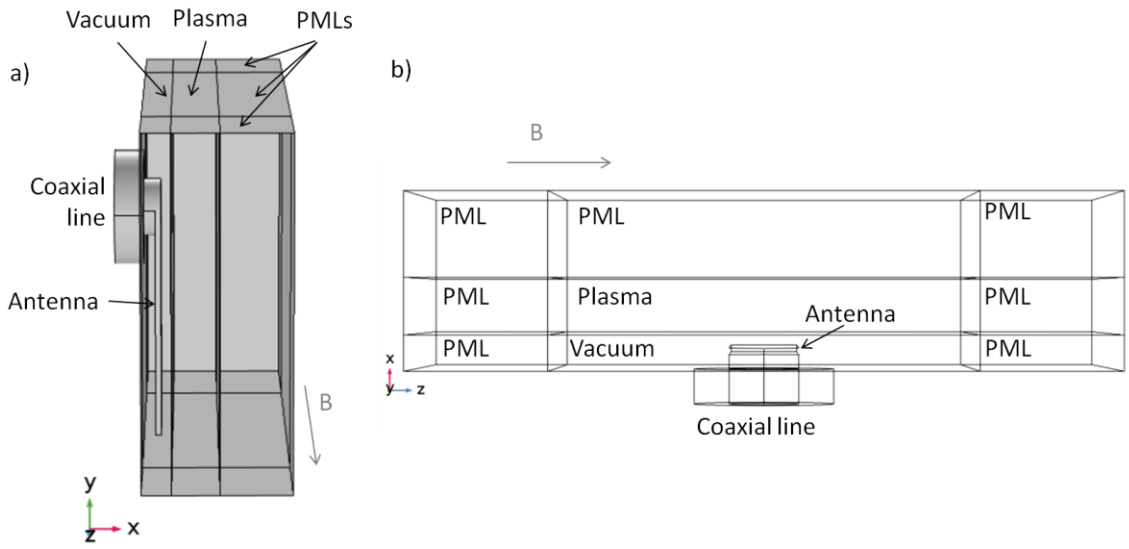

Fig. 4.35. COMSOL model geometry: (a) side view, (b) top view.

In the described COMSOL model the plasma is defined as a custom material with the permittivity tensor (2.6) and the permeability tensor $\bar{\bar{\mu}} = \bar{\bar{1}}$, according to the theory in Section 2.1.1. The PML is implemented as an artificial material. Its permittivity and permeability correspond to the material which the PML is adjacent to; it was either vacuum or plasma in the performed simulations. The form of the stretching functions in PMLs is polynomial and is defined by (2.39). Stretching was applied to the z coordinate in the side PMLs, to the x coordinate in the back PML and in the corner PML regions both the x and z coordinate were replaced by stretched coordinates.

The model was first tested with parameters typical for RAPLICASOL, the numerical tool that simulates fast wave propagation in the high-density plasma (details in Section 2.3.1). For the conditions characteristic for the ASDEX Upgrade tokamak (gas – D, frequency – 36.5 MHz, magnetic field – 2T), the elliptical fast wave mode structure is reproduced successfully in the model as shown in Fig. 4.36a (in all following figures E_x is plotted, unless other is specified, and all sizes are in meters). The antenna in this model is in vacuum and it can be seen that the propagation starts only in the plasma domain. The density in the plasma is constant n = 10^{20} m^{-3}, and equation (2.18) gives for this density: $k_\perp$ = 20.46 rad/m, so the wavelength is λ = 0.215 m. This is confirmed in the simulation, as well as the wave polarization: 56 % of E_x^2 and 44 % of E_y^2. The side view reveals quite good homogeneity of the field along y direction in plasma (Fig. 4.36b). However, it can be seen that periodic blobs of the size of the mesh appear on the vacuum-plasma interface. Their size changed when the simulation was performed on a finer mesh and remained equal to the mesh size. In this simulation the blobs do not introduce significant disturbance into the propagating wave fields. During the RF phase sweep the blobs move vertically along the vacuum-plasma interface but they cause no considerable propagating noise in the x and z directions. They are thought to be a numerical consequence of the sharp density jump from vacuum to plasma and a similar effect was also observed in RAPLICASOL FW simulations (not published).

There are 2 types of PML in this simulation: vacuum PML on the sides near the vacuum layer and plasma PML around the plasma domain. The coefficients of the stretching functions were the same in both PMLs and were chosen according to the guidelines in [Jacquout2013Thesis]: $S_x' = S_z'$ = 1, $S_x'' = S_z''$ = -2, $p_x = p_z$ = 2, suited for a forward wave (the FW mode is a forward wave). It can be

seen that wave damping is efficient enough with the chosen PML size. Successfully tested model including the plasma and the PML is accepted for further simulations of the slow wave mode. All simulations of the SW are done at f = 6 MHz and in Ar.

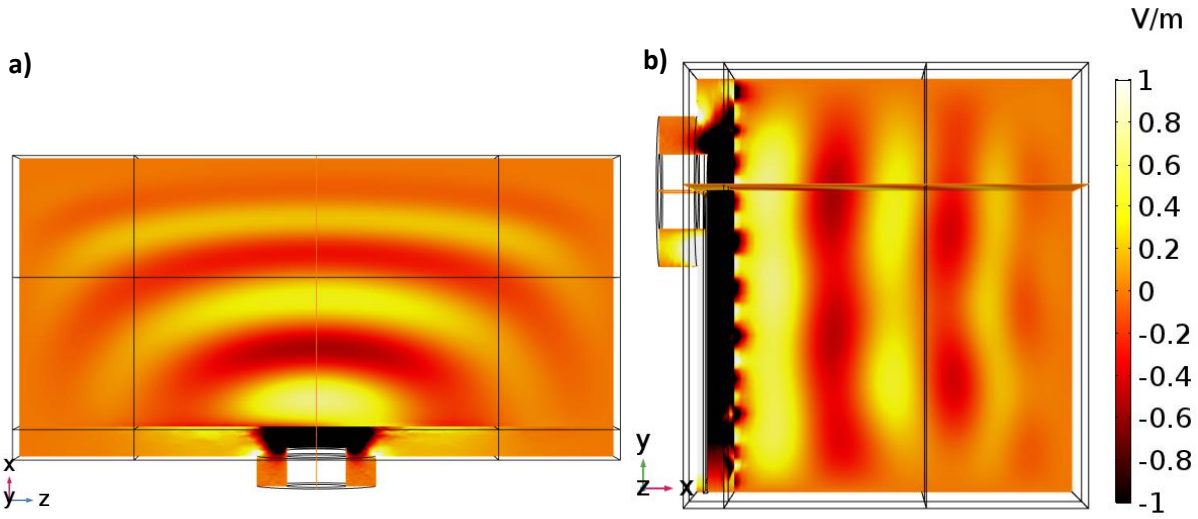

Fig. 4.36. Test of FW propagation, E_x is plotted: (a) top view, (b) side view.

4.5.2 Results with antenna in vacuum

A defining characteristic of the slow wave is the shape of the wavefront. From the hyperbolic form of the wave equation it follows that the slow wave propagation is restricted to a specific region - the resonance cone (RC), as was explained in Section 2.1.4. An example of it is shown in Fig. 4.37. The wave vector $\boldsymbol{k}$ in a resonance cone wave is directed perpendicularly to the cone front. The electric field polarization in this electrostatic wave can be found very simply from (2.29): $\boldsymbol{E}$ is parallel to $\boldsymbol{k}$. In Fig. 4.37a the strap is in vacuum and the cone appears in the plasma domain and stretches out at a nearly constant angle, because the density is varied very slowly (linearly) in the x direction (along y and z the density is constant in all simulations) in a small range: n = 6*10^{11}–10^{12} m^{-3} growing towards positive x. The density assigned in the front PML is equal to the density at the plasma/PML edge. In the side PMLs the density is the same function of x as in the plasma domain.

For n = 6*10^{11} m^{-3} equation (2.19) yields: $k_\perp$ = 12.24 rad/m. Since $k_\parallel$ = 20.93 rad/m, $\boldsymbol{k}$ should be directed at an angle

$$\alpha = \tan^{-1}\frac{k_\perp}{k_\parallel} = 30.3° \tag{4.3}$$

to the magnetic field (z axis). The modelling result in Fig. 4.37a shows excellent agreement with this value. For n = 10^{12} m^{-3}: $k_\perp$ = 23.3 rad/m, so the angle is around $45°$ which is also observed in the plot.

In Fig. 4.37b the RC direction changes much faster with the x coordinate. In this case the density profile is exponential: n = 6*10^{11}–5.4*10^{16} m^{-3}. The growing density leads to a rapid increase in the $k_\perp$ value (Fig. 4.3), so the vector $\boldsymbol{k}$ shifts towards the perpendicular direction and the cone propagates more to the sides than forward. At the position where the RC enters the side PML the

density is $n \approx 2*10^{13}$ m^{-3}. Weak reflections from the side PMLs outer walls appear in this case, and the reflected attenuated wave tends to be closer and closer to the direction parallel to $\boldsymbol{B}$ as it propagates towards higher density. Some noise also originates from the interface betweem the vacuum and the plasma layers. The reflections should be eliminated in order to get a correct field distribution in the region of the higher densities. For this the PMLs on the sides need to be improved. However, it can be already seen that, if the refections are not taken into account, the field outside of the resonance cone is considerably smaller than that inside the cone. In the present model the E_x near the plasma—front PML interface (at the density near the LH resonance) is around 2 orders of magnitude less than the field in the cone centre. And all other components of the electric field are negligibly small.

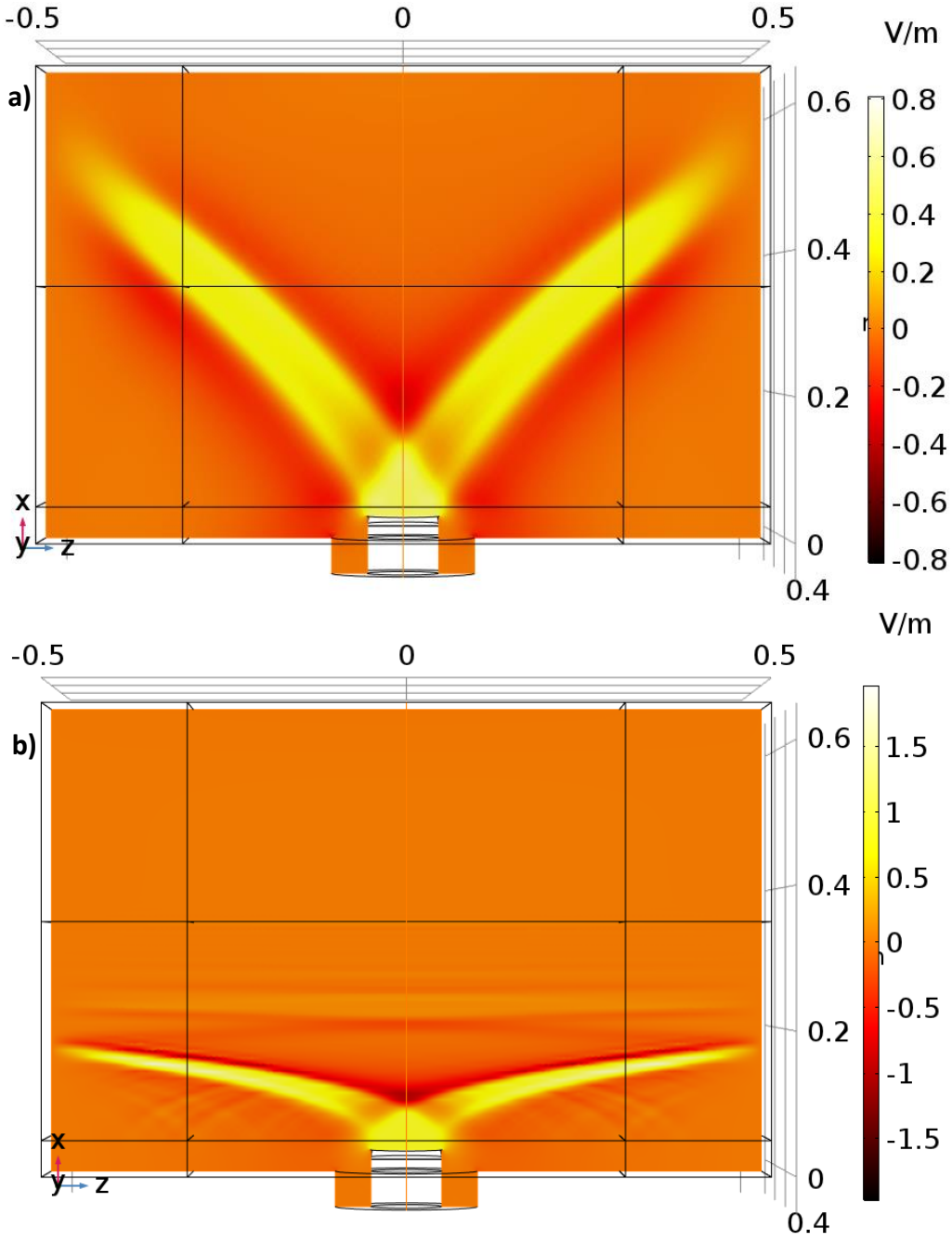

Fig. 4.37. Examples of resonance cone structure: (a) n = $6*10^{11}$–10^{12}, (b) n = $6*10^{11}$–$5.4*10^{16}$ m^{-3}.

The major part of the SW propagation region (Fig. 4.3) corresponds to $k_\perp \gg k_\parallel$, which means that the wave vector is nearly perpendicular, i.e. the RC is nearly parallel to the magnetic field. In order to see such a structure it is necessary to make a step forward in the model and introduce the strap into the plasma. If a vacuum layer is kept between the strap and the plasma, it is still possible to get a solution in some conditions, but the numerical noise on the vacuum-plasma interface, which is negligible for very-low-density plasma (for example $6*10^{11}$ m^{-3} in Fig. 4.37a,b), becomes significant for higher densities. An example is shown in Fig. 4.38-4.39, where the plasma density on the interface with the vacuum domain is n = 10^{15} m^{-3} (the exponential density profile is n = 10^{15}–$1.36*10^{16}$ m^{-3}). The RC is visible (Fig. 4.39) but covered heavily in the other structures which are generated on the border of the vacuum and plasma. It can be seen clearly on the side view (Fig. 4.38) as well. The homogeneity along y is not preserved. The artificial minima and maxima generated on the vacuum-plasma interface propagate further in the plasma in the x-y direction creating a picture which can be very misleading because it resembles a periodic wave structure. However, no waves are expected to propagate in that region, especially waves of this direction and shape, so it is obvious that the observed structure is a pure numerical noise. The size of the structures attributed to the numerical noise agrees with the mesh size (Fig. 4.38b). The RC size in x direction is of the same order as well and it looks poorly resolved.

A realistic density gradient instead of the introduced artificial density jump from 0 to a high value could be applied to approach the experimental conditions and achieve continuous change of the wave properties. A mesh that resolves the density (and wave properties) gradient would result in the numerical noise minimization. On the other hand, when the artificial density jump is present, sufficient resolution of the RC field might reduce the numerical noise in the plasma domain. For the model employed here and with the available computational resources it was not possible to refine the mesh enough to achieve considerably different results with any of the two suggested improvements.

4.5.3 Results with antenna in plasma

This step forward in the model is achieved not without difficulties. Since the fields need to be simulated on a very fine scale in x-direction and there can be field and/or density gradients along 10 mm of the antenna thickness, the precise geometry of the antenna strap starts to play an essential role, as well as the local mesh on the strap.

A simple strap with a perpendicular cross-section is replaced now by a strap with rounded corners and the edges where the strap is connected to the coaxial feeder are also nicely rounded. The mesh is modified as well; the mesh element minimum size is reduced to 0.8 mm and the maximum size to 10 mm in x direction. The mesh is made non-uniform in the 3 directions. The least important axis is y, along which we expect to see no or very little variations. In the direction of the magnetic field (z) the spatial variations of the fields are also much less significant than in x direction. So the mesh size is multiplied by different factors for the 3 direction: 1 - for x, 0.6 - for y, 0.75 - for z. The final mesh is the densest at the antenna strap and contains at least 7 elements along x on the strap.

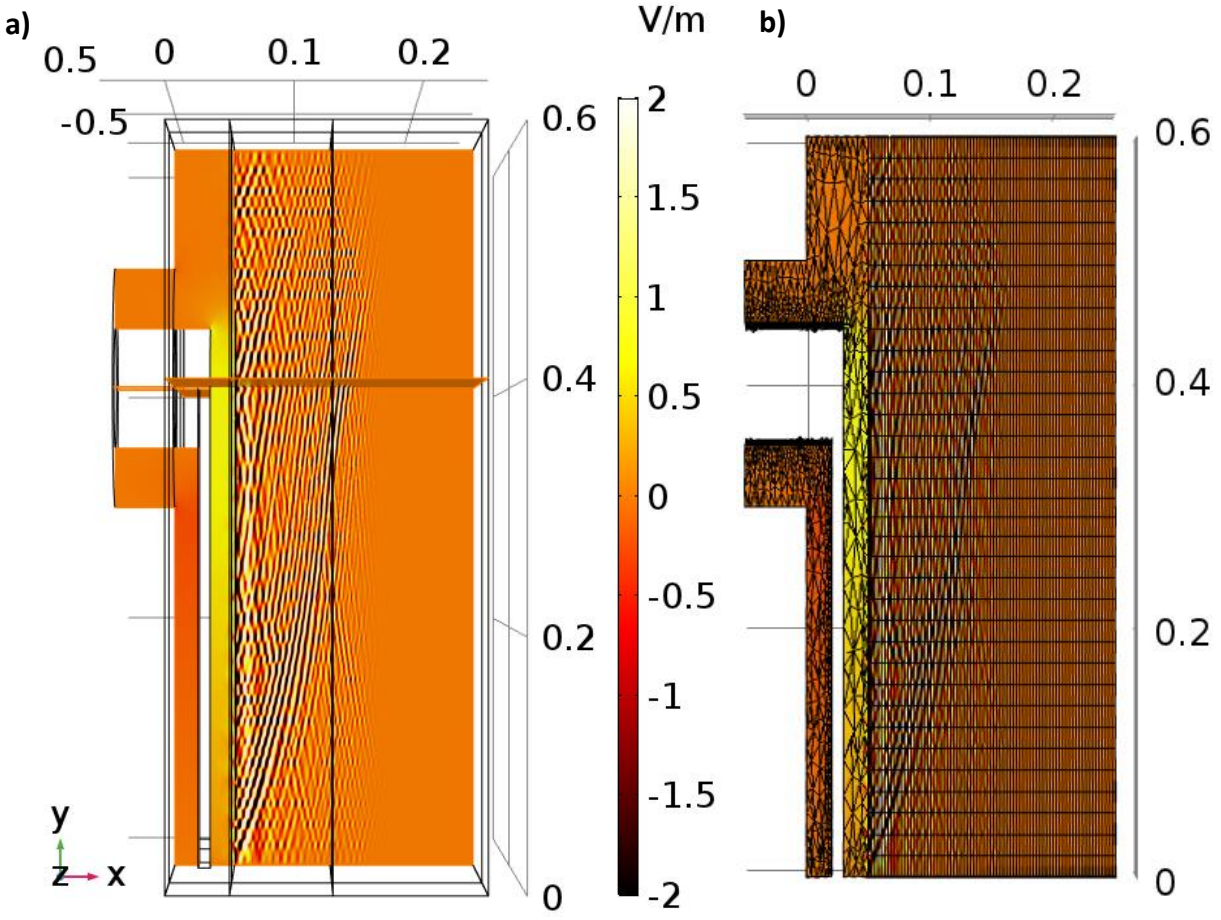

Fig. 4.38. Solution with high level of numerical noise generated at the vacuum interface with plasma: (a) side view, (b) side view with the mesh overlaid.

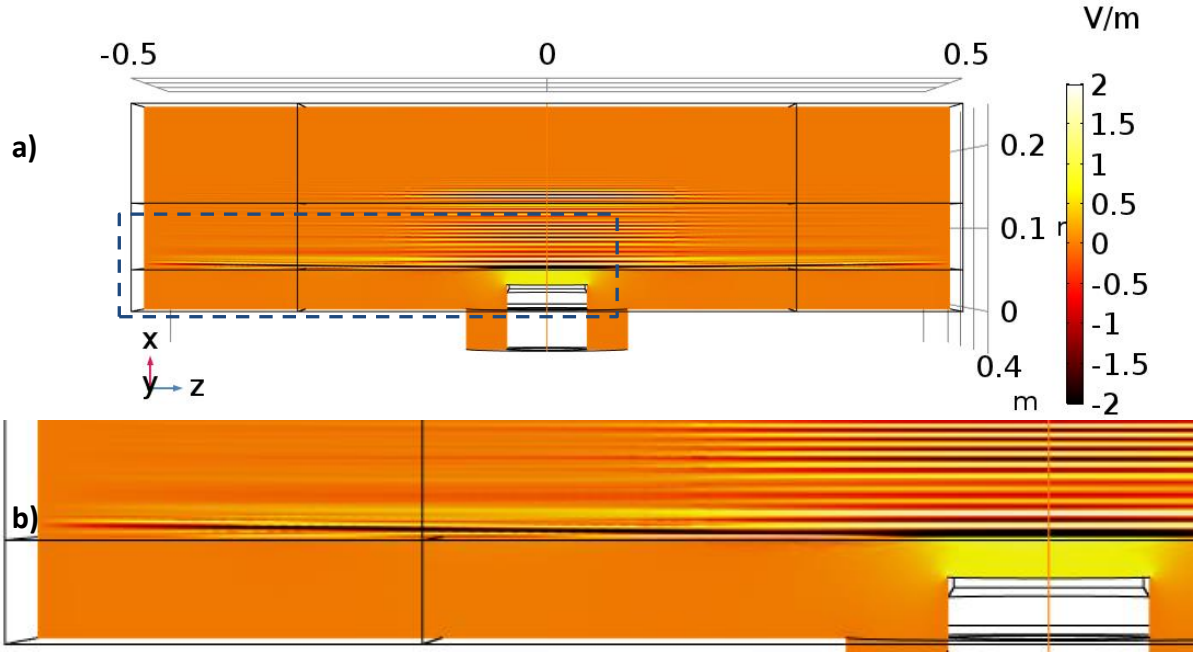

Fig. 4.39. Solution with high level of numerical noise generated at the vacuum interface with plasma: (a) top view, (b) same view zoomed-in on the RC left branch.

A solution with the high plasma density n = 5*10^{15} m^{-3} (constant in the domain) is demonstrated in Fig. 4.40, with the antenna in the plasma. It can be noticed that for this plasma density the RC angle to $\boldsymbol{B}$ is nearly 0. No problem of the artificial periodical structures in the plasma volume occurs, as in Fig. 4.38-4.39. The field near the vacuum-plasma interface is strong but rather homogeneous along y (Fig. 4.40b). It indicates that the resolution of the cone field structure is more critical in this case than the usage of a continuous density profile without an artificial jump. When the RC is resolved and its shape agrees to the theoretical predictions, no noticeable numerical noise is observed.

In all models in Sections 4.5.2 and 4.5.3 the RC carried the wave energy to the front or side PMLs, where it was attenuated and the wave energy was absorbed. The PMLs had to be adjusted for the RC waves and the main difference as compared to the PMLs used for the FW is the sign of the stretching function coefficient S''. It is negative for the forward FW, but should be positive for a backward wave, according to [Jacqout2013Thesis]. Since the SW is a backward wave, it was attempted to change the sign for both S_x'' and S_z'' to the opposite. However, it resulted in the non-physical negative energy absorption in the front and side PMLs. Therefore the coefficients were changed back to the negative values in order to get positive power dissipation. The proposed explanation is following: for the side PMLs (and front PML in Fig. 4.37a) the RC wave is not seen as a backward wave, but as a forward wave, so the sign has to be negative; for the front PML the absorbed power corresponds not to a propagating SW wave (because it does not propagate forward), but to an evanescent FW which is simultaneously excited and carries part of the energy in the forward direction, that is why the sign of the front PML should be as for the FW. It is confirmed in a simulation where the plasma domain is filled with vacuum and no propagation occurs: the absorbed power distribution in the front PML is identical and it can only correspond to an evanescent wave. A comparison is shown in Fig. 4.41 (the range is cut significantly in all absorbed power plots to highlight the regions of power dissipation). The amount of energy carried by the FW to the front PML is quite big for models like in Fig. 4.40, because the plasma domain has to be narrow in x direction in order to have a fine mesh in the plasma and a long enough propagating region along z. On such a short distance x the FW doesn't decay much.

4.5.4 Results with collisional losses

What happens in a real device at the location of the side PMLs? If a resonance cone wave meets a metallic wall perpendicular to $\boldsymbol{B}$, it will be reflected and it will continue to travel until it gets reflected again and again (Fig. 4.42). For a RC at a very small angle to the magnetic field the reflection would happen nearly perpendicularly and the cone fronts would overlap with the reflections with very small shifts in x direction. Such wave concentration in a narrow spatial location cannot be resolved numerically. Attempts to remove the side PMLs and to obtain a solution with the wave reflection from the side walls in relatively high-density plasma (> 10^{14} m^{-3}) failed.

A high-density plasma model without side PMLs cannot converge unless a mechanism of energy absorption is introduced. In the experimental devices the wave energy can be partially transferred to the sheath present on all conducting walls immersed in the plasma. Modelling of this physics was done in [Myra2008]. In this thesis, the non-linear sheath physics is not implemented. Another mechanism of the energy absorption is the collisional damping in the whole plasma volume and it is adopted as the next improvement of the discussed model.

The collisions are implemented to the COMSOL model by following replacements (according to the theory in [Booker1984]):

$$\Omega_{ce} \rightarrow \Omega_{ce} \frac{1}{1-i(\nu_{en}/\omega)} \tag{4.4}$$

$$\omega_{pe} \rightarrow \omega_{pe} \frac{1}{1-i(\nu_{en}/\omega)} \tag{4.5}$$

Corresponding replacements for the ions were omitted, since the collision frequencies of ions with any other particles are negligibly small in the considered case. For electrons the elastic electron-neutral collisions are dominant in the low-density edge plasma [Franz2009]. Their frequency is defined as:

$$\nu_{en} = n_n \sigma_{e-n} v_e \tag{4.6}$$

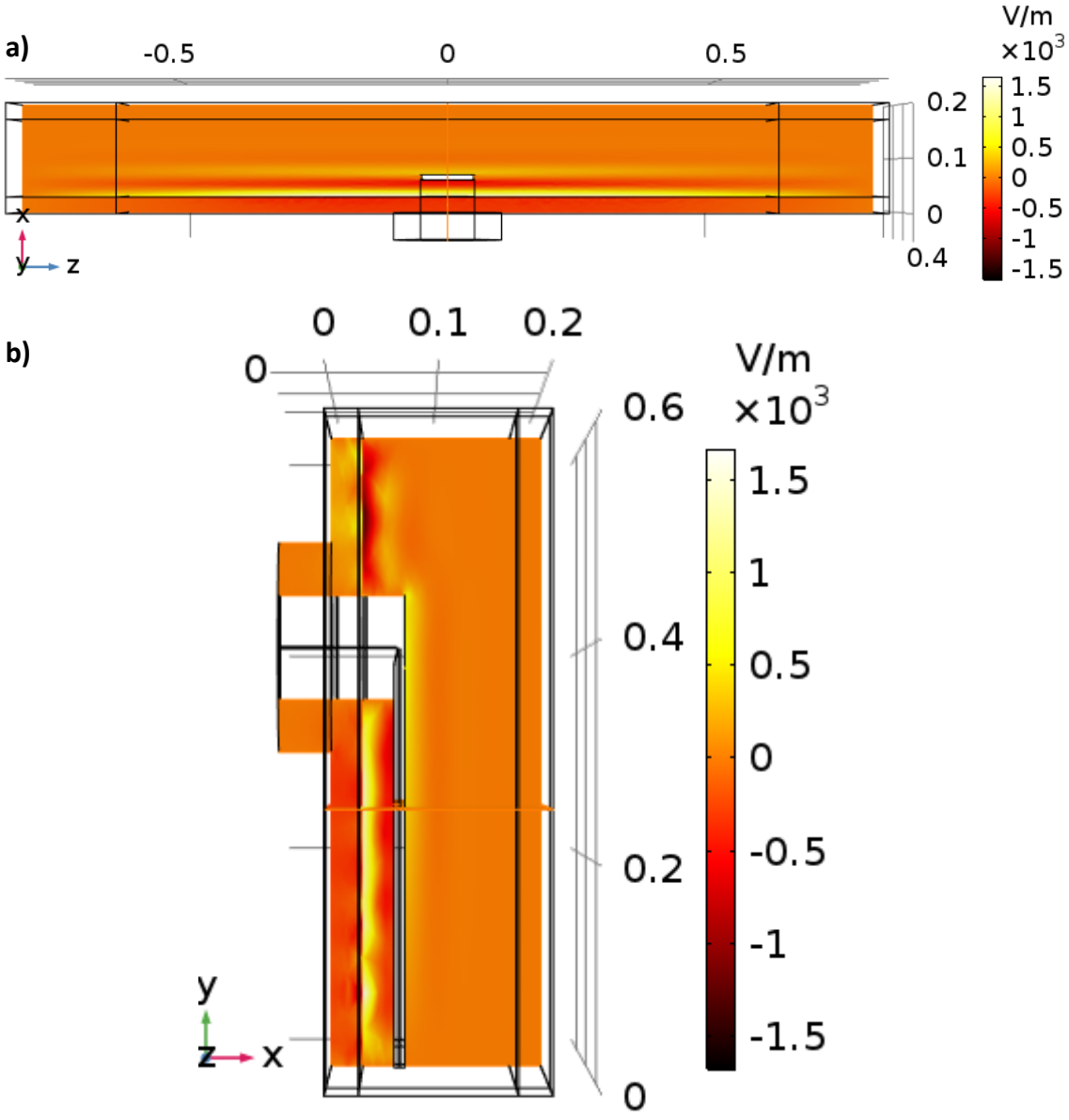

Fig. 4.40. Solution with the antenna in the plasma, n = 5*10^{15} m^{-3}: (a) top view, (b) side view.

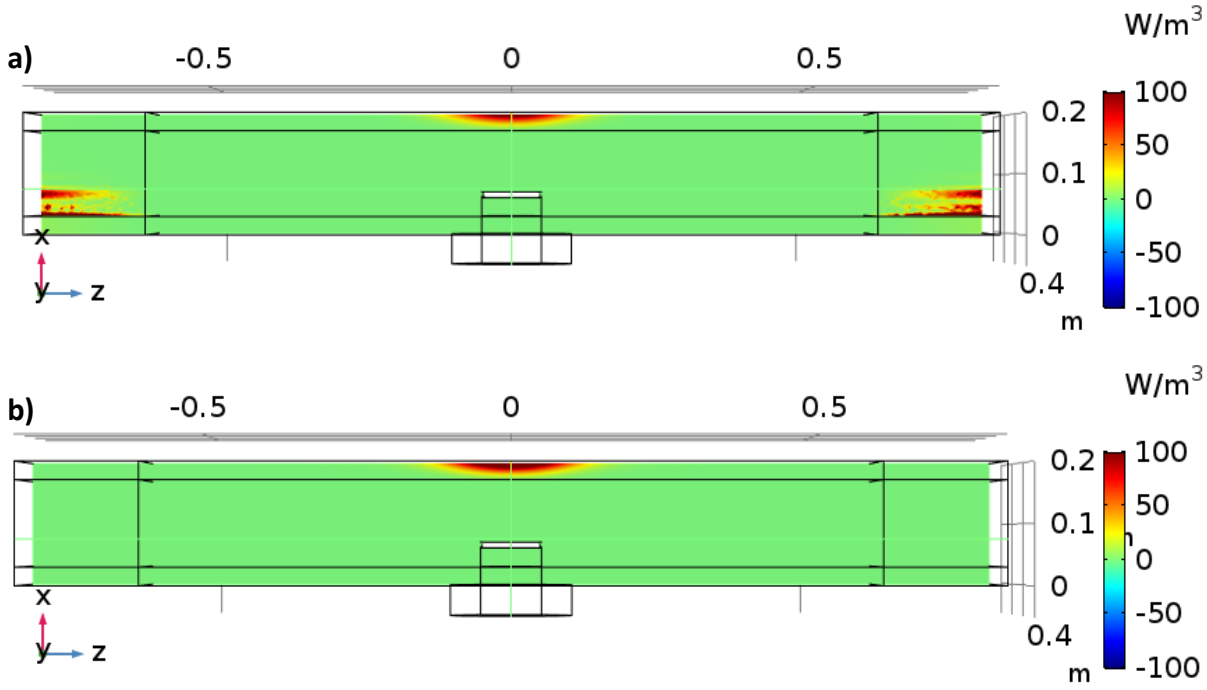

Fig. 4.41. Total power dissipation density: (a) with plasma, n = 5*10^{15} m^{-3}, (b) with vacuum.

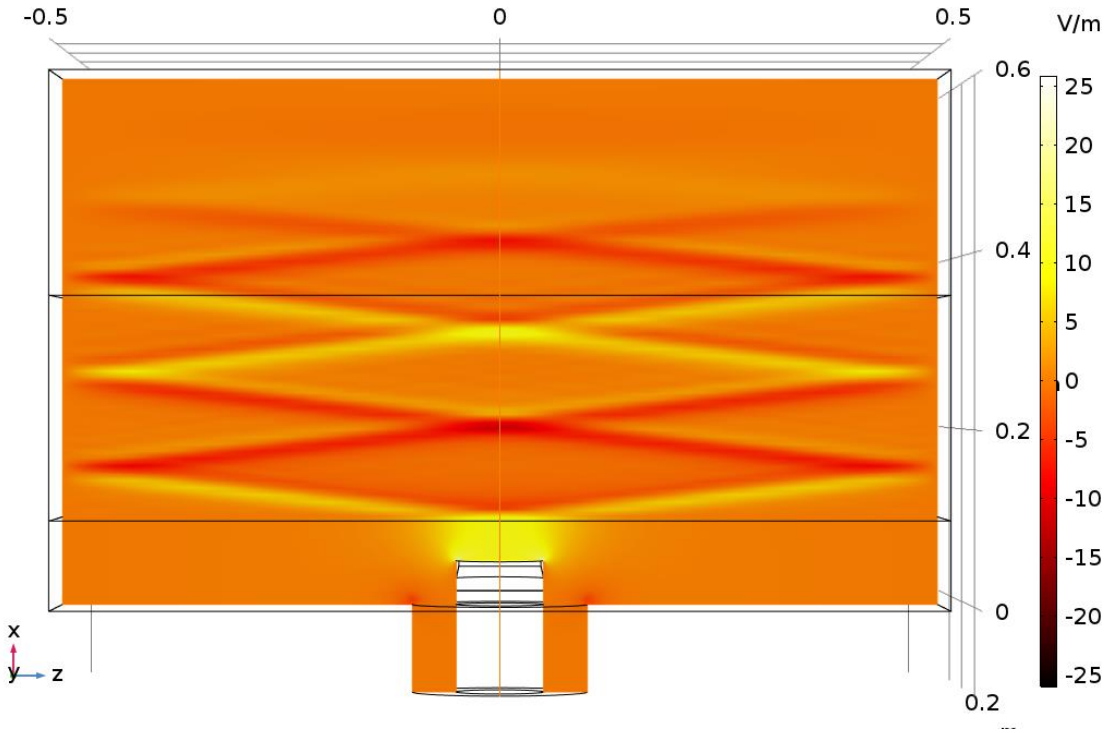

Fig. 4.42. Resonance cone reflection from metallic side walls (collisionless plasma).

For IShTAR conditions (Ar, T_e = 5 eV, p_n = 0.2 Pa, T_n = 300 K) the collision cross-section is σ_{e-n} = 8*10^{-20} m^2 [Franz2009], the neutral density is $n_n = \frac{p_n}{kT_n}$ and the average electron speed is $v_e = \sqrt{\frac{8kT_e}{\pi m_e}}$ for Maxwellian velocity distribution. It results in ν_{en} = 5.8 MHz*rad for Ar (and 3.6 MHz*rad for He).

This value is smaller than $\omega = 2\pi f \approx 36$ MHz*rad, but of the comparable order, so the energy loss through collisions should be significant.

A model without the side PMLs but with the collisional losses converged successfully and the result can be seen in Fig. 4.43 for the same density n = 5*10^{15} m^{-3} as in Fig. 4.40. The wave decays on the simulated length and no substantial reflections from the metallic walls occur which could prevent the model from converging to a steady-state solution. The absorption of the SW in the plasma volume is clearly seen (Fig. 4.43b), as well as the evanescent FW absorption in the front PML and can be compared to the Fig. 4.41 (note different color scale).

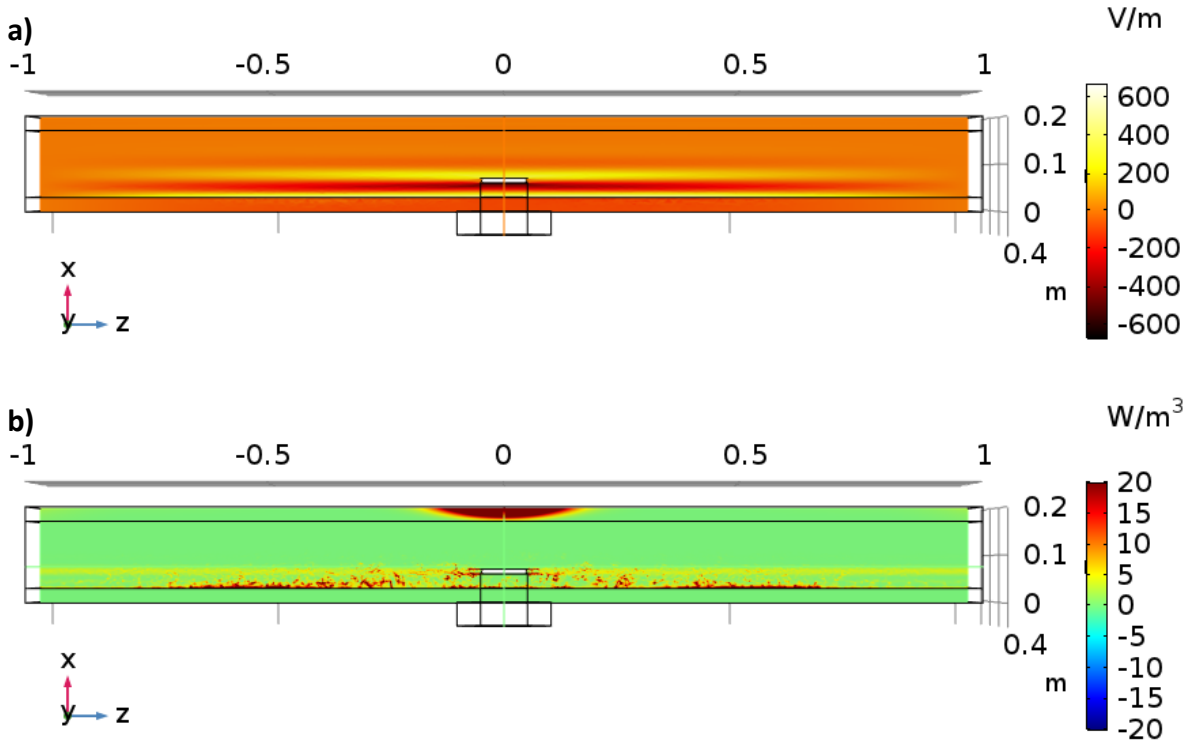

Fig. 4.43. Solution with the collisional losses and no side PMLs, n = 5*10^{15} m^{-3}: (a) electric field E_x, (b) total power dissipation density.

4.5.5 Results with antenna limiters

Since the wave propagates nearly parallel to the magnetic field in the conditions similar to the IShTAR experiments, the wave might never leave the antenna box, since it has limiters on the sides. The limiters can be implemented in the box model in order to obtain the wave behaviour in their presence. The modified geometry is shown in Fig. 4.44. The limiters run all the way from the bottom of the box to the top. They are located at the same distance along z from the antenna as in IShTAR and protrude forward as far as the limiters in the experimental device. The corners are rounded to replicate the real limiters and to avoid numerical problems on the sharp edges.

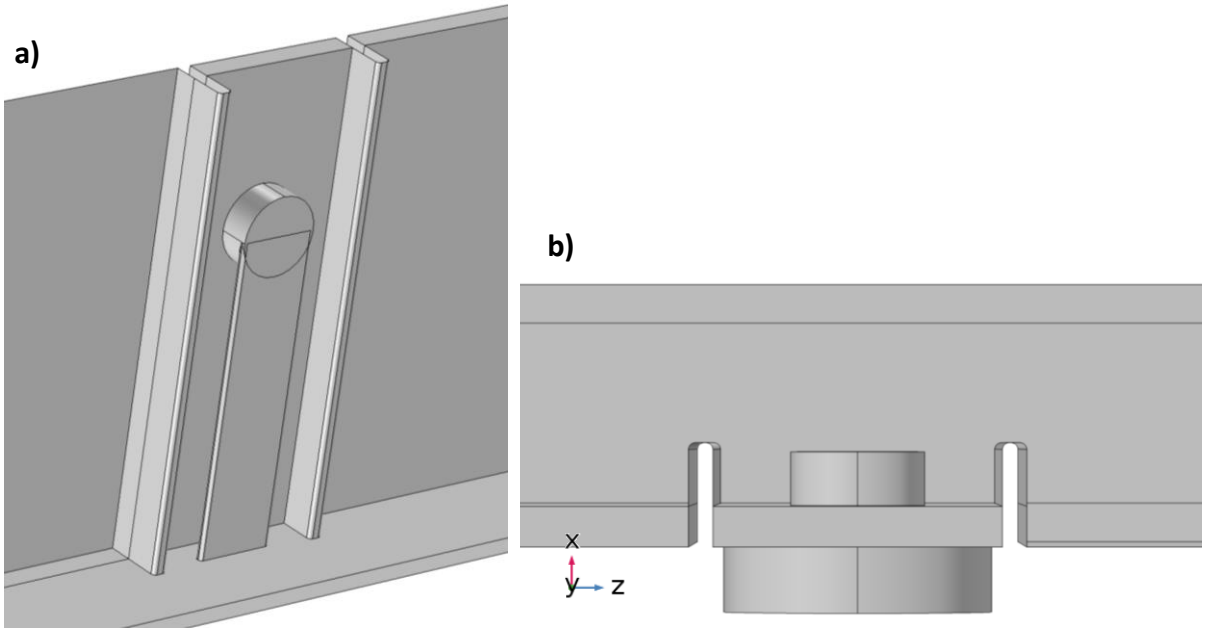

Fig. 4.44. Geometry with limiters added on the side: (a) side view, (b) top view.

The obtained solution for n = 5*10^{15} m^{-3} shows that it indeed happens that the wave is concentrated in a very small space in between the antenna limiters (Fig. 4.45). Almost all power is dissipated in that region (Fig. 4.46), the fraction of the FW power reaching the front PML is significantly reduced. For smaller density, for example n = 9*10^{13} m^{-3} the wave already propagates at an angle and the RC structure is seen outside the antenna limiters (Fig. 4.47). The parasitic structures beyond the RC are of the same size as a mesh element.

In IShTAR experiments in Ar densities of up to 5*10^{16} m^{-3} at the radial location of the antenna limiters are achievable in the present state of the device. For high densities (> 10^{14} m^{-3}) the wave structure is expected to resemble that of the Fig. 4.45, when the wave does not go outside of the antenna box. Lower densities at the antenna edge and inside the antenna box would result in a resonance cone structure that stretches outside of the antenna limiters. This kind of scenario is favorable if an RF sheath formation on the outer side of the antenna limiter needs to be studied.

From the results of the current Section 4.5 it can be noticed that the absolute values of the electric field differ a lot in the provided examples. They are dependent on the power which is coupled to the plasma, namely the field amplitude is proportional to the square root of the power (for the cases without collisional losses, where the field amplitude is constant along the RC). In the simulations the power, and as a result the field values as well, have random absolute magnitudes and it was not attempted to adjust them to the real experimental values. The reason is simple: the experimental values are unknown at the moment. The procedure of power measurements and the overview of the planned experiments are discussed in the next section. Once the experimental values are obtained, the absolute values in the numerical solutions can be calibrated.

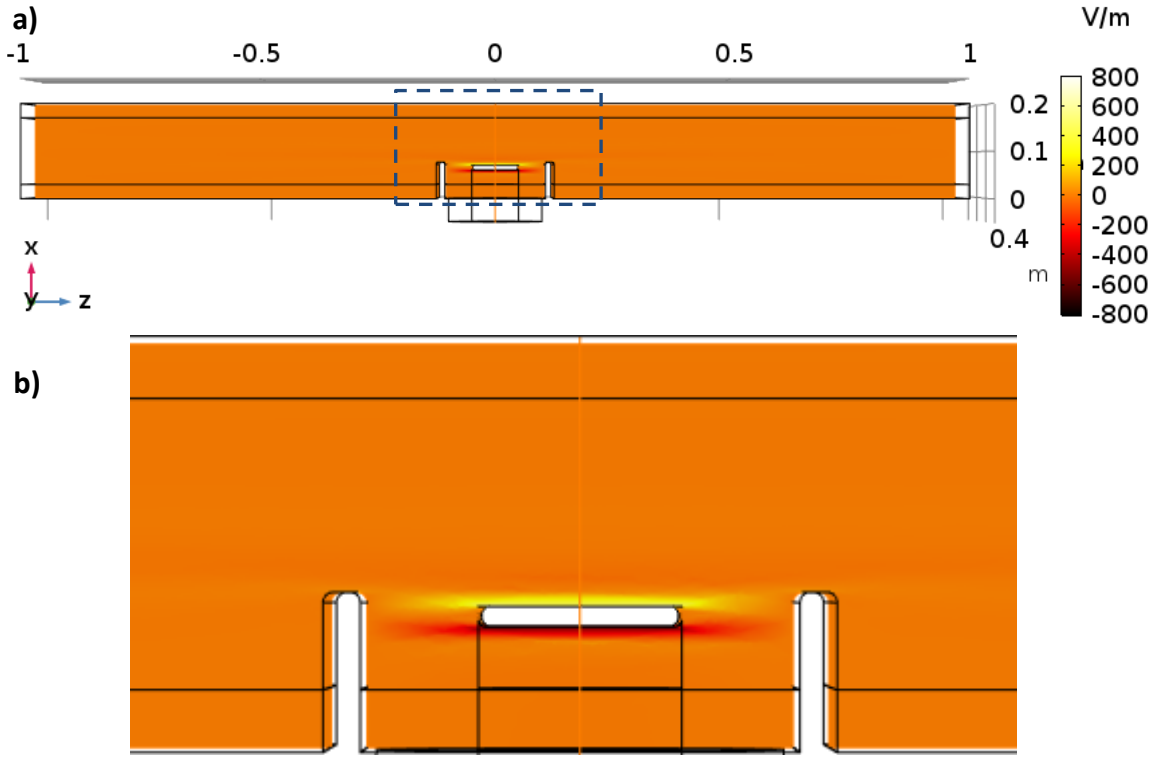

Fig. 4.45. Solution with antenna limiters, n = 5*10^{15} m^{-3}: (a) top view, (b) zoom of the central part of (a).

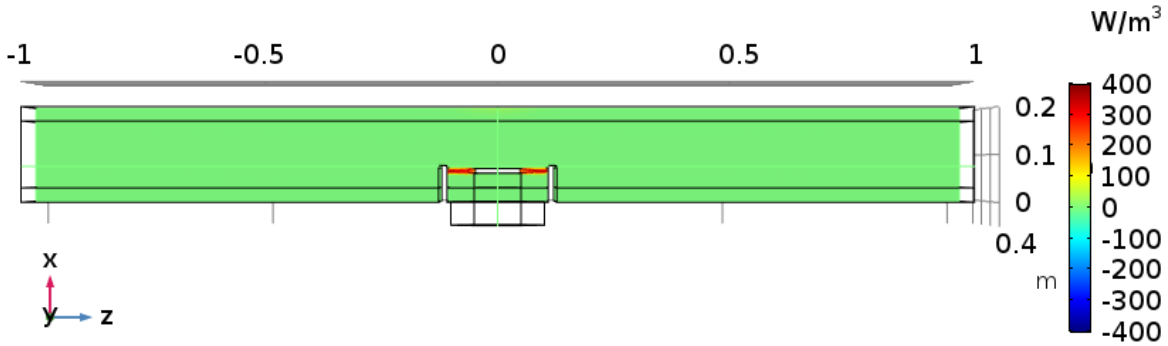

Fig. 4.46. Total power dissipation density in the model with antenna limiters, n = 5*10^{15} m^{-3}.

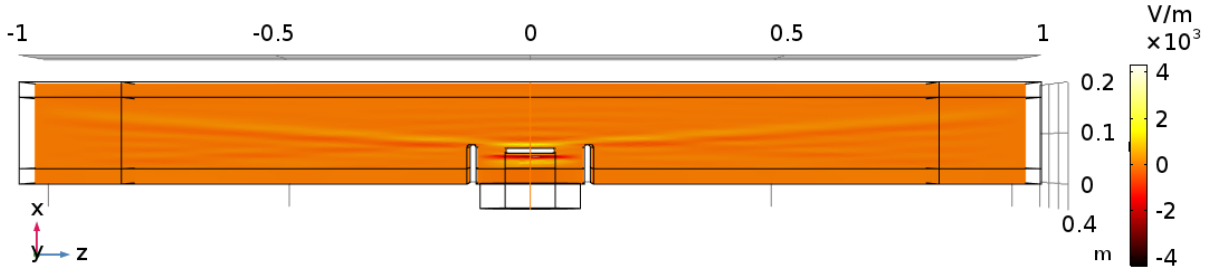

Fig. 4.47. Solution with antenna limiters, n = 9*10^{13} m^{-3}, top view.

4.6 Power coupled to plasma in IShTAR

The ICRF system principle was explained in Section 1.3 and schematically represented in Fig. 1.3. However, it was not mentioned that in real experiments not all the power which is generated,

amplified and sent to the plasma device actually reaches the plasma itself. The plasma is seen as a load in a resonance circuit which consists of a matching system, coaxial transmission lines, antenna grounded to the vacuum chamber and at the end the plasma itself (Fig. 4.48). The amount of power that is coupled to the plasma depends on the impedances of the parts of this circuit. The matching system plays a crucial role in maximizing the coupled power: by adjusting the components of the matching system (capacitors and inductors), the impedance of this part is varied; therefore a combination can be found which is favourable for the power transfer to the plasma. Such a combination is referred to as "good matching". The matching system of IShTAR is set up to provide the best matching conditions for the case when there is vacuum in IShTAR. Finding good settings for vacuum is much easier than for plasma (requires very simple equipment and only one-time adjustment). The present configuration was chosen as a first step, with the prospective of further adjustment of the matching system for the plasma conditions if needed.

4.6.1 Measurements in matched line

Measurements were done at the position (1) indicated in Fig. 4.48, in the "matched part" of the circuit (it is called so because it is located in the part where the matching is provided by the matching system; the line after the matching system is the "unmatched line"). A directional coupler (Fig. 4.49) was used to measure the forward power P_{fwd} and the reflected power P_{ref}. This device sends an attenuated small part of the wave power to the two outputs. By measuring these signals with logarithmic detectors (see Section 4.2.1.1 for the description) and knowing the attenuation factor of the directional coupler it is possible to calculate P_{fwd}, P_{ref} and then the reflection coefficient:

$$\Gamma = \frac{P_{ref}}{P_{fwd}} \tag{4.7}$$

The matching system of IShTAR is adjusted for vacuum, therefore it is expected that Γ is minimal when only vacuum is present in IShTAR and no plasma. The presence of the plasma would change the load impedance in the resonant circuit and would lead to a degraded power coupling. Results of the measurements in 3 plasma discharges are presented in Fig. 4.50. Each discharge includes different phases indicated on the picture. A discharge starts in vacuum, then the helicon antenna creates a low density plasma confined only by the small magnetic coils. After that the big magnetic coils are turned on and they provide higher magnetic field which leads to high plasma density. Then again a low density phase follows. Afterwards the helicon antenna is switched off and the very-low density plasma is sustained by the ICRF antenna only, first with the presence of the magnetic field of the small coils and then without. In the 3 discharges only the magnetic field in the high density phase was varied, leading to different plasma densities in that phase. All the other phases were identical.

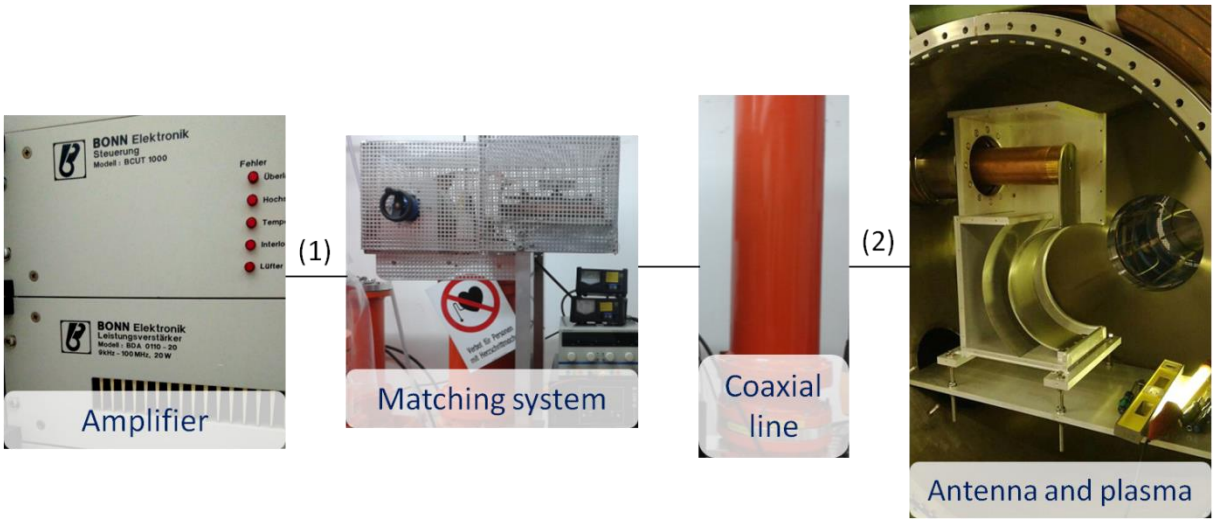

Fig. 4.48. Components of the circuit where the RF power is transferred. Numbers indicate the positions of power coupling measurements: (1) in the matched line, (2) in the unmatched line.

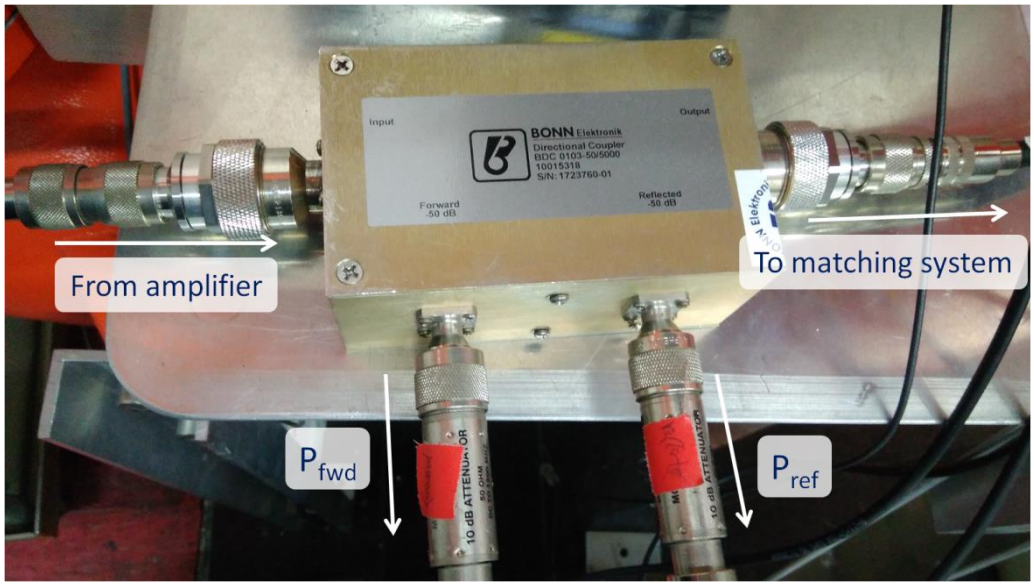

Fig. 4.49. Directional coupler setup.

The reflection coefficient is the smallest in the vacuum phase and in the presence of plasma more power is reflected for all plasma configuration. It is interesting that the two phases of low density helicon plasma provide different results, especially in He, and it can be explained by the vessel conditioning that happens during the high density phase. Since the reflection in the low density helicon plasma is larger than in the high density plasma, it means that the plasma load impedance differs more from vacuum in case of lower density. It might mean that the power absorption by plasma in this case is higher. However, this cannot be claimed with certainty unless the measurements of the power coupling are done in the unmatched line, at the location (2) in Fig. 4.48.

The power measurements in the matched line indicate only how much power is sent to and comes back from the whole resonant circuit which is after the matching system. Only part of this power is coupled to the plasma. The rest is dissipated to heat in the coaxial line and other metallic parts.

Measurements in the unmatched line together with the data from the matched line gives an opportunity to calculate the power that is coupled to the plasma.

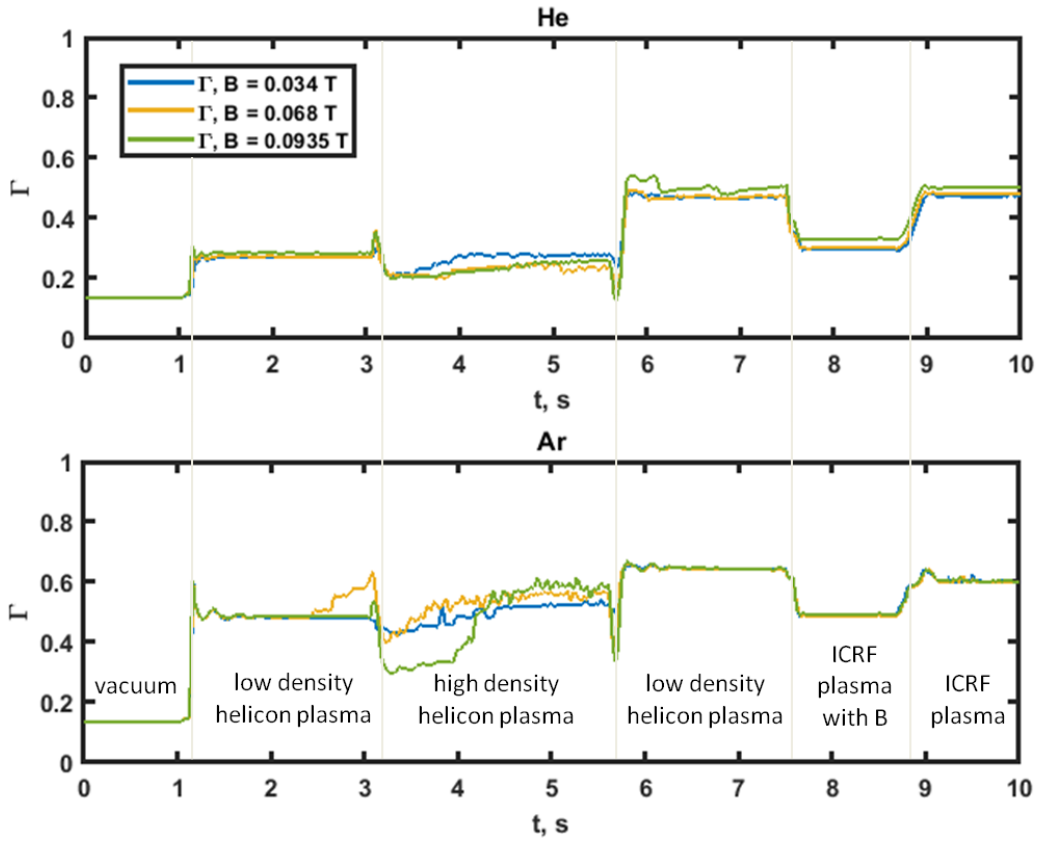

Fig. 4.50. Reflection coefficient during a discharge in He and Ar for 3 discharges in each gas.

4.6.2 Matching system in COMSOL

In COMSOL the RF wave excitation is defined at a special element – port. The coaxial port impedance value Z, if not specified, is defined by the port geometry:

$$Z = \frac{138 * \log_{10}\left(\frac{r_{out}}{r_{in}}\right)}{\sqrt{\varepsilon_r}} \quad (4.8)$$

where ε_r - relative permeability of the dielectric between the inner and outer conductors, r_{out} - outer radius, r_{in} - inner radius.

A possible way to build a matching system in COMSOL is to use the principle of matching with a central coaxial cable. The wave is excited at a lumped port (shaded in Fig. 4.51) on the left hand side of the coaxial cable 1 with U_0 = 1 V. The middle coaxial cable 2 performs impedance matching between the coaxial cable 1 and the load, which in this example is the coaxial cable 3. Two conditions must be fulfilled:

1. The length of the middle coaxial cable must be equal to one quarter of the wavelength: $l_{in2} = \frac{c}{4f_0}$.
2. The impedance ratios must be: $\frac{Z_1}{Z_2} = \frac{Z_2}{Z_3}$.

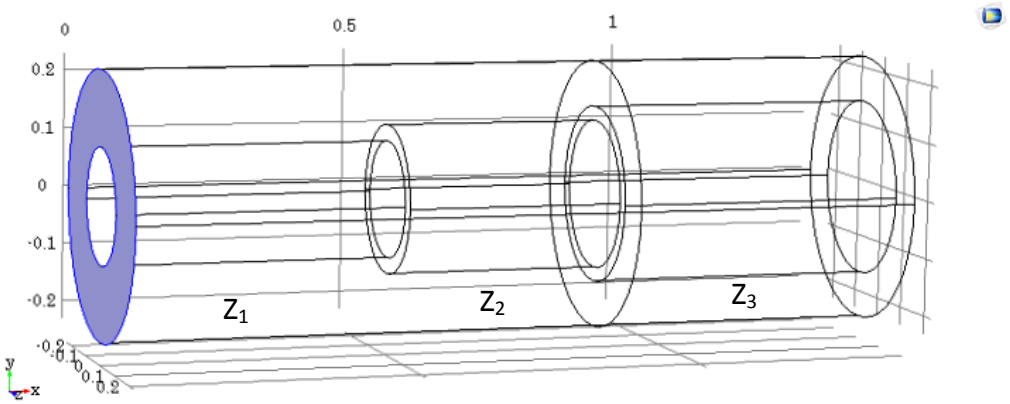

Fig. 4.51. Model with three adjacent coaxial cables.

The chosen conditions are: f_0 = 200 MHz, l_{in2} = 0.3747 m, Z_1 = 50 Ω, Z_3 = 25 Ω. For Z_2 a parametric sweep with 9 points is performed: r_{in2} = from r_{out}*0.025 to r_{out}*0.975 with a step of r_{out}/40, which means that Z_2 is in the range (221.18 Ω, 1.518 Ω). Thus, keeping the first parameter (l_{in2}) constant, the matching is tested for the varying second parameter (Z_2).

In COMSOL (and in some other RF related applications and literature) the reflection coefficient Γ is called S_{11} parameter (for port 1). S_{11} = 0 for a perfectly matched case and 1 for an absolute mismatch. In our test S_{11} should reach minimum at r_{in2} = 0.1276 m, i.e. Z_2 = 35.329 Ω. It coincides with data from modeling (fig. 4.52), which shows a minimum at r_{in2} = 0.1265 m, (with 0.0575 m step between points). The accuracy may be increased by a reduction of the step value.

For the same frequency two extreme cases of the load impedance were examined: $Z_3 \to 0$ and $Z_3 \to \infty$. For the $Z_3 \to 0$ case it is assumed that Z_3 = 5.45 Ω (r_{in3} = 0.21 m). The minimum of S_{11} should be at r_{in2} = 0.175 m (Z_2 = 16.5 Ω), which is confirmed in the modeling (Fig. 4.53). $Z_3 \to \infty$ is modelled as Z_3 = 260.2 Ω (r_{in3} = 0.003 m). The minimum of the reflection is expected at r_{in2} = 0.0344 m (Z_2 = 114 Ω), and modeling provides the same result (Fig. 4.54).

The tests are performed correctly, since for all three cases the minimum value agrees with the theory and for a broad parametric sweep the S_{11} parameter behaves as expected, i.e. it varies in the range from 0 to 1. The illustrated method can be used in modelling to perform matching of the two elements, if their impedances are known.

Another possibility to control the matching in COMSOL models is to use lumped elements, including a lumped port, for which the impedance can be specified. For such a port it is possible to see the port voltage, power and other parameters, as well as the impedance of the load, in the results of a computed solution.

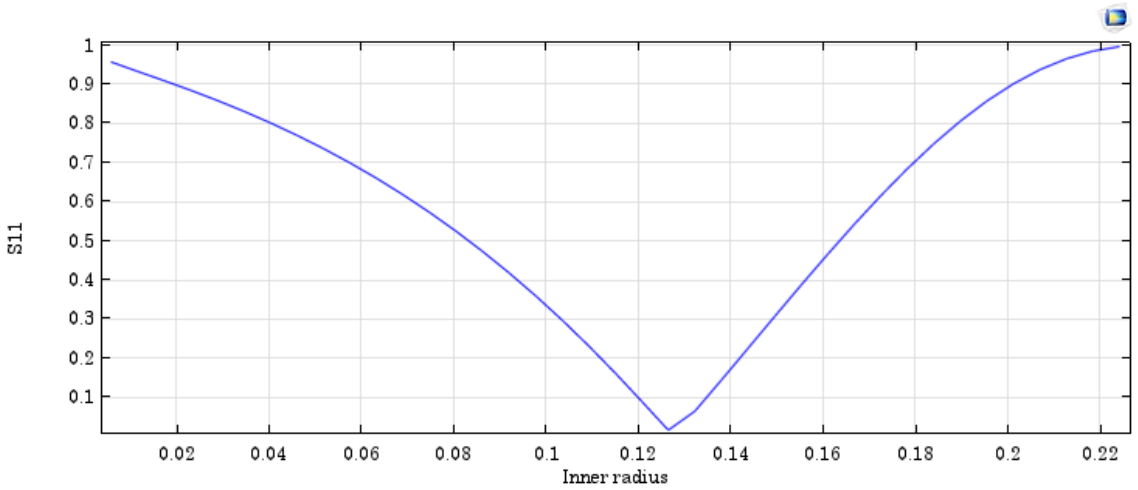

Fig. 4.52. Absolute value of S_{11} as a function of inner radius of the middle coaxial cable for Z_3 = 25 Ω.

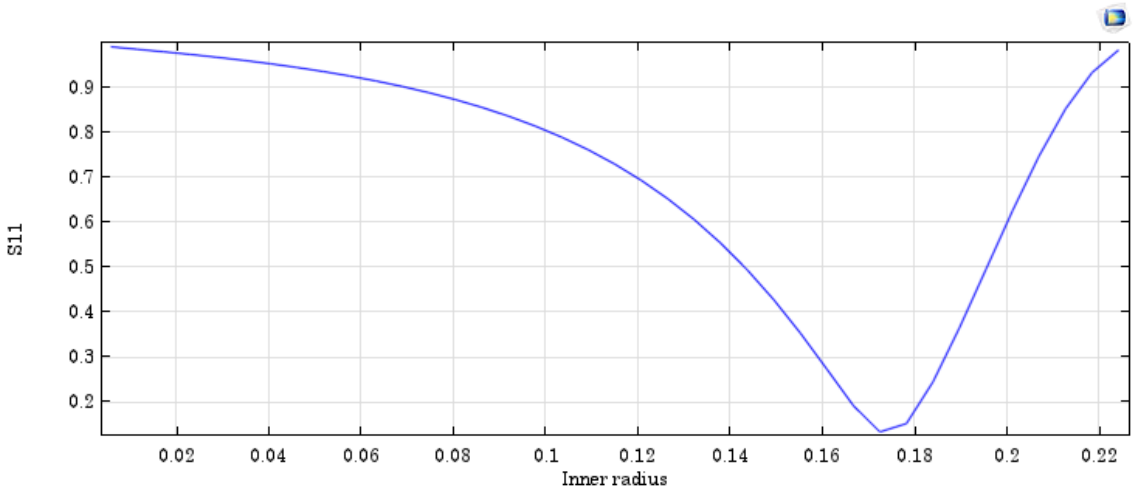

Fig. 4.53. Absolute value of S_{11} as a function of inner radius of the middle coaxial cable for Z_3 = 5.45 Ω.

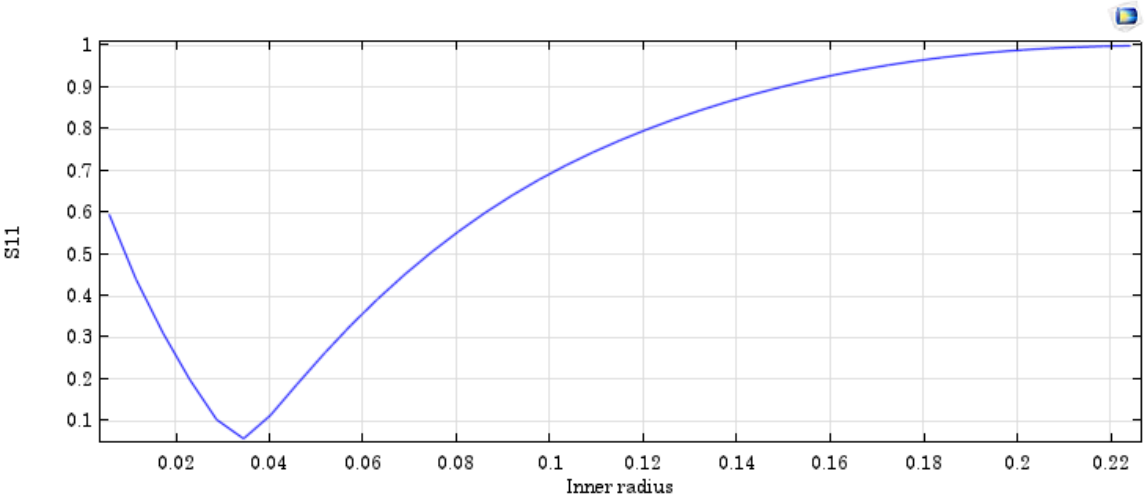

Fig. 4.54. Absolute value of S_{11} as a function of inner radius of the middle coaxial cable for Z_3 = 260.2 Ω.

4.6.3 Outlook for future measurements

As explained in 4.6.1, measurements in the unmatched line are necessary in order to compute the power coupled to the plasma. In the IShTAR coaxial transmission lines for this purpose a set of voltage probes were installed which are able to measure the voltage amplitude of the standing wave in the line (Fig. 4.55). Amplitudes of the components, the forward and the reflected waves, can be calculated, which gives the knowledge of how big the difference between these two values is. The difference is the power that reached the plasma.

Fig. 4.55. Array of voltage probes in the unmatched IShTAR coaxial line.

Different scenarios will be studied in order to find the conditions for which more power can be sent to the plasma. Since the supplied power is not as big in IShTAR as in tokamaks and the power absorption is quite low in the plasma, it is crucial to couple sufficient power to the plasma. Otherwise the generated RF fields will be too small to be measured by the installed diagnostics and the measurement of the RF fields in the sheath is the main objective of the device. In order to increase the amount of coupled power, one of the next steps should be a modification of the matching system to provide matching optimized not for vacuum but for the plasma.

4.7 Conclusions

A complex ICRF waves study for IShTAR is performed in this chapter. The wave equation solutions are applied to the IShTAR conditions and the plot of the wave modes propagation and evanescence is obtained. It is seen that only the SW mode can propagate and be studied in IShTAR, so the work is fully focused on this mode.

A comparison of the vacuum magnetic fields in the experiments and in COMSOL simulations proves the reliability of the created IShTAR model. The model is further used to calculate the spectrum of $k_{\parallel}$ of the antenna. The most important work is concentrated in the simulations of slow wave propagation in the plasma; it provides the insight into the slow wave physics and gives an idea of the field distribution that can be expected in IShTAR.

In experiments in Ar, densities up to $5*10^{16}$ m^{-3} at the radial location of the antenna limiters are achievable in the present state of the device. For higher densities (> 10^{14} m^{-3}) the wave structure in the experimental device is expected to resemble that of Fig. 4.45, when the wave does not go outside of the antenna box. The parallel electric field outside of the box is zero and cannot affect the sheath on the outer side of the limiters. Lower densities at the antenna edge and inside the antenna box would result in a resonance cone structure that stretches outside of the antenna limiters (Fig.

4.47). This kind of scenario is favorable if an RF sheath formation on the outer side of the antenna limiter needs to be studied.

From the obtained RC structures it is obvious that the simulations of the SW are only possible in 2D or 3D. A 1D model would not be able to represent the RC and to reproduce the wave propagation, in contrast with elliptic waves for which even in 1D a propagating wave can be simulated. The 3D modelling presented here assumed homogeneity along one coordinate (poloidal). The possibility to control the obtained solutions and to monitor the resulting violations of the assumed homogeneity gave a certainty in the identification of the numerical noise. It is very important that the distinction of the numerical noise in the SW simulations was achieved, since it was always an issue in previously attempted SW simulations.

A high numerical noise in the SW simulations is often attributed to the LH resonance vicinity. From the SW shape obtained in the presented simulations it is clear that the power of the SW is concentrated inside the small spatial region of the resonance cone. In case of a radial density gradient which includes the LH resonance at some distance from the antenna it is not possible for the SW to reach that region of densities, since the RC propagates nearly parallel to the magnetic field and not in the direction of the increasing density. The electric field outside of the cone is exponentially evanescent and is close to zero at some distance from the antenna. The characteristic size that needs to be resolved and that defines the wave field distribution is not the wavelength but the antenna radial and toroidal dimensions. A case when the SW propagation is resolved in the antenna vicinity and the LH density is present in the simulation domain was shown in Fig. 4.37b. The solution contained no propagation of the SW in the high density part (further radially from the antenna), so no wave structure was expected there and no significant numerical noise was caused. However, some reflections were still present and in order to have a clean solution the wave absorption in the modelling needs to be improved and all reflections eliminated.

The conclusion is that it is crucial to resolve the region of the SW propagation and to place the antenna inside the plasma if the SW propagation is expected to happen in a close proximity of the antenna strap. Otherwise the obtained solutions are most probably not reliable and contain high numerical noise, as was shown in one of the examples. If the LH resonance density is imposed directly around the antenna (not the case in IShTAR), the behaviour could differ, however it was observed that in a collisional plasma a case of quite high density (n = 5*10^{15} m^{-3}, Fig. 4.45) can be calculated and no significant numerical noise appears. The LH resonance presence at some distance from the antenna can be resolved and might not cause severe convergence problems in case the wave field reaching the LH density layer is considerably smaller than the field of the wave in the propagation region. The wave equation solution in plasma with radially varying density is integrable in case of the zero field at the LH resonance location, which means that the numerical solution in this case is identical to the true solution. In the presented simulations the field was not exactly zero, but a small non-zero value. Though the convergence was obtained, these solutions need to be further checked for the possible inconsistences with the theory.

Part of the work concerning the measurements of the power coupled to the plasma in IShTAR have been finished and is presented in this chapter. Future steps in order to complete this task are explained and the necessary diagnostics are being prepared. The absolute values of the coupled

power will give an estimate for the absolute values of the fields of the ICRF antenna, including the fields in the RF sheath.

References

[Booker1984] – H. G. Booker, "Cold plasma waves". Martinus Nijhoff Publishers, Dordrecht - Boston - Lancaster, 1984

[Crombe2014] – K. Crombé, D. Van Eester, R. Koch and V. Kyrytsya, "2D modeling of electromagnetic waves in cold plasmas", AIP Conf. Proc. **1580** (2014) 318

[Crombe2016JPP] – K. Crombé and D. Van Eester, "Parameter study of ICRH wave propagation in IShTAR", J. Plasma Phys. **82** (2016) 905820203

[Franz2009] – G. Franz, "Low Pressure Plasmas and Microstructuring Technology", ISBN 978–3–540–85849–2, 2009

[Jacquot2013Thesis] – J. Jacquot, "Description non-linéaire auto-cohérente de la propagation d'ondes radiofréquences et de la périphérie d'un plasma magnétisé", PhD Thesis (2013)

[Louche-Koch-lecture] – F. Louche and R. Koch, "The coupling of electromagnetic power to plasmas", FZ-Juelich

[Lu2016Thesis] – L. Lu, "Modelling of plasma-antenna coupling and non-linear radio frequency wave-plasma-wall interactions in the magnetized plasma device under ion cyclotron range of frequencies", PhD Thesis (2016)

[Myra2008] – J.R. Myra and D.A. D'Ippolito, "Resonance Cone interaction with a self-consistent radio-frequency sheath", Phys. Rev. Lett. **101** (2008) 195004

[Usoltceva2017] – M. Usoltceva et al., "IShTAR ICRF antenna field characterization in vacuum and plasma by using probe diagnostic", EPJ Web of Conferences **157** (2017) 03058

Conclusions

This thesis encompasses a range of smaller and bigger tasks, experimental, theoretical and numerical, which all are related to the ICRF physics. The framework of the studies is defined by the experimental devices Aline and IShTAR that are built especially to explore the RF sheath physics in simplified linear configurations with conditions similar to the plasma near the ICRF antennas at the edge of a tokamak. The ultimate goal of the dedicated testbeds is to explore the influence of the RF sheath, caused by the ICRF waves, on the local plasma conditions and on the plasma-wall interactions. These effects need to be understood in order to minimize them in the big plasma devices, where they lead to changes in the edge plasma density profiles, increased heat loads and hot spot formations on antenna structures and enhanced sputtering of plasma facing components.

Aline primary diagnostic is a Langmuir probe. With the high spatial precision of the 3D manipulator holding the probe and with the possibility to run very long and stable discharges where the whole region of interest can be mapped with the probe in unchanged conditions, the Langmuir probe diagnostic becomes a powerful tool for measuring finely resolved spatial distributions of plasma parameters. Such measurements are done in Aline with a simple RF antenna installed in the center of a vacuum chamber that creates a capacitive plasma discharge. Plasma potential, electron density and electron temperature distributions around the antenna, including the regions of the sheath, provide the information about the sheath properties and their dependency on the parameters such as magnetic field, pressure, RF power, etc.

Commonly for the Langmuir probes, the biggest difficulty in their operation lies in the data analysis. The interpretation of the IV characteristic is only easy for quite simple conditions, in magnetized plasma it is the case for planar probes with a relatively big area in the plane perpendicular to the magnetic field. Such a probe would cancel all the benefits of the Aline precise diagnostic system and would introduce non-negligible perturbations to the plasma. The work carried out in the frame of this thesis made it possible to interpret the data of a cylindrical probe that is placed parallel to the magnetic field or at a small angle to it and has a radius of the order of the electron Larmor radius. The main uncertainty - the collecting area of such a probe - has been resolved in the developed theories, which account for the particle transport in the probe vicinity and provide formulas for the effective collecting area as a function of the magnetic field and of the probe dimensions and orientation. It allowed calculating plasma density values. Improvements of the plasma potential and electron temperature evaluation also have been developed. The theories presented have been used to analyze the Aline data. Density profiles as a function of the magnetic field and the coupled RF power have been obtained. Averaged spatial density profiles are successfully validated with interferometry measurements. As a result of the work, the plasma parameters in the magnetized plasma on Aline can be obtained with high spatial resolution, which enables the studies of the plasma properties in the narrow sheaths.

IShTAR is closer to tokamak conditions than Aline in the context of the ICRF waves and plasma interaction. The main difference is the IShTAR antenna, which mimics tokamak ICRF antennas. A metallic strap couples power inductively to plasma, it is surrounded by limiters and the geometry is adjusted to the plasma shape to replicate poloidal symmetry. The goal of IShTAR is to study the RF sheath on the antenna structures. The first step preceding the local RF sheath studies was to investigate the global physics of the ICRF wave propagation in IShTAR and to explore it in various plasma scenarios. A comprehensive examination is presented in this thesis.

Using a theoretical description in the cold plasma approximation it was shown that the ICRF waves exist in two modes, slow wave and fast wave, which propagate in different density ranges and IShTAR conditions correspond to SW propagation. The FW is excited only in the evanescent form. Therefore it is possible in IShTAR experiments to decouple the role of the SW in contributing to the RF sheath effects. The presented research focused on physics of the SW. It was noted that the SW is electrostatic for the whole range of plasma conditions in the experimental device. Measurements of 4 radial profiles of the ICRF antenna magnetic field with an array of B-dot probes showed the same exponentially decaying behaviour in vacuum and in plasma. COMSOL simulations with realistic IShTAR geometry in vacuum also gave similar evanescent B-field profiles. The IShTAR model was further used to calculate the spectrum of $k_{\parallel}$ of the antenna.

The most important work is concentrated in the simulations of SW propagation in the plasma; it provided the insight to the slow wave physics and showed that this mode is considerably different from the fast wave. Theoretical calculations showed that the wavefront shape of the SW is not elliptic as that of the FW but hyperbolic; no periodic wave structure appears for such a wave shape, the whole energy of the wave is concentrated in the narrow region of the hyperbola. This type of waves is commonly called a "resonance cone" in the literature and it has been reported previously in the experimental and theoretical plasma physics articles, as well as in the papers related to metamaterials. The resonance cone structures were obtained in the 3D COMSOL simulations for the plasma conditions relevant for IShTAR. It was shown that the cone angle depends strongly on the density for a constant magnetic field; it gets smaller with the growing density. For relatively high densities the cone is nearly parallel to the magnetic field, which means that the SW is located at the radial position of the antenna and does not propagate further radially. Consequently, the SW cannot reach the LH resonance density layer unless the resonance layer is right next to the antenna. Numerical issues reported in other works in the vicinity of the LH resonance were not observed and some possible numerical noise was demonstrated and explained. By resolving the region of the SW propagation and by placing the antenna inside the plasma (instead of additional vacuum layer), it became possible to obtain converged solutions without significant numerical noise. The characteristic size that needs to be resolved is not the wavelength (it does not define the wave field distribution) but the antenna dimensions (radial and toroidal).

The SW energy density decays exponentially outside of the resonance cone. Power absorption plots were obtained from COMSOL which demonstrated that the energy is carried in the narrow cone region. Collisional damping plays a significant role in IShTAR where the neutral pressure is quite high, so the collisional absorption modelled in COMSOL resulted in strong wave amplitude attenuation in the plasma volume. Without any absorption the wave would reflect from the metallic walls at a nearly normal angle and such multiple reflections would lead to continuous pumping of the energy in the narrow region near the antenna. In numerical simulations it cannot lead to a steady-state

converged solution, so it is necessary to introduce any kind of losses (PML, collisions, ohmic losses, etc.).

The power absorption in the experiment should provide an input for the simulations in order to obtain absolute values of the fields. The procedure of power coupling measurements was explained and results were given for the first steps that are already completed. The amount of power coupled to the plasma needs to be measured and also possibly maximized by adjusting the matching system; the RF sheath fields in IShTAR should be strong enough ($>10^5$ V/m) to be detected with the dedicated spectroscopic diagnostic. Further experimental work on the power coupling optimization is foreseen as described.

Advancements in Langmuir probe diagnostic for precisely localized measurements, such as in the RF sheath, and in the modelling of the ICRF slow wave in 3D, achieved as an outcome of this PhD thesis work, contribute in general to the ICRF physics research and in particular to the task of understanding and avoiding parasitic effects on the antennas during active operations in the plasma. The results obtained will be used primarily in the continuing studies on the dedicated linear RF sheath experiments Aline and IShTAR. Applications of the results on other devices, e.g. tokamaks, are also possible and can be beneficial in order to refine and complement the techniques applied there, both for the Langmuir probes diagnostic systems and for the numerical simulations of the ICRF waves.